Assembly & disassembly of bioinspired single-chain polymer nanoparticles

by Ana Belén Sánchez Sánchez

Thesis Director: Prof. José A. Pomposo

Donostia-San Sebastián 2014

eman ta zabal zazu

Universidad del País Vasco

Euskal Herriko Unibertsitatea

Materials Physics Center

Centro de Física de Materiales

Eskerrik asko / Muchas gracias / Thank you!

Durante estos cuatro años son muchas las personas e instituciones que han participado en este trabajo y a quienes quiero expresar mi gratitud por el apoyo y la confianza que me han prestado.

En primer lugar quiero agradecer al Prof. Juan Colmenero por acogerme en el grupo "Polymers and Soft Matter", a la Universidad del País Vasco por la oportunidad que me ha dado para poder realizar la Tesis y al Gobierno Vasco por la concesión de una beca PREDOC para la obtención de la misma.

Quisiera agradecer especialmente a mi director de tesis Josetxo Pomposo por su ayuda constante y seguimiento diario de mi trabajo. Josetxo gracias por tu apoyo y confianza en mi trabajo. Gracias además por tu cercanía y disponibilidad mostradas durante estos años.

Agurtzane Múgicari eskertu nahi nioke, ni Manchesterren negoen bitartean nitaz gogoratu zelako Tesia egiteko aukera sortu zenean, eskerrikasko benetan! Horretaz gain, tesi honetan Kimika Fakultateko zenbait iraskasleekin lana egiteko aukera izan dut. Eskerrikasko Agustin, beti laguntzeko prest egoteagatik eta Lourdes Irusta erakutsi didazun guztiagatik.

Quisiera agradecer especialmente a toda la gente que forma parte de "Polymers and Soft Matter" por toda su ayuda y apoyo mostrados durante estos años. Gracias Arantxa Arbe por tu ayuda, por tu interés en mi trabajo y por aquellos días midiendo es Suiza (PSI). Gracias a Ángel Moreno y Federica Lo Verso por el trabajo realizado en la simulación multiescala de las nanopartículas unimoleculares y por los buenos momentos que hemos compartido en diferentes congresos. También gracias a Ángel Alegría, Daniele, Fabienne, Silvina, Gustavo, Gerardo, Guiddo, Virginie, Mustafa, Luis y tantos otros con

los que he compartido buenos momentos durante las horas de trabajo o bien durante algunos congresos.

I would like to express my deepest gratitude to Dr. David Fulton for his guidance and support during my stay in Newcastle and I am also very grateful to Niza, Marta, Maria, Natalia and Alex for their support and help.

Ahora vuelvo al CFM ya que quiero recordar las comidas de los viernes, donde tan buenos momentos hemos pasado, tanto nos hemos reído y tanto hemos cocinado. Gracias especialmente a Giussepe, Eneko, Itziar, Yasmin, Lucciana, Rubén, Alicja, Manuel (¡siempre tienes historias sorprendentes que contar!) y a todos los que estuvieron ayudando, charlando o aportando recetas. Ahora me toca hablar de mis COMPAÑERAS de despacho de las que están y de las que no están: Lourdes, Lorea, Isabel, Irma, Luisa (de otro despacho aunque como si fuera del nuestro). Muchas gracias por los buenos momentos que hemos pasado, por las cenas (el famoso TSI TAO…), los viajes, por las charletas que hemos tenido y por aguantarme…Gracias de verdad! Alex, Natalia, Izaskun y Marina, sois los últimos en uniros al grupo, me lo pasó muy bien con vosotros ¡sois muy majos!, que pena no haberos conocido antes.

Kuadrilarentzat ere, pare bat hitz. Eskerrikasko hor egoteagatik eta beti hor egoteagatik eta nere txapa bukaezinak aguantatzeagatik!!

Y por supuesto el agradecimiento más grande a toda mi familia y en especial a mis padres y a mi hermano porque una pequeña parte de esta tesis y gran parte de lo que soy os lo debo a vosotros. Os quiero!

Azkenik bereziki zuri eskertu nahi dizut Jon Ander, eskerrikasko zure konfidantza eta animoengatik. Zu izan zara momentu txarretan Tesi hau idazteko momentuan ondoan izan dudana ta nahiz eta zuk ez pentsa asko lagundu didazu. Eskerrikasko nere ondoan egoteagatik.

Contents

CHAPTER 1:

Introduction, motivations and goals

1.1 Nanotechnology

The ideas and concepts behind nanoscience and nanotechnology started with a talk entitled "There's Plenty of Room at the Bottom" by physicist Richard Feynman in 1959, long before the term nanotechnology was used. In his talk, Feynman described a process in which scientists would be able to manipulate and control individual atoms and molecules. Over a decade later, in his explorations of ultraprecision machining, Prof. Norio Taniguchi coined the term nanotechnology. It wasn't until 1981, with the development of the scanning tunneling microscope (STM) which could image and manipulate single atoms that modern nanotechnology began.[1, 2]

Nanotechnology is commonly defined as the understanding, control, and restructuring of matter on the order of nanometers (from 1 to 100 nanometers) to create materials with fundamentally new properties and functions. In fact, a nanometer is a unit of spatial measurement that is 10^{-9} meter. Nanotechnology includes fields of science as diverse as surface science, chemistry, molecular biology, semiconductor physics, microfabrication, etc.[3] Solid-state physics and electronics have entered the field of nanostructures by making use of lithography and etching processes ("top-down" approach), which enable the fabrication of structures no smaller than ~20 nm. Nature, on the other hand, may serve as a model for the building-up of smaller structures. In this case, individual molecules are integrated into larger functional units and complex structural hierarchies *via* self-organization ("bottom-up" approach), leading to such advanced materials as DNA or viruses.

It is one of the great challenges in research disciplines like chemistry, physics, or materials science to have control over the composition, size, shape and functionality of **hard** and **soft** synthetic nano-objects. The huge interest in **hard** nanoparticles (e.g. metallic, metal oxides) has been a direct consequence of several new, nano-scale effects found in hard nanosized materials compared with their bulk counterparts.[4] A classical example concerns spherical gold

nanoparticles (Figure 1.1 A), showing a specific UV−Visible plasmon resonance band as a consequence of electron surface confinement, which can easily be tuned by changing nanoparticle size and shape.

Concerning artificial **soft** nano-objects, significant advances have been made in the last decades in the control of macromolecular architectures thanks, mainly, to the development of efficient controlled radical polymerization (CRP) techniques. In fact, several complex architectures such as: star polymers, comb-like copolymers and hyperbranched macromolecules have been generated using CRP techniques;[5-8] the resulting materials possessing properties very different from those of their linear counterparts of equivalent molecular weight (Figure 1.1 B). A particular class of artificial soft nano-objects is single-chain nanoparticles (SCNPs).

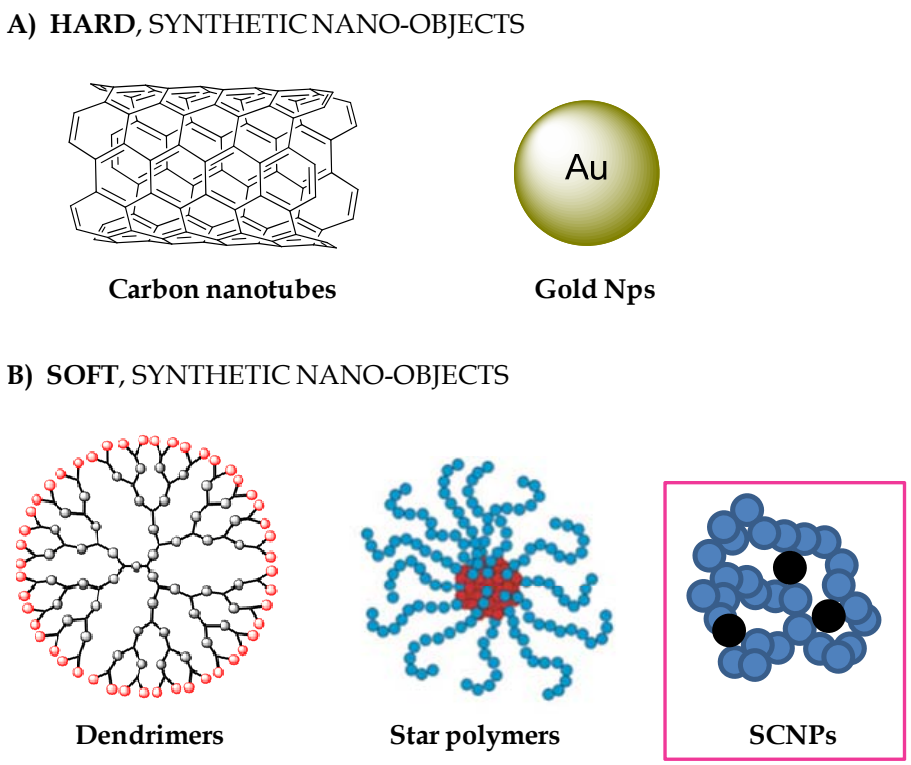

Figure 1.1. A) Interest in hard, synthetic nano-objects like gold nanoparticles or carbon nanotubes was driven by the interesting nano-scale properties shown by these nanosized particles compared with the corresponding bulk materials.[4] **B)** Controlled radical polymerization (CRP) techniques paved the way to the synthesis of soft, synthetic nano-objects of complex architecture such as star polymers, comb-like copolymers, hyperbranched polymers[5−8] or single-chain nanoparticles (SCNPs).[9]

1.2 Single-chain polymer nanoparticles

Single-chain nanoparticles (SCNPs) are individual intrachain crosslinked polymer chains that have attracted significant attention in the polymer field and the nanoscience arena.[9] One of the main characteristics of SCNPs compared with conventional latex particles is their ultra-small size (<15 nm) and consequently their inherent large surface-to-volume ratio as well as the absence of any emulsifier during their synthesis at high dilution.

It is worth mentioning that the controlled folding/collapse process during SCNP formation is reminiscent of protein folding to the native functional state, although single-chain nanoparticles mimic the globular structure of biomacromolecules only in a very rough, primitive manner. This is a consequence of the polydisperse nature (in size and composition) of current synthetic polymers showing a distribution of molar mass when compared to the perfectly monodisperse nature and precise chemical sequence of natural biomacromolecules. Even so, due to their exceptional properties, unimolecular polymeric nanoparticles have been evaluated as rheology agents[10-11], enzyme mimics[12-13], drug/siRNA/peptide nanocarriers[14–17], image contrast agents[18–20], sensors[21], catalytic systems in water[22] and smart gels.[23] As illustrated in Figure 1.2, synthesis of single-chain nanoparticles relies on the use of a combination of three main techniques.

The first one is *controlled polymerization*, allowing the development of well-defined single-chain polymeric precursors of controlled molar mass and narrow size distribution to guarantee as much as possible the uniformity of the resulting unimolecular nanoparticles.

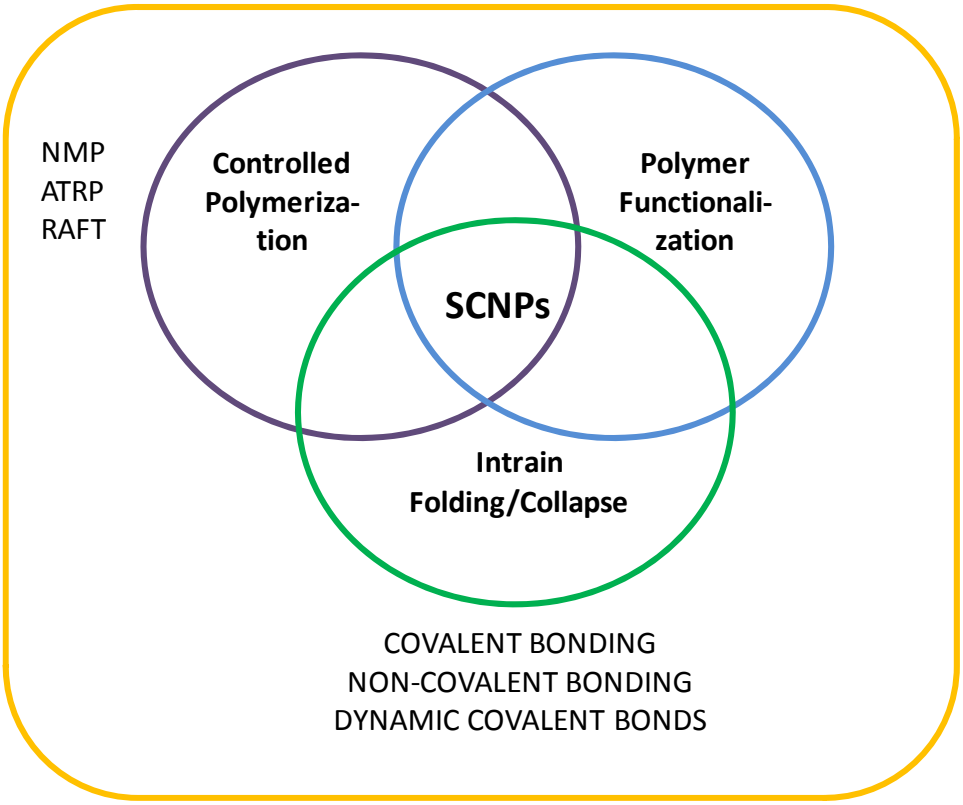

Figure 1.2. Illustration of the different techniques involved in the construction of single-chain nanoparticles (SCNPs): controlled polymerization, polymer functionalization and polymer folding/collapse.

The second technique involved is *polymer functionalization*, allowing the decoration of the uniform polymeric precursor chains with appropriate functional groups for the corresponding folding step to collapsed single-chain nanoparticles. Under certain circumstances, as will be shown in Chapter 2, 3 and 4, the use of this second technique can be avoided through the preparation of well-defined copolymer precursors containing both inert and reactive functional groups distributed along the individual chains (often in a random, statistical fashion).

The third fundamental technique involved is using *intrachain folding/collapse* for the efficient transformation of the precursor coils to folded unimolecular nanoparticles. In the following sections, we will describe in detail each of these techniques.

1.2.1 Controlled radical polymerization techniques

The development of controlled radical polymerization (CRP) processes allowing the facile construction of polymers approaching the polydispersity values of well-defined anionic "living" polymers with controlled architectures (stars, combs, dendrimers) and good tolerance towards the presence of a broad range of monomer functional groups has given rise to an exponential use of specialty polymers synthesized *via* CRP in nanoscience and nanotechnology applications.[24] Currently, the most common CRP techniques employed are reversible addition fragmentation chain transfer (RAFT) polymerization[25], atom transfer radical polymerization (ATRP)[26], nitroxide mediated radical polymerization (NMP)[27] and recently, ring opening metathesis polymerization (ROMP) using second (or higher) generation of Grubbs catalysis has gained significant interest as a relatively new controlled polymerization technique.[28] Of the several controlled polymerization methods mentioned above, in this PhD thesis **RAFT** polymerization was used because it allows an exquisite control of the molecular weight distribution of the single-chain nanoparticle precursor and is a tolerant technique for monomers that have a broad range of functional groups, without involving any metal catalyst.

A) Reversible addition fragmentation chain transfer (RAFT) polymerization

Reversible addition fragmentation chain transfer, the RAFT polymerization process, using dithiocarbamate RAFT agents was first reported by CSIRO (specifically by G. Moad, E. Rizzardo and S.Thang) in early 1998. Researchers from France reported a process with an analogous mechanism but using xanthate RAFT agents (MADIX) in late 1998. A CSIRO patent claiming the use of xanthate and dithiocarbamate RAFT agents appeared in early 1999.[29] The RAFT method has some crucial advantages over ATRP and NMP in terms of a wide range of accesible functionalities, monomers and solvents.[30] Well-defined polymers with complex macromolecular structure can be readily generated *via* RAFT technique that has more tolerance to different monomers and functional

groups. Moreover, free radical polymerizations can be readily converted into a RAFT process by adding an appropriate RAFT agent while other reaction parameters can be kept unchanged. The RAFT polymerization is composed of a small amount of RAFT agent, a monomer and a radical initiator.[29]

In fact, the RAFT process is a reversible deactivation radical polymerization (RDRP) technique that offers exceptional versatility in providing polymers of predetermined molecular weight and very narrow polydispersity. This is achieved by performing the polymerization in the presence of certain dithio compounds (e.g. dithiobenzoates) which act as highly efficient reversible addition fragmentation chain transfer agents (CTAs) and provide the polymerization with living characteristics.[29, 31]

The mechanism of chain activation/deactivation in RAFT is shown in Scheme 1.1:

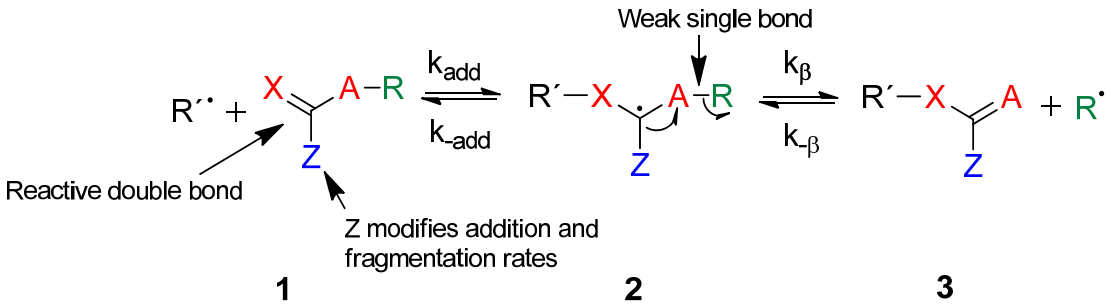

Scheme 1.1. Mechanism of chain activation/deactivation in RAFT polymerization.

The polymerization is performed with a conventional initiator (*e.g.* AIBN) in the presence of the chain-transfer agent (CTA, **1**). Reversible chain transfer requires that both **1** and **3** are active transfer agents under the polymerization conditions. More specifically, the general mechanism of RAFT polymerization is the following:

A. *Initation*

Upon thermal decomposition, the initiator (I) reacts with a monomer unit to create a radical species which starts the polymerization.

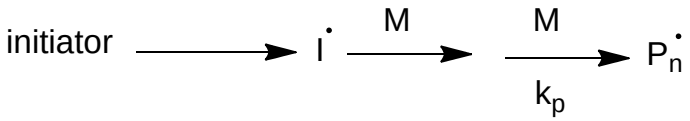

B. *Reversible chain transfer / propagation*

The active chain (P_n•) reacts with the CTA (*e.g.* a dithioester compound) and the R group becomes a reactive species. It is a reversible step, in which an intermediate species are capable of losing either the group (R•) or the active species (P_n•).

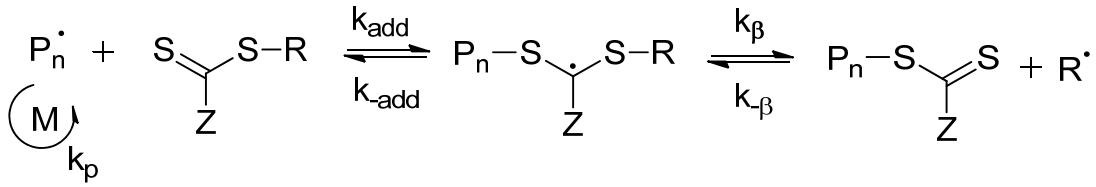

C. *Reinitation*

The group (R•) reacts with another monomer species, starting a new active chain (P_m•), which participate in the addition fragmentation equilibrium steps.

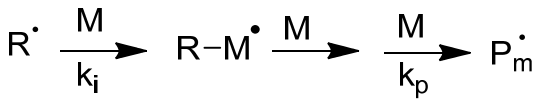

D. *Chain equilibration / propagation*

It is the fundamental step in which an equilibrium between dormant polymer chains and propagating radicals occurs.

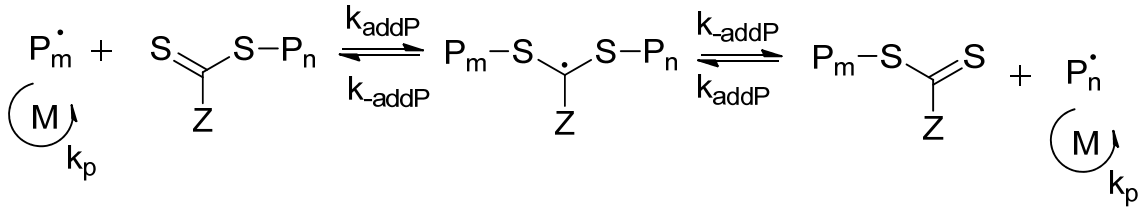

E. *Termination*

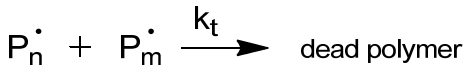

Radical-radical termination is not suppressed by the RAFT process although it is severely reduced. Retention of the thiocarbonylthio groups in the polymeric product is responsible for the living character of RAFT polymerization and renders the process suitable for synthesizing block copolymers and end functional polymers. Finally, selection of the RAFT agent (ZC(=S)SR) for the monomers and reaction conditions is crucial for the success of a RAFT polymerization experiment.

1.2.2 Polymer Functionalization

Polymer functionalization aims at the quantitative and selective modification of a given polymer using relatively mild conditions without any side reactions. Polymer functionalization is also known as post-polymerization modification or polymer analogous modification and it has a long history in polymer science.[32] The variety of chemical reactions available for post-polymerization modification has increased significantly since the middle 1990s due to the emergence of controlled/living radical polymerization techniques (RAFT, ATRP, NMP) showing improved functional group tolerance when compared to classical living anionic or cationic polymerization processes.

The most efficient and widely-used polymer functionalization reactions are:[32] (1) thiol-ene/thiol-yne additions (click reactions), (2) modification of epoxides, anhydrides, oxazolines and isocyanates by reaction with amines/alcohols/thiols (click reactions), (3) modification of active esters by reaction with amines, (4) thiol-disulfide exchange, (5) Diels-Alder reaction (click reaction), (6) Michael-type addition, (7) Copper-catalyzed azide alkyne cycloaddition (CuAAC) (click reaction) and (8) Modification of ketones and aldehydes with amines / alkoxyamines / hydrazines. A summary of the

different groups needed for the preparation of functionalized polymers *via* post-polymerization modification reactions is shown in Table 1.1. In this PhD thesis (except in Chapter 5) this step will be avoided through the direct preparation of well-defined copolymer precursors containing reactive functional groups distributed along the individual chains in a random manner.

Table 1.1. Highly-efficient reactions available for the preparation of functionalized polymers *via* post-polymerization modification.

Polymer Functionalization Technique	**Functional Groups Involved**	**Functionalizable Polymers**
Thiol-ene / thiol-yne additions	Thiol/alkene, alkyne	Polymers bearing alkene-, alkyne- or thiol-groups
Modification of epoxides, anhydrides, oxazolines and isocyanates by reaction with amines / alcohols / thiols	Epoxide, anhydride, oxazoline, isocyanate/ amine, alcohol, thiol	Polymers containing epoxide-, anhydride-, oxazoline-, isocyanate-, amine-, alcohol- or thiol-groups[33]
Modification of active esters by reaction with amines	*N*-Hydroxy-succinimide, pentafluorophenyl ester/ amine	Polymers bearing *N*-hydroxy-succinimide-, pentafluorophenyl ester- or amine-groups
Thiol-disulfide exchange	Pyridyl disulfide/thiol	Polymers containing pyridyl disulfide- or thiol-groups[14]
Diels-Alder reaction	Diene/alkene	Diene- or alkene-bearing polymers[34-36]
Michael-type addition	Acrylate, *N*-substituted-maleimide, vinyl sulfone/ thiols	Polymers bearing acrylate-, *N*-substituted-maleimide-, vinyl sulfone- or thiol-groups
Copper-catalyzed azide alkyne cycloaddition (CuAAC)	Azide / alkyne	Azide- or alkyne-bearing polymers[37-39]
Modification of ketones and aldehydes with amines/ alkoxyamines/hydrazines	Ketone, aldehyde / amine, alkoxyamine, hydrazine	Polymers containing ketone-, aldehyde-, amine-, alkoxyamine- or hydrazine-groups

1.2.3 Intrachain folding / collapse

Notably, three different strategies have been developed for single-chain nanoparticle construction: 1) intrachain homocoupling, 2) intrachain heterocoupling, and 3) crosslinker-induced collapse.

1) *Intrachain homocoupling*

In a homofunctional chain-collapse, the copolymer chain is functionalized with reactive self complementary ''R'' groups (i.e., vinyl double bonds) which are then reacted intramolecularly under diluted conditions (blue beads in Figure 1.3).

2) *Intrachain heterocoupling*

The heterocoupling chain collapse approach is very similar to the previous one, but instead of using one functional group, it requires two complementary functionalities ''R'' and ''X" simultaneously on the same polymer chain (blue and green beads respectively, in Figure 1.3). In this case, the reaction also needs to be performed under diluted conditions.

3) *Crosslinker-Induced Collapse*

The crosslinker mediated chain collapse strategy makes use of a crosslinker in order to synthesize unimolecular NPs. The polymer chain, which is functionalized with a suitable ''R'' functional group, is collapsed by reacting with the two ''X'' end groups of the crosslinker (blue and green beads respectively, in Figure 1.3). Undesired intermolecular crosslinking is often avoided by slowly adding one of the components to the other. The main benefits of this method are the easier synthesis of the precursor polymers and the possibility of introducing extra functionality through the crosslinking agent.

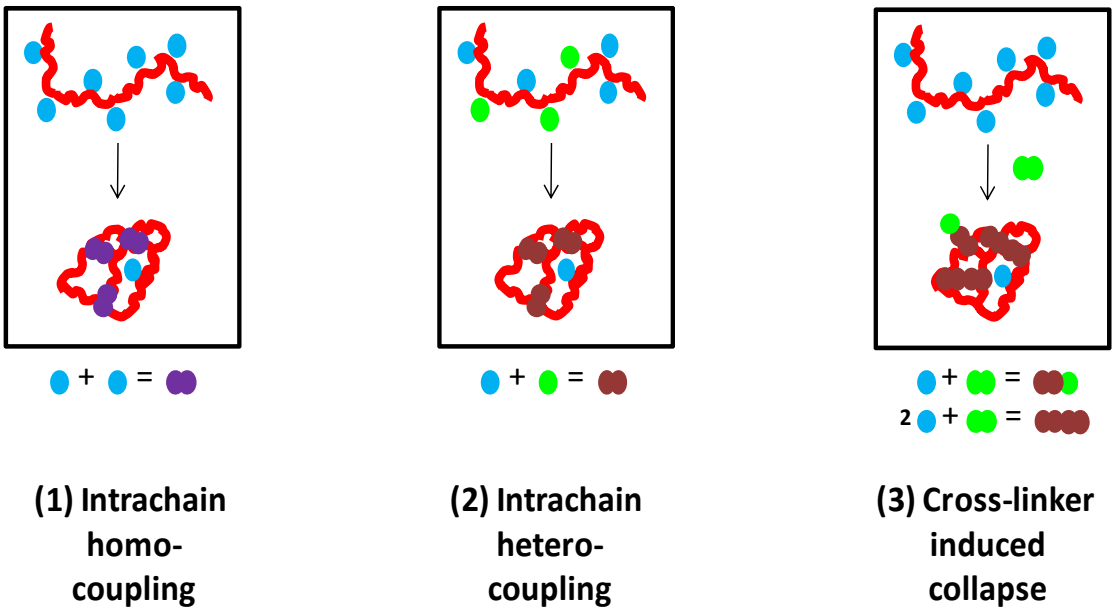

Figure 1.3. Three different methods have been developed for single-chain nanoparticle construction: (1) intrachain homocoupling, (2) intrachain heterocoupling, and (3) crosslinker-induced collapse.

Concerning the bonding interactions employed, single-chain nanoparticles can be formed through intrachain covalent bonding interactions (irreversible SCNPs) or intrachain non-covalent interactions and dynamic-covalent bonds (reversible SCNPs). Figure 1.4 and 1.5 provide a summary of the different irreversible and reversible single-chain polymer nanoparticle systems reported in the literature.

A) <u>Irreversible single-chain polymer nanoparticle systems</u>

The irreversible interaction that can be used for the synthesis of permanent single-chain nanoparticles (SCNPs) is covalent bonding.

• **<u>Covalent bonding</u>**

In the case of single polymer nanoparticles obtained *via* intramolecular covalent bonds, conventional organic reactions and "click" chemistry reactions have been utilized for the efficient preparation of robust unimolecular soft nanoparticles. It has to be noted that the covalent fixation of the polymer

geometry removes the dynamic nature of the single chain folded entity and does thus limit their application in biomimetic systems that rely on a dynamic configuration process, such as the folding / unfolding action that determines the functions of certain proteins.

The evolution of the field of single-chain polymeric nanoparticles synthesized by intramolecular covalent bonds is illustrated schematically in Figure 1.4.

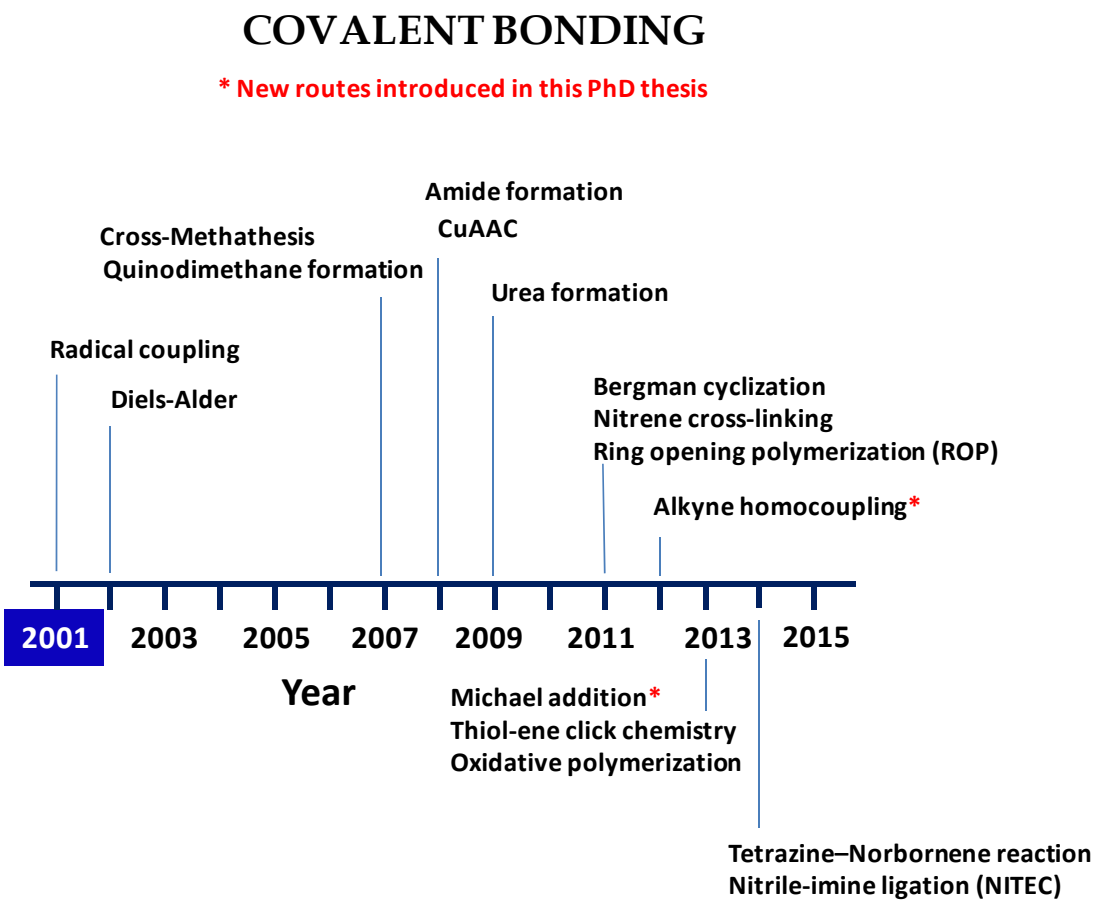

Figure 1.4. Evolution of the emerging field of irreversible single-chain polymer nanoparticles *via* covalent interactions. First synthesis of permanent single-chain nanoparticles was carried out by Mecerreyes, Hawker and colleagues[40] in 2001.

First reports about the synthesis of permanent single-chain nanoparticles by means of the intrachain homocoupling technique under high dilution conditions by Mecerreyes *et al*. relied on the use of poly(styrene)-, poly(alkyl methacrylate)- and poly(ε-caprolactone)-based precursors containing vinyl reactive functional groups.[40] Unsaturated functional groups were also used for

synthesizing poly(4-N-Boc-aminostyrene)- and poly(carbonate)- based single-chain nanoparticles by Jiang *et al*. and Cherian *et. al.*, respectively.[41,42] Poly(styrene)- and poly(alkyl methacrylate)-based unimolecular nanoparticles were synthesized in multigram quantities by Hawker and co-workers using benzocyclobutene containing precursors *via* intramolecular Diels-Alder reactions at a very high temperature (250^{o}C).[35] Later, benzosulfone-decorated poly(styrene)- and poly(cyclohexylacrylate)-based precursors were synthesized for the preparation of individual unimolecular nanoparticles *via* quinodimethane formation using this procedure by Harth and co-workers, although crosslinking reaction conditions were still very harsh (250 ^{o}C).[34, 43] Poly(methyl methacrylate) based single-chain nanoparticles have been obtained *via* intramolecular Bergman cyclization at relatively lower temperatures (150 ^{o}C) by Zhu *et al*.[44, 45] The synthesis of poly(styrene) and poly(alkyl methacrylate) based unimolecular nanoparticles *via* intramolecular cross-linking of sulfonyl azide- [46] and benzoxazine- [47] functionalized polymers still required very high temperatures (190–200 ^{o}C).

To solve the potential problems of precursor and nanoparticle thermal degradation, a new route has been introduced in this PhD thesis (Chapter 2), where naked propargylic-decorated single-chain nanoparticle precursors synthesized *via* redox-initiated RAFT polymerization were intrachain collapsed at room temperature under normal air conditions by means of Glaser-Hay coupling (C-C "click"chemistry).[48] Very recently, poly(styrene)-based unimolecular nanoparticles have also been prepared by Dirlam *et al.* through intrachain crosslinking *via* oxidative polymerization of 3,4-propylenedioxy-thiophene functional groups at 50 ^{o}C.[49]

As mentioned above, the fabrication of SCNPs has also been carried out using the intrachain heterocoupling technique. A representative example of the use of the intrachain heterocoupling technique was the construction of permanent single-chain nanoparticles through highly-efficient azide-alkyne

"click"chemistry (i.e., copper-catalyzed [3+2] cycloaddition of alkynes and azides (CuAAC)).[37] By using this technique, biofunctionalized poly(methyl methacrylate) unimolecular nanoparticles were prepared at room temperature at a high yield based on azide- and protected alkyne-decorated polymer precursors by Ruiz de Luzuriaga *et al*.[37] The technique was further simplified by Pomposo and co-workers starting with copolymers containing protected alkyne groups as well as chloromethyl groups, that were transformed rapidly and quantitatively to azidomethyl groups by means of a simple substitution reaction using sodium azide.[11] The intrachain heterocoupling technique has also been used to prepare thermoresponsive single-chain nanoparticles.[50] More recently, nitrile imine mediated tetrazole-ene cycloaddition (NITEC) has been used to synthesize well defined fluorescent single-chain nanoparticles.[51]

The difunctional crosslinker mediated collapse of polymer chains is another efficient and straightforward method for obtaining SCNPs. Water-soluble poly(γ-glutamic acid)-based single chain-nanoparticles have been fabricated through the crosslinker-induced collapse technique by using a biosynthetic poly(γ-glutamic acid) precursor and 2,2´-(ethylenedioxy) diethylamine as bifunctional crosslinker in the presence of carbodiimide.[52] The synthesis of poly(methyl methacrylate)- and poly(styrene)-based single-chain nanoparticles by intramolecular crosslinking of isocyanate functionalized copolymers with diamines (under severe anhydrous conditions) has also been reported by Hawker and co-workers.[33] Additionally, the high versatility of the crosslinker-induced collapse method *via* intrachain CuAAC was demonstrated by Ruiz de Luzuriaga *et al*.[38] in 2010 during the synthesis of single-chain nanoparticles of very different chemical natures. In this PhD thesis, as will be explained in Chapter 3, the Michael addition reaction will be introduced to synthesize poly(methyl methacrylate)-based single-chain nanoparticles mimicking transient-binding disordered proteins under mild reaction conditions (at room temperature and in the presence of oxygen).[53] More recently, single-chain polymer nanoparticles have been formed using polystyrenes decorated with

pendent norbornenes and a bifunctional tetrazine crosslinker, demonstrating that the formation of SCNPs can be carried out *via* a tetrazine-norbonene (Tz-Nb) reaction.[54]

B) <u>Reversible single-chain polymer nanoparticle systems</u>

The two main classes of reversible interactions that can be used for the synthesis of responsive structurally dynamic single-chain nanoparticles (SCNPs) are: i) supramolecular (non-covalent) interactions and ii) dynamic covalent bonds.

● **<u>Non-covalent interactions</u>**

Non-covalent bonds have fascinated scientists from different disciplines since the excellent work about hydrogen bonding by Linus Pauling in the 1930´s.[55] More recently, the "supramolecular chemistry" concept introduced by Jean Marie Lehn[56] opened the door to exploiting non-covalent bonds for the construction of a variety of advanced artificial architectures, including supramolecular polymers. A clear demonstration that main-chain supramolecular polymers are susceptible to external environment changes is that their molecular weights often depend on solvent polarity and concentration. This is a consequence of the effect of many factors (i.e., temperature, pressure, concentration, etc.) on the strength of non-covalent bonds and, consequently, on the equilibrium between bonded and non-bonded or free species.

Non-covalent interactions, also called supramolecular interactions, can fall into three major classes: i) *weak interactions* of 0-15 kcal/mol in bond strength, such as van der Waals forces, hydrophobic interactions, π-π stacking interactions and hydrogen bonds; ii) *medium interactions* covering 15-60 kcal/mol in bond strength, such as multiple hydrogen bonds and (weak) metal coordination complexes; and iii) *strong interactions* showing >60 kcal/mol in

bond strength, such as ionic interactions, host-guest interactions and (robust) metal coordination or chelate complexation. It is worth mentioning that the particular strength of non-covalent bonds depends on external influences such as the type of solvent, the temperature, the concentration etc. So most non-covalent interactions do not fall into a single category.[57] Furthermore, non-covalent or supramolecular interactions have been used to generate complex architectures involving non-covalent side-chain polymers,[58] multi-block supramolecular polymers[59] and multi-arm self-assembled stars.[60]

● **Dynamic covalent bonds**

Dynamic covalent chemistry deals with reversible covalent reactions that allow the free exchange of molecular components to achieve thermodynamic minimum of the system at equilibrium.[61] The dynamic covalent bond, having the nature of a robust covalent bond, can be broken and reformed only when specific external factors are present (e.g., catalysts). Otherwise, the reversible covalent bond is not susceptible to changes in concentration, solvent or, in certain cases, temperature. Moreover, dynamic covalent chemistry has been applied with success in the development of dynamic combinatorial libraries[62] and for drug discovery[63] and controlled delivery of fragrances.[64]

The evolution of the field of single-chain polymeric nanoparticles *via* non-covalent and dynamic covalent bonds is illustrated schematically in Figure 1.5. In this figure we have distinguished the different routes to supramolecular single-chain nanoparticles in blue, and the pathways to structurally dynamic unimolecular polymer nanoparticles in red.

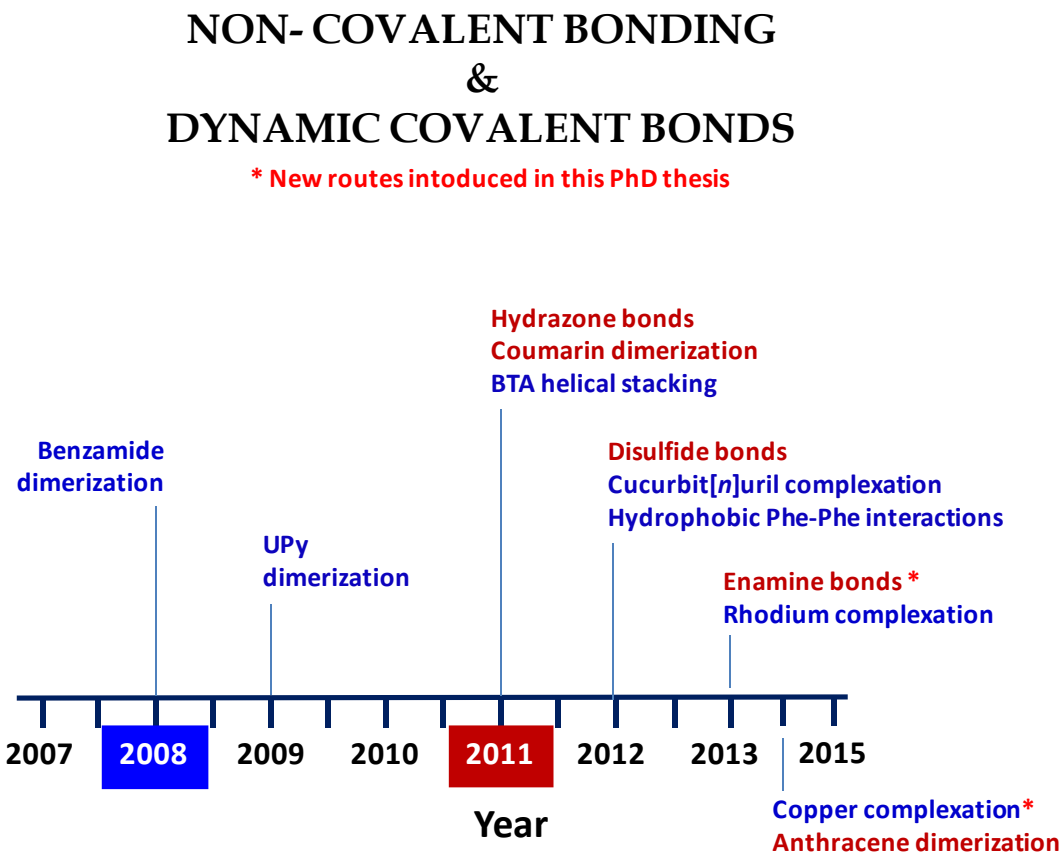

Figure 1.5. Evolution of the emerging field of reversible single-chain polymer nanoparticles *via* non-covalent interactions (blue) and dynamic covalent bonds (red). First synthesis of supramolecular single-chain nanoparticles was carried out by Hawker, Kim and colleagues[65] in 2008. First preparation of dynamic covalent single-chain nanoparticles was reported by Fulton and coworkers[66] in 2011.

Pioneering work by Hawker, Kim and colleagues[65] in 2008 demonstrated an efficient route to supramolecular single-chain nanoparticles through benzamide dimerization with a formation of quadruple hydrogen bonds between benzamide hydrogen bonding motifs. A huge amount of work was later performed by Meijer, Palmans and coworkers to push forward the field of metastable non-covalent bonded single-chain nanoparticles by introducing two orthogonal techniques based on ureidopyrimidinone (UPy)[67] and benzene-1,3,5-tricarboxamide (BTA)[68] hydrogen bonding motifs. The sequential synthesis of supramolecular nanoparticles involving the complementary self-assembly of UPy and BTA moieties has recently been demonstrated by Meijer´s group.[69] More recently, host-guest interactions involving cucurbit[*n*]uril complexation[70] and hydrophobic L-phenylalanine Phe-Phe interactions[71] have

been employed to synthesize water-borne supramolecular single-chain nanoparticles. Direct access to organometallic single-chain nanoparticles *via* poly(cyclooctadiene) complexes of rhodium (I) has been also reported.[72] Thus, in this PhD thesis we have developed metallo-folded SCNPs containing complexed Cu (II) ions showing catalytic specificity during oxidative coupling of mixtures of chemically related terminal acetylene substrates (see Chapter 4).[73]

Additionally, the seminal work by Fulton and coworkers[66] in 2011, covering the synthesis of single-chain polymeric nanoparticles *via* dynamic covalent hydrazone bonds, paved the way to the construction of structurally dynamic unimolecular nanoparticles. Independently, Zhao and colleagues in 2011 reported single-chain nanoparticle construction/disassembly based on the reversible photo-cross-linking reaction of coumarin activated by UV light at two different wavelengths.[74] A biomimetic approach to reversible polymer nano-objects using intramolecular disulfide bond formation was reported by Berda and colleagues[75] in 2012. In this PhD thesis, structurally dynamic single-chain nanoparticles that can reversibly undergo a coil to particle transition *via* dynamic enamine bonds will be demonstrated (see Chapter 5).[76] Recently, soft nanoparticles fabricated from single polymer chains *via* intramolecular photodimerization of pendant anthracene units has also been reported by Berda and coworkers.[77]

1.3 Applications of SCNPs

The potential applications of single-chain nanoparticles include: 1) catalysis, 2) sensing and 3) nanomedicine.

1.3.1 Catalysis

The use of catalytic single-chain nanoparticles for carbonate hydrolysis was first reported by Wulff *et al*.[12] Soluble single-molecule nanogels with a molecular

imprinted internal structure and containing just one active site per particle were reported by these authors in 2006. These single-chain nanoparticles showing 40 kDa in molecular weight were soluble in water/acetonitrile mixtures and displayed Michaelis-Menten kinetics in close analogy to natural enzymes.

Reversible single-chain polymethacrylate-based nanoparticles synthesized by Zhao and coworkers[74] *via* coumarin (CMA) photo-dimerization were evaluated as nanoreactors for the synthesis of gold nanoparticles (AuNP) *in situ*. Interestingly, the intrachain CMA photo-dimerization degree was found to have a strong effect on the rate of AuNP formation. Hence, the relative rate of AuNP formation in a THF solution containing single-chain nanoparticles with 64 and 27% CMA photo-dimerization degree was 4 and 2 times faster than that in a THF solution of the precursor.

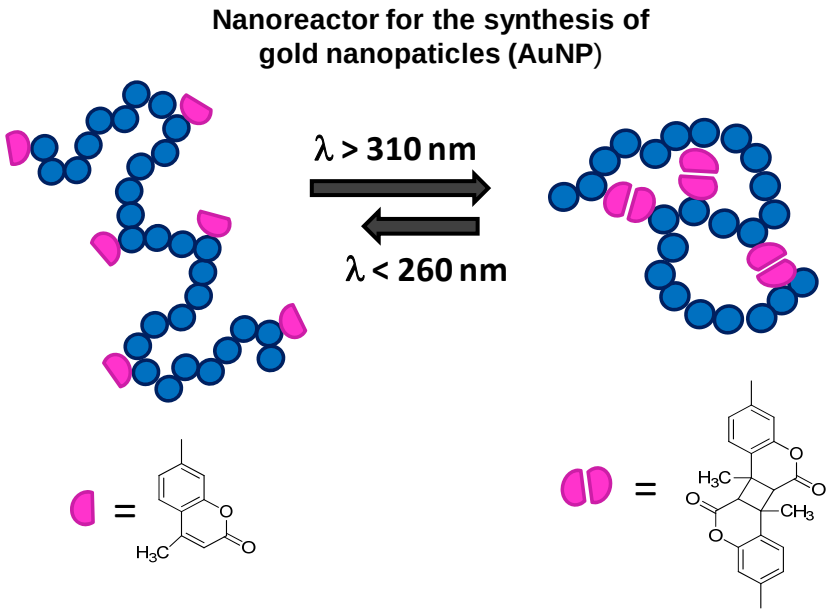

Figure 1.6. Schematic illustration of the synthesis of single-chain nanoparticles *via* coumarin photo-dimerization upon UV irradiation at a wavelength, λ, above 310 nm. Nanoparticle disassembly was observed upon irradiation at λ < 260 nm, although the process was found to be not totally reversible.[74]

Water-soluble single-chain polymethacrylate-based nanoparticles with a catalytically active Ru-containing hydrophobic cavity have been used by Meijer, Palmans and coworkers[22] to transfer hydrogenation in water. The nanoparticles were synthesized *via* BTA helical stacking and were stable in the

conditions under which catalysis was performed. As an example, by using these catalytic nanoparticles and a [substrate] / [Ru] ratio of 200 /1 the quantitative reduction of cyclohexanone to cyclohexanol was carried out in 18 h. In a further extension of this work,[13] L-proline-funcionalizated precursors were transformed to unimolecular nanoparticles *via* BTA helical stacking and used as an efficient catalyst for the aldol reaction between p-nitrobenzaldehyde and cyclohexanone, showing high conversion (99 % after 120 h), high diastereoselectivity (92%) but moderate enantioselectivity (73%). One clear advantage of these nanostructured catalysts is that they can be easily recovered from the aqueous phase after separation of the aldol products by filtration and reused several times without additional purification. More recently, the synthesis of single-chain polymer nanoparticles showing both reductase- and polymerase-like behavior has been demonstrated by Pomposo and coworkers.[78]

1.3.2 Sensing

Flurorescent single-chain polynorbornene-based nanoparticles have been recently reported by Palmans and coworkers[79] based on the intrachain self-assembly in THF/methylcyclohexane (MCH) mixtures of polynorbornene precursors containing bipyridine substituted BTA units (BiPy-BTAs). An increase in green fluorescent intensity at 520 nm was observed upon decreased solvent polarity and an increased degree of BiPy-BTA functionalization. Interestingly, the high propensity of BiPy-BTA to self-assemble intramolecularly was found to avoid the presence of a significant amount of multi-aggregates for precursors with a BiPy-BTA content of 12 mol%. Due to the affinity of the bipyridine moieties towards metal ions such as copper (II), these single-chain nano-objects were efficient sensors for these metal ions.

1.3.3 Nanomedicine

For nanomedicine, unimolecular nanoparticles have been used for the delivery of peptidic molecules into cells [17], selective L-phenylalanine anilide absorption[15], gene-silencing using siRNA[16] and image contrast agents [18] as well as drug delivery nano-carriers.[53]

Certain stable paramagnetic metal ion complexes, such as Gd^{3+} ones, enhance water proton relaxivity during image contrast in magnetic resonance imaging, MRI, of body tissues and fluids. Gd^{3+}-containing nanoparticles were reported by Perez-Baena *et al.*[18] in 2010 by using a dialkyne crosslinker which was able to complex Gd^{3+} ions. The relaxivity value of the Gd^{3+}-loaded single-chain nanoparticles on a per Gd basis was 6.78 mM^{-1} s^{-1}, representing a modest 2-fold increase over a reference commercial low-molecular-weight Gd^{3+} chelate.

As illustrated by Oria *et al.*[11] in 2010, poly(styrene)-based single-chain nanoparticles, in which the intrachain crosslinking points consist of triazole-benzene-triazole segments, show a high level of fluorescence, that could be used for potential *in vivo* imaging applications. These single-chain nanoparticles present, after excitation at 350 nm, two maxima located at 391 and 407 nm respectively, in the fluorescence spectrum as well as a small shoulder at 424 nm.

Moreover, it is well-known that disulfide bonds are susceptible to biochemical reductants such as glutathione (GSH), thioredoxin and peroxiredoxin. Thus, Thayumanavan and coworkers[14] developed biocompatible and biodegradable nanogels with sizes from 16 to 190 nm using disulfide bonds as crosslinkers through an emulsion-free method that promotes the encapsulation of hydrophobic guest molecules. The release of entrapped guest molecules induced by GHS was observed to occur at high GSH concentration (10^{-2} M), which corresponds to the concentration found inside cells. Whereas, there was no significant release of guest molecules at low GSH concentration (10^{-5} M), which corresponds to the concentration found outside the cell and within the

blood plasma. This approach that allowed cell internalization after decoration of the nanogel nanoparticles with cell penetrating peptides could also be very promising for the case of single-chain nanoparticles, as those developed recently by Berda and coworkers[75] using disulfide bonds as reversible intrachain crosslinkers.

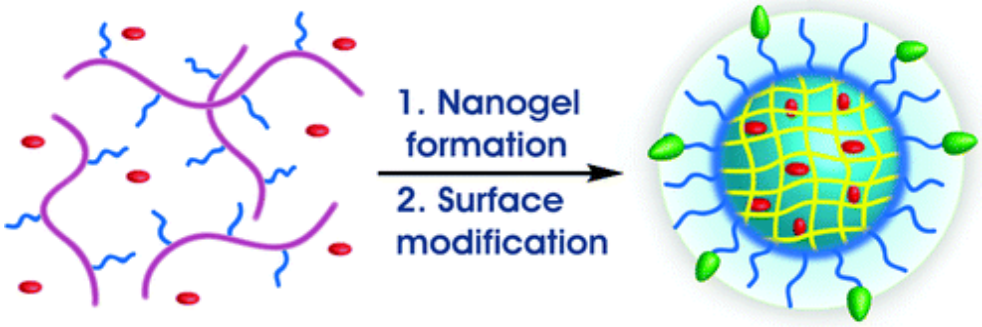

Figure 1.7. Schematic representation of the preparation of biodegradable nanogels with surface modification.[14] These biocompatible nanogels provide the ability to encapsulate hydrophobic guest molecules and surface functionalization which has the potential for targeted delivery.

The preparation of nanoparticles with sizes between 30 and 200 nm for the development of vaccine and drug carriers by self-association of hydrophobically modified polyaminoacids was investigated by Akagi and colleagues.[80] They found that the size of the nanoparticles plays a critical role in controlling immune responses. These results motivated these authors to synthesize hydrophobically self-assembled single-chain nanoparticles[71] based on modified poly(γ-glutamic acid), a naturally occurring, water-soluble, biodegradable, edible, and non-toxic polyamide that is synthesized by several strains of *Bacillus*.

Recently, thermoresponsive water-soluble dynamic covalent single-chain polymer nanoparticles that reversibly transform into a hydrogel have been reported by Fulton and coworkers.[23] The triggered gel formation required the simultaneous application of both low pH and temperature which would be highly convenient for the development of improved drug delivery systems.

1.3.4 Other Uses

Additional use of single-chain nanoparticles for different applications has been proposed, such as rheology-improving agents for melts of thermoplastics[10], elastomeric polymers[11], nanocomposites[81], polyelectrolytes with unconventional behavior[38] , compartmentalised sensors for metal ions[21] and templates for the preparation of photoluminiscent carbon nanodots.[20] A significant effect of morphology on viscosity was found by Hawker, Kim and coworkers[65] for reversible single-chain nanoparticles synthesized through benzamide dimerization by performing measurements in two different solvents: toluene, in which the individual nanoparticles showed reduced viscosities when compared to control polymers lacking the benzamide moiety, and THF, in which no differences between the nanoparticles and the control polymers were observed since this polar solvent suppresses intrachain supramolecular interactions.

The thermal triggered transformation of a solution-processable formulation containing hydrogen bonded single-chain nanoparticles to a high-performance supramolecular material was reported by Meijer and colleagues.[82] Hence, soluble films of nanoparticles were found to undergo a curing process upon heating above the materials glass transition temperature, reorganizing the material into an insoluble supramolecular network with intermolecular non-covalent crosslinks. This feature is of particular interest for the development of self-curing coatings and potentially self-healing surfaces.

1.4 Motivation and goals

The field of single macromolecule folding is of substantial interest to both academia and industry for several applications ranging from the potential design of synthetic macromolecular proteins to bio-delivery systems. The aim of the present work has been to find new, easy-to-prepare systems and to apply biomimetic concepts for the generation of well-defined polymer chains that can subsequently undergo single chain folding driven by covalent, non-covalent or dynamic covalent bonds.

In the present work, in order to introduce functional groups to the uniform polymeric precursor to allow the corresponding folding/collapse; a methyl methacrylate (**MMA**) monomer will be copolymerizated with two different monomers:

A) Propargyl acrylate (PgA)

Propargyl acrylate monomer has a versatile acetylenic functional group (Figure 1.8). The acetylenic moiety has been revealed as one of the more appropriate functional groups in organic chemistry[83] showing multiple functionalization possibilities, spanning from old Glaser-Hay coupling[84] to relatively recent "click" chemistry procedures. Because of that, as is shown in Chapter 2, these acetylenic functional groups will be used for rapid and quantitative intrachain crosslinking *via* metal-catalyzed carbon-carbon coupling (i.e. C-C "click" chemistry) leading to single-chain nanoparticles.

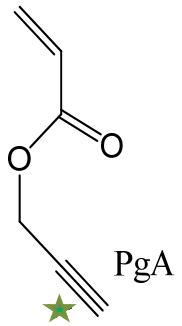

Figure 1.8. Chemical structure of propargyl acrylate (**PgA**) monomer with reactive site marked in green.

B) 2-(Acetoacetoxy) ethyl methacrylate (AEMA)

Acetoacetoxyethyl methacrylate (**AEMA**) is a methacrylic monomer with three sites available for chemical reaction. The methacrylic functionality may be used to react **AEMA** into a well-defined polymer, leaving an acetoacetyl group pendant to the monomer chain. This pendant group contains the two remaining reactive sites which may be used for single polymer chain crosslinking. These sites are the methylene group and the ketone carbonyl group (Figure 1.9).

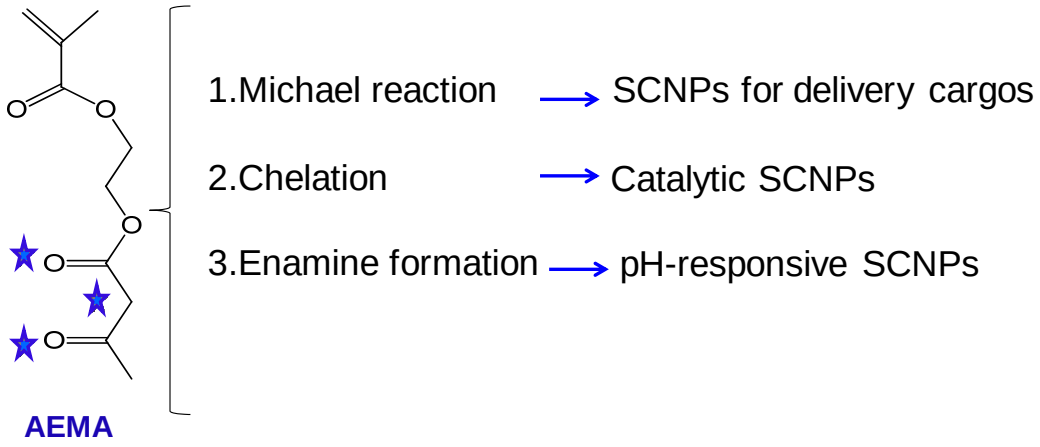

Figure 1.9. Chemical structure of 2-(acetoacetoxy) ethyl methacrylate (**AEMA**) monomer with reactive sites marked in blue. These reactive sites are used for single chain polymer crosslinking by using different chemical reactions.

Taking into account the high versatility of the **AEMA** monomer, random poly(MMA-*co*-AEMA) copolymers of different molecular weight and relatively

narrow size dispersity were firstly synthesized by RAFT copolymerization of methyl methacrylate (**MMA**) and 2-(acetoacetoxy)ethylmethacrylate (**AEMA**), which showed similar reactivity ratios.

After that, as will be explained in Chapter 3, single-chain polymer nanoparticles that resemble intrinsically disordered proteins will be prepared by Michael addition reaction. The resulting SCNPs will be used as transient binding disordered nanocarriers from which controlled delivery of both dermal protective (folic acid) and anticancer (hinikitiol) cargos in water will be investigated.

In Chapter 4 it will be shown how metallo-folded SCNPs will be prepared *via* intrachain Cu (II) complexation of **AEMA** units. These metallo-folded SCNPs were found to show catalytic specificity during the oxidative coupling of mixtures of chemically related terminal acetylene substrates.

Chapter 5 will describe the use of dynamic covalent enamine bonds for the construction of pH-responsive SCNPs, starting from poly(MMA-*co*-AEMA) copolymers. These pH-responsive SCNPs will be able to undergo component exchange processes and to display a coil-to-particle transition *via* enamine bond formation.

In Chapter 6, the details of the techniques and instruments used for the characterization of the samples will be briefly explained.

Finally, Chapter 7 will draw the major conclusions of this PhD thesis.

1.5 References

[1] Sanchez, F. and K. Sobolev, *Construction and Building Materials.*, **2010**, *24*, 2060.

[2] Uskoković, V., *Technology in Society.*, **2007**, *29*, 43.

[3] S. Rajiv, S. Santosh, S. Sugandha, *Journal of Cutaneous and Aesthetic Surgery.*, **2010**, *3*, 32.

[4] Grzelczak M, Vermant J, Furst EM and Liz-Marzan LM, *ACS Nano.*, **2010**, *4* , 3605.

[5] Taton D, Gnanou Y, Matmour R, Angot S, Hou S, Francis R *et al*., *Polym Int.*, **2006**, *55,* 1138.

[6] Hadjichristidis N, Iatrou H, Pitsikalis M and Mays J, *Prog Polym Sci.*, **2006**, *31,* 1068.

[7] Matyjaszewski K, *Nat Chem.*, **2009**, *1,* 276.

[8] Gregory A. and Stenzel MH, *Prog Polym Sci.*, **2012**, *37,* 38.

[9] Altintas O. and Barner-Kowollik C, *Macromol Rapid Commun.*, **2012,** *33***,** 958.

[10] Mackay, M.E.; Dao, T.T.; Tuteja, A.; Ho, D.L.; Horn, B.V.; Kim, H.-C.; Hawker, C.J., *Nature Mater.*, **2003**, *2*, 762.

[11] Oria, L.; Aguado, R.; Pomposo, J.A.; Colmenero, J. A ., *Adv. Mater.*, **2010**, *22*, 3038.

[12] Wulff, G.; Chong, B.-O.; Kolb, U., *Angew. Chem. Int. Ed.*, **2006**, *45*, 2955.

[13] Huerta, E.; Stals, P.J.M.; Meijer, E.W.; Palmans, A.R.A., *Angew. Chem. Int. Ed.*, **2013**, *52*, 2906.

[14] Ryu, J.-H.; Chacko, R.T.; Jiwpanich, S.; Bickerton, S.; Babu, R.P.; Thayumanavan, S., *J. Am. Chem. Soc.*, **2010**, *132*, 17227.

[15] Njiang, G.; Liu, G.; Hong, L., *Langmuir.*, **2012**, *27*, 7176.

[16] Tamura, A.; Oishi, M.; Nagaski, Y., *Biomacromolecules.*, **2009**, *10*, 1818.

[17] Hamilton, S.K.; Harth, E., *ACS Nano.*, **2009**, *3*, 402.

[18] Perez-Baena, I.; Loinaz, I.; Padro, D.; Garcia, I.; Grande, H.J.; Odriozola, I., *J. Mater. Res.*, **2010**, *20*, 6916.

[19] Qian, G.; Zhu, B.; Wang, Y.; Deng, S.; Hu, A., *Macromol. Rapid Commun.*, **2012**, *33*, 1393.

[20] Zhu, B.; Sun, S.; Wang, Y.; Deng, S.; Qian, G.; Wang, M.; Hu, A., *J. Mater. Chem. C.,* **2013**, *1*, 580.

[21] Gillissen, M.A.J.; Voets, I.K.; Meijer, E.W.; Palmans, A.R.A. *Polym. Chem.*, **2012**, *3*, 3166.

[22] Terashima, T.; Mes, T.; De Greef, T.F.A.; Gillissen, M.A.J.; Besenius, P.; Palmans, A.R.A.; Meijer, E.W.. *J. Am. Chem. Soc.,* **2011**, *133*, 4742.

[23] Whitaker, D.E.; Mahon, C.S.; Fulton, D.A. *Angew. Chem. Int. Ed.,* **2013**, *52*, 956.

[24] Destarac, M., *Macromol. React. Eng.,* **2010**, *4*, 165.

[25] Chiefari, J.; Chong, Y.K.; Ercole, F.; Krstina, J.; Jeffery, J.; Le, T.P.T.; Mayadunne, R.T.A.; Meijs, G.F.; Moad, C.L.; Moad, G.; *et al*., *Macromolecules.*, **1998**, *31*, 5559.

[26] Wang, J.-S.; Matyjaszewski, K., *J. Am. Chem. Soc.,* **1995**, *117*, 5614.

[27] Hawker, C.J.; Bosman, A.W.; Harth, E. *Chem. Rev.,* **2001**, *101*, 3661.

[28] Lynn, D.M.; Kanaoka, S.; Grubbs, R.H., *J. Am. Chem. Soc.,* **1996**, *118*, 784.

[29] G. Moad, E. Rizzardo, S. H. Thang, *Acc. Chem. Res.,* **2008**, *41*, 1133.

[30] C. Barner-Kowollik, *Handbook of Raft Polymerization.,* **2008**, Wiley-VCH, Weinheim.

[31] Moad, G., E. Rizzardo, S. H. Thang. (2005). *Australian Journal of Chemistry.,* **2005**, *58*, 379.

[32] Günay, K.A.; Theato, P.; Klok, H.-A. H, 1st ed.; Theato, P., Klok, H.-A., Eds.; Wiley-VCH Verlag GmbH & Co. KGaA: Weinheim, Germany, **2013**; pp. 1–44.

[33] Beck, J.B.; Killops, K.L.; Kang, T.; Sivanandan, K.; Bayles, A.; Mackay, M.E.; Wooley, K.; Hawker, C.J. *Macromolecules.,* **2009**, *42*, 5629.

[34] Croce, T.A.; Hamilton, S.K.; Chen, M.L.; Muchalski, H.; Harth, E. *Macromolecules.,* **2007**, *40*, 6028.

[35] Harth, E.; Horn, B.V.; Lee, V.Y.; Germack, D.S.; Gonzales, C.P.; Miller, R.D.; Hawker, *J. Am. Chem. Soc.,* **2002**, *124*, 8653.

[36] Dobish, J.N.; Hamilton, S.K.; Harth, E. *Polym. Chem.,* **2012**, *3*, 857.

[37] Ruiz de Luzuriaga, A.; Ormategui, N.; Grande, H.J.; Odriozola, I.; Pomposo, J.A.; Loinaz, I., *Macromol. Rapid Commun.,* **2008**, *29*, 1156.

[38] A. Ruiz de Luzuriaga , I. Perez-Baena, S. Montes, I. Loinaz, I. Odriozola, I. Garcia, JA. Pomposo, *Macromol. Symp.,* **2010,** *293*, 303.

[39] Cengiz, H.; Aydogan, B.; Ates, S.; Acikalin, E.; Yagci, Y. *Des. Monomers Polym.,* **2011**, *14*, 68.

[40] Mecerreyes, D.; Lee, V.; Hawker, C. J.; Hedrick, J. L.; Wursch, A.; Volksen, W.;Magbitang, T.; Huang, E.; Miller R. D. *Adv. Mater.,* **2001**, *13*, 204.

[41] Jiang, J.; Thayumanavan. *Macromolecules.,* **2005**, *38*, 5886.

[42] Cherian, A. E.; Sun, F. C.; Sheiko, S. S., Coates G. W. *J. Amer. Chem. Soc.,* **2007**, *129*,11350.

[43] Adkins, C.; Muchalski, H.; Harth, E. *Macromolecules.,* **2009**, *42*, 5786.

[44] Zhu, B.; Ma, J.; Li, Z.; Hou, J.; Cheng, X.; Qian, G.; Liu, P.; Hu, A. *J. Mater. Chem.,* **2011**, *21*, 2679.

[45] Zhu, B.; Qian, G.; Xiao, Y.; Deng, S.; Wang, M.; Hu, A. *J. Polym. Sci., Polym. Chem.,* **2011**, *49*, 5330.

[46] Jiang, X.; Pu, H.; Wang, P. *Polymer.,* **2011**, *52*, 3597.

[47] Wang, P.; Pu, H.; Jin, M. *J. Polym. Sci., Polym. Chem.,* **2011**, *49*, 5133.

[48] Sanchez-Sanchez, A.; Asenjo-Sanz, I.; Buruaga, L.; Pomposo, J. A. *Macromol. Rapid Commun.,* **2012**, *33*, 1262

[49] Dirlam, P. T.; Kim, H. J.; Arrington, K. J.; Chung, W. J.; Sahoo, R.; Hill, L. J.; Costanzo, P. J.; Theato, P.; Char, K.; Pyun, *J. Chem. Commun.,* **2013**, *4*, 3765.

[50] Ormategui, N.; Garcia, I.; Padro, D.; Cabanero, G.; Grande, H. J.; Loinaz, I. *Soft Mater.,* **2012**, *8*, 734.

[51] Johannes W.,Kilian N. R. W.,Mueller J.O, Kaupp M.,Wagenknecht H.A., Barner-Kowollik C. *ACS Macro Lett.*, **2014**, *3*, 574.

[52] Radu, J. E. F.; Novak, L.; Hartmann, J. F.; Beheshti, N.; Kjoniksen, A.-L.; Nyström, B.;Borbély, J. *Colloid. Polym. Sci.,* **2008**, *286*, 365.

[53] Sanchez-Sanchez, A.; Akbari, S.; Etxeberria, A.; Arbe, A.; Gasser, U.; Moreno, A. J.;Colmenero, J.; Pomposo, J. A. *ACS Macro Lett.,* **2013**, *2*, 491.

[54] F. Hansell C., Annhelen L., Patterson J.P, K. O'Reilly R. *Nanoscale.*, **2014**, 6, 4102.

[55] L. Pauling, *The Nature of the Chemical Bond and the Structure of Molecules and Crystals.,* Oxford University Press., **1939**.

[56] J.-M. Lehn, *Supramolecular Chemistry*., Wiley-VCH, **1995**.

[57] J. M. Pollino, M. Weck, *Chem. Soc. Rev.,* **2005**, *34*, 193.

[58] T, Kato, J. M. J. Fréchet, *Macromolecules.,* **1989**, *22*, 3818.

[59] X. Yang, F. Hua, K. Yamato, E. Ruckenstein, B. Gong, W. Kim, C. Y. Ryu, *Angew. Chem. Int. Ed.,* **2004**, *43*, 6471.

[60] E. M. Todd, S. C. Zimmerman, *Tetrahedron.,* **2008**, *64*, 8558.

[61] Jin Y., Q. Wang, P. Tayton, W. Zhang, *Accounts of Chemical Research*., **2014**, *47*, 1575.

[62] P. T. Corbett, J. Leclaire, L. Vial, K. R. West, J.-L. Wietor, J. K. M. Sanders, S. Otto, *Chem. Rev.,* **2006**, *106,* 3652.

[63] O. Ramström, J.-M. Lehn, *Nat. Rev. Drug Discov.,* **2002**, *1*, 26.

[64] B. Levrand, Y. Ruff, J.-M. Lehn, A. Herrmann, *Chem. Commun.,* **2006**, 2965.

[65] M. Seo, B. J. Beck, J. M. J. Paulusse, C. J. Hawker, S. Y. Kim, *Macromolecules*., **2008**, *41*, 6413.

[66] B. S. Murray, D. A. Fulton, *Macromolecules.,* **2011**, *44*, 7242.

[67] E. J. Foster, E. B. Berda, E. W. Meijer, *J. Am. Chem. Soc.,* **2009,** *131,* 6964.

[68] T. Mes, R. van der Weegen, A. R. A. Palmans, E. W. Meijer, *Angew. Chem. Int. Ed.,* **2011**, *50*, 5085.

[69] N. Hosono, M. A. J. Gillissen, Y. Li, S. S. Sheiko, A. R. A. Palmans, E. W. Meijer, *J. Am. Chem. Soc.,* **2013,** *135,* 501.

[70] E. A. Appel, J. Dyson, J. del Barrio, Z. Walsh, O. A. Scherman, *Angew. Chem. Int. Ed.,* **2012**, *51*, 4185.

[71] T. Akagi, P. Piyapakorn, M. Akashi, *Langmuir.,* **2012**, *28*, 5249.

[72] Mavila, S.; Diesendruck, C. E.; Linde, S.; Amir, L.; Shikler, R.; Lemcoff, N. G. *Angew.Chem. Int. Ed.,* **2013**, *52*, 5767.

[73] Sanchez-Sanchez,; Arbe, A.;Colmenero, J.; Pomposo, J. A. *ACS Macro Lett.,* **2014**, *3*, 439.

[74] J. He, L. Tremblay, S. Lacelle, Y. Zhao, *Soft Matter.,* **2011**, *7*, 2380.

[75] B. T. Tuten, D. Chao, C. K. Lyon, E. B. Berda, *Polym. Chem.,* **2012**, *3*, 3068.

[76] Sanchez-Sanchez, A.; Fulton, D. A.; Pomposo, J. A. *Chem. Commun.,* **2014**, *50*, 1871.

[77] Frank, P. G.; Tuten, B. T.; Prasher, A.; Chao, D.; Berda, E. B. *Macromol. Rapid Commun.,* **2014**, *35*,249.

[78] Perez-Baena, I.; Barroso-Bujans, F.; Gasser, U.; Arbe, A.; Moreno, A. J.; Colmenero,J.; Pomposo, J. A. *ACS Macro Lett.,* **2013**, *2*, 775.

[79] M. A. J. Gillissen, I. K. Voets, E. W. Meijer, A. R. A. Palmans, *Polym. Chem*., **2012**, *3*, 3166.

[80] H. Kim, T. Uto, T. Akagi, M. Baba, M. Akshi, *Adv. Funct. Mater.,* **2010**, *20*, 3925.

[81] Tuteja, A.; Duxbury, P.M.; Mackay, M.E. *Macromolecules.,* **2007**, *40*, 9427.

[82] E. B. Berda, E. J. Foster, E. W. Meijer, *Macromolecules.,* **2010**, *43*, 1430.

[83] C. J. Li. *Accounts Chem. Res.,* **2010**, *43*, 581.

[84] C. Glaser. *Ber. Dtsch. Chem. Ges.,* **1869**, *2*, 422.

CHAPTER 2:

Self-Clickable Propargylic Decorated Single-Chain Nanoparticle Polymer Precursors *via* Redox-initiated RAFT Polymerization

2.1 Introduction

As mentioned in Chapter 1, single-chain polymer nanoparticles are emerging soft nanomaterials with promising properties for different end-use applications such as processing additives,[1] blend compatibilizers,[2] artificial enzymes,[3] photostable bio-imaging agents[4] and drug / siRNA-delivery systems,[5] among others. Different routes for the synthesis of single-chain polymer nanoparticles with a size below 20 nm have been progressively introduced relying[6] either on covalent[7], noncovalent[8] or dynamic covalent bonds. These different routes can be classified in three different methods: (1) intrachain homocoupling, (2) intrachain heterocoupling, and (3) crosslinker-induced collapse.

During intrachain homocoupling collapse, an intramolecular reaction of suitable self complementary reactive groups occurs leading to the synthesis of single-chain polymer nanoparticles. The first use of intrachain homocoupling *via* "click" chemistry reaction for single-chain nanoparticle construction was reported by Harth *et al.*[9] in 2002, relying on the use of a Diels-Alder-type reaction involving benzocyclobutene (BCB) functional groups that were activated at a very high temperature (250 °C). Although the efficiency of this technique was certainly recognized, the synthesis at 250 °C in a high boiling point solvent (benzyl ether, BE) and its later removal were demanding procedures that limited their broad use. Further refinements of this technique were performed by Croce *et al.*[10] in 2007 by introducing benzosulfone reactive groups instead of BCB moieties and by Dobish *et al.*[11] in 2012 by developing substituted BCB functional groups reactive at lower temperatures (150 °C).

Nevertheless, there was still a lack of nearly monodisperse precursors arising from commercial unprotected monomers allowing facile single-chain nanoparticle synthesis *via* highly-efficient functional group homocoupling (i.e. "self-click" chemistry, intrachain homocoupling).

Among others, the acetylenic moiety has been revealed as one of the more versatile functional groups in organic chemistry[12] showing multiple functionalization possibilities, spanning from old Glaser-Hay coupling[13] (Scheme 2.1) to relatively recent "click" chemistry procedures.[14]

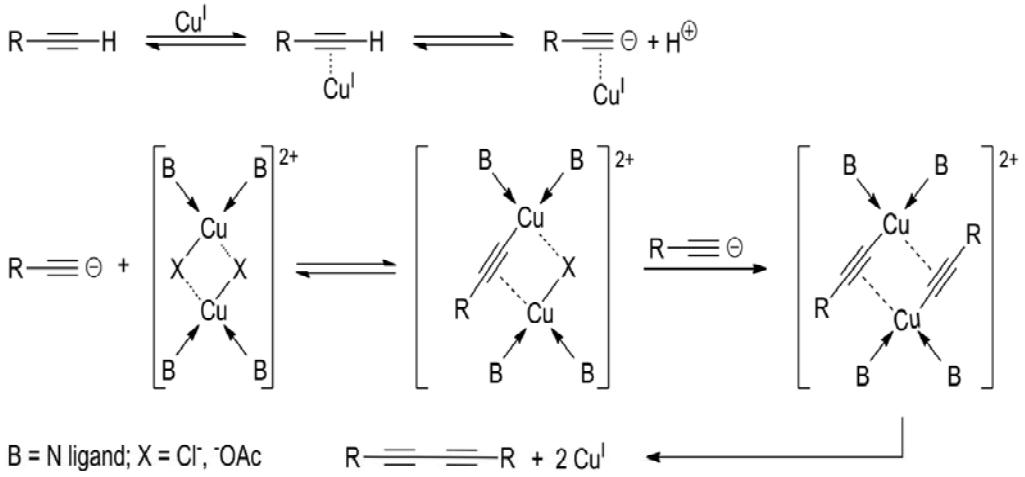

Scheme 2.1. Mechanism for the Hay coupling reaction suggested by Bohlmann *et. al*.[15]

In this sense, the Glaser-Hay coupling reaction could be used to link different acetylenic moieties that are distributed randomly along linear polymer chains to construct single-chain polymer nanoparticles; resulting in a new and efficient synthetic route to obtain single-chain polymer nanoparticles by covalent intrachain homocoupling. However, for linear polymer synthesis, protection of the acetylenic triple bond has often been necessary to avoid the alkyne side group being involved in branching events and chain transfer reactions during radical polymerization. D´Lalelio and Evers[16] first reported that insoluble, crosslinked polymers were formed during radical polymerization of (metha)acrylic ester monomers containing acetylenic moieties. The difficulty in avoiding secondary reactions that increase the polydispersity index (M_w / M_n) has also been noted during polymerization of alkyne-based monomers by means of controlled radical polymerization techniques. Summerling *et al*.[17] showed that atom transfer radical polymerization (ATRP) of propargyl methacrylate (PgMA) resulted in high polydispersity values and multimodal molecular weight distributions (M_w / M_n > 3.3 at 50% monomer conversion), as

well as crosslinked networks at high conversion (> 80%). Similar results were obtained by Zhu *et al*.[18] by means of both reversible addition fragmentation chain transfer (RAFT) polymerization (M_w / M_n = 2.2 at 42 % monomer conversion) and single electron transfer (SET) controlled/living radical polymerization techniques (M_w / M_n = 1.7 at 40 % monomer conversion), whereas a combined SET-RAFT technique provided better control over the homopolymerization process (M_w / M_n = 1.55 at 76% monomer conversion).

To some extent, secondary reactions involving the acetylenic moiety could be minimized by copolymerization, due to the dilution effect expected when the acetylenic monomer is the minority component. Further improved control over the polymerization of alkyne monomers would be obtained by performing the process at room temperature and without the presence of transition metal catalysts, to reduce the extension of parasitic side reactions (branching/crosslinking and alkyne homocoupling, respectively). Due to the reported photo-crosslinking of acetylenic monomers during irradiation, radical initiation promoted by UV light should preferably be avoided.[19] A more promising approach could be the use of a redox initiator system, such as the conventional benzoyl peroxide (BPO) / N,N-dimethylaniline (DMA) pair, which allows radical polymerization of unstable monomers to be conducted at room temperature. It is well known that redox polymerization has many advantages such as low activation energy (40–85 kJ/mol^{-1}) to allow performing polymerizations at room temperature or even at lower temperatures, and ease of control of the polymerization reaction due to the reduction of the side reactions at low temperatures. In addition, the polymerization process consumes less energy.[20]

2.2 Objectives

In this work, we attempt to find a simple and efficient route to synthesise single-chain nanoparticle polymer precursors that contain the unprotected acetylenic functional group. In order to reduce the extension of parasitic side reactions in which the acetylenic functional group can be involved, the precursors will be synthesized using redox initiated RAFT polymerization at room temperature. In this manner, polymer precursors containing well-defined amounts of naked, unprotected acetylenic functional groups should be obtained. These acetylenic functional groups will be useful for rapid and quantitative intrachain crosslinking *via* metal-catalyzed carbon-carbon coupling (i.e. C-C "click" chemistry). To illustrate the useful "self-clickable" character of the new unprotected acetylenic precursors, single-chain nanoparticles will be prepared for the first time in a simple and highly-efficient manner by copper-catalyzed alkyne homocoupling (i.e. Glaser-Hay coupling) at room temperature under normal atmospheric conditions (Scheme 2.2).

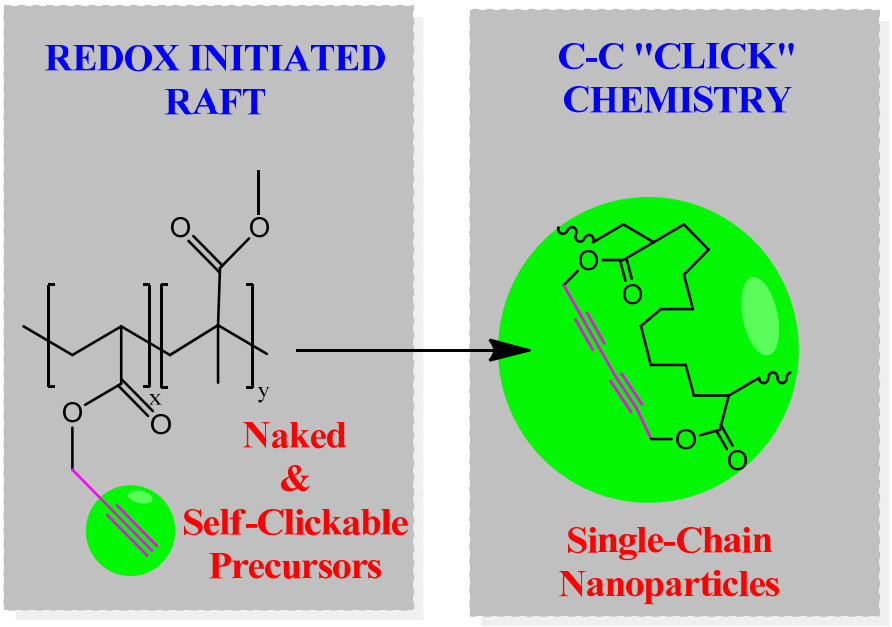

Scheme 2.2. The formation of single-chain polymer nanoparticles by copper-catalyzed alkyne homocoupling.

2.3 Experimental Section

a) Synthesis of Polymer Precursors *via* Redox Initiated RAFT Polymerization. Before polymerization, both monomers, methyl methacrylate (**MMA**) and **PgA** (propargyl acrylate) were purified using neutral alumina; and benzoyl peroxide (BPO) was recrystallized by dissolving in $CHCl_3$ at room temperature and adding an equal amount of MeOH. In a typical procedure, methyl methacrylate (**MMA**, 1.0 ml, 9.3 mmol), propargyl acrylate (**PgA**, 0.44 ml, 4.0 mmol), 2-Cyanoprop-2-yl-dithiobenzoate (CPDB, 4.1 mg, 1.9 $\times 10^{-2}$ mmol), benzoyl peroxide (BPO, 14.9 mg, 6.2×10^{-2} mmol), N,N-dimethylaniline (DMA, 7.4 μL, 5.8×10^{-2} mmol) and tetrahydrofuran (THF, 1 mL) were placed in a dry glass tube with a septum cap, purged by bubbling argon through the reaction mixture for 15 min, and then placed in a bath at 25 ^{o}C under magnetic stirring. After 20 h of reaction, the reaction mixture was dissolved in THF and the resulting P(MMA-*co*-PgA) copolymer, **1** (see Scheme 2.3), was recovered by precipitation in methanol (MeOH) and dried under dynamic vacuum. Yield: 24%. The yield was determined by gravimetric measurements as the ratio of the weight of copolymer to the weight of monomers in the feed. **PgA** content in copolymer was 19.5 mol%, as determined by ^{1}H NMR. Weight average molecular weight, M_w: 57.9 kDa. Polydispersity index, M_w / M_n: 1.28.

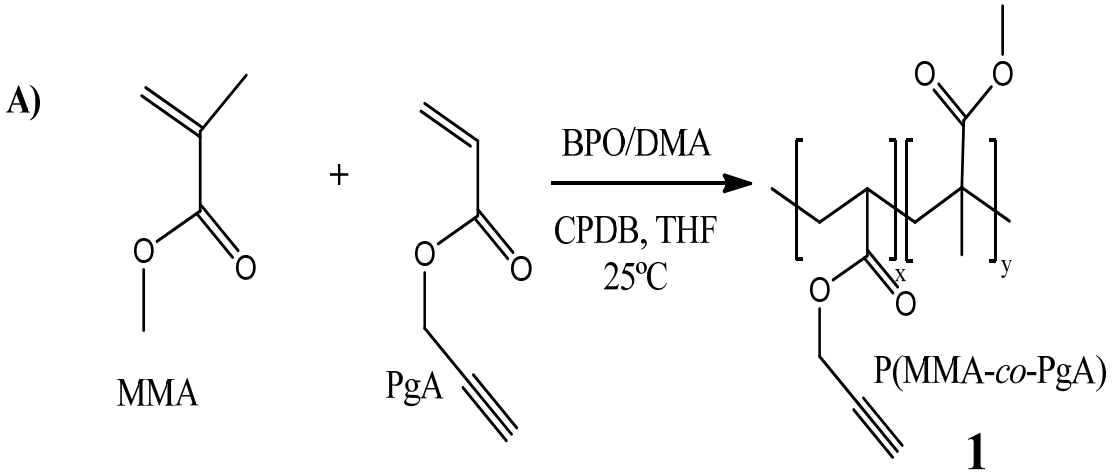

Scheme 2.3. Redox-initiated RAFT copolymerization of **MMA** and **PgA**. Chain-ends have been omitted for clarity.

b) Synthesis of Single-Chain Nanoparticles *via* C-C "Click" Chemistry.

Typically, P(MMA-*co*-PgA) copolymer, **1** (150 mg, 0.29 mmol of **PgA**, M_w = 57.9 kDa, M_w / M_n = 1.28) was placed in an open 250 mL round bottom flask containing 150 mL of THF at room temperature under stirring. Then, copper(I) iodide (CuI, 2.7 mg, 5 mol%), N,N,N,N-tetramethylethylenediamine (TMEDA, 4.3 μL, 10 mol%) and triethylamine (Et_3N, 0.12 mL, 3 mmol) were added and the reaction was allowed to proceed for 24 h. Finally, trifluoroacetic acid (TFA, 74 μL, 0.87 mmol) was added to deactivate the catalyst. After that, the reaction mixture was filtered, concentrated and precipitated in MeOH. The resulting nanoparticles, **2** (Scheme 2.4), were purified by solution-precipitation cycles and finally dried under dynamic vacuum for 48 h prior to characterization. The yield of the reaction was 81%, as determined by gravimetric measurements. Degree of alkyne homocoupling, as revealed by ^{1}H NMR: 86%. Average hydrodynamic size by dynamic light scattering (DLS) at room temperature in THF solvent: 7 nm.

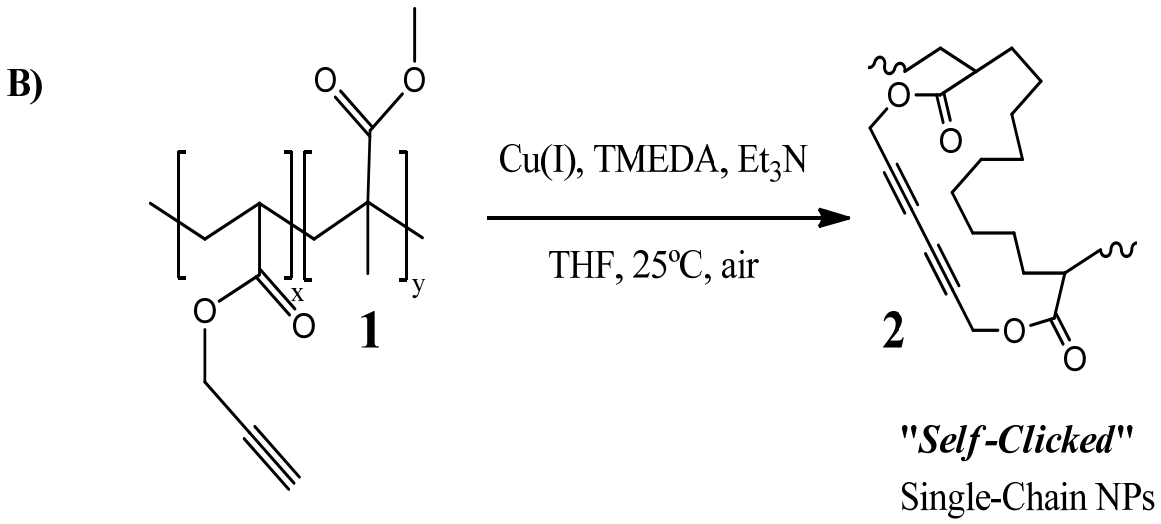

Scheme 2.4. Single-chain nanoparticle construction at 25 ºC under normal atmospheric conditions from naked P(MMA-*co*-PgA) precursors *via* C-C "click" chemistry (Glaser-Hay coupling).

2.4 Results and Discussion

The synthesis of single-chain nanoparticles that are uniform in size by covalent intrachain crosslinking relies on the use of linear polymer precursors of narrow molecular weight dispersity and high intrachain reactivity under appropriate reaction conditions.[7] Attempts to synthesize well-defined single-chain nanoparticle precursors containing **MMA** and unprotected **PgA** units through conventional, and RAFT copolymerization failed, probably as a consequence of the increased extension of parasitic side reactions involving the propargylic group at a relatively high temperature. As can be seen in the Table 2.1, employing conventional radical polymerization and RAFT polymerization, crosslinked copolymers or copolymers with high molecular weight dispersity (M_w / M_n) were obtained. This was because the alkyne side group is involved in branching events and chain transfer reactions during polymerization at high temperatures.

Table 2.1. Molecular weight characteristics of P(MMA-*co*-PgA) copolymers synthesized by different polymerization techniques.

Polymerization	Reaction conditions	M_w (kDa)	M_w/M_n
Free radical, Conventional initiator	AIBN, [MMA]/[PgA]=1.4 T=65°C, t=24h	Crosslinked material	-
RAFT, Conventional initiator	AIBN,CDTC,[MMA]/[PgA]=1.4 T=65°C, t=24h	639.6	9.9
RAFT, redox initiated	BPO/DMA,CDTC,[MMA]/[PgA]=1.4 T=25°C, t=24h	127.9	3.22
RAFT, redox initiated	BPO/DMA,CDTC,[MMA]/[PgA]=2.3 T=25°C, t=6h	37.8	1.25

To solve this problem we turned our attention to redox initiation systems allowing performance of the RAFT process at room temperature as depicted in Table 2.1. The results of redox initiated RAFT copolymerization of **MMA** and **PgA** at 25 °C by means of the BPO/DMA redox pair, using CPDB as chain-

transfer agent, are illustrated in Figures 2.1, 2.2 and 2.3. In figure 2.1 the evolution of the copolymerization process can be observed, as a function of reaction time. As the reaction time of the copolymerization is increased (from 2 h to 18 h) the retention time (t_R) of the SEC trace decreases because the molecular weight of the copolymer is higher.[21-22]

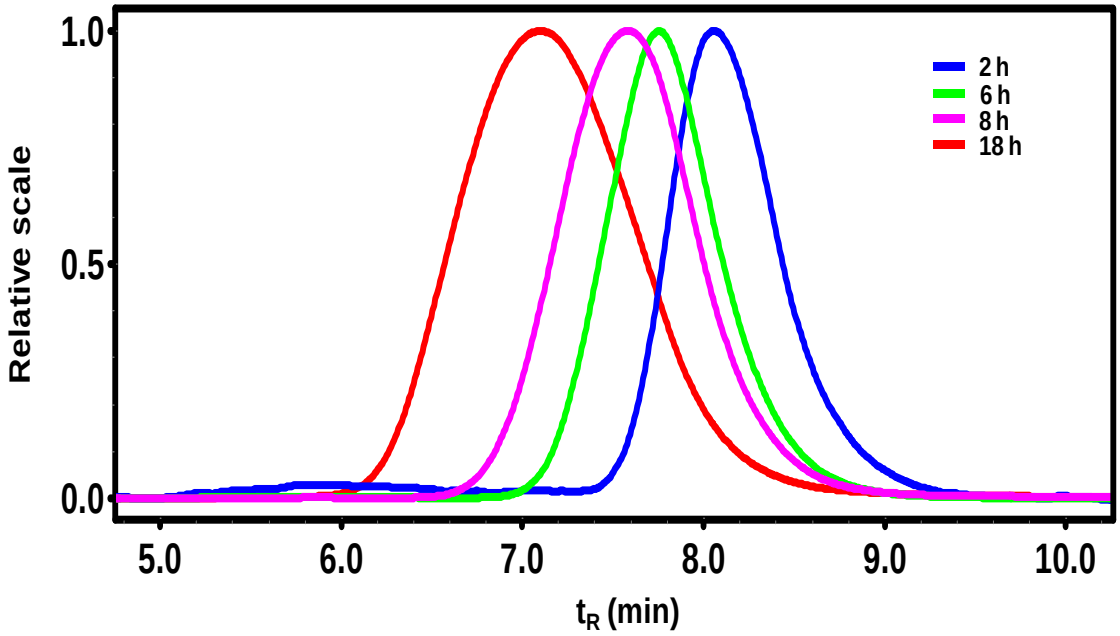

Figure 2.1. SEC traces as a function of reaction time during copolymerization of **MMA** and **PgA** ([MMA] / [PgA] = 2.3) *via* redox initiated RAFT polymerization at 25ºC**.**

As expected for a RAFT polymerization process, the molecular weight of P(MMA-*co*-PgA) copolymers increases linearly with monomer conversion (Figure 2.2 A). A linear relationship (for fractional conversion c < 0.3) between $\ln([M]_0/[M])$ and polymerization time can be observed in Figure 2.2 B, which indicates that the polymerization is a first-order reaction with respect to monomer concentration and that the number of active radicals remains constant during polymerization. Additionally, it can be observed that molecular weight distribution remains very narrow during the polymerization.

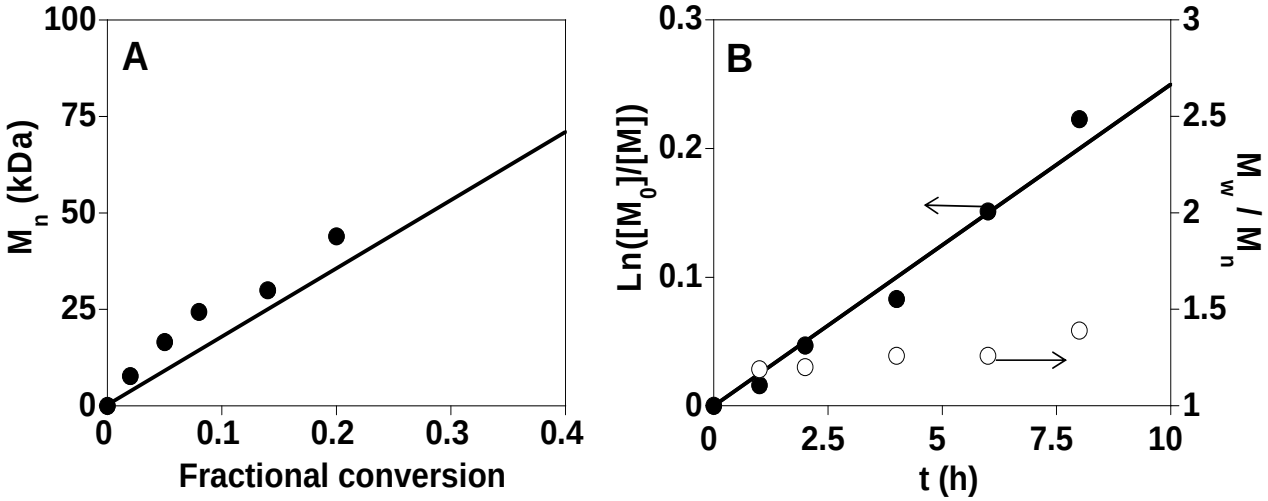

Figure 2.2. **A)** Dependence of M_n on fractional conversion for copolymerization of **MMA** and **PgA** *via* redox initiated RAFT polymerization at 25°C ([MMA] / [PgA] = 2.3). Continuous line is the theoretical M_n vs. *c*. **B)** Kinetic plot (closed symbols) and evolution of the polydispersity index (M_w/M_n) with reaction time (open symbols) for [MMA] / [PgA] = 2.3.

The range in which copolymerization was under control was determined by monitoring the evolution of weight average molecular weight (M_w) and molecular weight dispersity (M_w/M_n) with fractional conversion (c) as illustrated in Figure 2.3.

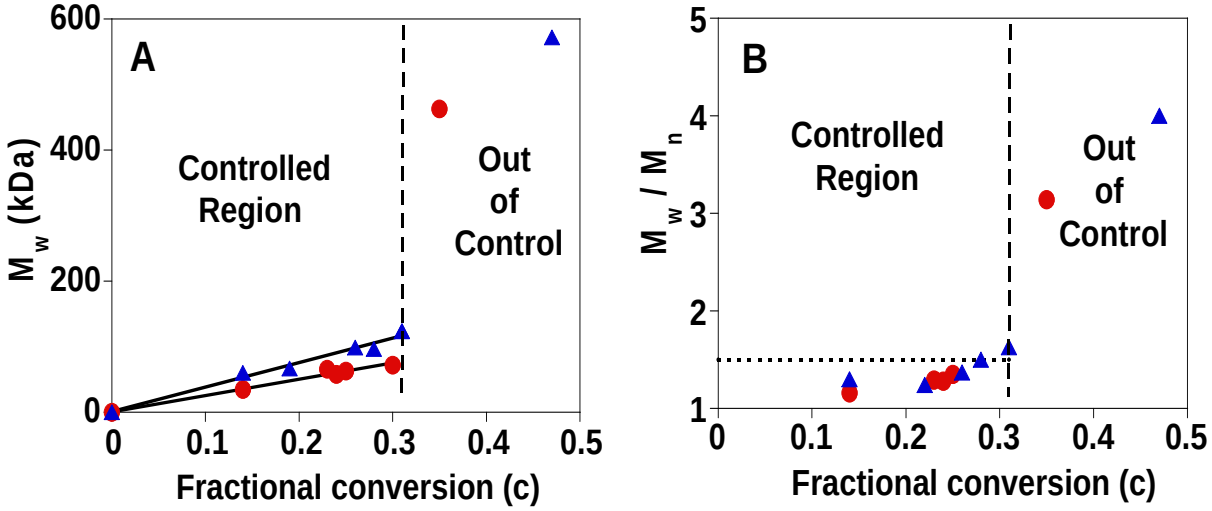

Figure 2.3. **A)** Evolution M_w with fractional conversion for: [MMA] / [PgA] = 2.3 (circles), and [MMA] / [PgA] = 4 (triangles). **B)** Dependence of M_w/M_n on fractional conversion: for [MMA] / [PgA] = 2.3 (circles) and [MMA] / [PgA] = 4 (triangles).

As is depicted in Figure 2.3, out-of-control copolymerization was observed at the higher conversions (i.e. t > 24 h and c > 0.3) leading to polydisperse P(MMA-*co*-PgA) copolymers of very high molecular weight (M_w / M_n > 3, M_w > 400 kDa) or even to insoluble, crosslinked materials at very high conversion. Because of this reason, well-defined statistical P(MMA-*co*-PgA) copolymers with low molecular weight dispersity (M_w / M_n = 1.12 – 1.37) up to a limiting molecular weight of M_w ≈ 100 kDa were obtained by working at c < 0.3 as can be seen in Table 2.2.

Table 2.2. Data of P(MMA-*co*-PgA) copolymers synthesized in a series of different polymerization reactions, displaying narrow molecular weight dispersity, M_w / M_n = 1.12 - 1.37 up to M_w ~ 100 kDa.

$f_{PgA(\%)}$	c	M_w (kDa)	M_w/M_n
13	0.05	16.8	1.12
13	0.27	99.1	1.37
18	0.08	30.8	1.26
19	0.13	37.8	1.25
20	0.15	33.2	1.16
20	0.24	57.9	1.28

f_{PgA} is the **PgA** mol% in the copolymer as determined by ^{1}H NMR spectroscopy, and c the fractional conversion as determined by gravimetric measurements. (SEC/SLS, dn/dc =0.083).

Figure 2.4 illustrates the ^{1}H NMR spectrum of a typical, linear P(MMA-*co*-PgA) precursor, **1**, synthesized by redox initiated RAFT polymerization (M_w = 57.9 kDa, M_w/M_n = 1.28). Copolymer sequence effects are[23] clearly seen in Figure 2.4 for peak **f** (propargylic methylene protons) and peak **a** (methoxy protons), which split into a quadruplet and a doublet, respectively. The copolymer composition estimated from the normalized areas of peaks **b** and **g** in Figure 2.4 was 19.5 **PgA** mol%, so **1** was found to be enriched in **MMA** units when compared to the molar fraction of **MMA** in the feed (the molar ratio in the feed was: 70% MMA/30%PgA). Interestingly, the ratio of the areas of the peaks at 2.5 ppm (**g**, acetylenic proton) and 4.57 - 4.68 ppm (**f**, methylene

protons of propargylic group) was found to be 1:2 suggesting that alkyne groups remained intact upon copolymerization.

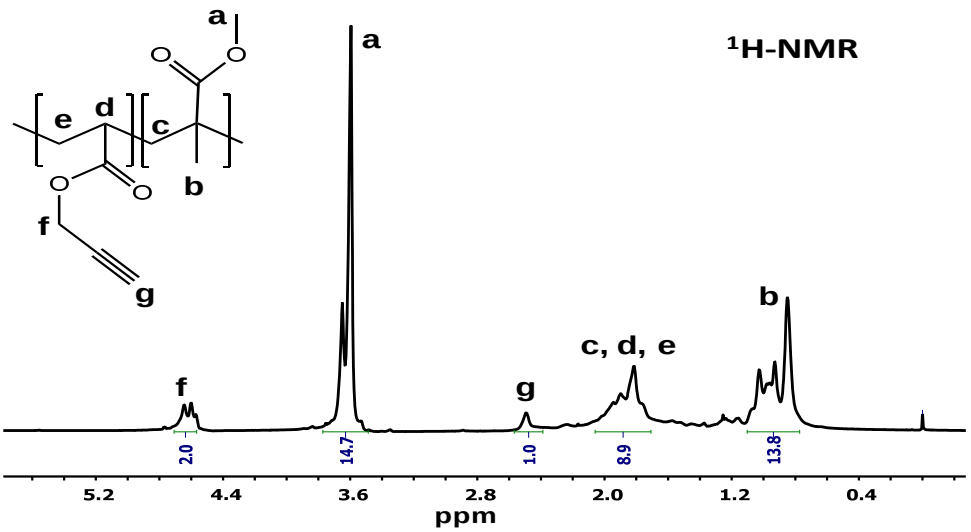

Figure 2.4. ^{1}H NMR spectrum of linear P(MMA-*co*-PgA) precursor **1** in $CDCl_3$.

Additional ^{13}C NMR measurements showed no peaks in the 120-135 ppm region arising from branched **PgA** units[24-26] (see Figure 2.5). In fact the strong, very intense signals expected for a branched P(MMA-*co*-PgA) copolymer (see Figure 2.6, red circles) at 130.6 and 131.6 ppm (from vinylic protons), as well as those at 61.2 and 31.7 ppm (both from methylene protons) are not present in Figure 2.5.

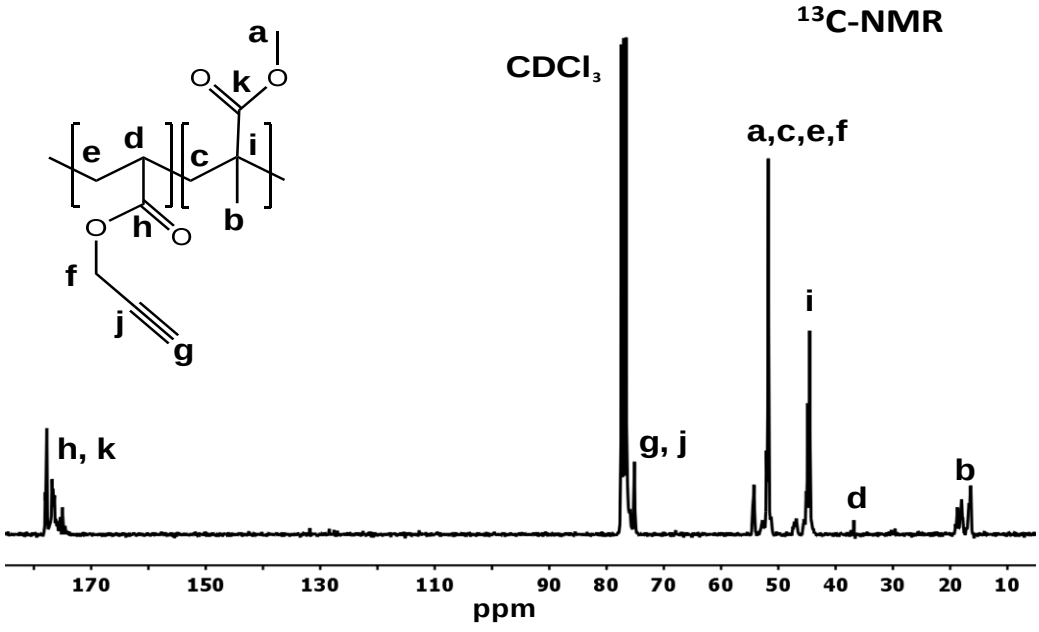

Figure 2.5. ^{13}C NMR spectrum of linear P(MMA-*co*-PgA) precursor **1**.

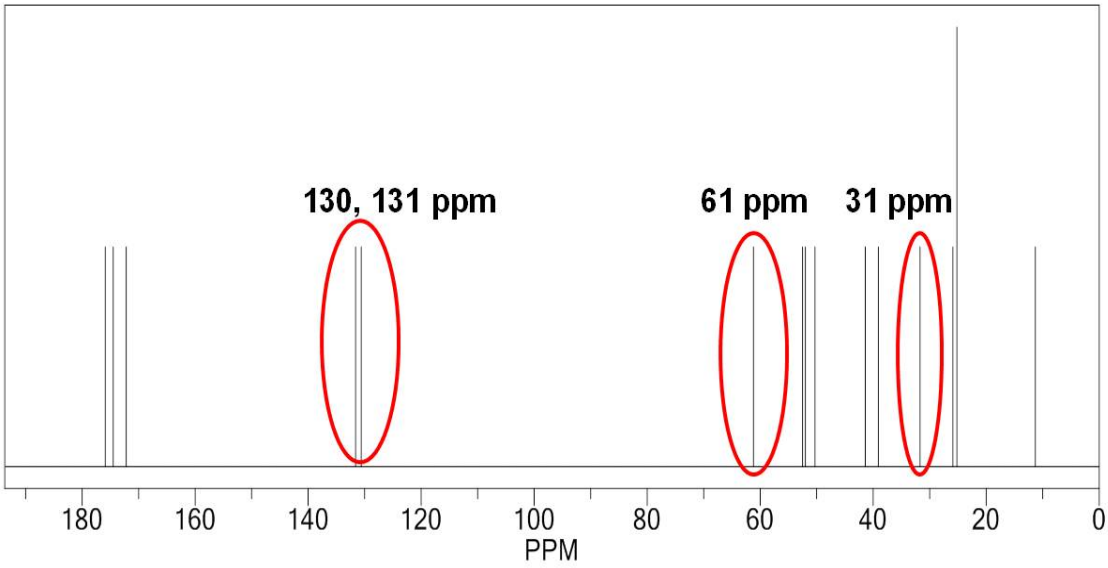

Figure 2.6. Predicted ^{13}C NMR spectrum of a branched copolymer containing **MMA** and monosubstituted **PgA** units.

Accurate control over the composition, molecular weight and polydispersity of linear P(MMA-*co*-PgA) copolymers was obtained by working up to a maximum polymerization time of 20 h, and a maximum **PgA** monomer in the feed of 35 mol%.

As schematically depicted in Scheme 2.4, single-chain nanoparticles *via* C-C "click" chemistry, **2**, can be prepared in a facile manner from the naked, propargylic-decorated precursors, **1**, *via* intramolecular copper-catalyzed carbon-carbon coupling (Glaser-Hay coupling). To guarantee individual nanoparticle formation through irreversible intrachain crosslinking of the linear P(MMA-*co*-PgA) precursor chains, the C-C "click" reaction was conducted under diluted conditions (1 mg/ml). After a careful screening of reaction conditions based on alkyne homocoupling of low molecular weight model compounds, nanoparticle synthesis was performed in THF under normal atmospheric conditions at 25ºC in the presence of Et_3N and by using catalytic amounts of CuI and TMEDA[27]. Under such conditions, terminal aliphatic alkynes provide the corresponding diynes in 20 h with good to excellent yields (80-92 %).[27]

The irreversible chain collapse accompanying nanoparticle formation was monitored by size exclusion chromatography (SEC), with multi-angle laser light scattering (MALLS) and differential refractive index (RI) detectors providing *actual* values of M_w and its distribution as a function of SEC retention time, t_R (see Figure 2.7). When the values of t_R corresponding to a linear precursor chain, **1**, and a single-chain nanoparticle, **2**, both of exactly the same M_w were compared, an increase in retention time ($\Delta t_R \approx 0.22$ min.) and, hence, a decrease in hydrodynamic size ($D_H \propto 1/t_R$) was systematically observed for single-chain nanoparticles, suggesting the presence of significant intramolecular collapse.[28] Alternatively, for identical hydrodynamic size values (i.e. identical t_R values) **2** showed a M_w value, which was typically 45% higher than for a linear precursor chain **1** eluting at exactly the same t_R, as a consequence of its internally crosslinked, compact structure when compared to the random coil precursor chain. [29-30]

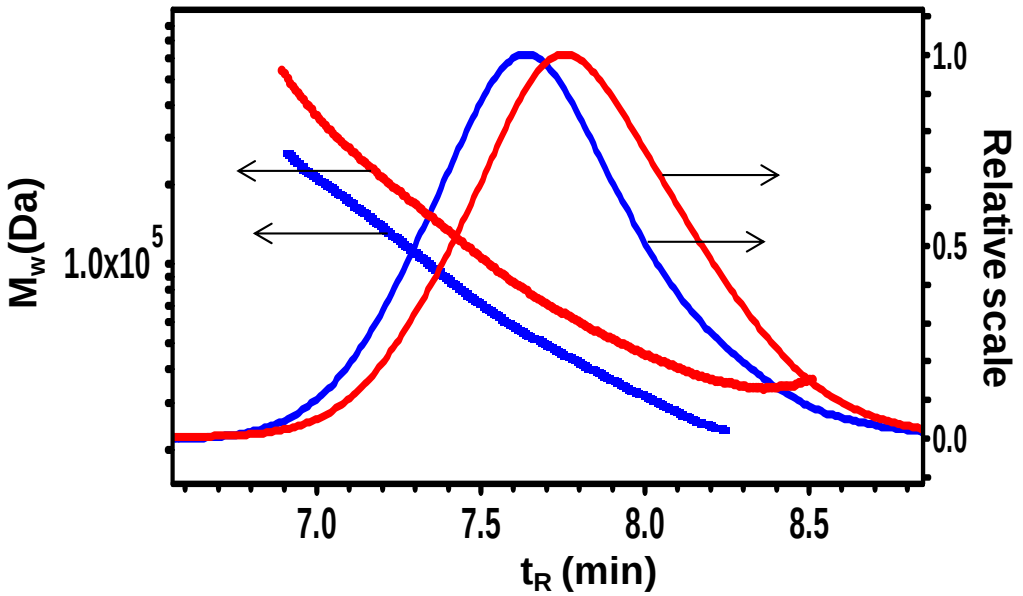

Figure 2.7. Actual M_w data and molecular mass distribution of linear P(MMA-*co*-PgA) copolymer (**1**, blue line) and single-chain nanoparticles (**2**, red line).

After 24 h of reaction time, the chain collapse of **1** was completed since no further change was observed by SEC at a longer reaction time (see Figure 2.8). Prior to the isolation of single-chain nanoparticles by concentration of the reaction mixture and further precipitation in MeOH, catalyst deactivation by

acid addition was performed to suppress potential intermolecular crosslinking between residual propargylic groups of different nanoparticles. Upon drying, single-chain nanoparticles, **2**, were found to be soluble in common organic solvents such as THF, chloroform and dimethyl formamide. The average hydrodynamic size of **2** was found to be 7 nm, as determined by DLS at room temperature in THF solvent (see Figure 2.9).

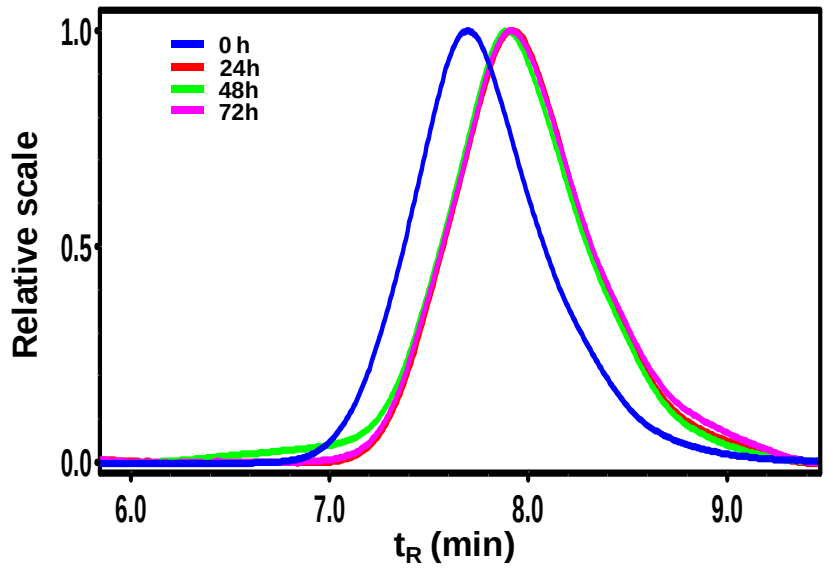

Figure 2.8. SEC traces as a function of reaction time during intrachain crosslinking of linear P(MMA-*co*-PgA) precursor **1** *via* metal-catalyzed carbon-carbon coupling.

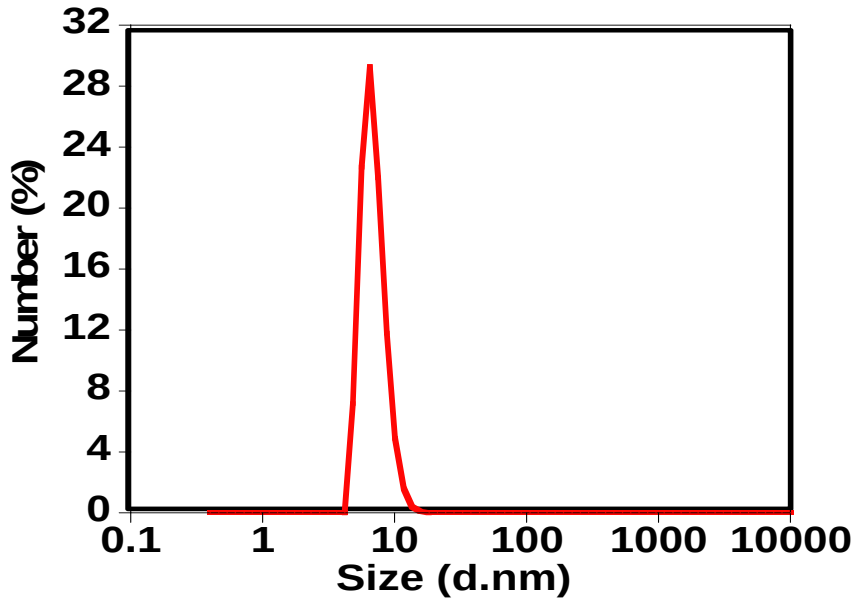

Figure 2.9. Size distribution by DLS of single-chain nanoparticles **2** synthesized by intrachain crosslinking of linear P(MMA-*co*-PgA) precursor **1** *via* metal-catalyzed carbon-carbon coupling. Average hydrodynamic size in THF by DLS, D_h= 7 nm.

The extent of intrachain C-C coupling in the single-chain nanoparticles was investigated qualitatively by infrared (IR) spectroscopy and quantitatively by ^{1}H NMR spectroscopy. Fourier Transform Infrared Spectroscopy (FTIR) results illustrated in Figure 2.10 show the presence of a new, sharp vibration band at 1685 cm^{-1} in single-chain nanoparticles which can be attributed to diyne-bonded carbonyl groups,[31] as well as the almost complete disappearance of the vibration bands at 3272 and 677 cm^{-1} corresponding to ≡C-H stretching and ≡C-H bending, respectively.[32]

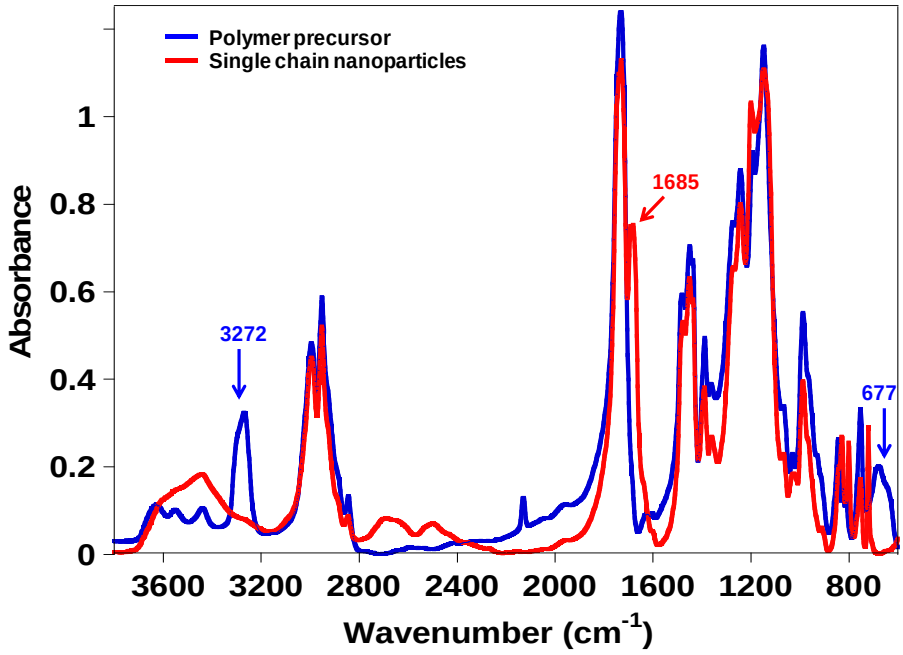

Figure 2.10. IR spectra of P(MMA-*co*-PgA) precursor (blue line) and single-chain nanoparticles (red line).

Upon intrachain crosslinking of **1** a clear broadening in all ^{1}H NMR signals was observed (see Figure 2.11) which was accompanied by a decrease in the relative intensity of some bands. Two effects are responsible for this behavior: i) intramolecular crosslinking (e.g. affecting peak **g**) and ii) insolubilization of those functional groups placed at the inner part of the single-chain nanoparticle (e.g. affecting peak **b**). Based on the residual intensity of the peak **g** (≡C-H) relative to the intensity of peak **f** (-CH$_2$-C≡), the degree of alkyne homocoupling in **2** was found to be 86%.

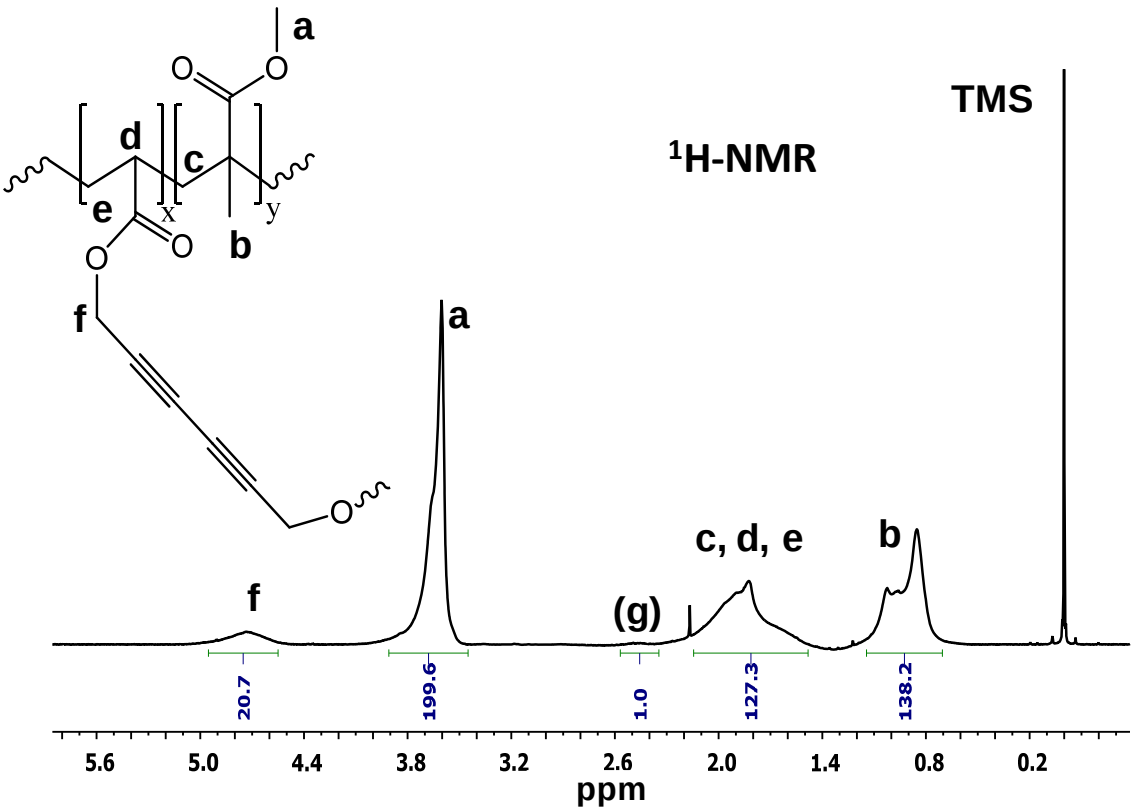

Figure 2.11. ^{1}H NMR spectrum in $CDCl_3$ of single-chain nanoparticles synthesized *via* C-C "click" chemistry.

2.5 Conclusion

In summary, successful synthesis of well-defined naked, propargylic-decorated single-chain nanoparticle precursors (M_w / M_n = 1.12 - 1.37, up to M_w = 100 kDa) *via* redox initiated RAFT polymerization at room temperature has been demonstrated. Accurate control over the molecular weight, polydispersity and composition of the linear poly(methyl methacrylate-*co*-propargyl acrylate), poly(MMA-*co*-PgA) precursor, was demonstrated by working up to a maximum polymerization time of 20 h and a maximum **PgA** monomer content in the feed of 35 mol%. The versatility of such "self-clickable" P(MMA-*co*-PgA) precursors has allowed, for the first time, the rapid and highly-efficient preparation of uniform single-chain polymer nanoparticles at r.t. under normal atmospheric conditions. This was achieved through intrachain C-C "click" chemistry using a highly efficient copper-catalyzed alkyne homocoupling (i.e., Glaser-Hay coupling).

2.6 References

[1] A. Tuteja, P. M. Duxbury, M. E. Mackay, *Macromolecules.,* **2007**, *40*, 9427.

[2] J. A. Pomposo, A. Ruiz de Luzuriaga, I. García, A. Etxeberria, J. Colmenero, *Macromol. Rapid Commun.,* **2011**, *32*, 573.

[3] G. Wulff, B.-O. Chong, U. Kolb, *Angew. Chem. Int. Ed.,* **2006**, *45*, 2955.

[4] C. T. Adkins, H. Muchalski, E. Harth, *Macromolecules.,* **2009**, *42*, 5786.

[5] A. Tamura, Y. Nagasaki, *Nanomedicine-U.K.,* **2010**, *5*, 1089.

[6] Altintas, O.; Barner-Kowollik, C, *Macromol. Rapid Commun.,* **2012**, *33*, 958.

[7] [7a] X. Jiang, H. Pu, P. Wang, *Polymer.,* **2011**, *52*, 3597; [7b] L. Buruaga, J. A. Pomposo, *Polymers.,* **2011**, *3*, 1673; [7c] L. Oria, R. Aguado, J. A. Pomposo, J. Colmenero, *Adv. Mater.,* **2010**, *22*, 3038; [7d] A. Ruiz de Luzuriaga, I. Perez-Baena, S. Montes, I. Loinaz, I. Odriozola, I. Garcia, J. A. Pomposo, *Macromol. Symposia.,* **2010**, *296*, 303; [7e] J. B. Beck, K. L. Killops, T. Kang, K. Sivanandan, A. Bayles, M. E.Mackay, K. L. Wooley, C. J. Hawker, *Macromolecules.,* **2009**, *42*, 5629; [7f] A. Ruiz de Luzuriaga, N. Ormategui, H. J. Grande, I. Odriozola, J. A. Pomposo, I. Loinaz, *Macromol. Rapid Commun.,* **2008**, *29*, 1156; [7g] A. E. Cherian, F. C. Sun, S. S. Sheiko, G. W. Coates, *J. Am. Chem. Soc.,* **129**, *2007*, 11350; [7h] J. Jiang, S. Thayumanavan, *Macromolecules.,* **2005**, *38*, 5886; ; [7i] D. Mecerreyes, V. Lee, C. J. Hawker, J. L. Hedrick, A. Wursh, W. Volksen, T. Magbitang, E. Huang, R. D. Miller, *Adv. Mater.,* **2001**, *13*, 204.

[8] [8a] B. S. Murray, D. Fulton, *Macromolecules.,* **2011**, *44*, 7242; [8b] J. He, L. Tremblay, S. Lacelle, Y. Zhao, *Soft Matter.,* **2011**, *7*, 2380; [8c] E. J. Foster, E. B. Berda, E. W. Meijer, *J. Am. Chem. Soc.,* **2009**, *131*, 6964; [8d] M. Seo, B. J. Beck, J. M. J. Paulusse, C. J. Hawker, S. Y. Kim, *Macromolecules.,* **2008**, *41*, 6413. [8e] R. Deans, F. Ilhan, V. M. Rotello, *Macromolecules.,* **1999**, *32*, 4956.

[9] Harth, E.; Horn, B.V.; Lee, V.Y.; Germack, D.S.; Gonzales, C.P.; Miller, R.D.; Hawker, C.J. *J. Am. Chem. Soc.,* **2002**, *124*, 8653.

[10] Croce, T.A.; Hamilton, S.K.; Chen, M.L.; Muchalski, H.; Harth, E. *Macromolecules.,* **2007**, *40*, 6028.

[11] Dobish, J.N.; Hamilton, S.K.; Harth, E. *Polym. Chem.,* **2012**, *3*, 857.

[12] C. J. Li. *Accounts Chem. Res.,* **2010**, *43*, 581.

[13] C. Glaser. *Ber. Dtsch. Chem. Ges.,* **1869**, *2*, 422.

[14] [14a] J. E. Hein, V. V. Fokin, *Chem. Soc. Rev.*, **2010**, *39*, 1302; [14b] M. Mendal, C. W. Tornøe, *Chem. Rev.,* **2008**, *108*, 2952; [14c] C. W. Tornøe, C. Christensen, M. Meldal, *J. Org. Chem.,* **2002**, *67*, 3057; [14d] V. V. Rostovtsev, L. G. Green, V. V. Fokin, K. B. Sharpless, *Angew. Chem. Int. Ed.,* **2002**, *41*, 2596; [14e] H. C. Kolb, M. G. Finn, K. B. Sharpless, *Angew. Chem. Int. Ed.,* **2001**, *40*, 2004.

[15] F.Bohlmann, H.Schönowsky, E.Inhoffen, G.Grau. *Chem.Ber.,* **1964**, *97,* 794.

[16] G. F. D´Alelio, R. C. Evers, J. *Polym. Sci., Part A-1.,* **1967**, *5*, 999.

[17] B. S. Sumerlin, N. V. Tsarevsky, G. Louche, R. Y. Lee, K. Matyjaszewski. *Macromolecules.*, **2005**, *38*, 7540.

[18] W. Zhang, W. Zhang, Z. Zhang, J. Zhu, X. Zhu. *Macromol. Rapid Commun.*, **2010**, *31*, 1354.

[19] M. Kato, Y. Yoneshige. *J. Polym. Sci., Polym. Lett. Ed.,* **1979**, *17*, 79.

[20] G. Li, H. Zheng, R. Bai. *Macromol. Rapid Commun.,* **2009**, *30*, 442.

[21] J. Chiefari, Y. K. Chong, F. Ercole, J. Krstina, J. Jeffery, T. P. T Le, R. T. A Mayadunne, G.F. Meijs, C.L. Moad, G. Moad, E. Rizzardo, S.H. Thang. *Macromolecules*., **1998**, *31*, 5559.

[22] G. Moad, E. Rizzardo, S.H. Thang. *Aust J. Chem*., **2005**, *58*, 379.

[23] A.S. Brar, Sunita Hooda, Ashok Kumar Goval., *Journal of Molecular Structure*., **2006**, *828*, 25.

[24] K. D. Demir, B. Kiskan and Y. Yagci. *Macromolecules*., **2011**, *44*, 1801.

[25] C. J. Ochs, G. K. Such and F. Caruso, *Langmuir.*, **2011**, *27*, 1275.

[26] D. D. Evanoff, S. E. Hayes, Y. Ying, G. H. Shim, J. R. Lawrence,J. B. Carroll, R. D. Roeder, J. M. Houchins, C. E. Huebner and, S. H. Foulger, *Adv. Mater*., **2007**, *19*, 3507.

[27] S. Zhang, X. Liu, T. Wang, *Adv. Synth. Cata.,* **2011**, *353*, 1463.

[28] J. A. Pomposo, I. Perez-Baena, L. Buruaga, A. Alegra, A. J.Moreno, J. Colmenero, *Macromolecules.,* **2011**, *44*, 8644 – 8649.

[29] B.T Tuten; D. Chao; C. K Lyon; E. B. Berda, *Polym. Chem.,* **2012**, *3*, 3068.

[30] D. Chao; X. Jia; B. Tuten; C. Wang; E.B. Berda. *Chem. Commun.,* **2013**, *49*, 4178.

[31] L. Fomina, S. Fomine, T. Ogawa, *Polym. Bull.*, **1995**, *34*, 547.

[32] R. A Nyquist, W. J Potts, *Spectrochimica Acta*., **1960**, *16*, 419

CHAPTER 3:

Single-Chain "Michael" Nanocarriers

3.1 Introduction

Nature is a continuous source of inspiration for scientists across different disciplines.[1] In particular, the –native– conformation of proteins which allows these large biomolecules to carry out sophisticated tasks such as binding and transporting small organic molecules inspired the construction of a first generation of artificial enzymes based on a variety of molecular and macromolecular structures such as macrocyclic compounds,[2] star and helical polymers,[3] dendrimers[4], micelles[5] and as will be demonstrated below single-chain polymer nanoparticles.

As described in the Introduction, single-chain polymer nanoparticles are emerging soft nano-objects showing unique and remarkable physicochemical, rheological and sensing properties,[6] as a result of their locally collapsed structure and their ultra-small size.[7,9] The potential use of single-chain nanoparticles as drug / siRNA nanocarriers and photostable bioimaging agents relies on the improved construction of functional folded/collapsed single polymer chains. Moreover, the controlled synthesis of single-chain nanocarriers becomes critical to the elucidation of useful structure-property relationships in material science and to deepen our current understanding of complex cooperative folding events taking place in synthetic single polymer chains, emulating protein folding.[10] Unfortunately, most of the current synthesis routes to stable single-chain nanoparticles suffer from different shortcomings, such as the use of extremely high temperatures, the requirement of severe anhydrous conditions, the involvement of metallic catalysts or the necessity of exotic, non-commercial monomers, which severely limit their potential applications in some promising fields (e.g., nanomedicine).[11] Despite all recent advances, the development of a natural route to well-defined single-chain nano-objects allowing the investigation into how far, or close, the structure and function of these synthetic nanocarriers are from those of globular, or intrinsically disordered, proteins is still a challenging issue.

In nature, we can find perfectly ordered (or folded, globular) proteins[12−15] or intrinsically disordered (unfolded or coil-like) proteins [16-20] . Among others, the vitamin D-binding protein (DBP) or GC-globulin, identified about a half a century ago,[21] is a multi-functional globular protein found in human serum that binds and transports various forms of vitamin D, as well as other biomolecules like actin or fatty acids. DBP´s main function is to retain vitamin D for the organism and make it available to various tissues and cell types for usage.[22] In contrast to globular proteins (such as DBP) adhering to the classical structure-function paradigm, intrinsically disordered proteins (IDPs) lack a well-defined unique structure, adopting a complete ensemble of rapidly interconverting conformations in solution.[23] Interestingly, in spite of their disordered structure, IDPs can bind several ligands, such as ions, small organic molecules, other proteins and nucleic acids (RNA, DNA). The interplay between structure and function in IDPs has not been recognized until very recently and it is not completely understood yet.[20] Although some IDPs are simple coils that bond other proteins together, most of them have transient-binding or permanent-binding recognition sites. Moreover, a large number of IDPs exhibit what is referred to as binding promiscuity[16], where one protein or region is able to bind to multiple partners.[24]

Inspired by the multifunctionality of vitamin D-binding protein and the remarkable binding promiscuity of some intrinsically disordered proteins (IDPs), an efficient strategy to construct single-chain polymer nanoparticles (SCNPs) that resemble intrinsically disordered proteins (IDPs) will be reported in the first part of this Chapter. In the second part, the resulting SCNPs will be investigated as transient binding disordered nanocarriers from which controlled delivery of both dermal protective (vitamin B_9) and anticancer (hinikitiol) cargos in water will be demonstrated.

In particular, SCNPs that resemble intrinsically disordered proteins will be prepared by the Michael addition reaction. The Michael reaction has previously been employed in the synthesis of linear, graft, hyperbranched, dendritic and network polymers, as well as in post-polymerization modification and bioconjugation, being one of the most useful and versatile reactions to create new carbon-carbon bonds.[25] The Michael reaction typically refers to the base-catalyzed addition of a nucleophile such as an enolate anion (Michael donor) to an activated α,β-unsaturated carbonyl-contained compound (Michael acceptor). The mechanism of the Michael reaction (see Scheme 3.1) is dependent on the relative strengths of the base and the type of acetoacetate. The acetoacetate is first deprotonated by the base, providing an enolate anion (Michael donor) in equilibrium. The enolate anion then reacts with an electron-deficient olefin (Michael acceptor) and finally the carbonyl of the acrylate stabilizes the resulting anion until proton transfer occurs, regenerating the base.[25]

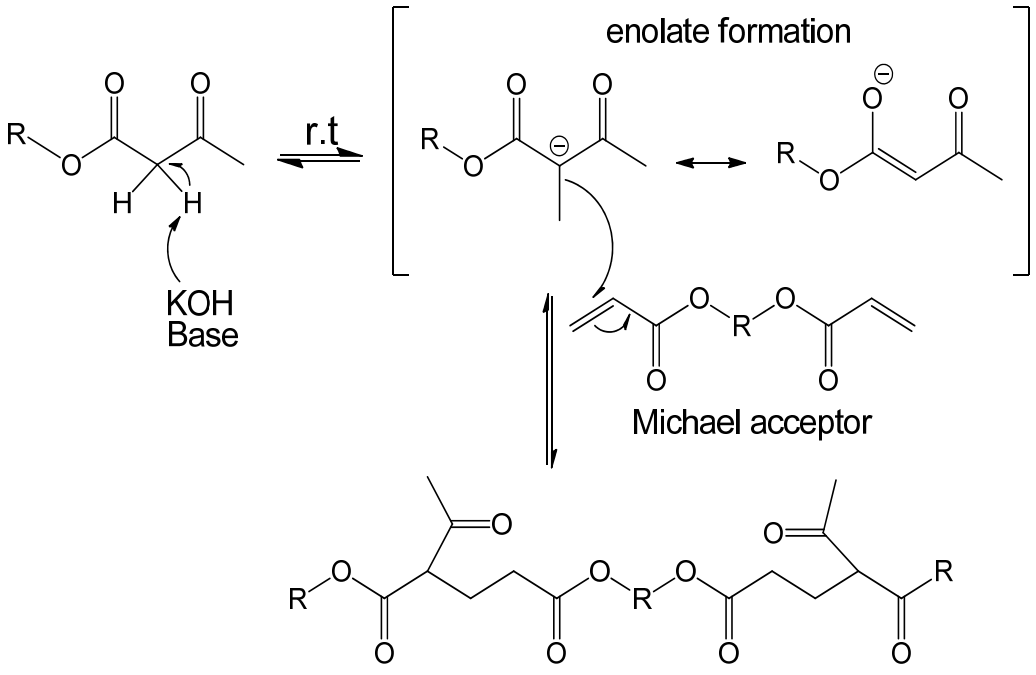

Scheme 3.1. General carbon-Michael reaction mechanistic scheme.

3.2 "Michael" Nanocarriers Mimicking Trasient-Binding Disordered Proteins

3.2.1 Objectives

In this part of this Chapter, we report a simple and highly-efficient bio-inspired method for transient-binding nanocarrier construction that relies on multidirectional self-assembly of individual polymeric chains at r.t. driven by Michael addition reactions involving external multifunctional acrylate-based crosslinkers (see scheme 3.2). Single-chain nano-object formation through multidirectional self-assembly is inspired by protein assembly to the folded state. For proteins, the driving force for folding depends on the sequence of amino acids, their mutual interactions and their interactions with solvent molecules, whereas for "Michael" nanocarriers the driving force is replaced by multiple, cooperative, omnidirectional chemical (Michael addition) reactions taking place across the collapsing polymer chains under good solvent conditions (Scheme 3.3).

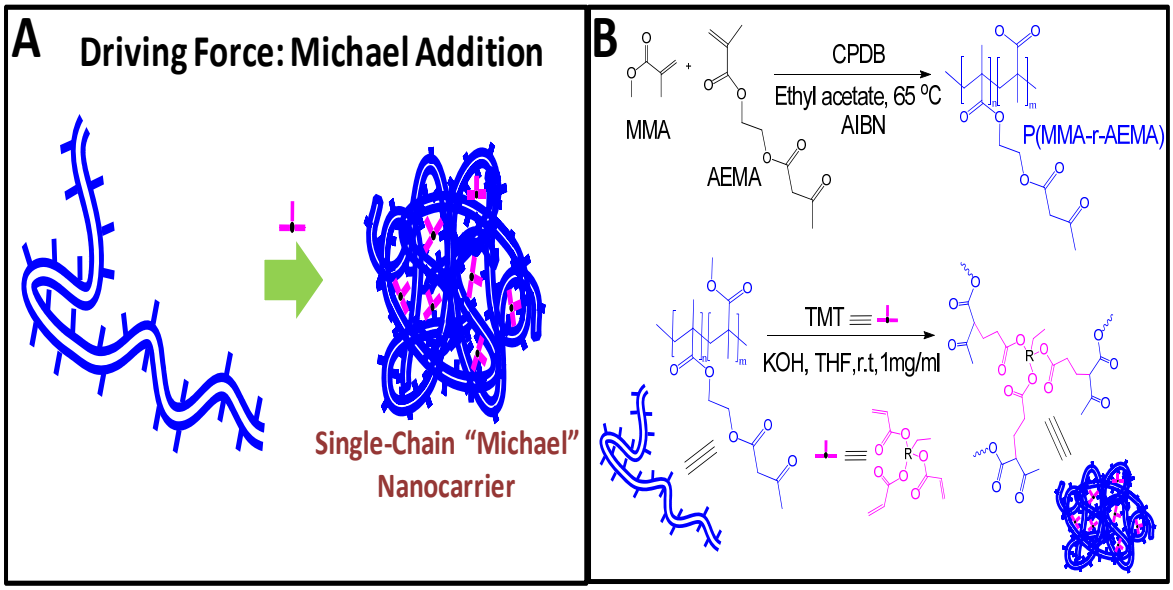

Scheme 3.2. The construction of transient–binding Michael nanocarriers. **A)** Intramolecular Michael addition reactions take place to form single-chain Michael nanocarriers. **B)** Acrylate based crosslinkers react with β-ketoester groups of the unfolded linear polymer chain under appropriate, solvent, stoichiometric and dilution conditions.

As will be shown later, Michael addition-mediated multidirectional self-assembly of individual polymeric chains at r.t. leads to "Michael" nanocarriers that in solution resemble disordered multidomain proteins as revealed by a combination of small angle neutron scattering (SANS) measurements and coarse-grained molecular dynamics (MD) results. Whereas in the dry state, the "Michael" nanocarriers, adopt a collapsed, globular morphology, as observed by transmission electron microscopy (TEM). This extended-to-compact morphology transition taking place upon solvent removal is of paramount importance, among other applications, for the construction of efficient biosensors based on immobilized protein-mimic nano-objects and for the development of transient vitamin-binding systems. As a proof of concept, we show the controlled delivery of vitamin B_9 from these novel transient-binding nanocarriers.

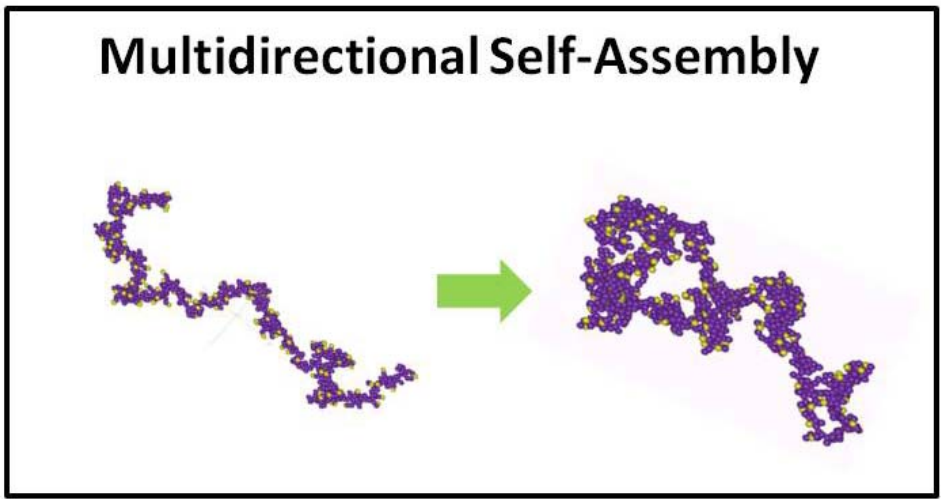

Scheme 3.3. Multidirectional self-assemby during the synthesis of "Michael" nanocarriers.

3.2.2 Experimental Section

a) Synthesis of "Michael"nanocarrier precursors.

Before polymerization methyl methacrylate (**MMA**) was purified by distillation and 2-(acetoacetoxy) ethyl methacrylate (**AEMA**) was purified by passing through basic alumina. In a standard procedure, **MMA** (1 ml, 9.4 mmol), **AEMA** (0.6 ml, 3.1 mmol), 2-cyanoprop-2-yl-dithiobenzoate (CPDB, 0.8 mg, 3×10^{-2} mmol) and 2,2-azobis(2-methylpropionitrile) (AIBN, 1 mg, 3×10^{-2} mmol) were dissolved in ethyl acetate (3.2 ml). The reaction mixture was degassed by bubbling argon for 15 min. The copolymerization reaction was carried out at 65 ^{o}C for 18 h. The resulting nanoparticle precursor was isolated by precipitation in methanol and further drying (**P2**: Yield (%) = 42, M_p (SEC/MALLS) = 289 kDa, M_w/M_n = 1.39, R_g = 14.5 ± 0.4 nm, composition (^{1}H NMR) = 28 mol% **AEMA**). The main characteristics of copolymers **P1-P4** are summarized in Table 3.1.

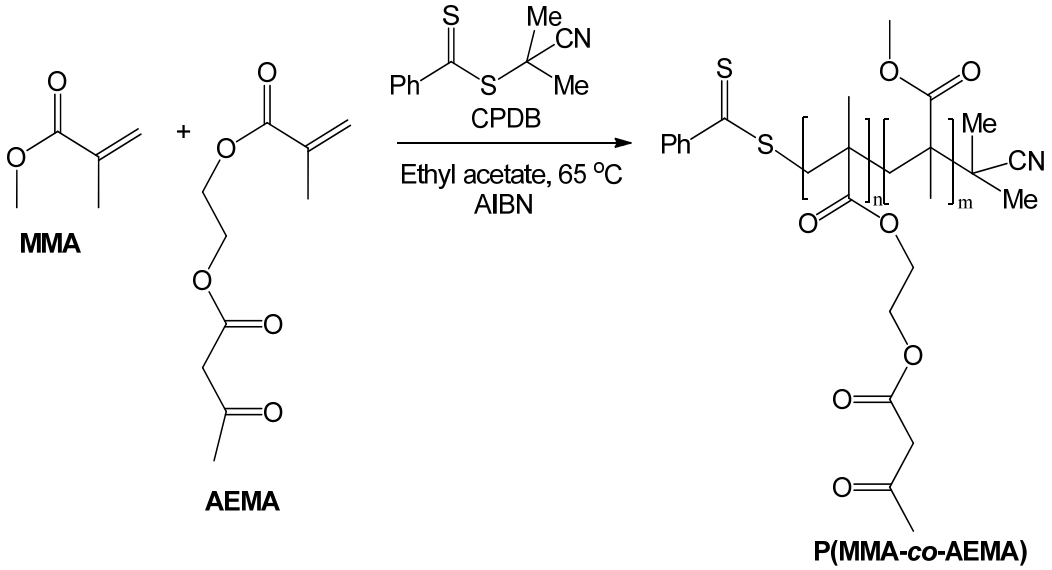

Scheme 3.4. Synthesis of single-chain Michael nanocarrier precursor *via* reversible addition-fragmentation chain-transfer RAFT polymerization.

b) Synthesis of "Michael" nanocarriers.

In a typical reaction, P(MMA-*co*-AEMA) polymer precursor (**P2**, 150 mg, 0.32 mmol), multifunctional cross-linker (**a**: 1,3- butanediol diacrylate (BDD), 30.7 µL, 0.16 mmol; **b**: trimethylolpropane triacrylate (TMT), 29.6 µL, 0.11 mmol)

and catalyst (KOH, 8.9 mg, 0.16 mmol) were dissolved in THF (150 ml) at room temperature (see Scheme 3.5). The progressive folding/collapse process was followed through simultaneous SEC/MALLS measurements. After reaction completion (after 3 days), a few drops of trifluoroacetic acid were added to deactivate the catalyst, the mixture was concentrated and the single-chain Michael nanocarriers were isolated by precipitation in diethyl ether and further drying (**NP2a**: Yield (%) = 79, M_p (SEC/MALLS) = 290 kDa, M_w/M_n = 1.32, R_g = 12.9 ± 0.9 nm; **NP2b**: Yield (%) = 81, M_p (SEC/MALLS) = 297 kDa, M_w/M_n = 1.18, R_g = 8.5 ± 0.5 nm).

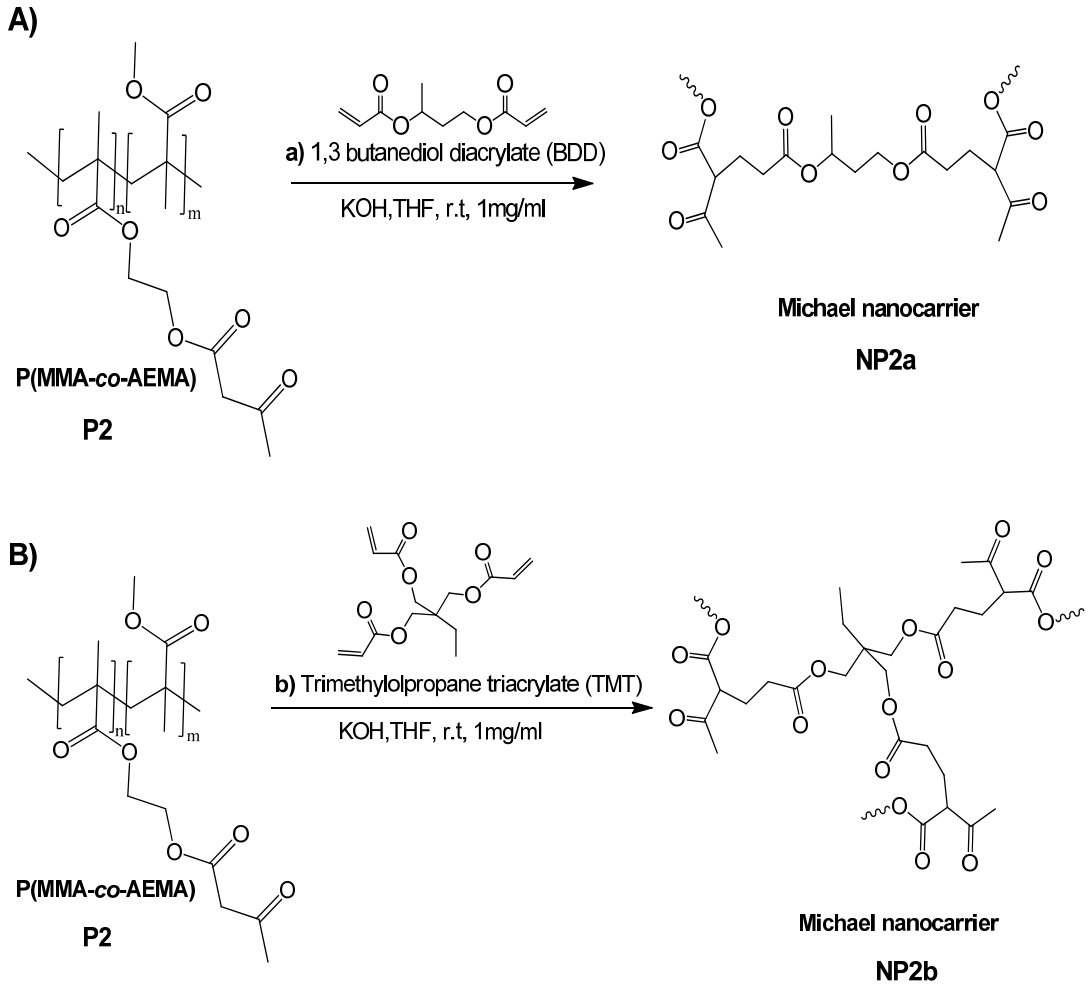

Scheme 3.5. Single-chain Michael nanocarrier formation with multifunctional cross-linkers (**A**: with 1,3-butanediol diacrylate (BDD); **B**: with trimethylolpropane triacrylate (TMT)).

c) Model reactions for the kinetic study of Michael reaction with low molecular weight model compounds.

Typically, methyl acetoacetate **(3)** (4.48µL, 0.04 mmol), a multifunctional cross-linker (**a**: 1,3-butanediol diacrylate (BDD), 4µl, 0.02 mmol; or **b**: trimethylolpropane triacrylate (TMT), 3.7 µl, 0.0138 mmol) and catalyst (KOH, 1.12 mg, 0.02 mmol) were dissolved in d-THF at r.t (see Scheme 3.6). Hexamethyldisiloxane (HMDSO) was used as an internal standard. A ^{1}H NMR spectrum was taken every hour starting at 0 time until 10 hours in order to follow the kinetics of the Michael reaction. The same experiment was carried out with a P(MMA-*co*-AEMA) precursor. But in the latter case a ^{1}H NMR spectrum was taken every hour starting at 0 time until 60 hours.

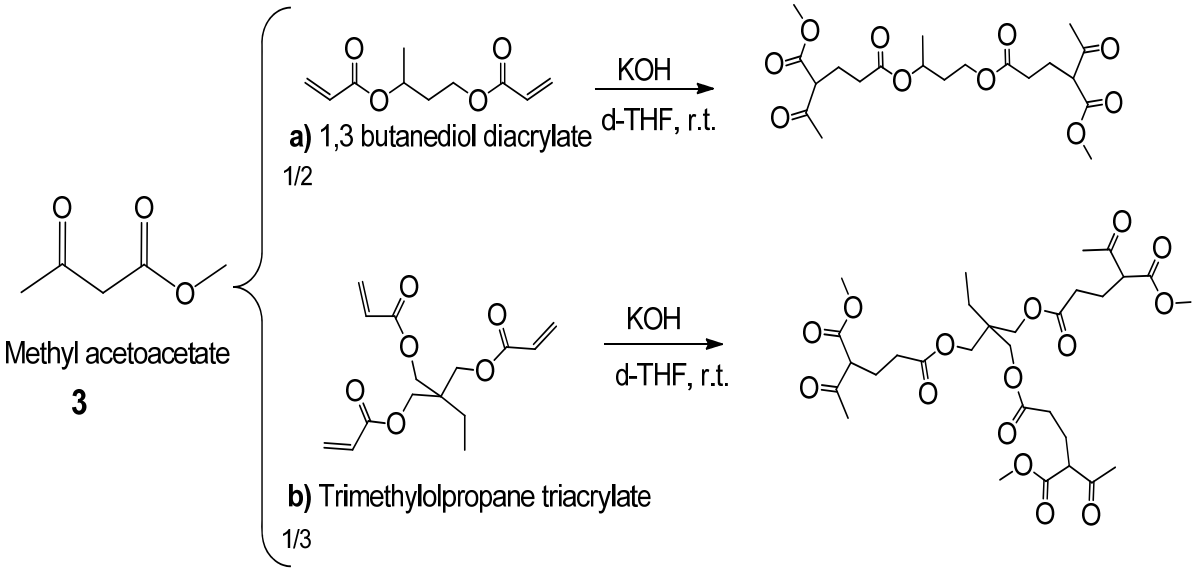

Scheme 3.6. Michael reaction with methyl acetoacetate **(3)** and **a**: 1,3-butanediol diacrylate (BDD) or **b**: trimethylolpropane triacrylate (TMT).

d) Vitamin B_9-loaded Michael nanocarriers.

Single-chain Michael nanocarriers, **NP2b**, were loaded with vitamin B_9 (Scheme 3.7 A) by following typical drug-loading protocols reported in the literature.[26] Single-chain Michael nanocarriers, **NP2b,** (2 mg) and vitamin B_9 (2 mg) were dissolved and mixed in dimethylsulfoxide (DMSO, 0.5 ml). After complete dissolution, the vitamin B_9 loaded Michael nanocarriers, **NP2b**, were

precipitated in 10 ml of diethyl ether and filtered using a conventional filter paper. Alkaline water was used to remove the excess of vitamin B_9 (that was visible as yellow impurities in the sample). Then, the vitamin B_9 loaded Michael nanocarriers were transferred to a flask containing 100 ml of water (at pH= 7) at 25 ^oC. Samples for UV measurements were taken every 1 hour, starting at 0 time until 8 hours. The delivery of vitamin B_9 from the single-chain Michael nanocarriers was determined from UV/Vis spectroscopy measurements at 283 nm using a standard calibration curve obtained with appropriate vitamin B_9/water solutions (Scheme 3.7 B).

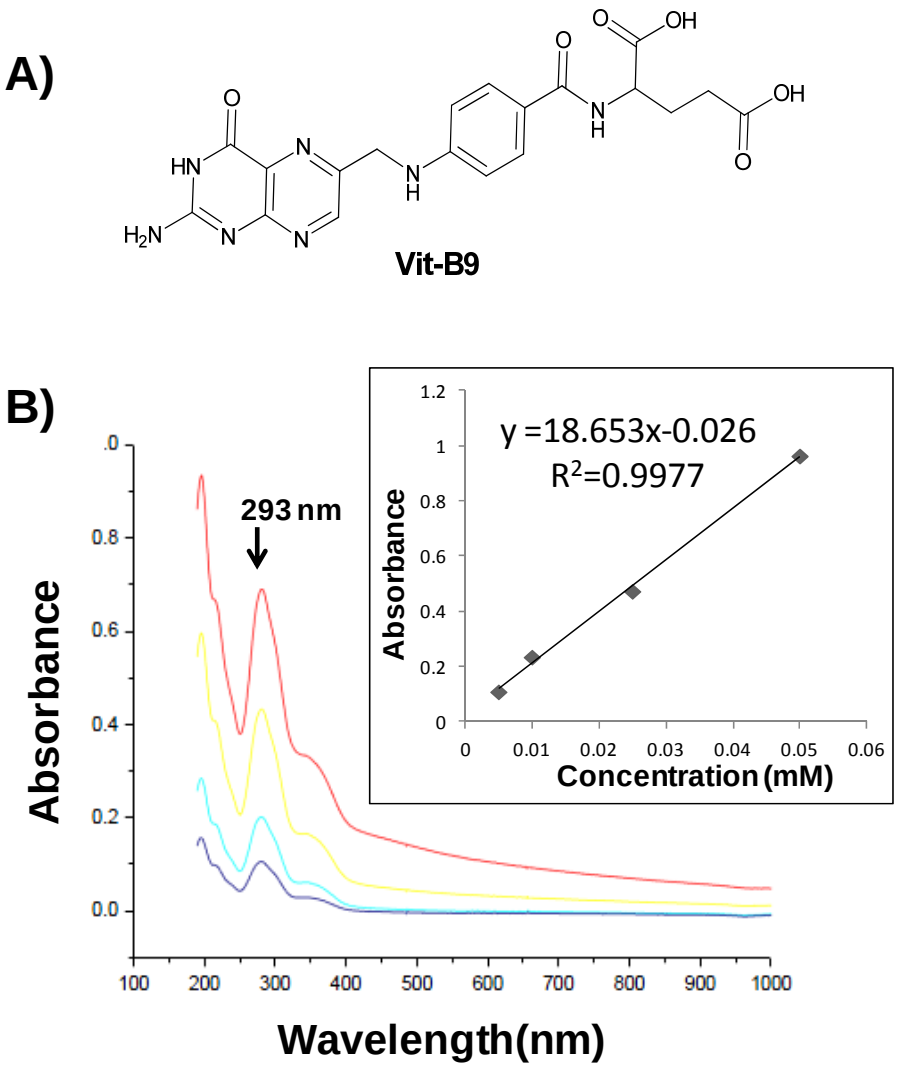

Scheme 3.7. **A)** Chemical structure of vitamin B_9, also known as folic acid, folate, or vitamin M. **B)** Calibration curve for vitamin B_9 in neutral water at 25 ^oC, as determined by UV/Vis spectroscopy at 283 nm, using vitamin B_9 / water solutions of varying concentration.

3.2.3 Results and Discussion

As will be shown in this section, the benefits of Michael addition-mediated multidirectional self-assembly as a synthesis strategy for artificial protein-mimic nano-objects are: *i)* versatility of the method in terms of reaction conditions (i.e., absence of metal catalysts, room temperature, air atmosphere), *ii)* commercial availability of reagents allowing the facile synthesis of Michael nanocarriers (gram-scale) for potential end-use in nanomedicine, bioimaging and sensing applications, *iii)* convenient time-span for direct monitoring in solution of the self-organized, cooperative folding/collapse process, *iv)* versatility for obtaining nano-objects resembling transient-binding disordered proteins in solution, and *v)* promising nanocarrier properties of the resulting multidomain nano-objects.

"Michael" nanocarriers were prepared from polymeric precursors synthesized through reversible addition-fragmentation chain-transfer (RAFT)[27-28] polymerization by starting with commercially available methyl methacrylate (**MMA**) and (2-acetoacetoxy) ethyl methacrylate (**AEMA**) monomers (Table 3.1). Statistical copolymers of P(MMA-*co*-AEMA) were obtained due to the similar reactivity ratios of **MMA** (r = 0.90) and **AEMA** (r = 0.95)[29] providing materials of high molar mass, relatively narrow size dispersity and random distribution of *β*-ketoester functional groups (i.e., Michael donors) along the polymer chain.

Table 3.1. Characteristics of P(MMA-*co*-AEMA) copolymers **P1-P5.**

Sample	M_w (g/mol)[a]	M_w/M_n	AEMA (mol %)
P1	1850000	1.4	27
P2	289800	1.4	28
P3	213900	1.3	19
P4	151500	1.2	9
P5	134100	1.1	28

[a]Actual weight average molecular weight as determined by combined SEC/MALLS measurements. (SEC/MALLS, dn/dc= 0.083).

The ^{1}H NMR spectrum of sample **P2** in $CDCl_3$, shown in Figure 3.1, confirmed the expected chemical structure of the P(MMA-*co*-AEMA) copolymer. The spectrum showed the characteristic signals of both acetoacetoxy tautomers (keto: δ =2.3 ppm; enol: δ= 5.1 and 11.9 ppm, two possible enol forms), the first one (keto form) being the preferred structure (~90%). The copolymer composition estimated from the normalized areas of peaks **d, e** and **f** in Figure 3.1 was 28 **AEMA** mol%, so **P2** was found to be slightly enriched in **AEMA** units when compared to the molar fraction of **AEMA** in the feed (25% **AEMA**).

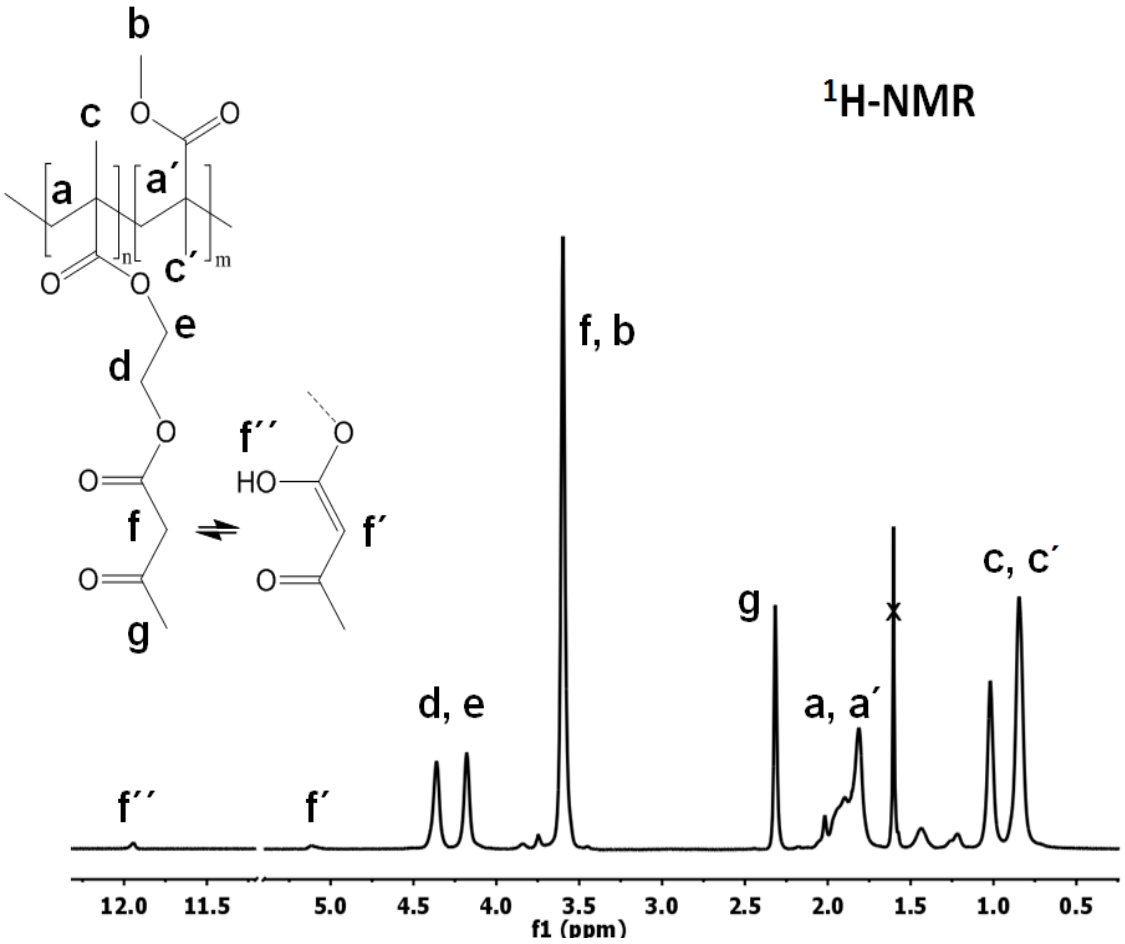

Figure 3.1. ^{1}H NMR spectrum of linear P(MMA-*co*-AEMA) in $CDCl_3$.

As external cross-linkers playing the role of Michael acceptors[30], we selected commercially available low-molecular-weight multi-functional (bi-, tri-, tetra-, penta / hexa-) acrylate compounds (Scheme 3.8).

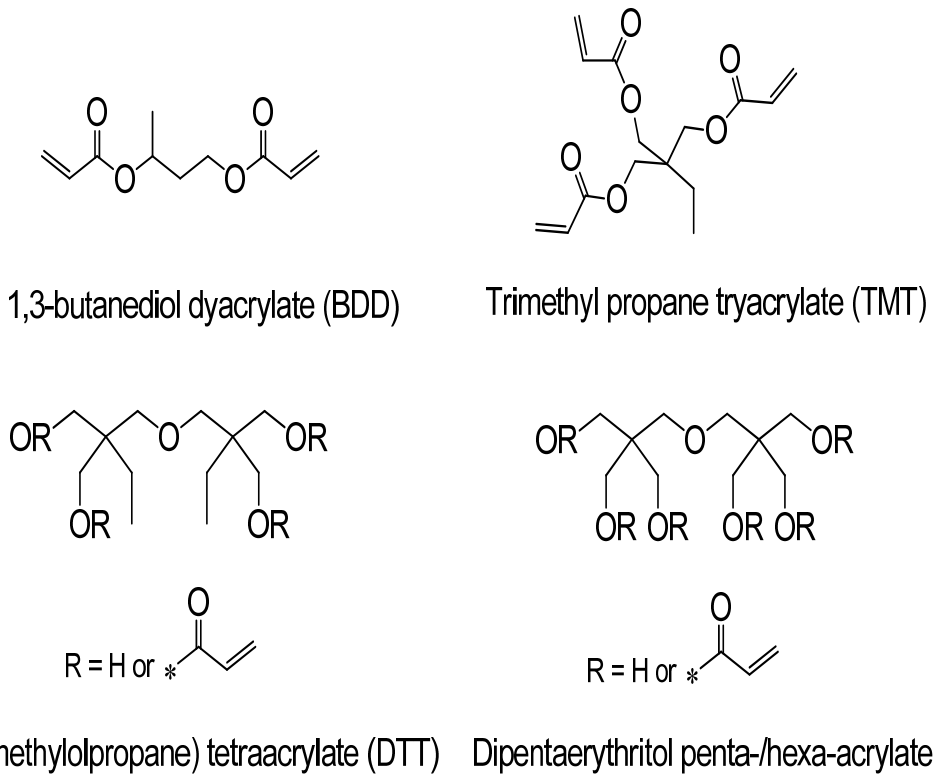

Scheme 3.8. Chemical structures of multi-functional acrylate compounds used in this work.

The multidirectional self-assembly of the individual P(MMA-*co*-AEMA) polymeric precursor to Michael nanocarriers was performed in tetrahydrofuran (THF), at r.t. under potassium hydroxide (KOH) catalysis and air atmosphere, at a concentration of polymeric precursor of 1 mg / ml by using equimolar amounts of β-ketoester and acrylate functional groups. As an example, Figure 3.2 shows the systematic shift in size exclusion chromatography (SEC) traces towards longer retention time during the synthesis of single-chain Michael nanocarriers in the presence of a tri-functional crosslinker (trimethylolpropane triacrylate, TMT). The noticeable shift observed is a consequence of the progressive reduction in hydrodynamic size and, consequently, in apparent molar mass (M_p ^{app}) with reaction time (open circles in Figure 3.2).[31-33] The absence of significant inter-particle aggregation was confirmed through simultaneous MALLS measurements from which, as expected, a nearly constant value of actual molar mass was observed ($M_p \approx 293$ kDa, closed circles in Figure 3.2).[34-35]

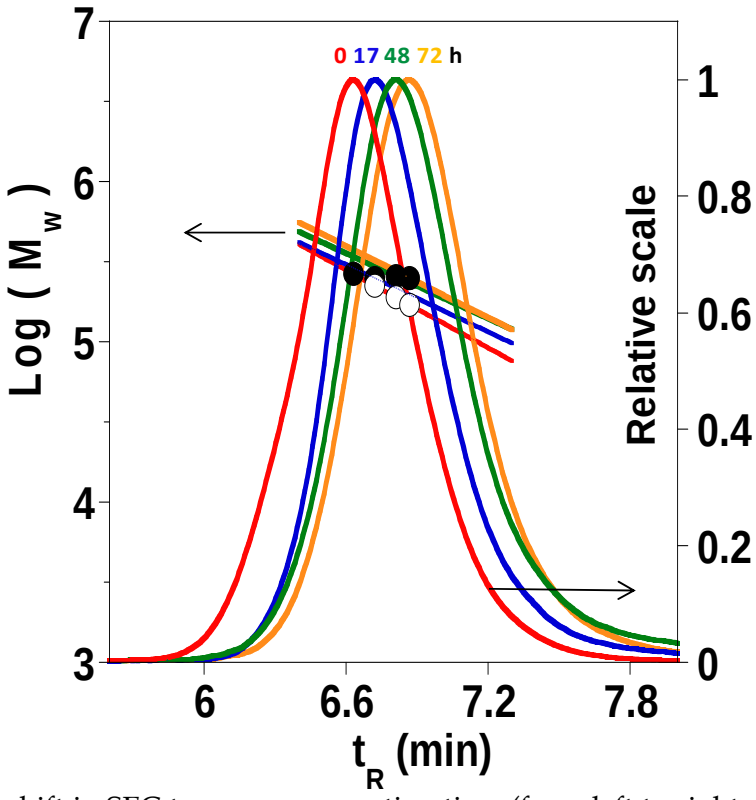

Figure 3.2. The shift in SEC traces upon reaction time (from left to right: 0 h, 17 h, 48 h and 72 h) is due to a progressive reduction in hydrodynamic volume and, consequently, in apparent molar mass, ($M_{p\ app}$, open symbols), whereas the nearly constant value of actual molar mass ($M_p \approx 293$ kDa, closed symbols) points to the collapse of individual polymer chains without significant inter-particle aggregation.

The kinetics of the Michael addition reaction for construction of Michael nanocarriers and the kinetics of the condensation *via* Michael addition of mixtures of low-molecular-weight model compounds were determined by ^{1}H NMR measurements under identical reaction conditions (i.e., solvent, temperature, and reagent concentration). In order to determine the kinetics of the Michael reaction the disappearance of the ^{1}H NMR peaks corresponding to the double bonds of the acrylate based crosslinkers were followed (Figure 3.3).

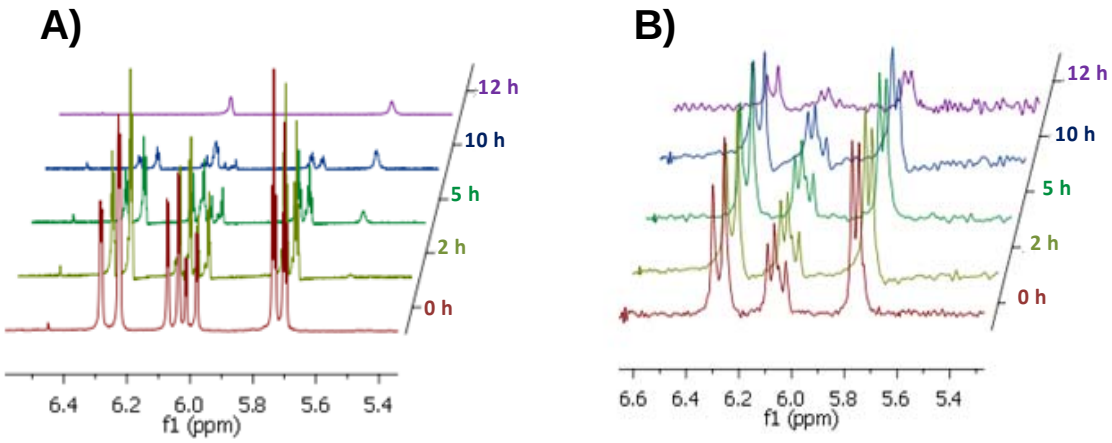

Figure 3.3. Evolution of the ^{1}H-NMR spectra during the condensation *via* Michael addition of **A)** methyl acetoacetate / BDD mixtures and **B)** methyl acetoacetate / TMT mixtures. After 12 h the signals corresponding to the double bonds of acrylate based crosslinkers totally disappeared.

The kinetics of the Michael addition reaction for multidirectional self-assembly was *ca.* 50-fold slower than that corresponding to condensation *via* Michael addition of mixtures of low-molecular-weight model compounds (e.g., methyl acetoacetate / TMT mixtures) as determined by ^{1}H NMR measurements (Figure 3.4).

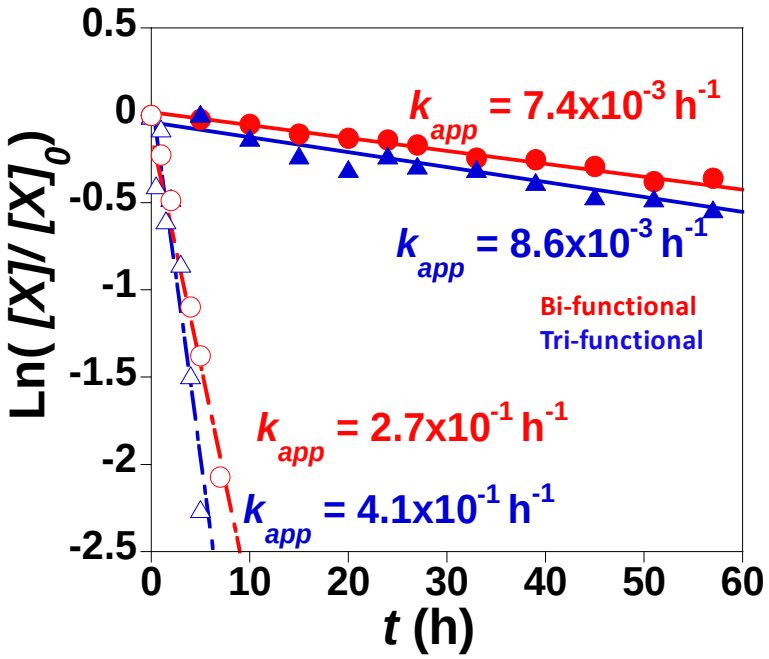

Figure 3.4. Pseudo-first order kinetics plots corresponding to the consumption of bi-functional (closed circles) and tri-functional (closed triangles) cross-linker units (X). Also displayed for comparison are the corresponding kinetics plots for low-molecular-weight model compound mixtures (open symbols).

The main reason for the significantly slower kinetics seems to be the macromolecular character of the polymeric precursor which imposes diffusional constrains and significantly restricted intrachain accessibility to the low-molecular-weight acrylate cross-linker units.

Additionally, ^{1}H NMR spectra of the Michael nanocarrier formation shows that apart from the disappearance of peaks corresponding to double bonds of the acrylate based crosslinkers; there is a decrease in the relative intensity of some bands corresponding to protons of the polymer chain (Figure 3.5, green circles)). Insets in Figure 3.5 show clear band broadening in signals arising from –CH_2 protons of **AEMA** (4.3 ppm, broad signal) and -CH_3 protons of the main-chain methyl groups (0.7–1.2 ppm, broad signal) of Michael nanocarriers. For single-chain polymer nanoparticles, signal broadening in the ^{1}H NMR spectrum can be attributed to the restricted mobility of some of the nanoparticle protons as a consequence of the progressive cross-linking.[36]

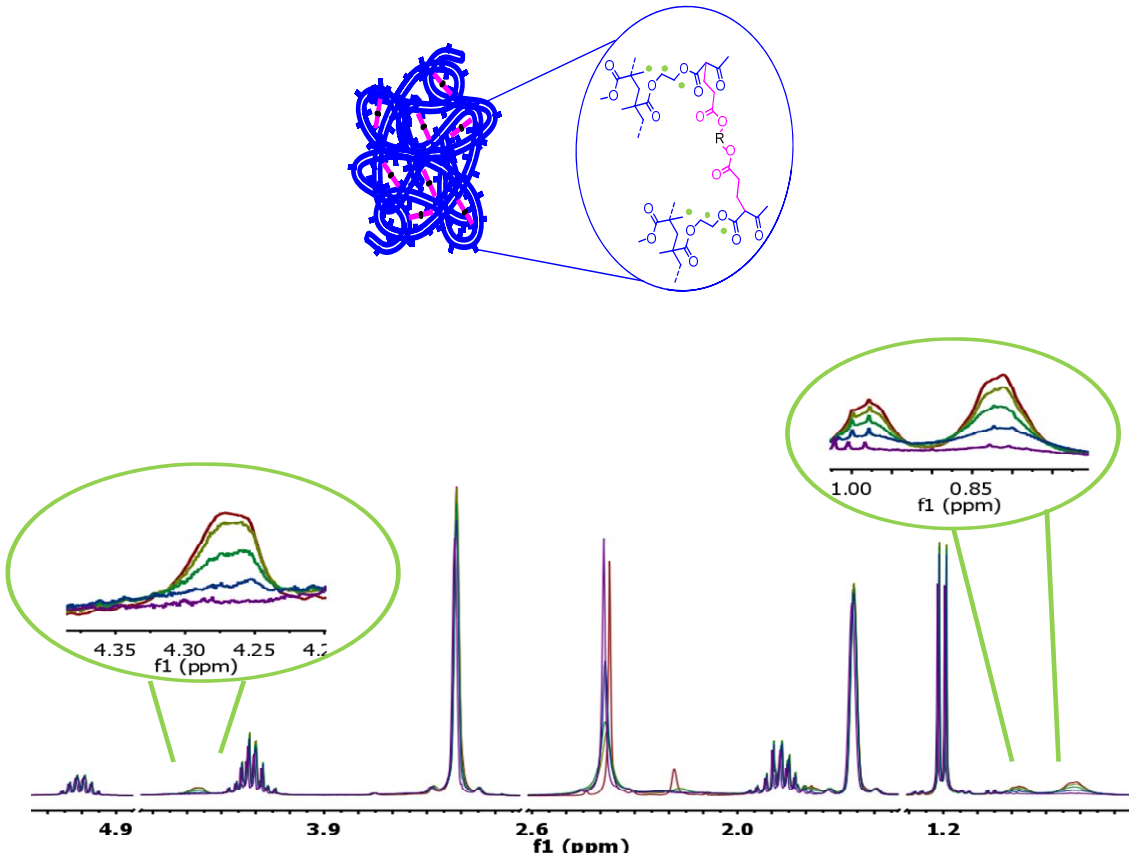

Figure 3.5. Evolution of the ^{1}H-NMR spectra during the condensation *via* Michael addition of P(MMA-*co*-AEMA) / BDD mixture.

We have determined the kinetics of the folding/collapse process in solution through the direct monitoring of the value of z-average radius of gyration (R_g) of the polymeric precursor as a function of reaction time, by means of MALLS measurements (Figure 3.6 A). The kinetics of the folding/collapse process was found to be *ca.* 5-fold slower than that of the Michael-mediated intrachain cross-linking reaction, which can be attributed to the coexistence of non-efficient and efficient folding events. In this sense, the first anchoring step of a multifunctional cross-linker molecule through reaction of a single acrylate group can be considered as a non-efficient folding event that does not contribute to chain collapse. Conversely, the delayed, subsequent intrachain Michael reactions of the remaining acrylate groups are truly folding/collapse-promoting events. As illustrated in Figure 3.6 A, the kinetics of folding/collapse is slightly faster upon decreasing the molar mass of the polymeric precursor. Even displaying much slower folding kinetics when compared to that of natural proteins (from microseconds to hours),[37] the resulting Michael nanocarrriers in the dried state showed a compact spherical morphology as illustrated in Figure 3.6 B.

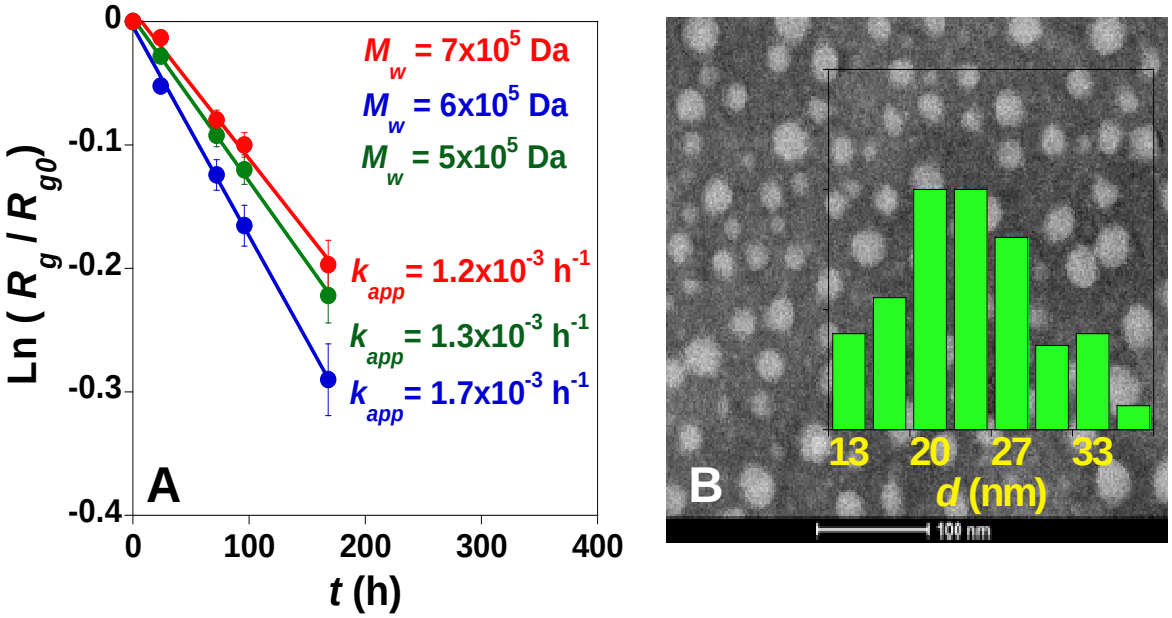

Figure 3.6. A) Pseudo-first order kinetics plots corresponding to the folding/collapse process in solution at r.t. in the presence of tri-functional cross-linker units. **B)** TEM image showing the morphology of Michael nanocarriers in the dry state.

Upon isolation by precipitation, drying under dynamic vacuum and further solubilization, Michael nanocarriers were found to form transparent, colorless dispersions in common organic solvents (tetrahydrofuran, chloroform, dimethyl formamide).

As is illustrated below, Michael nanocarriers with different sizes can be easily obtained by changing the following parameters:

- The fraction of reactive β-ketoester functional groups in the polymer precursor. The β-ketoester content in the polymer precursors was varied from 10 to 45 mol%.
- The functionality degree of the external crosslinker. (Figure 3.8)
- The polymer precursor molar mass (Figure 3.7). As expected and illustrated in Figure 3.7 A and Figure 3.7 B, the size of the Michael nanocarrier is smaller upon decreasing the molar mass of the polymer precursor.

A)

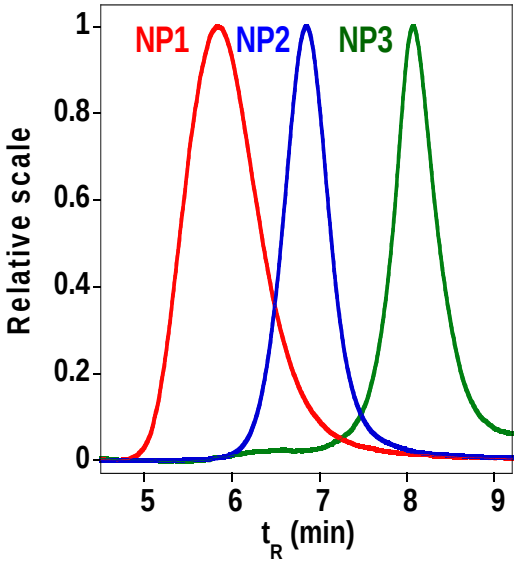

B)

Sample	M_w (g/mol)[a]	R_g (nm)[b]
NP1	1850000	45
NP2	234800	8.6
NP3	33000	< 5

Figure 3.7. A) Ilustration of SEC traces for Michael nanocarriers with different sizes. **B)** Characteristics of Michael nanocarriers. [a]Actual weight average molecular weight as determined by combined SEC/MALLS measurements. [b] Determined by MALLS at the peak maximum.

As explained above, by changing the functionality degree of the external crosslinker the size of Michael nanocarriers can be tuned. In fact, Michael nanocarriers synthesized using cross-linkers of functionality f = 3 (R_g =8.5 nm ± 0.5) are smaller than Michael nanocarriers synthesized using cross-linkers of functionality f = 2 (R_g =12.9 nm ± 0.9)) as revealed by SEC/MALLS data (Figure 3.8).

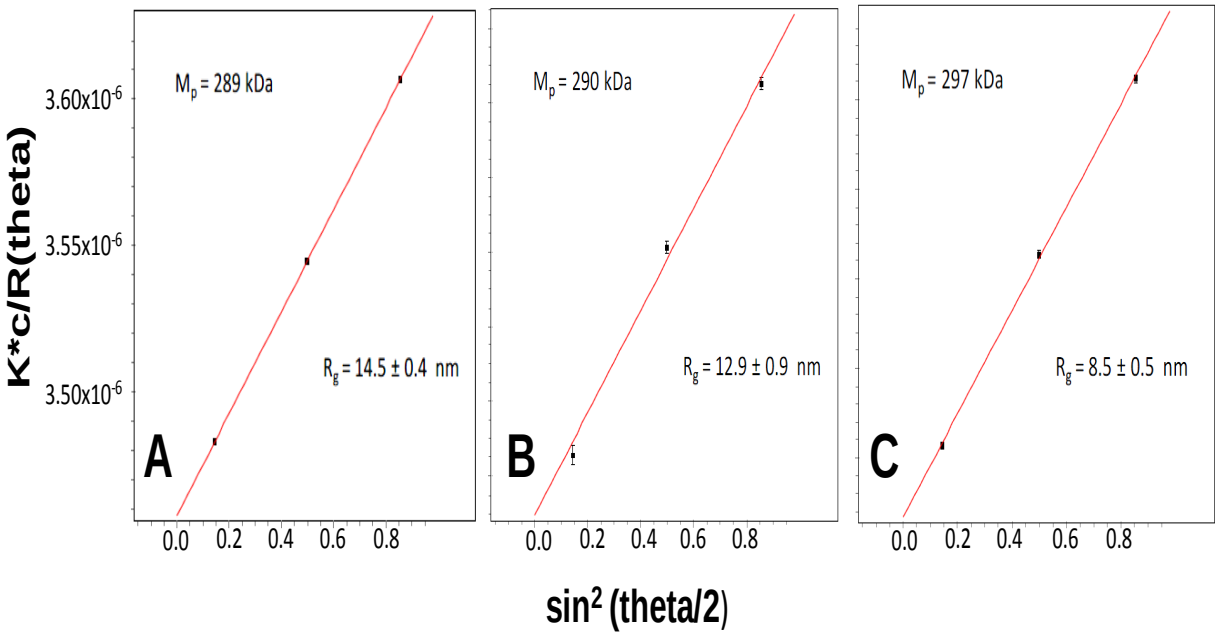

Figure 3.8. **A)** SEC/MALLS data of the Michael nanocarrier precursor synthesized *via* RAFT polymerization. **B)** SEC/MALLS data of Michael nanocarriers synthesized using cross-linkers of functionality f = 2 (BDD). **C)** SEC/MALLS data of Michael nanocarriers synthesized using cross-linkers of functionality f = 3 (TMT).

Unfortunately, all our attempts to synthesize well-defined Michael nanocarriers by means of tetra- or penta/hexa-acrylate crosslinker molecules failed, suggesting that under our reaction conditions the optimum cross-linker functionality is f = 3. We suspect that the increased steric hindrance for cross-linkers of f > 3 and the higher tendency to form insoluble macroscopic gels due to inter-particle coupling events could be responsible for this behavior. In addition, inter-particle coupling events are also observed when using a polymer precursor with a very high molar mass (> 400 kDa) or using a high content of β-ketoester units (>40%).

Valuable information about the *actual* structure in solution of single-chain Michael nanocarriers synthesized by means of bi- and tri-functional crosslinker units was obtained through small angle neutron scattering (SANS) measurements in deuterated solvent and complementary molecular dynamics (MD) simulations (see Chapter 6). Figure 3.9 A shows Kratky plots for the unfolded polymer chains and the Michael nanocarriers synthesized in the presence of bi- and tri-functional crosslinkers. It is worth mentioning that multidirectional self-assembled Michael nanocarriers (f = 3) display a clear maximum in the Kratky plot in resemblance to partially folded proteins. For globular proteins, it is well-known that the significant decrease observed in IQ^2 (I = scattered intensity, Q = scattering vector) at large Q is characteristic of a compact structure.[38] However, Kratky plots of Michael nanocarriers in solution more closely resemble those of disordered multidomain proteins with semiflexible linkers (e.g., $p67^{phox}$)[39] than those expected for globular proteins (e.g., polX).[40] We are not claiming here that "Michael" nanocarriers have a precise sequence similar to proteins but that their *form factor* in solution resembles that of disordered proteins, as a consequence of the multidirectional self-assembly process which leads to the formation of local globules along the individual polymer chains. In resemblance to transient-binding disordered proteins, as explained below, the resulting Michael nanocarriers are able to bind temporarily vitamin B_9 that can be delivered in a controlled manner (Figure 3.10). Kratky plots from the results of MD simulations corresponding to the unfolded polymeric precursor and the resulting nano-objects are shown in Figure 3.9 B. It is worth noting the qualitative agreement between SANS and MD simulation results. For both kinds of nanoparticles, MD simulation data showed increased compact conformations on decreasing the quality of the solvent, which is consistent with the globular conformation observed by TEM for the Michael nanocarriers in a dry state (Figure 3.6 B).

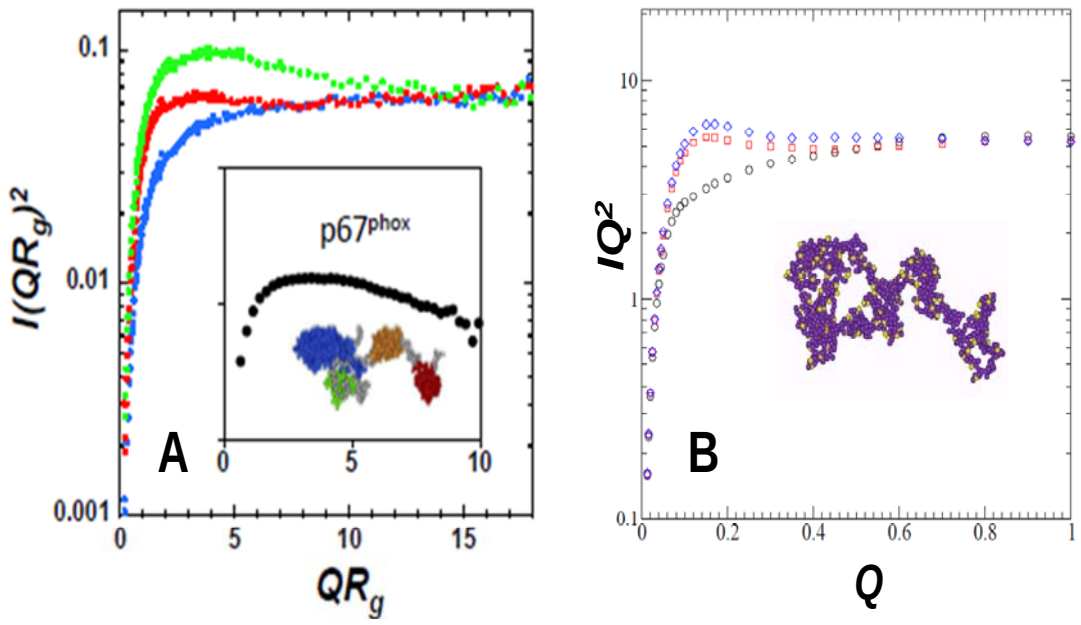

Figure 3.9. "Michael" nanocarriers in solution: **A)** Kratky plots for solutions of unfolded polymer chains (blue symbols) and Michael nanocarriers synthesized with cross-linkers of functionality f = 2 (red symbols) and f = 3 (green symbols), as determined by SANS. Note that multidirectionally self-assembled Michael nano-objects (f = 3) display a clear maximum in the Kratky plot in resemblance to disordered multi-domain proteins with semi-flexible linkers (see inset taken from ref. 39). **B)** Kratky plots from MD simulations under good solvent conditions of linear precursor (black symbols) and Michael nano-objects of functionality f = 2 (red symbols) and f = 3 (blue symbols). The inset shows a typical snapshot from the MD simulations of the nano-object conformation.

Inspired by the behavior of natural transient-binding disordered proteins, we have investigated the drug-delivery properties of Michael nanocarriers synthesized with tri-functional crosslinker units for potential application in a dermal supply of vitamin B_9 (i.e., folate or folic acid). Several *in vitro* and *in vivo* studies have indicated that this essential vitamin may offer a treatment option for photo-aged skin when incorporated in topical formulations.[41] Hence, vitamin B_9 nanocarriers based on single-chain Michael nanoparticles were placed in distilled water at neutral pH to investigate their controlled delivery properties. Figure 3.10 illustrates the progressive delivery of vitamin B_9 from the single-chain Michael nanocarriers as determined from UV/Vis spectroscopy measurements at 283 nm. The continuous line is a best-fit to the well-known power law model.

The power law model, introduced by Peppas and co-workers, is a semi-empirical model to describe drug release from polymeric systems:[42]

$$\frac{C_t}{C_f} = Kt^n \qquad (3.1)$$

Where Ct = concentration of drug released at time t, C_f = total concentration of drug released, K= is a constant, incorporating geometrical and structural characteristics of the nanocarrier and the drug, n = release exponent.[43]

Table 3.2. Exponent n of power law and drug release mechanism from polymeric delivery systems.

Exponent *n*	**Drug release mechanism**
0.5	Fickian diffusion
$0.5 < n < 1.0$	Anomalous (non Fickian) transport
1.0	Zero-order release

The value obtained for the release exponent, $n \approx 0.5$, suggests that the delivery process proceeds through a Fickian diffusion mechanism. Complete delivery of vitamin B_9 from Michael nanoparticles with a drug loading content of 41 wt % was observed to take place in 5-6 h. These promising results pave the way for mimicking the multiple transient-binding behavior of intrinsically disordered proteins (IDPs)[44] using Michael nanocarriers, as will be shown in Section 3.3.

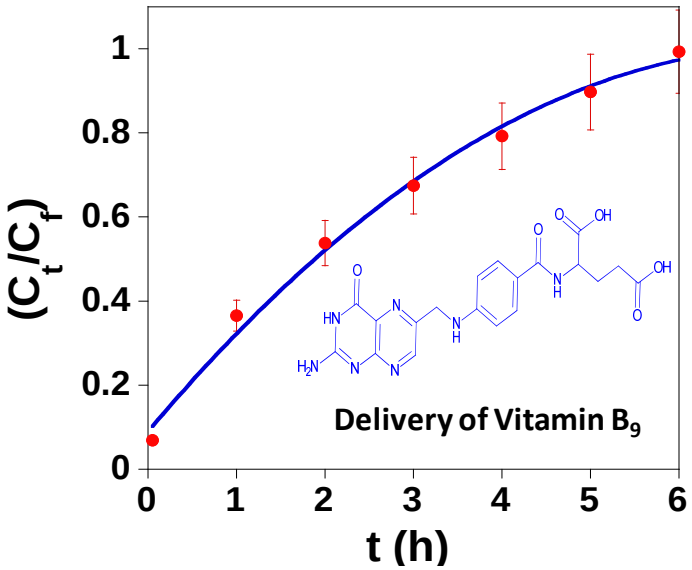

Figure 3.10. Delivery curve in water at neutral pH from vitamin B_9–loaded Michael nanocarriers (red symbols) and best-fit of the experimental data to the well-known power law model ($C_t / C_f = K\ t^n$, see text) (blue line).

3.2.4 Conclusion

In summary, we have developed a highly-efficient strategy for the permanent multidirectional self-assembly of unfolded polymeric chains to Michael nanocarriers that in solution resemble disordered multidomain proteins with semiflexible linkers. Conversely, in the dry state they adopt a collapsed, globular morphology. This natural synthesis route proceeds under very mild reaction conditions (without metal catalysts, at room temperature, under normal atmospheric conditions), using commercially available reagents. We have also demonstrated that by using single-chain Michael nano-objects as vitamin B_9 nanocarriers, the sustained release of vitamin B_9 in water at neutral pH is possible following a Fickian diffusion mechanism. Both the multidirectional self-assembly approach, as a synthesis strategy to nano-objects resembling partially folded multidomain proteins in solution, and the Michael nanocarriers themselves, resembling transient-binding disordered proteins, are expected to be applicable to different fields, such as nanomedicine, biosensing / bioimaging uses, and heterogeneous catalysis.

3.3 Single-Chain "Michael" Nanocarriers Mimicking Disordered Proteins for Combined Delivery of Dermal Bioactive Cargos

3.3.1 Objectives

In the first part of this Chapter, we have reported that the structure of multi-directionally self-assembled single-chain polymer particles (SCNPs) under good solvent conditions closely resemble that of intrinsically disordered proteins (IDPs) in solution.[45] Kratky plots from small angle neutron scattering (SANS) measurements showed a structure factor in close analogy to that of disordered multi-domain proteins (e.g., $p67^{phox}$) so, from a structural point of view, they could be considered, to a good approximation, as *artificial* mimics of IDPs and denoted as intrinsically disordered protein mimetics (IDPMs). It is worth mentioning that the Kratky plot has the capacity to enhance particular features of scattering profiles, thus allowing easier identification of degrees of compactness.[23] Hence, according to SANS results, SCNPs in good solvents show multiple local-scale domains separated by flexible linkers, whereas SCNPs in the dry state adopt a globular morphology, as observed by TEM. Moreover, in this previous study the ability of the SCNPs to deliver vitamin B_9 in water at neutral pH was assessed. The delivery curve of vitamin B_9 was fitted to a power law model from which the value of the release exponent was found to be *ca.* 0.5, suggesting that the process proceeds through a Fickian diffusion mechanism and completes in less than 5 hours.[45]

We hypothesized that in analogy to some disordered proteins, IDPMs could also have some degree of binding promiscuity towards some relevant bioactive compounds that could be then delivered to water in a pH-dependent manner. In particular, we investigate herein the potential use of SCNPs as artificial IDPM nanocarriers for the simultaneous delivery of both dermal protective and anticancer cargos (see Scheme 3.9). As a model system of dermal protective

compounds, we selected folic acid (also known as folate or vitamin B_9), **(1)**. According to several *in vitro* and *in vivo* studies, dermal delivery of **(1)** using topical formulations offers a treatment option for photo-aged skin.[46-47] As a natural anticancer drug, we selected hinokitiol (β-thujaplicin), **(2)**, as a tropolone-related compound found in the heartwood of *cupressaceous* plants that exhibits anticancer activity against human malignant melanoma cells[48] as well as other cancer cell lines, including the human leukemic cell K562 and the human stomach cancer cell KATO-III.[49-50] The selective anticancer mechanism of **(2)** in melanoma cancer cells *versus* normal human melanocytes has been recently reported to involve strong G1 cell cycle arrest due to p27 protein accumulation, down-regulation of Skp2 proteins, and inhibition of Cdk2 kinase activity.[51] As a proof of concept we will demonstrate, for the first time ever, the simultaneous delivery of **(1)** and **(2)** to water solutions at different pH values using SCNPs as artificial IDPM nanocarriers.

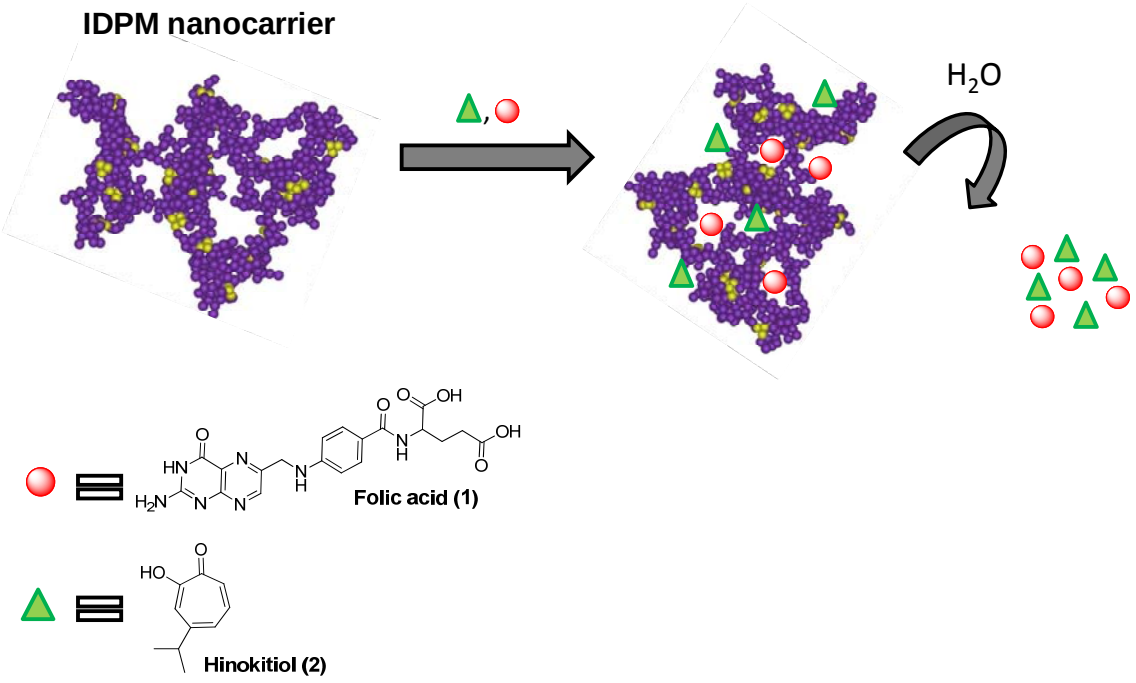

Scheme 3.9. Simultaneous delivery of both dermal protective (folic acid) and anticancer (hinokitiol) cargos from single-chain "Michael" nanocarriers mimicking intrinsically disordered proteins.

3.3.2 Experimental Section

a) Synthesis of IDPM precursors.

As explained in the first part of this Chapter, in a typical procedure, **MMA** (1 ml, 9.4 mmol), **AEMA** (0.6 ml, 3.1 mmol), 2-cyanoprop-2-yl-dithiobenzoate (CPDB, 0.8 mg, 3×10^{-2} mmol) and 2,2-azobis(2-methylpropionitrile) (AIBN, 1 mg, 3×10^{-2} mmol) were dissolved in ethyl acetate (3.2 ml). The reaction mixture was degassed by passing argon for 15 min. The copolymerization reaction was carried out at 65ºC for 18 h. The resulting nanoparticle precursor was isolated by precipitation in methanol and further drying (**3**: Yield = 47 %, M_p (SEC/MALLS, dn/dc = 0.083) = 3.02×10^5 Da, M_w/M_n = 1.37, R_g = 14.8 ± 0.5 nm, composition (^{1}H NMR) = 25 mol% **AEMA**).

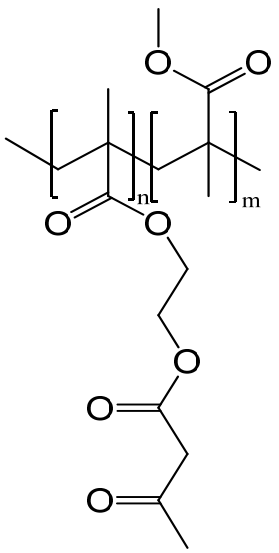

IDPM precursor (3)

Scheme 3.10. Chemical structure of single-chain nanocarrier precursor **(3).** Chain-ends have been omitted for clarity.

b) Synthesis of IDPMs.

In a standard reaction, the IDPM precursor (**3**, 150 mg, 0.29 mmol), multifunctional cross-linker trimethylolpropane triacrylate (TMT, 27.8 mg, 0.097 mmol) and catalyst (KOH, 8 mg, 0.15 mmol) were dissolved in THF (**a**: 50

ml, **b**: 150 ml) at room temperature (see section 3.2.2 for details). The progressive folding/collapse process was followed through simultaneous SEC/MALLS measurements. After reaction completion, a few drops of trifluoroacetic acid were added to deactivate the catalyst, the mixture was concentrated and the IDPMs were isolated by precipitation in diethyl ether and further drying (**4a**: Yield = 78 %, M_p (SEC/MALLS, dn/dc = 0.083) = 3.22×10^5 Da, M_w/M_n = 1.33, R_g = 10.6 ± 1.0 nm; **4b**: Yield (%) = 83 %, M_p (SEC/MALLS, dn/dc = 0.083) = 2.83×10^5 Da, M_w/M_n = 1.15, R_g = 8.1 ± 0.7 nm).

c) IDPMs loaded simultaneously with folic acid (1) and hinokitiol (2).

IDPMs, **4b**, were loaded with folic acid, **(1)**, and hinokitiol, **(2)**, by following typical drug-loading protocols reported in the literature[26-45] and as is explained in the previous part of this Chapter (see section 3.2.2 for details). The simultaneous delivery of **(1)** and **(2)** from the IDPMs was determined from UV/Vis spectroscopy measurements at 283 nm (for **1**) and 240 nm (for **2**). Standard calibration curves were obtained with appropriate water solutions of compounds **(1)** and **(2)** at pH = 8 and pH = 6 (see Figure 3.11).

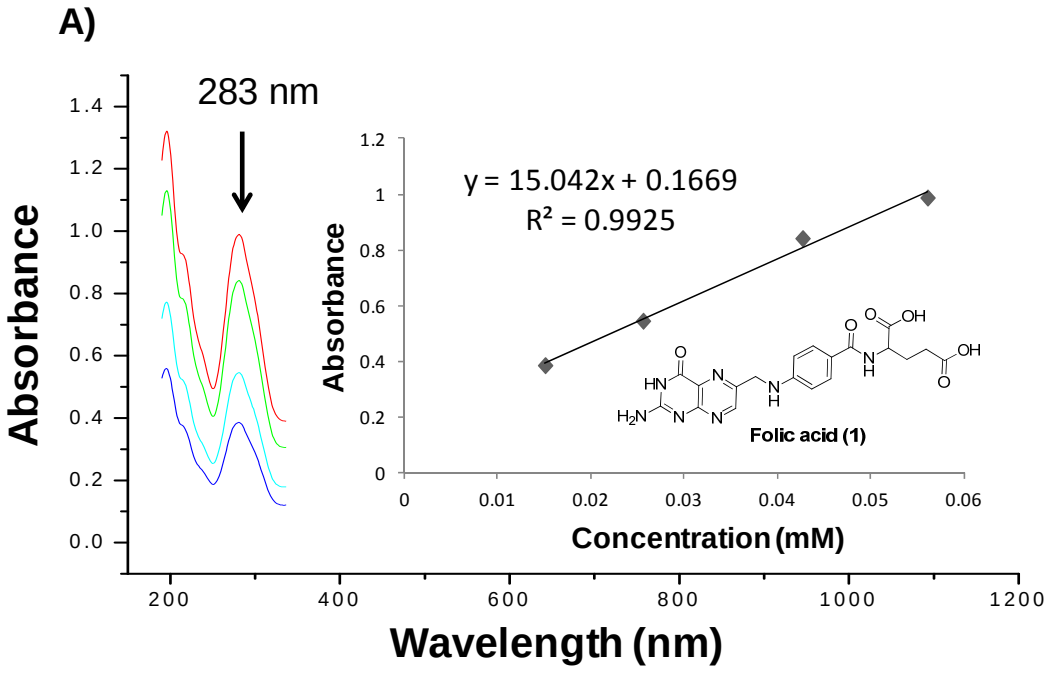

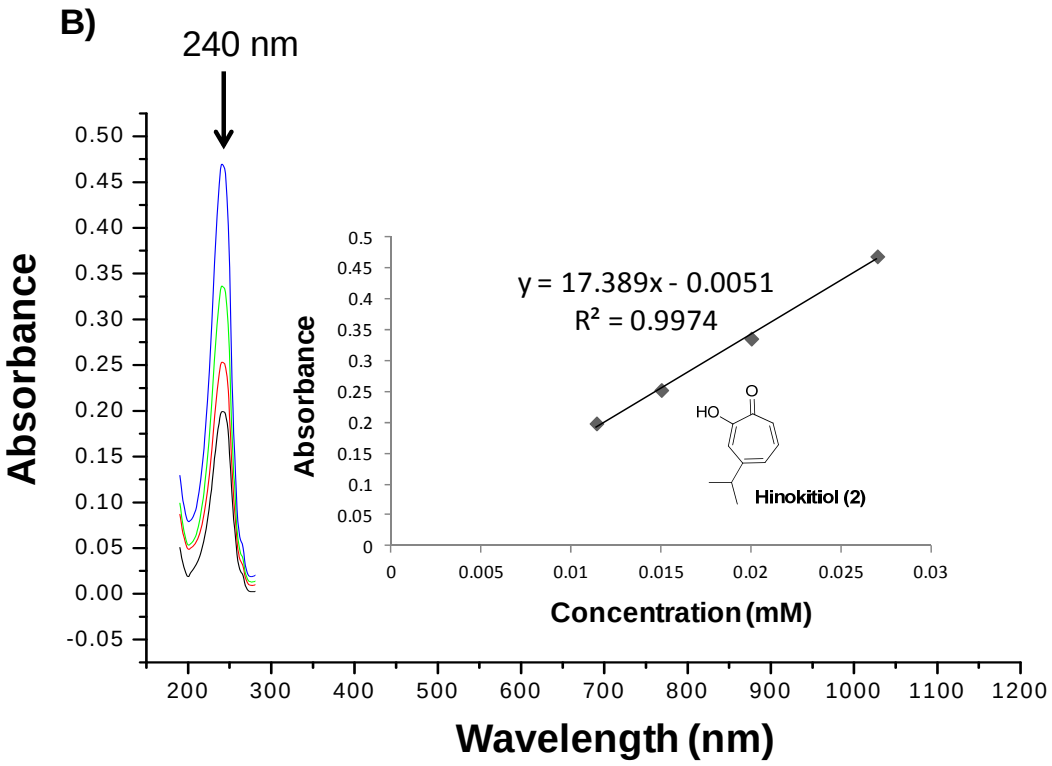

Figure 3.11. A) Calibration curve for folic acid, **(1)**, in water (pH = 8, T = 25 ºC) as determined by UV/Vis spectroscopy at 283 nm, using standard solutions of varying concentration of **(1)**. **B)** Calibration curve for hinokitiol, **(2)**, in water (pH = 8, T = 25 ºC) as determined by UV/Vis spectroscopy at 240 nm, using standard solutions of varying concentration of **(2)**.

3.3.3 Results and Discussion

First, the effect of different parameters, such as precursor chain length, and functionality of reactive groups along the chain on the final structure and morphology of the resulting IDPMs in solution was investigated by molecular dynamics (MD) simulations. Molecular dynamics (MD) simulations of isolated polymers were performed by Dr. Angel Moreno and co-workers using the well-known Kremer-Grest model.[52] A detailed description of the MD simulations performed is provided in Chapter 6. In brief, a precursor chain of N beads of radius σ having a fraction of monomers x = 0.2 of functionality *f*, able to form permanent intrachain cross-links, was first equilibrated as a self-avoiding random walk (i.e. good solvent conditions). Then, MD simulations were carried out allowing the progressive formation of irreversible links between reactive monomers in the chain when the distance between monomers is lower than a certain capture radius (1.3σ). Once the intrachain cross-linking process was completed, the average radius of gyration (R_g) of the resulting nano-objects was determined.[52-58]

Based on the MD simulation results, IDPM size was found to depend more strongly on precursor length than on the functionality of the reactive groups. In order to define the structure of the nanoparticles, taking into account multi-body correlations among the monomers, we use the Euler characteristic as a topological fingerprint.[59,60] This morphometric approach has been proven to be robust and suitable for ascertaining quantitative details of the spatial organization of molecules.[56-59] The Euler characteristic χ is one of the four scalar Minkowski functionals[59–61] that characterize a given surface embedded in three dimensions, the others being the enclosed volume, total surface area and the integral mean curvature. The coefficient itself is proportional to the integral Gaussian curvature and its value is not affected by any continuous, topology-preserving deformations of the surface. In three dimensions it takes the form $\chi = \mathcal{N}_D + \mathcal{N}_C - \mathcal{N}_T$, where $\mathcal{N}_D$ is the number of disconnected aggregates, $\mathcal{N}_C$ the number of enclosed cavities and $\mathcal{N}_T$ the number of

perforations, i.e., tunnels that percolate through the system. Values for some archetypical topogies are: i) n for n disconnected spherical polyhedra; ii) 1-n for a n-fold torus; iii) 1+n for a sphere with n inner holes.

As a first step we construct a cubic box containing the nanoparticle, and discretize the box into a cubic lattice, of spacing d. Each lattice site is surrounded by a Wigner-Seitz cell, which in this case is an elementary cube having the size of the lattice constant. This construction is space-filling. We then introduce a family of surfaces parameterized by an appropriate length scale R that can be constructed from a given configuration of the monomers. To this end, we consider the surfaces S *(R)* formed by spheres with a radius R located at the centers of every monomer. We denote each lattice site inside S *(R)* as 'full' and all others sites as 'empty'. Once S *(R)* is constructed, the Euler characteristic is computed as explained in reference.[59]

For small values of R we have a collection of disjointed spheres. By increasing R, some of the spheres will join, merge, and later form rings and cavities. Eventually, the collection of spheres will fully occupy the space containing the molecule, and the surface will vanish. It must be noted that the so-obtained Euler characteristic corresponds to a *discretized* configuration of the surface $\mathcal{S}(R)$. Therefore, the lattice spacing d must be sufficiently small to avoid artifacts arising from the discretization. For each value of R we have controlled the sensitivity of the results to the selected values of d, finding an upper value $d_o(R)$ below which the obtained $\chi(R{:}d)$ is d-independent within statistics. In other words, for $d \leq d_o(R)$ the Euler characteristic is undistinguishable from that of the real surface ($d \to 0$). Results presented in Figure 3.12 have been calculated by using $d = d_o(R)$, for computational efficiency. For radii $R > \sigma$, we have used $d_o(R) = 0.2\sigma$. For $R < \sigma$ smaller spacing is necessary, in particular around the minimum of $\chi(R)$, where we have used $d_o(R) = 0.05\sigma$.

In Figure 3.12 we can observe a deep minimum (R ≈ 0.5σ) which gives us information on the typical (limited) hole size. The deep minimum and the lack of any further positive peak suggest an elongated sparse structure instead of a compact, globular structure. No significant differences in the typical morphology of the resulting IDPMs were observed by increasing the functionality of the reactive groups in the polymer precursor.

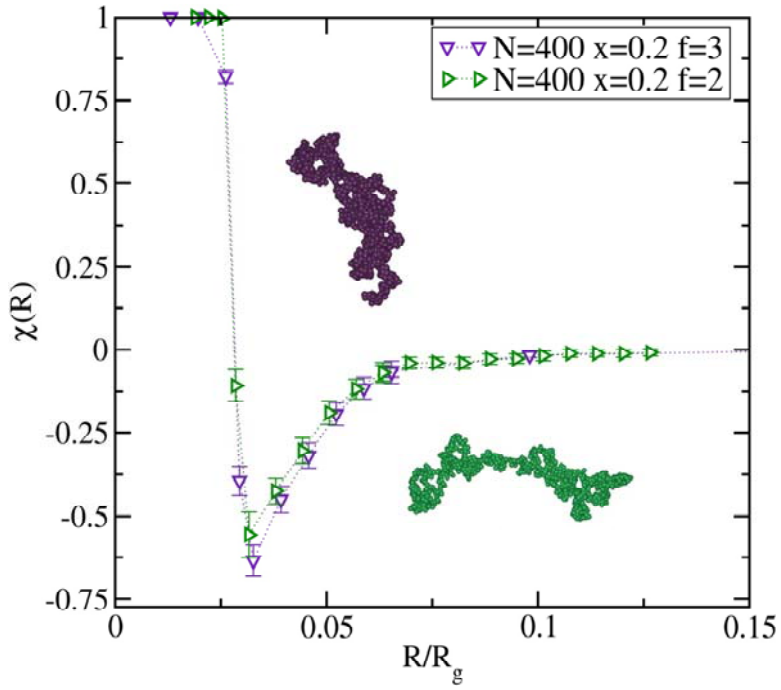

Figure 3.12. Euler characteristic χ(R) of intrinsically disordered protein mimetics (IDPMs) as a function of R/R_g. R is the appropriate length scale characterizing the size of the family of surfaces constructed from a given configuration of particles (see Chapter 6 for details). IDPM configurations were determined from coarse-grained MD simulations under good solvent conditions for nanocarriers of N = 400, x = 0.2, f = 2, $\langle R_g^2 \rangle^{1/2}$ = 15.8σ, and N = 400, x = 0.2, f = 3, $\langle R_g^2 \rangle^{1/2}$ = 15.3σ. The snapshots represent typical conformations for f = 3 (top) and f = 2 (bottom). (N = number of beads, x = fraction of reactive groups in the chain, f = functionality, number of reactive groups that are allowed to be bonded per cross-linking point, R_g = radius of gyration).

On the other hand, a broad range of morphologies were observed as a consequence of the statistical placement of reactive groups along the individual chains and the stochastic nature of the cross-linking process (see Figure 3.13).

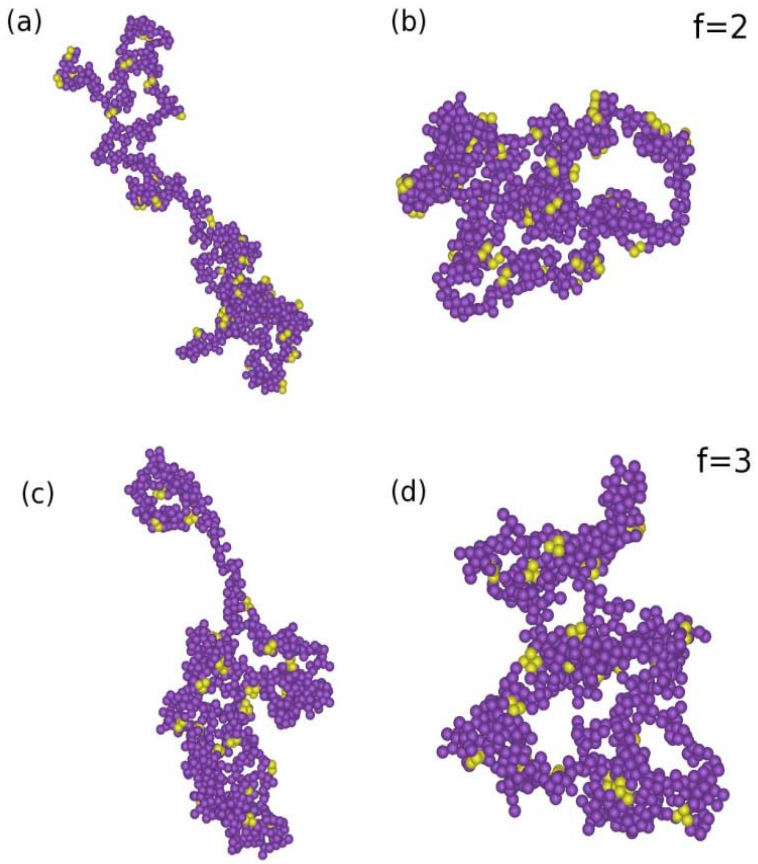

Figure 3.13. Snapshots of four different fully cross-linked nanoparticles obtained *via* MD for the bifunctional (f = 2) and trifunctional (f = 3) case. In all panels N = 400. Panels (a) and (c) correspond to open, elongated configurations. Panels (b) and (d) display closer configurations where bigger loops appear.

Both the precursor chains and the nano-objects follow a $R_g^2 \propto N^{2\nu}$ scaling law; the values of the ν exponent were found to be ν = 0.63 ± 0.01, ν = 0.57 ± 0.01 and ν = 0.55 ± 0.01 for the precursor, bifunctional and trifunctional cross-linked nanoparticles, respectively (see Figure 3.14). Figure 3.14 shows the average squared radius of gyration, $\langle R_g^2 \rangle$, versus the number of backbone monomers, N. Hence, the reduction in size upon IDPM formation from the linear precursor was found to grow with increasing precursor size. Based on the obtained scaling laws, precursor chains (f = 3) of N = 100 and N = 3000 will show $R_g^{(IDPM)}$ / $R_g^{(Precursor)}$ ratios of 0.75 and 0.59, respectively.

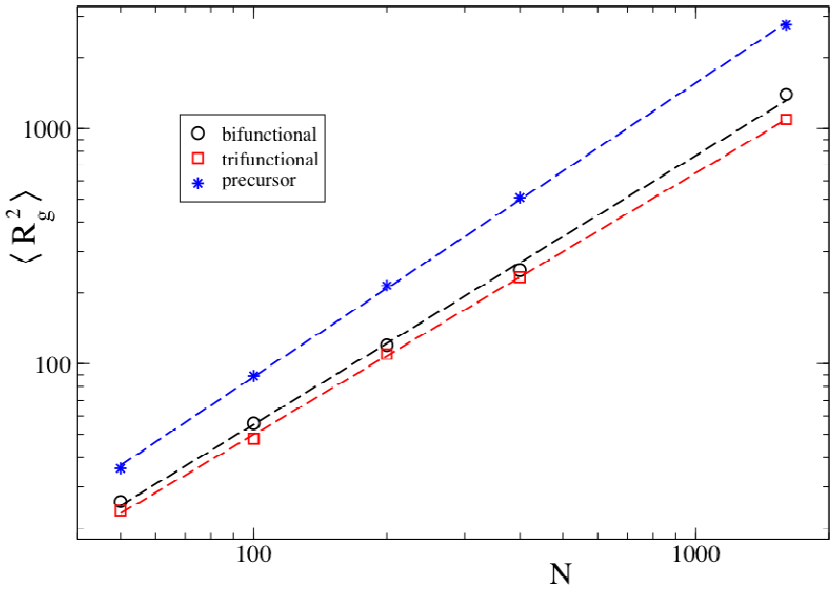

Figure 3.14. Scaling plot of the squared radius of gyration *versus* the number of monomers per backbone. Circles and squares are MD data for the bifunctional and trifunctional case, respectively. For comparison, we include data for the unlinked precursor (stars). Dashed lines are power-law fits, $\langle R_g^2 \rangle \sim N^{\nu}$, with ν = 0.63±0.01, 0.57±0.01 and 0.55±0.01 for the precursor and for the bifunctional and trifunctional nanoparticles, respectively.

Thus, the characterization of the topological structure and the scaling behavior of the soft nanoparticles demonstrate that these are not compact but sparse objects.

Guided by the MD simulation results, we target a precursor molecular weight of 3×10^5 Da with a representative amount of cross-linking groups of 25 mol % for which we expect a $R_g^{(IDPM)}$ / $R_g^{(Precursor)}$ ratio of 0.59 when collapsed to individual IDPM under good solvent conditions. Such a high molecular weight will allow us to determine the evolution of R_g during IDPM formation *via* SEC/MALLS measurements. In this sense, SEC chromatography discriminates macromolecules according to their hydrodynamic radius (R_h) which is roughly inversely proportional to SEC elution time (t_R), whereas the MALLS technique provides values of both absolute molecular weight (M_w) and R_g. The polymer precursor was synthesized from commercially available methyl methacrylate (**MMA**) and (2-acetoacetoxy) ethyl methacrylate (**AEMA**) monomers *via* reversible addition-fragmentation chain-transfer (RAFT) copolymerization (see

section 3.3.2 for details), showing an average R_g = 14.8 ± 0.5 nm, relatively narrow polydispersity (M_w / M_n = 1.37) and a random distribution of reactive β-ketoester moieties from **AEMA** repeat units, as determined by ^{1}H NMR spectroscopy. To construct the IDPMs, the polymer precursor was individually collapsed under controlled stoichiometric and dilution conditions in tetrahydrofuran (THF) at r.t. through multidirectional Michael addition reactions involving the single-chain β-ketoester groups, as Michael donors, and external acrylate-based cross-linkers of functionality f=3, as Michael acceptors (Section 3.2).[45] This method produces robust, covalent bonded single-chain nano-objects.[62] The effect of precursor concentration during the synthesis of IDPMs on nano-object size and size distribution is summarized in Table 3.3, as determined by combined SEC/MALLS and complementary dynamic light scattering (DLS) measurements.

Table 3.3. Effect of precursor concentration on nanocarrier size during the synthesis of intrinsically disordered protein mimetics (IDPMs).

System	t_R (min)[a]	M_w (Da)[b]	M_w/M_n	R_g (nm)[c]	R_h (nm)[d]	R_g/R_h
Precursor	6.59	3.02×10^5	1.37	14.8	10.1	1.47
IDPM-3[e]	6.76	3.22×10^5	1.33	10.6	8.5	1.25
IDPM-1[f]	6.85	2.83×10^5	1.15	8.1	7.7	1.05

[a] SEC retention time. [b] Absolute molecular weight at the SEC peak maximum. [c] Determined by MALLS at the SEC peak maximum. [d] Determined by DLS in THF. [e] Synthesis of IDPMs performed at 3 mg/ml. [f] Synthesis of IDPMs performed at 1 mg/ml.

By working at 3 mg/ml, an increase in the value of the actual molecular weight was observed even when a moderate reduction in the values of R_h and R_g was clearly observed. Upon decreasing the precursor concentration to 1 mg/ml, the absolute molecular weight values at the SEC peak maximum of the precursor and the IDPMs were found to be very similar, and a larger reduction in the values of R_h and R_g was found. No further reduction was observed by working at precursor concentrations < 1 mg/ml. In this sense, it is worth mentioning that potential intermolecular crosslinking events are increasingly avoided by passing from a semi-concentrated to a highly diluted solution.[63,64]

A vertical shift (downward) in the curve of R_g *versus* t_R was observed upon nano-object formation (see Figure 3.15 A) which can be attributed to a change in the R_g/R_h ratio on passing from linear coils to IDPMs. For a flexible polymer chain under good solvent conditions $R_g/R_h \approx 1.56$, whereas for globular particles $R_g/R_h \approx 0.77$.[65] IDPMs synthesized at 3 mg/ml show a ratio of $R_g/R_h = 1.25$, whereas IDPMs synthesized at 1 mg/ml display $R_g/R_h = 1.05$, the latter being an intermediate value between those expected for a coil and a globule. The collapse degree ($R_g^{(IDPM)}$ / $R_g^{(Precursor)}$) for nanoparticles (f = 3) synthesized at 1 mg/ml was 0.55, in good agreement with the value estimated from MD simulations. According to data summarized in Table 3.3, IDPM-1 shows a structure more collapsed than IDPM-3.

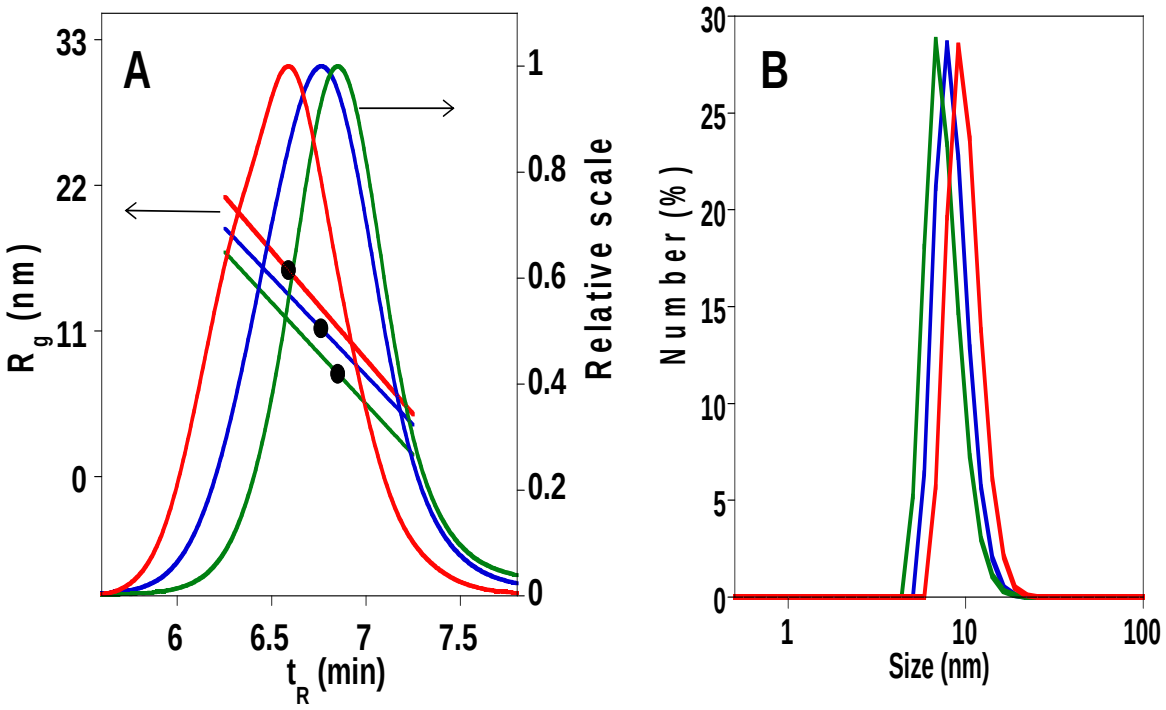

Figure 3.15. Synthesis and characterization of intrinsically disordered protein mimetics (IDPMs) allowing simultaneous delivery of both dermal protective and anticancer cargos. **A)** Illustration of SEC/MALLS data for the precursor (red lines), IDPMs synthesized at 3 mg/ml (blue lines) and IDPMs synthesized at 1 mg/ml (green lines). For each SEC trace, the value of R_g at the peak maximum is indicated by a black circle. **B)** DLS curves in THF for the precursor (red line), IDPMs synthesized at 3 mg/ml (blue line) and IDPMs synthesized at 1 mg/ml (green line).

The typical morphology of the IDPMs under good solvent conditions was deduced from small angle X-ray scattering (SAXS) measurements, showing a Kratky plot resembling that observed in natural intrinsically disordered proteins and very different from that of the linear precursor (see Figure 3.16 A).[23] As expected, SAXS results were in good agreement with previous SANS and MD simulation data.[45] Conversely, the morphology of individual IDPMs in the dry state was undoubtedly globular, as observed by TEM, showing collapsed nanoparticles with a spherical shape (Figure 3.16 B).

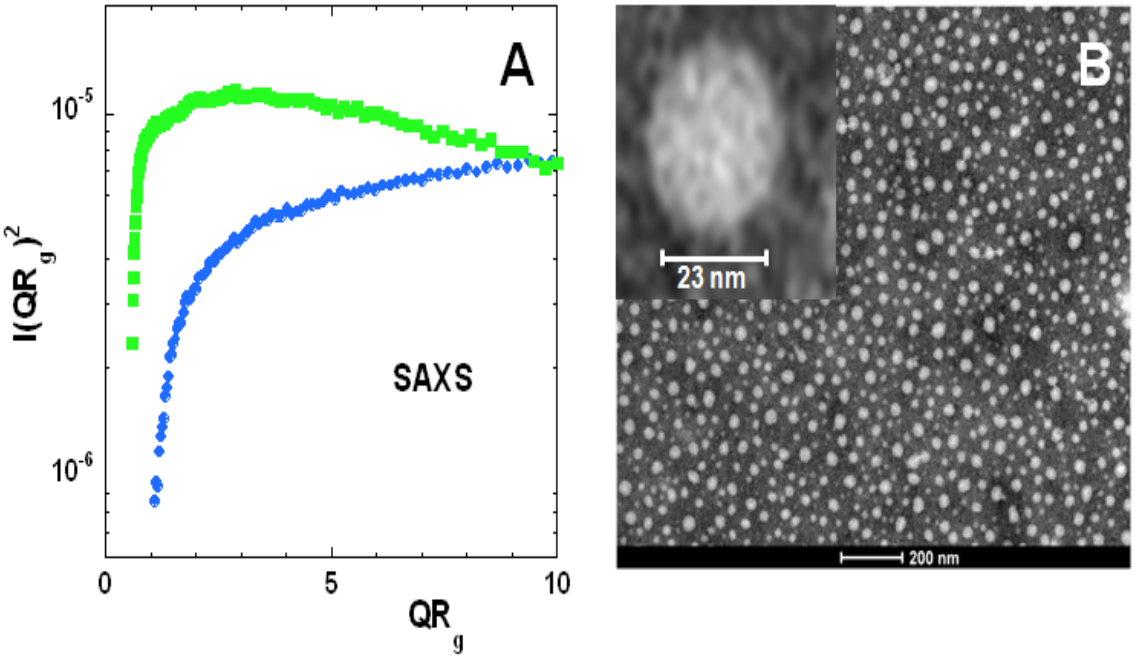

Figure 3.16. Synthesis and characterization of intrinsically disordered protein mimetics (IDPMs) allowing simultaneous delivery of both dermal protective and anticancer cargos. **A)** Kratky plot from small angle X-ray scattering (SAXS) measurements in THF of the precursor (blue line) and the corresponding IDPMs (green line). **B)** TEM picture showing the spherical shape of IDPMs onto a carbon-coated grid upon solvent removal.

To test our hypothesis of IDPM multi-binding ability, the nanocarriers were loaded with both folic acid **(1)** and hinokitiol **(2)** and the controlled delivery of these protective and anticancer dermal bioactive cargos, respectively, in water at two relevant pH values (pH = 6 and pH = 8) was monitorized by UV/Vis spectroscopy. To quantify the delivery process, the intensities of the UV absorption maxima of **1** and **2** at 283 nm and 240 nm, respectively, as well as

appropriate calibration curves, were employed. Figure 3.17 illustrates the experimental data corresponding to the simultaneous delivery of **1** and **2** at pH = 6 and pH = 8 from IDPMs loaded with 51 % of dermal bioactive compounds (ratio **2** : **1** = 0.53). According to these data, on average, there are 410 molecules of **2** and 170 molecules of **1** per IDPM carrier. The delivery process for both compounds was faster at pH = 8 than at pH = 6, especially at short delivery time, whereas total delivery was found to take place in about 4 hours at both pH values. All our attempts to characterize the presumably weak **1**/IDPM and **2**/IDPM interactions under the highly diluted experimental conditions by ^{1}H NMR, UV-Vis and FTIR spectroscopies failed. Nevertheless, the simultaneous delivery of **1** and **2** to water solutions at relevant pH values from SCNPs as artificial IDPM nanocarriers pave the way to the long-term development of multifunctional topical formulations containing IDPMs.

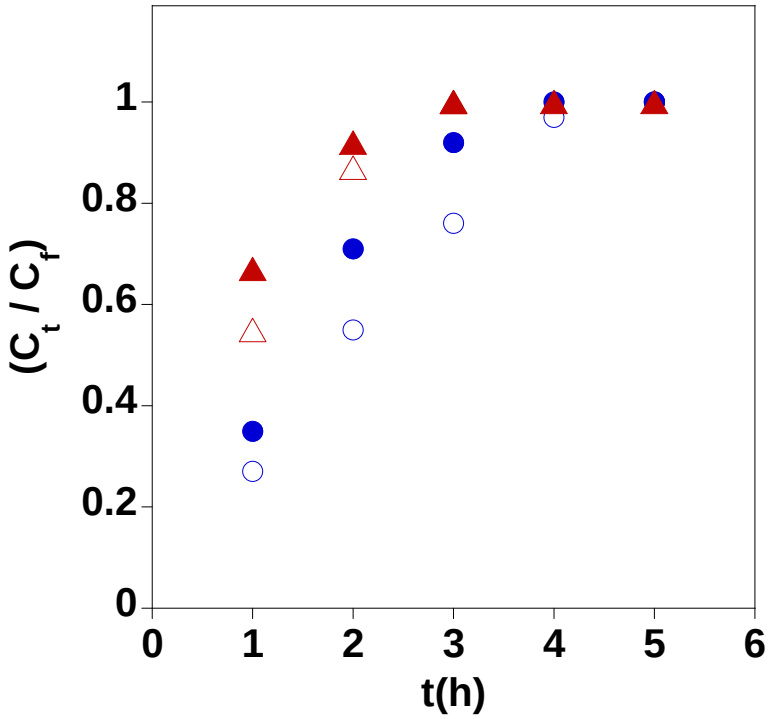

Figure 3.17. Simultaneous delivery data in water at pH = 6 (blue symbols) and pH = 8 (red symbols) of folic acid, **1**, (open symbols) and hinokitiol, **2**, (solid symbols) from IDPMs.

3.3.4 Conclusion

Guided by the results of MD simulations we have developed and characterized single-chain nanocarriers mimicking disordered proteins (IDPMs) for the combined delivery of dermal bioactive cargos. These results have shown that IDPM size depends more strongly on precursor length than on the functionality of the reactive groups in the precursor. By using the Euler characteristic as a topological fingerprint, we have found that the average hole size is similar to the bead size employed in the simulations. Snapshots of the IDPMs showed elongated sparse structures instead of compact, globular morphologies displaying $R_g^{(IDPM)}$ / $R_g^{(Precursor)}$ ratios between 0.75 and 0.59, depending on the precursor length. Good agreement was found between the collapse degree of IDPMs synthesized *via* Michael addition-induced self-assembly ($R_g^{(IDPM)}$ / $R_g^{(Precursor)}$ = 0.55) and the value estimated from MD simulations ($R_g^{(IDPM)}$ / $R_g^{(Precursor)}$ = 0.59) when intrachain cross-linking was carried out at high dilution. SAXS measurements supported the MD simulation results showing an IDPM form factor in the Kratky plot similar to that observed in natural disordered proteins. TEM pictures, however, displayed a globular IDPM morphology upon drying; pointing to a transition from extended to compact nano-objects when solvent was removed. The multi-binding ability of the single-chain nano-objects was demonstrated by simultaneous delivery of hinokitiol and folic acid to water solutions at relevant pH values, paving the way to the development of multifunctional topical formulations containing IDPMs.

3.4 References

[1] Studart, A. R. *Adv. Mater.,* **2012**, *24*, 5024.

[2] Breslow, R.; Dong, S. D. *Chem. Rev*., **1998**, *98*, 1997.

[3] a) Inoue, K. *Prog. Polym. Sci.,* **2000**, *25*, 453. b) Yamamoto, T.; Yamada, T.; Nagata, Y.; Suginome, M. *J. Am. Chem. Soc.,* **2010**, *132*, 7899.

[4] Liang, C.; Fréchet, J. M. J. *Prog. Polym. Sci.,* **2005**, *30*, 385.

[5] Wang, Y.; Xu, H.; Ma, N.; Wang, Z.; Zhang, X.; Liu, J.; Shen, J. *Langmuir.,* **2006**, *22*, 5552.

[6] a) Mackay, M. E.; Dao, T. T.; Tuteja, A.; Ho, D. L.; Horn, B. V.; Kim, H.-C.; Hawker, C. J. *Nat. Mater.,* **2003**, *2*, 762. b) Oria, L.; Aguado, R.; Pomposo, J. A.; Colmenero, J. *Adv. Mater.,* **2010**, *22*, 3038. c) Gillissen, M. A. J.; Voets, I. K.; Meijer, E. W.; Palmans, A. R. A. *Polym. Chem.,* **2012**, *3*, 3166.

[7] Pérez-Baena, I.; Barroso-Bujans, F.; Gasser, U.; Arbe, A.; Moreno, A. J.; Colmenero, J.; Pomposo, J. A. *ACS Macro Letters.,* **2013**, *2* , 775.

[8] Wulff, G.; Chong, B.-O.; Kolb, U. *Angew. Chem. Int. Ed.,* **2006**, *45*, 2955.

[9] Terashima, T.; Mes, T.; De Greef, T. F. A.; Gillissen, M. A. J.; Besenius, P.; Palmans, A. R. A.; Meijer, E. W. *J. Am. Chem. Soc.*, **2011**, *133*, 4742.

[10] Dill, K. A.; MacCallum, J. L. *Science.,* **2012**, *338*, 1042.

[11] Altintas, O.; Barner-Kowollik, C. *Macromol. Rapid Commun.,* **2012**, *33*, 958.

[12] Hartl FU and Hayer-Hartl M, *Science*., **2002**, *295*, 1852.

[13] Hardesty B and Kramer G, *Prog Nucleic Acid Res Mol Biol.,* **2001***, 66***,** 41.

[14] Baker D, *Nature.,* **2000***, 405*, 39.

[15] Baldwin RL, *Nature.,* **1994**, *369*,183.

[16] Uversky VN, *BBA-Proteins Proteom.,* **2013***, 1834*, 932.

[17] Tompa P, *Trends Biochem Sci.,* **2002**, *27*, 527.

[18] Dunker AK, Brown CJ, Lawson JD, Iakoucheva LM and Obradovic *Z, Biochemistry−UK.,* **2002***, 41*, 6573.

[19] Wright PE and Dyson HJ, *J. Mol Biol.,* **1999***, 293*, 321.

[20] Tompa P. and Han KH, *Phys Today.,* **2012***, 65*, 64.

[21] J. Hirschfeld, *Phatol. Microbio. Scand.,* **1959**, *47*, 160.

[22] R. Bouillon, "The Vitamin D Binding Protein DBP", In *Vitamin D* (3rd edn.), Vol. 1; Academic Press, London, **2011**.

[23] P. Bernado, D. I. Svergun, *Mol. BioSyst.,* **2012**, *8*, 2955.

[24] V.N. Uversky, C.J. Oldfield, A.K. Dunker, *J. Mol. Recognit*., **2005**, *18*, 343.

[25] Mather, B. D.; Viswanathan, K.; Miller, K. M.; Long, T. E. *Prog. Polym. Sci.* **2006.**, *31*, 487.

[26] T. Qu, A.Wang, J. Yuan, J. Shi, Q. Gao, *Colloid. Surface. B*., **2009**, *72*, 94.

[27] T. Krasia, R. Soula, H. G. Borner and H. Schlaad*, Chem. Commun*., **2003**, *4*, 538.

[28] G. Moad, Y.K. Chong, A. Postma, E. Rizzardo and S. H. Thang, *Polymer*., **2005**, *46*, 8458.

[29] L. Buruaga, J. A. Pomposo, *Polymers.,* **2011**, *3*, 1673.

[30] Ivoclar AG, *Polymer Bulletin*., **1994**, *33*, 43.

[31] Sun T, Chance RR, Graessley WW, Lohse DJ, *Macromolecules*., **2004**, *37*, 4304.

[32] Grubisic Z, Rempp P, Benoit HJ. *Polym Sci Part B Polym Lett*., **1967**, 5, 753.

[33] Moore JCJ, *Polym Sci Part A Gen Pap*., **1964**, *2*, 835.

[34] Chao, D.; Jia, X.; Tuten, B.; Wang, C.; Berda, E. B. *Chem. Commun.,* **2013**, *49*, 4178.

[35] Frank PG, Tuten BT, Prasher A, Chao D, Berda EB. *Macromol Rapid Commun.*, **2014**, *35*, 249.

[36] A. Ruiz de Luzuariaga, J. A. Pomposo, H.Grande, A. Etxeberria. *Macromol Rapid Commun*., **2009**, *30*, 932.

[37] Ivankov, D. N.; Finkelstein, A. V. *PNAS.,* **2004**, *101*, 8942.

[38] Pollack, L.; Tate, M. W.; Darnton, N. C.; Knight, J. B.; Gruner, S. M.; Eaton, W. A.; Austin, R. H. *PNAS.,* **1999**, *96*, 10115.

[39] Durand, D.; Vives, C.; Cannella, D.; Perez, J.; Pebay-Peyroula, E.; Vachette, P.; Fieschi, F.; *J. Struct. Biol.,* **2010**, *169*, 45.

[40] Receveur-Brechot, V.; Durand, D. *Curr. Protein Pept. Sc.,* **2012**, *13*, 55.

[41] Knott, A.; Mielke, H.; Koop, U.; Wolber, R.; Burkhardt, T.; Vietzke, J.-P.; Stäb, F.; Wenck, H.; Gallinat, S. *J. Invest. Dermatol.,* **2007**, *127*, 2463.

[42] Peppas, N.A., Sahlin, J.J., *Int. J. Pharm.*, **1989**, *57*, 169.

[43] Laoa, L. L.; Peppas, N. A.; Boeya, F. Y. C.; Venkatramana, S. S. *Int. J. Pharm.,* **2011**, *418*, 28.

[44] Tompa, P. *FEBS Lett.,* **2005**, *579*, 3346.

[45] A. Sanchez-Sanchez, S. Akbari, A. Etxeberria, A. Arbe, U. Gasser, A. J. Moreno, J. Colmenero, J. A. Pomposo, *ACS Macro Lett.,* **2013**, *2*, 491.

[46] A.Knott, H. Mielke, U. Koop, R. Wolber, T. Burkhardt, J.-P.Vietzke, F. Stäb, H. Wenck, S. Gallinat, *J. Invest. Dermatol.,* **2007**, *127*, 2463.

[47] Fischer, F.; Achterberg, V.; März, A.; Puschmann, S.; Rahn, C.-D.; Lutz, V.; Krüger, A.; Schwengler, H.; Jaspers, S.; Koop, U.; Blatt, T.; Wenck, H.; Gallinat, S. *J. Cosmet. Dermatol.,* **2011**, *10*, 15.

[48] T. Baba, H. Nakano, K. Tamai, D. Sawamura, K. Hanada, I. Hashimoto, Y. Arima, *J. Invest. Dermatol.,* **1998**, *110*, 24.

[49] Y. Inamori, H. Tsujibo, H. Ohishi, F. Ishii, M. Mizugaki, H. Aso, N. Ishida, *Biol. Pharm. Bull.,* **1993**, *16*, 521.

[50] D. Miyamoto, N. Endo, N. Oku, Y. Arima, T. Suzuki, Y. Suzuki, *Biol. Pharm. Bull.*, **1998**, *21*, 1258.

[51] S. Liu, H. Yamauchi, *Cancer Lett.,* **2009**, *286*, 240.

[52] K. Kremer, G. S. Grest, *J. Chem. Phys.,* **1990**, *92*, 5057.

[53] M. P. Allen, D. J. Tildesley, *Computer simulation of liquids*., Oxford University Press, Oxford (UK), **1989**.

[54] J. A. Izaguirre, D. P. Catarello, J. M. Wozniak, R. D. Skeel, *J. Chem. Phys.*, **2001**, *114*, 2090.

[55] D. R. Rottach, J. G. Curro, J. Budzien, G. S. Grest, C. Svaneborg, R. Everaers, *Macromolecules.*, **2006**, *39*, 5521.

[56] B. Capone, I. Coluzza, F. Lo Verso, C. N. Likos, R. Blaak, *Phys. Rev. Lett.*, **2012**, *109*, 238301.

[57] F. Lo Verso, A. Z. Panagiotopoulos, C. N. Likos, *Phys. Rev. E.*, **2009**, *79*, 010401.

[58] C. Koch, C. N. Likos, A. Z. Panagiotopoulos, F. Lo Verso, *Mol. Phys.,* **2011**, *109*, 3049.

[59] C. N. Likos, K. R. Mecke, and H. Wagner, *J. Chem. Phys.*, **1995**, *102*, 9350.

[60] N. Hoffmann, F. Ebert, C. N. Likos, H. Lowen, and G. Maret, *Phys. Rev. Lett.*, **2006**, *97*, 078301.

[61] N. Hoffmann, C. N. Likos, H. Lowen, *J. Phys.: Condens. Matte.,* **2006**, *18*, 10193.

[62] A. Sanchez-Sanchez, I. Pérez-Baena, José A. Pomposo, *Molecules.*, **2013**, *18*, 3339.

[63] a) E. Harth, B.V. Horn, V.Y. Lee, D.S. Germack, C.P. Gonzales, R.D. Miller, C. J. Hawker, *J. Am. Chem. Soc.,* **2002**, *124*, 8653; b) B. T. Tuten, D. Chao, C. K. Lyon, E. B. Berda, *Polym. Chem.,* **2012**, *3*, 3068;

[64] J. A. Pomposo, I. Perez-Baena, L. Buruaga, A. Alegría, A. J. Moreno, J. Colmenero, *Macromolecules.*, **2011**, *44*, 8644.

[65] Y. Oono, M. Kohmoto, *J. Chem. Phys.,* **1983**, *78*, 520.

CHAPTER 4:

Metallo-Folded Single-Chain Nanoparticles with Catalytic Selectivity

4.1 Introduction

Enzymes showing outstanding catalytic activity and extreme substrate specificity are a continuing source of inspiration for green chemistry practitioners. Concerning catalytic activity, several artificial enzyme-mimic molecular structures and soft nano-entities approaching the size of natural enzymes have been synthesized based on macrocyclic compounds,[1] star,[2] hyperbranched[3-5] and helical[6] polymers as well as dendrimers,[7-9] among other systems.[10-14] However, examples of soluble nano-sized soft catalysts displaying pronounced enzyme-like substrate specificity are relatively scarce. For instance, limited control over substrate specificity was achieved with 4-(dialkylamino) pyridine-functionalized polymers during the solvolysis of *p*-nitrophenyl alkanoates in buffered aqueous methanol solution.[15] Efficient hydrolysis of a phenyl ester compound was shown by a molecularly imprinted soluble polymer nanogel with a molecular weight of 40 kDa.[12] To our best knowledge, no example of extraordinary catalytic specificity (*i.e.,* the reaction of only one substrate from a mixture of chemically related substances) has been reported by using synthetic soft nano-entities approaching the size of natural enzymes (5-15 nm).

The synthesis of biomimetic catalysts based on individual self-cross-linked polymer chains (single-chain nanoparticles, SCNPs) is challenging due to the polydisperse nature in size and composition of current synthetic polymers and the lack of efficient folding protocols.[16-18] Consequently, current SCNPs mimic the structure of folded biomacromolecules only in an approximate manner (Chapter 3).[19-20]

In spite of these limitations, single-chain nanoparticles (SCNPs) have been revealed as simple model systems to which valuable enzyme-like activity can be endowed by means of imprinted particle,[12] hydrophobic cavity[21-22] or concurrent binding/folding[23] strategies. In particular, the recently reported "concurrent" strategy opens new, promising avenues for endowing SCNPs

with enzyme-mimetic properties such as outstanding catalytic activity and extreme substrate specificity.

In this Chapter, a new route to metallo-folded SCNPs containing complexed Cu (II) ions is described. These metallo-folded polymer chains containing complexed Cu (II) ions were found to show catalytic specificity during the oxidative coupling of mixtures of chemically related terminal acetylene substrates (Scheme 4.1). Moreover, a wide range of other metallo-folded SCNPs can be envisioned by the appropriate selection of metal ions (*e.g.*, Pd, Ni, Co, Fe, Mn, Mo) pointing to the potential broad scope of the concurrent binding/folding strategy.

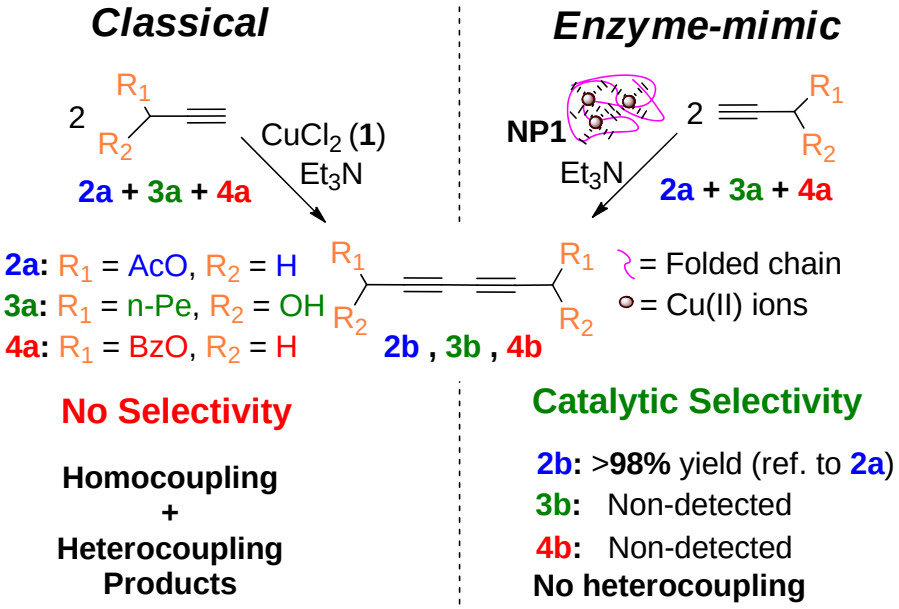

Scheme 4.1. Catalytic specificity displayed by metallo-folded single-chain polymer nanoparticles during alkyne dimerization.

4.2 Objectives

In this Chapter we focus on the synthesis and characterization of single-chain nanoparticles (SCNPs) based on previously synthesized P(MMA-*co*-AEMA) copolymers[19-20] that feature β-ketoester functional groups which can be folded/collapsed *via* intrachain Cu(II) complexation of **AEMA** units. We will demonstrate that the metallo-folded SCNPs containing complexed Cu(II) ions produced by means of this versatile approach (Scheme 4.2, **NP1**) do display catalytic specificity during the oxidative coupling of mixtures of chemically related terminal acetylene substrates. Such specificity is not afforded by classical catalysts (*i.e.*, $CuCl_2$, $Cu(OAc)_2$, $Cu(acac)_2$) under exactly the same reaction conditions.

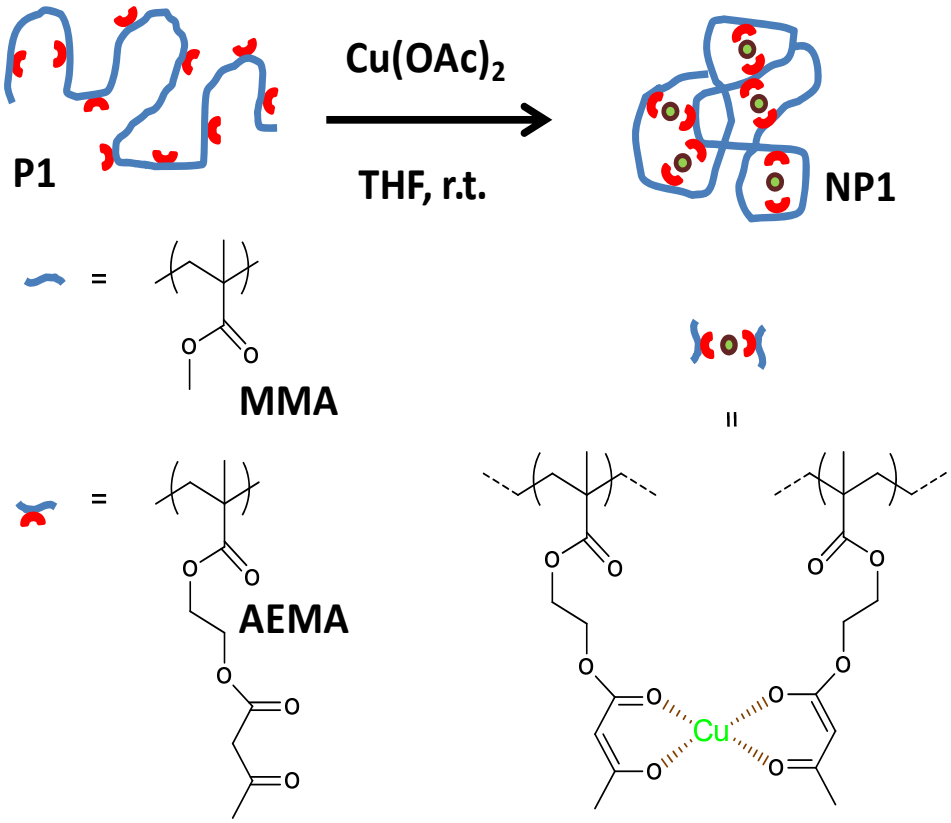

Scheme 4.2. Idealized picture of metallo-folded single-chain nanoparticle **NP1** synthesized from precursor **P1**.

4.3 Experimental Section

a) Synthesis of polymer precursors.

Before polymerization methyl methacrylate (**MMA**) was purified by distillation and 2-(acetoacetoxy) ethyl methacrylate (**AEMA**) was purified by passing through basic alumina. In a typical procedure, **MMA** (1 ml, 9.4 mmol), **AEMA** (0.6 ml, 3.1 mmol), CPDB (0.8 mg, 3×10^{-2} mmol) and 2,2-azobis(2-methylpropionitrile) (1 mg, 3×10^{-2} mmol) were dissolved in ethyl acetate (3.2 ml). The reaction mixture was degassed by passing argon for 15 min. The copolymerization reaction was carried out at 65 ^{o}C for 18 h. The resulting nanoparticle polymer precursor P(MMA-*co*-AEMA) (**P1**), was isolated by precipitation in methanol and further drying (**P1**: Yield (%) = 72, M_w (SEC/MALLS, dn/dc = 0.083) = 375 kDa, M_w/M_n = 1.4, R_g = 26 ± 1.4 nm, composition (^{1}H NMR) = 30 mol% **AEMA**). (**P2**: Yield (%) = 65, M_w (SEC/MALLS, dn/dc = 0.083) = 320 kDa, M_w/M_n = 1.4, composition (^{1}H NMR) = 26 mol% **AEMA**).

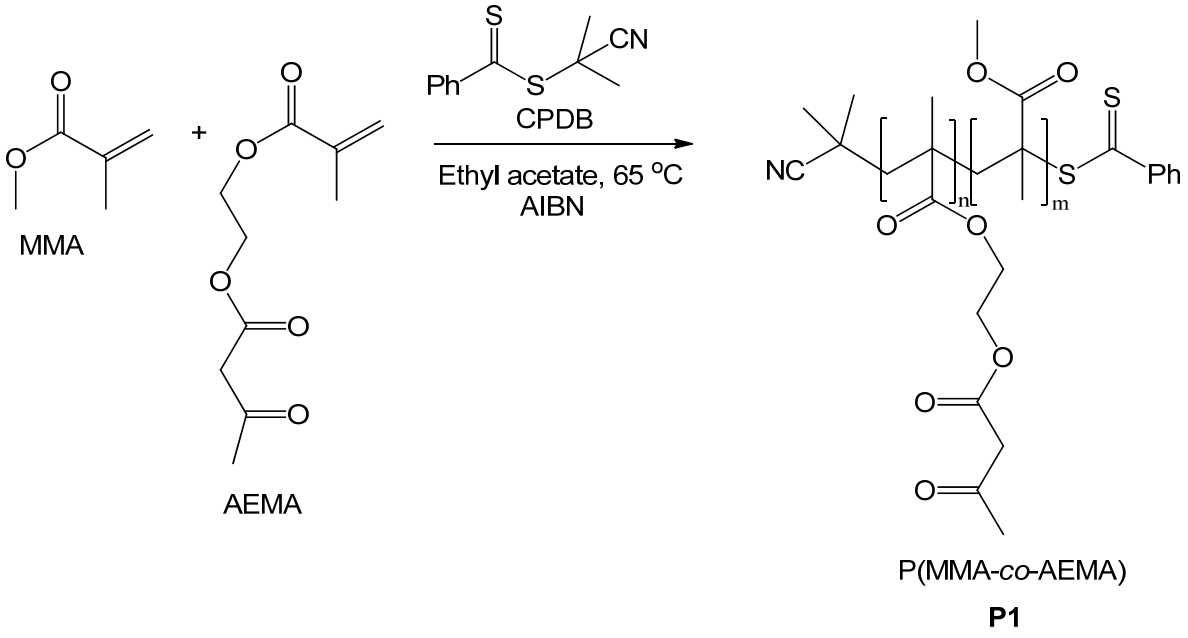

Scheme 4.3. Synthesis of polymer precursor *via* reversible addition-fragmentation chain-transfer RAFT polymerization.

b) Synthesis of metallo-folded nanoparticles.

In a typical reaction, the precursor (**P1**, 150 mg, 0.32 mmol) was dissolved in THF (150 ml) at room temperature. Then, a solution of $Cu(OAc)_2$ (15 mg, 0.08 mmol Cu) in THF was progressively added, and the mixture was maintained under stirring for 24 h. Finally, the metallo-folded SCNP **NP1** was isolated by precipitation in diethyl ether and further drying under dynamic vacuum. The progressive folding/collapse process was followed through simultaneous SEC/MALLS measurements. (**NP1**: Yield (%) = 71, M_w (SEC/ MALLS, dn/dc = 0.083) = 390 kDa, M_w/M_n = 1.3, R_g = 15 ± 1.1 nm) (**NP2**: Yield (%) = 68, M_w (SEC/MALLS, dn/dc = 0.083) = 285 kDa, M_w/M_n = 1.3)

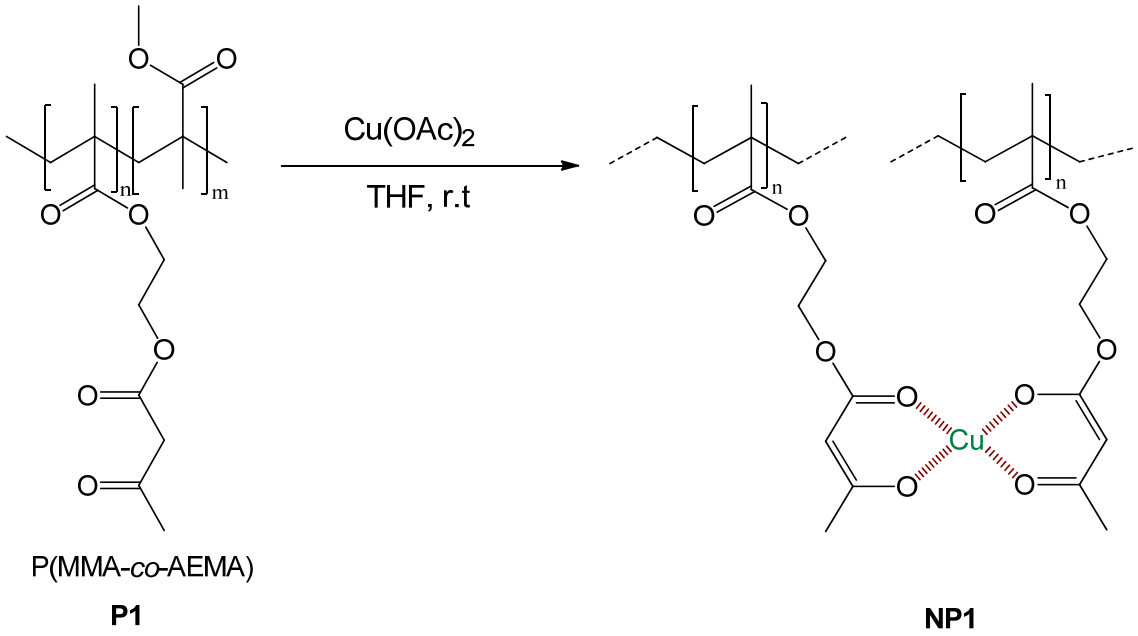

Scheme 4.4. Synthesis of metallo-folded nanoparticles (**NP1**) from P(MMA-*co*-AEMA) copolymer **P1**, *via* intrachain Cu(II) complexation of **AEMA** units.

c) Oxidative coupling of terminal alkynes.

To a mixture of $CuCl_2$ (**1**) (3 mol% Cu) or **NP1** (5 mg, 0.5 mol% Cu) and triethylamine (Et_3N, 3 mol %) the corresponding terminal alkyne (1.0 mmol) was added. The mixture was stirred at 60 ^oC for 8 h in air under solvent-free conditions. After cooling to room temperature, the mixture was diluted with deuterated chloroform and filtered for characterization of the crude reaction medium through ^1H NMR spectroscopy. The resulting 1,3-diyne product was

isolated by removing the residual terminal alkyne through reduced pressure distillation and characterized by ^{1}H NMR, GC and FTIR spectroscopy. The same procedures were followed during the dimerization of binary and ternary mixtures of alkynes.

d) Synthesis of (1-benzyl-1*H*-1,2,3-triazol-4-yl) methyl acetate.

In order to investigate the potential formation of Cu(I) species during alkyne dimerization, synthesis of (1-benzyl-1*H*-1,2,3-triazol-4-yl) methyl acetate was carried out. Propargyl acetate (1.0 mmol), benzyl azide (1.0 mmol) and CuBr (3 mol% Cu) were dissolved in chloroform (1.0 ml). The reaction mixture was degassed by passing argon for 15 min and then stirred at room temperature (r.t) for 2 h. Then, the mixture was diluted with chloroform and filtered for characterization of the crude reaction medium through ^{1}H NMR spectroscopy (Figure 4.1).

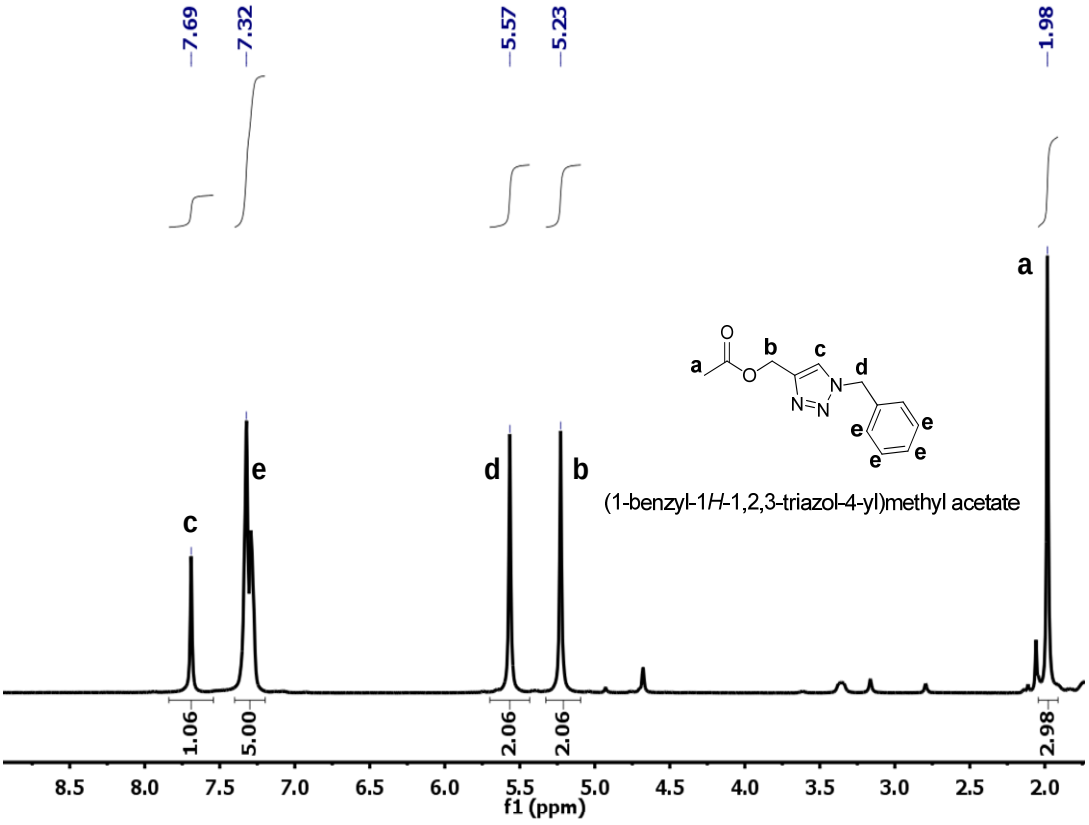

Figure 4.1. The ^{1}H NMR spectrum in $CDCl_3$ of (1-benzyl-1*H*-1,2,3-triazol-4-yl) methyl acetate and the corresponding proton assignment.

4.4 Results and Discussion

We prepared metallo-folded single-chain nanoparticles (SCNPs) based upon previously synthesized copolymers[19-20] containing methyl methacrylate (**MMA**) and 2-(acetoacetoxy) ethyl methacrylate (**AEMA**) repeat units (Scheme 4.3) that feature β-ketoester reactive functions which serve as handles for concurrent binding/folding *via* intrachain Cu(II) complexation of **AEMA** units (Scheme 4.4).

SCNP formation was carried out under very mild conditions, in tetrahydrofuran (THF) at room temperature by using $Cu(OAc)_2$ as a reagent at high dilution conditions (1 mg/ml) to minimize, as much as possible, unwanted inter-particle coupling events. We selected P(MMA-*co*-AEMA) precursor (**P1)** with a content of reactive **AEMA** units of 30 mol%, relatively high M_w (weight average molecular weight, M_w = 375 kDa) and relatively low dispersity ($Đ$ = 1.4) to facilitate the accurate detection of size reduction upon SCNP formation by combined size-exclusion chromatography / multi-angle laser light scattering (SEC / MALLS) measurements.

The collapse of the linear copolymer precursor **P1** to SCNP **NP1** upon progressive addition of $Cu(OAc)_2$ is illustrated in Figure 4.2. A significant increase in retention time was observed for **NP1** when compared to **P1** as a consequence of the reduction in hydrodynamic size upon SCNP formation; an observation which is consistent with previous works in this field.[24] The average radius of gyration was found to decrease from 26 nm for **P1** to 15 nm for **NP1**, as determined by the MALLS technique.

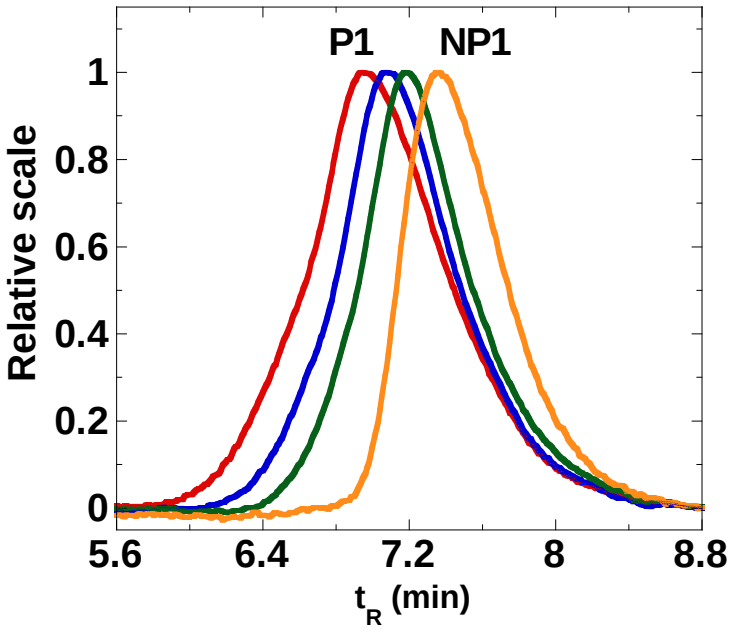

Figure 4.2. Size-exclusion chromatography traces in THF corresponding to the formation of **NP1** by progressive addition of $Cu(OAc)_2$: 0.17 mM (blue curve), 0.34 mM (green curve) and 0.51 mM (orange curve) to a **P1** solution (red curve).

Evidence of **AEMA** complexation by copper ions was obtained by infra-red (IR) spectroscopy, in which characteristic vibration bands were observed in the IR spectrum of **NP1** located at 1600 cm^{-1} (stretching C=O vibration, enol tautomer bonded to Cu) and 1515 cm^{-1} (stretching C=C vibration, enol tautomer bonded to Cu)[25-27] (Figure 4.3).

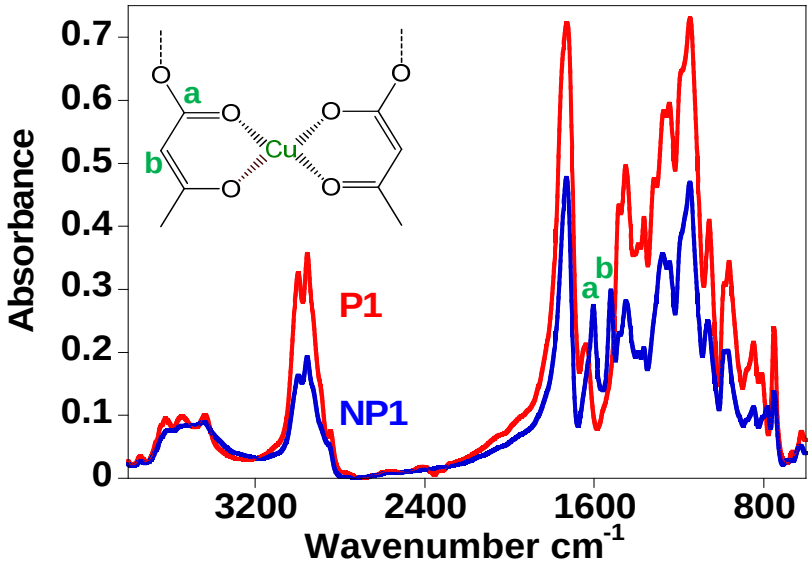

Figure 4.3. IR spectra of precursor **P1** (red line) and **NP1** (blue line) showing specific vibration bands (a, b) arising from $Cu(AEMA)_2$ complexes.

Additionally, we performed ^{1}H NMR experiments to investigate the formation of SCNPs. Comparison of the ^{1}H NMR spectrum of the P(MMA-*co*-AEMA) random copolymer **P1** with that of its corresponding SCNP **NP1** reveals significant peak broadening upon intramolecular crosslinking (Figure 4.4). For SCNPs, signal broadening in the ^{1}H NMR spectrum can be attributed to the restricted mobility of some of the SCNP protons as a consequence of the progressive crosslinking and is a well-documented signature of the formation of SCNPs.[28-29]

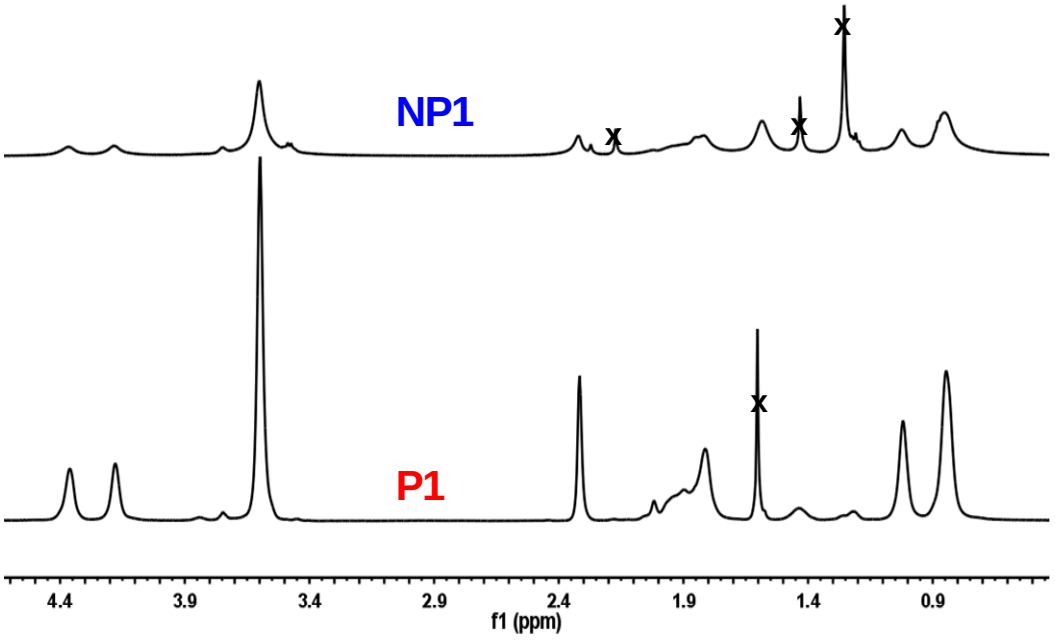

Figure 4.4. Comparison of the ^{1}H NMR in $CDCl_3$ spectrum of the P(MMA-*co*-AEMA) random copolymer **(P1)** with that of its corresponding SCNP **(NP1)**.

As revealed by small angle neutron scattering (SANS) experiments (see Figure 4.5), in good solvent conditions **NP1** does not show a clear, marked peak corresponding to a compact,[30] globular morphology; instead, a shoulder is observed at $Q < 1$ nm^{-1} values due to a more compact conformation of **NP1** in solution when compared to that of **P1**.

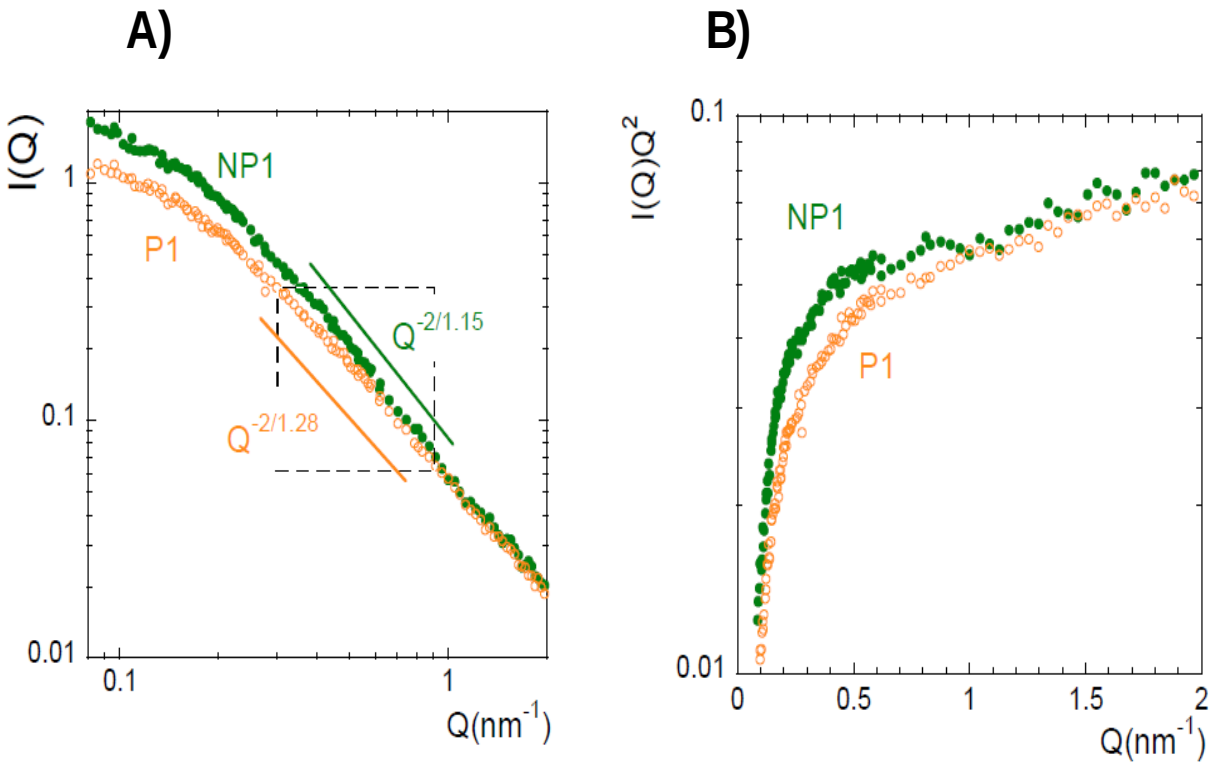

Figure 4.5. A) SANS results revealing the form factor of the metallo-folded SCPN **NP1** in solution when compared to precursor **P1**. Lines represent the asymptotic Ornstein−Zernike regime $I(Q) \sim Q^{-2/\nu}$ (I =intensity; Q = wavevector; ν = scaling exponent).[31] The exponent value for **NP1**, ν = 1.15, is significantly higher than that expected for globular, compact nanoparticles, ν = 0.66 pointing to the non-compact conformation of **NP1** in solution. As an example, globular nano-objects such as native folded proteins do show a $Q^{-2/0.66}$[31] scaling law. Due to the high molecular weight of the sample and the limited window of experimental Q values, reliable information about the actual radius of gyration and molar mass cannot be extracted with confidence from Figure 4.5 A. **B)** Kratky plots for solutions of **P1** and **NP1**. A shoulder is observed at low Q values due to a more compact conformation of **NP1** in solution when compared to that of **P1**.

Conversely, **NP1** adopts a collapsed, globular morphology in its dry state as observed by transmission electron microscopy (TEM) (see figure 4.6 A). This extended-to-compact morphology transition taking place upon solvent removal was also observed in "Michael" nanocarriers (Chapter 3) which is consistent with the results of molecular dynamics (MD) simulations as explained in Chapter 3.

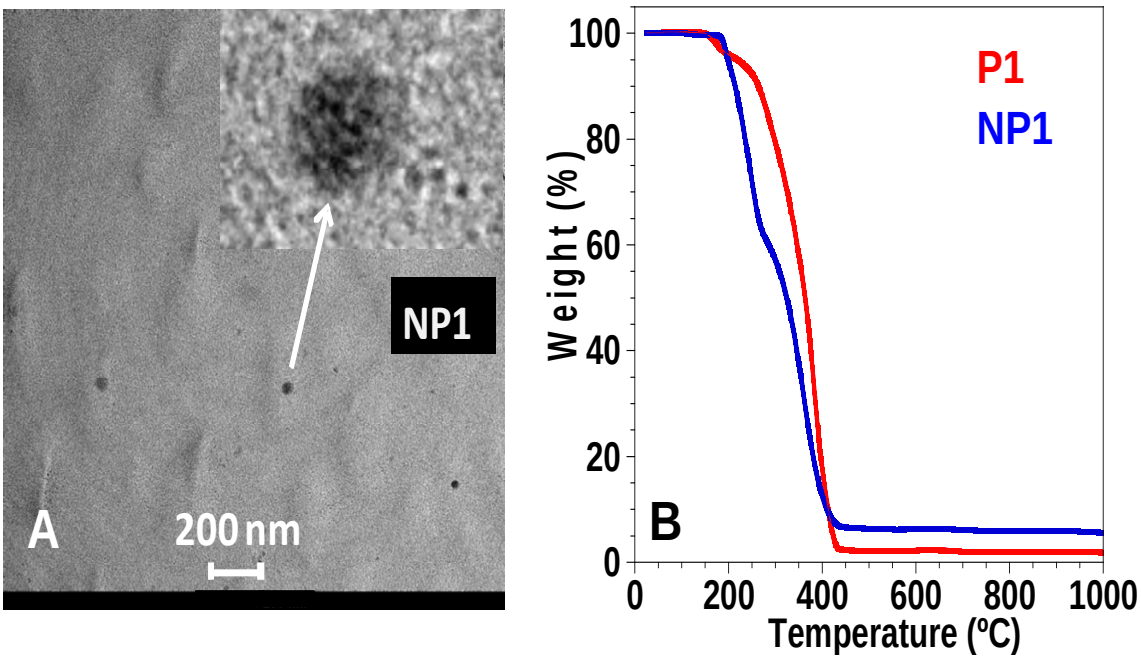

Figure 4.6. **A)** TEM image of **NP1** in its dry state (inset is a magnification; **NP1** size ≈ 20 nm). **B)** TGA curves for precursor **P1** (red line) and metallo-folded SCNP **NP1** (blue line).

The copper incorporated into **NP1** amounted to 26 mol % with respect to **AEMA** units as deduced from thermal gravimetric analysis (TGA) (see Figure 4.6 B). In Figure 4.6 B the content of copper in **NP1** was estimated from the residual weight that can be assigned to CuO species (6.6 wt%) due to the black color of the residues. It is worth noting that the precursor **P1**, which was taken as a control, was totally decomposed at temperatures above 450°C, so the residues observed for **NP1** can only be attributed to metal oxide species. The amount of metal incorporated into **NP1** was similar to that in organometallic nanoparticles synthesized through intramolecular chelation of individual ROMP-derived poly(1,5-cyclooctadiene) chains by Rh(I) ions.[32]

The oxidation state of copper ions in the $Cu(AEMA)_2$ complexes of **NP1** was determined to be +2 by means of X-ray photoelectron spectroscopy (XPS) measurements. Figure 4.7 illustrates a XPS spectrum showing the detailed Cu 2p region of **NP1**. The Cu 2p region exhibits a doublet structure with a separation of approximately 20 eV, due to the non-degenerate 2p ground state. The position of the $2p_{3/2}$ and $2p_{1/2}$ peaks could suggest either Cu^{+} or Cu^{2+} as

there is a little difference in the binding energy position of these species.[33] However, the satellite peaks highlighted are characteristic of Cu^{2+}, indicating that the copper in **NP1** is in this oxidation state.[34,35]

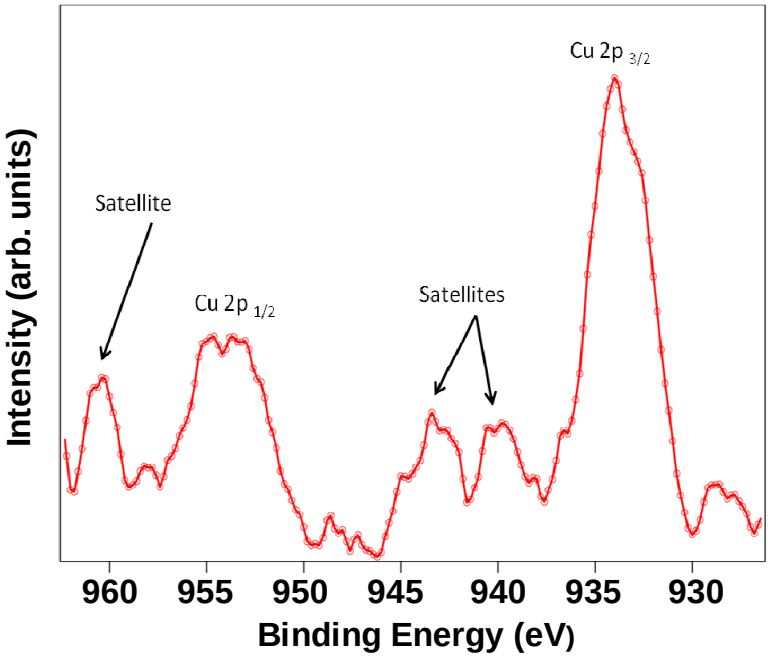

Figure 4.7. XPS spectrum showing the detailed Cu 2p region of **NP1**. The Cu 2p region exhibits a doublet structure with a separation of approximately 20eV, due to the non-degenerate 2p ground state.

Having shown a mild and efficient synthetic procedure to prepare metallo-folded SCNPs containing complexed Cu (II) ions, we turned our attention towards the potential enzyme-mimic properties of these soft nano-entities when compared to classical catalysts (*i.e.*, $CuCl_2$, $Cu(OAc)_2$, $Cu(acac)_2$). To evaluate the catalytic activity and substrate specificity of copper-containing SCNPs, we explored their use as soft catalysts in an environmentally friendly, economical and efficient method[36a] for transforming terminal acetylenes into 1,3-diynes *via* oxidative coupling. It is worth mentioning that 1,3-diynes have attracted significant interest as building blocks for the construction of supramolecular materials,[37] π-conjugated acetylenic oligomers and polymers,[38] industrial and pharmaceutical intermediates,[39] as well as antitumor agents.[40]

Thus, as a first control experiment we performed the coupling of a series of terminal alkyne compounds to 1,3-diynes under optimized reaction conditions[36b] involving the use of catalytic amounts of $CuCl_2$ (**1**) (3 mol%) and triethylamine (Et_3N, 3 mol%). These acetylenic compounds were selected to cover a broad range of chemically related substrates (Scheme 4.5). The bulk homocoupling procedure gave the corresponding diynes in good to excellent yields (36 - 98%, Table 4.1) with the exception of compound **8a** which has a bromo functional group (Table 4.1**,** entry 8). As expected, catalyst $CuCl_2$ (**1**) showed no specificity, since binary or ternary mixtures of terminal alkynes, as reagents, lead to complex mixtures of diynes, as products, due to both homo- and cross-coupling reactions (Table 4.1, entries 22, 24, 26, 28 and Figure 4.8). By reducing the amount of catalysts to 0.5 mol% Cu, no reaction was observed to take place. The catalyst was also found to work in the presence of aromatic solvents (Table 4.1, entry 2).

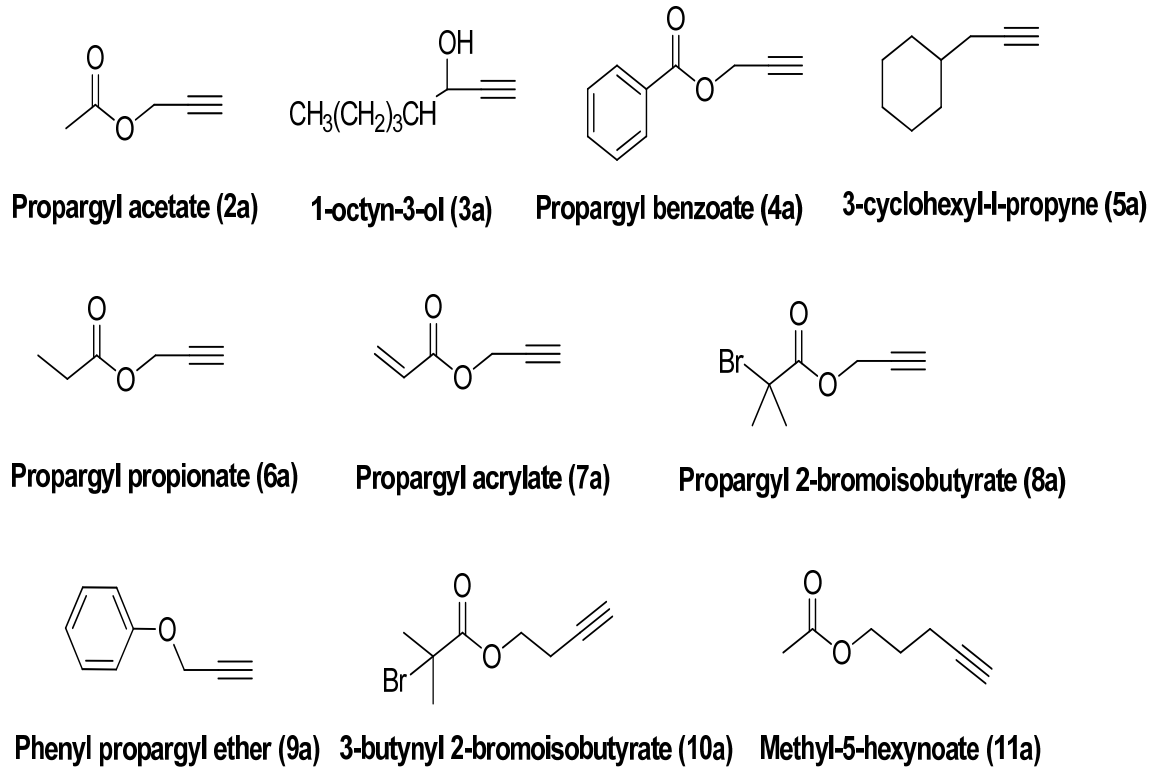

Scheme 4.5. Chemical structures of terminal alkynes used in this work.

Table 4.1. Unprecedented catalytic selectivity of **NP1** when compared to $CuCl_2$ (**1**) during the coupling of terminal alkynes to 1,3-diynes under solvent-free conditions.

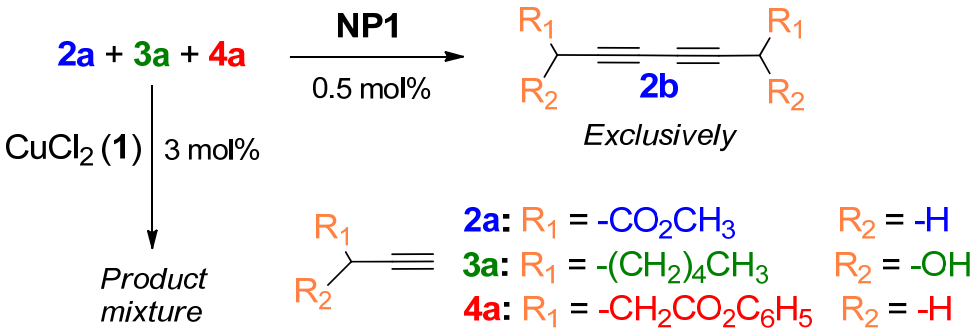

Entry	Catalyst[a]	Reagents	Products[b]	Yield (%)[b]	Selectivity
1	**1**	**2a**	**2b**	>98	-
2	**1**	**2a**	**2b**	93[c]	-
3	**1**	**3a**	**3b**	>98	-
4	**1**	**4a**	**4b**	57	-
5	**1**	**5a**	**5b**	>98	-
6	**1**	**6a**	**6b**	>98	-
7	**1**	**7a**	**7b**	36	-
8	**1**	**8a**	**8b**	0	-
9	**1**	**9a**	**9b**	77	-
10	**NP1**	**2a**	**2b**	>98	-
11	**NP1**	**2a**	**2b**	91[c]	-
12	**NP1**	**2a**	**2b**	33[i]	-
13	**NP1**	**3a**	**3b**	0	-
14	**NP1**	**4a**	**4b**	0	-
15	**NP1**	**5a**	**5b**	0	-
16	**NP1**	**6a**	**6b**	27	-
17	**NP1**	**7a**	**7b**	0	-
18	**NP1**	**8a**	**8b**	0	-
19	**NP1**	**9a**	**9b**	0	-
20	**NP1**	**10a**	**10b**	0	-
21	**NP1**	**11a**	**11b**	0	-
22	**1**	**2a+3a**	***Mixture***[d]	97	No
23	**NP1**	**2a+3a**	**2b**[e]	>98[f]	Yes
24	**1**	**2a+4a**	***Mixture***[d]	51	No
25	**NP1**	**2a+4a**	**2b**[e]	>98[f]	Yes
26	**1**	**3a+4a**	***Mixture***[d]	52	No
27	**NP1**	**3a+4a**	***Mixture***[g]	0	Yes
28	**1**	**2a+3a+4a**	***Mixture***[d]	84	No
29	**NP1**	**2a+3a+4a**	**2b**[e]	>98[f]	Yes
30	**NP1**	**2a+3a+4a**	**2b**[e]	>98[c,f]	Yes
31	**NP1**	**2a+3a+4a**	**2b**[e]	>98[f,j]	Yes
32	**NP1**	**2a+3a+6a**	***Mixture***	66[h]	Yes
33	**$Cu(acac)_2$**	**2a**	**2b**	0[k]	-

[a] Reaction conditions: solvent-free, 1 mmol of alkyne, Et_3N (3 mol%), **1:** 3 mol% Cu or **NP1:** 0.5 mol% Cu, 60 °C, 8 h, air. [b] From GC and ^1H NMR data. [c] Diluted with toluene to half of the original alkyne concentration. [d] Mixture of products as a result of combined homo- and cross-coupling reactions. [e] No by-products from cross-coupling reactions were detected. [f] Referred to **2a**. [g] Reaction time: 24 h. [h] Referred to (**2a+3a+6a**). [i] Diluted with ethyl acetate to half of the original alkyne concentration. [j] Diluted with benzene to half of the original total alkyne concentration. [k] The concentration of $Cu(acac)_2$ was increased to 3 mol%.

Interestingly, when we replaced the classical catalyst **1** by the metallo-folded SCNP **NP1** at a lower concentration of 0.5 mol% Cu we observed unprecedented catalytic specificity towards the propargylic substrate **2a** (> 98% yield, R_1 = -CO_2CH_3) and, to a minor extent, towards the related compound **6a** (27 % yield, R_1 = -$CO_2CH_2CH_3$) (see Table 4.1 and Figure 4.8). A very good yield was also observed by performing the reaction in aromatic solvent (Table 4.1, entry 11). Moreover, in competitive experiments involving ternary mixtures of **2a**, **3a** and **4a** (Table 4.1, entry 29, 30, 31) no sign of cross-coupling products was observed by gas chromatography (GC), giving only **2b** as the product in a highly selective manner (Figure 4.8). **NP1** showed catalytic selectivity towards the propargylic substrates in mixtures of **2a**, **3a** and **6a** (Table 4.1, entry 32). Moreover, this selectivity towards **2a**, and to a minor extension **6a**, was maintained in control experiments using compounds with a group more bulky than a proton near the acetate, or having an additional methylene group between the acetate group and the alkyne moiety (Table 4.1, entry 20, 21). It is worth mentioning that neither $Cu(OAc)_2$ nor $Cu(acac)_2$ compounds were found to display significant catalytic activity at a concentration of 0.5 mol% Cu for compounds **2a-11a**. Although this behavior could be tentatively attributed to a local environment in **NP1** with a high enough amount of Cu complex concentration since the presence of a competitive solvent such as ethyl acetate slows the reaction (Table 4.1, entry 12), no reaction was observed in control experiments by increasing the $Cu(acac)_2$ concentration even to 3 mol% Cu (Table 4.1, entry 33). At this stage, one can hypothesize that the pronounced substrate specificity displayed by **NP1** when compared to $CuCl_2$, $Cu(OAc)_2$ and $Cu(acac)_2$ complexes could result from the formation of multiple, compartmentalized local catalytic sites composed of $Cu(AEMA)_2$ complexes surrounded by an environment of methyl methacrylate repeat units allowing an optimum transition state stabilization for the propargylic substrate **2a** and, to a minor extent, **6a**.[12, 23]

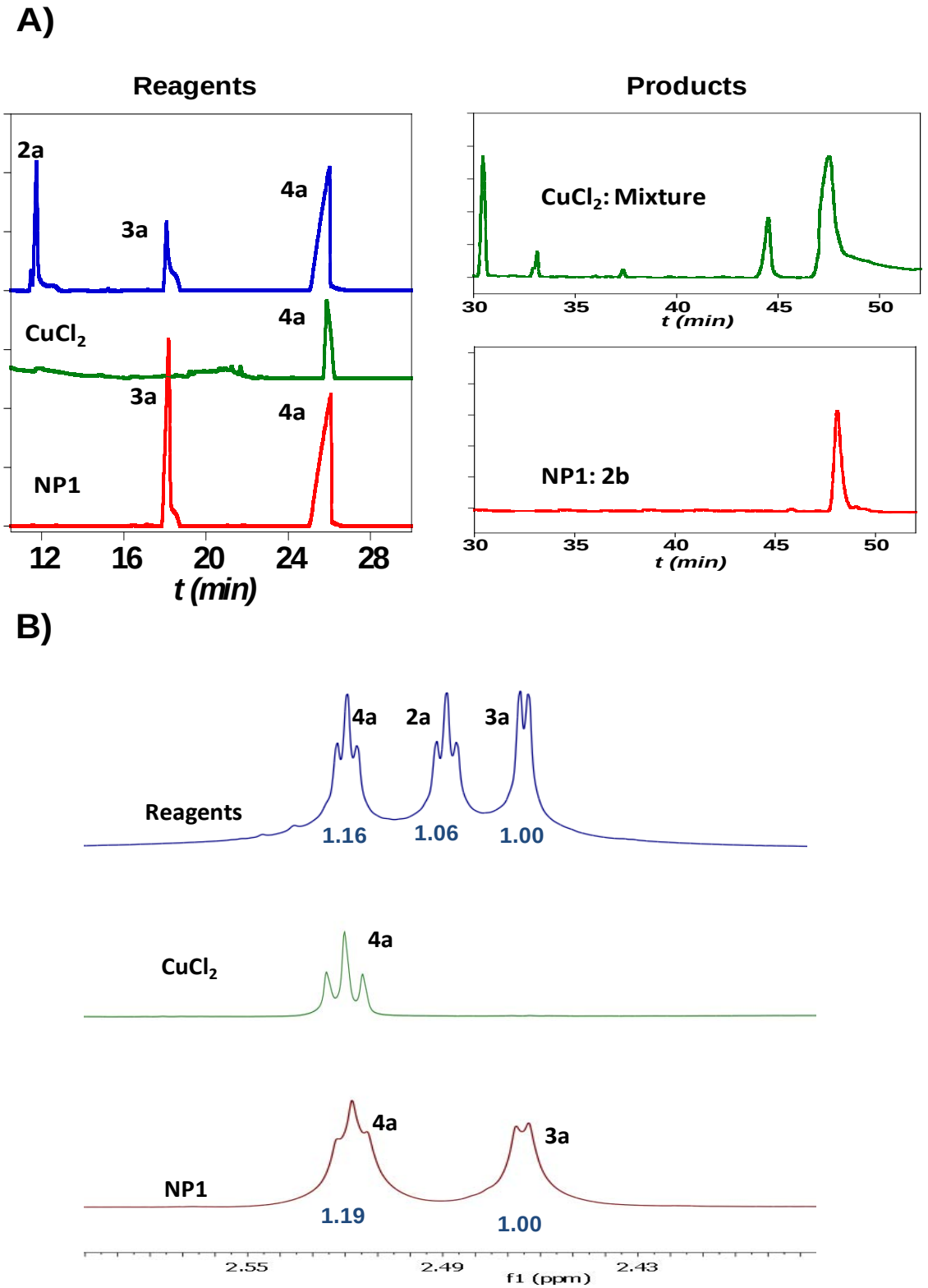

Figure 4.8. **A)** Gas chromatography (GC) traces of the **2a + 3a + 4a** reagent mixture (blue trace) and products obtained by using $CuCl_2$ (**1**) (green curve) or metallo-folded SCNPs **NP1** (red curve) as catalysts during oxidative coupling. **B)** ^1H NMR spectra showing signals from acetylenic protons of the **2a + 3a + 4a** reagent mixture (blue trace) and same spectral zone after reaction using $CuCl_2$ (**1**) (green trace) or metallo-folded SCNPs **NP1** (red trace) as catalysts during oxidative coupling. The peak area relative to that of peak **3a** is indicated for the blue and red traces.

To further investigate the origin of the catalytic selectivity, the electronic absorption spectra of $Cu(OAc)_2$, $Cu(acac)_2$ and **NP1** in dimethyl sulfoxide (DMSO) were recorded as illustrated in Figure 4.9. The UV-Vis spectrum of the $Cu(OAc)_2$ complex showed one very broad *d-d* band at 720 nm and a band in the UV region centered at 260 nm due to Cu-to-OAc metal to ligand charge transfer (MLCT) transitions.[41] The $Cu(acac)_2$ complex displayed only a MLCT band at 297 nm, whereas the **NP1** showed a MLCT band centered at 271 nm, a value in between those observed for the $Cu(OAc)_2$ and $Cu(acac)_2$ complexes. Both steric and electronic complementarities in the rate-determining transition step of the catalytic sites for **2a,** and to a minor extent **6a** could be responsible for the catalytic selectivity displayed by **NP1**.

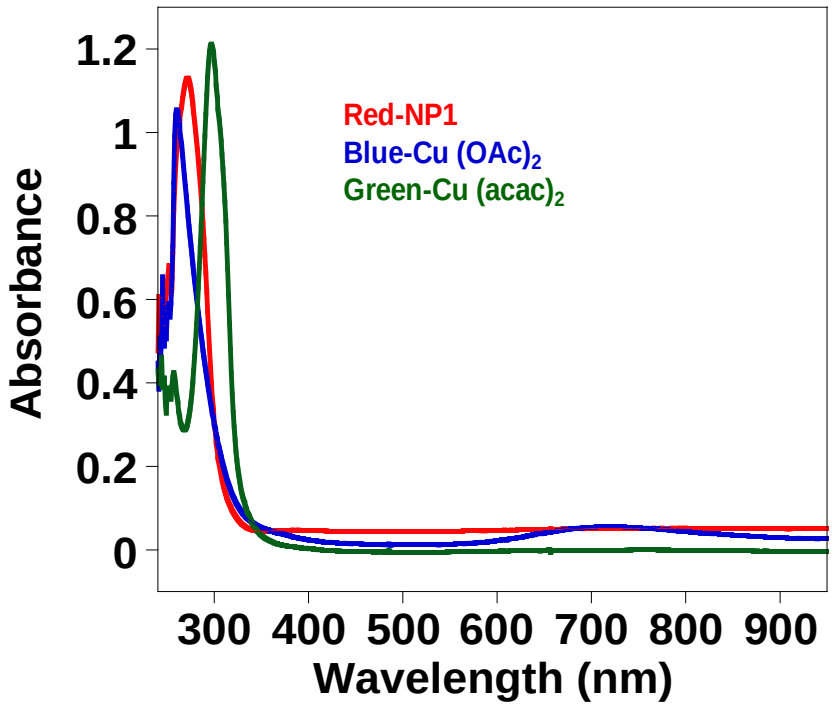

Figure 4.9. UV-Vis spectra of $Cu(OAc)_2$, $Cu(acac)_2$ and **NP1** in DMSO.

Analysis of kinetics data using **2a** as reagent (Figure 4.10) provided a value of the apparent catalytic constant of $k_{cat}(app)$ = 8.8×10^{-3} s^{-1}, which is higher than that determined for molecularly imprinted soluble polymer nanogels (k_{cat} = 1.2×10^{-6} s^{-1})[6c] and similar to that reported very recently for hydrophobic cavity-

based catalytic SCNPs (k_{cat} = 5.3×10^{-2} s^{-1}).[21] Analysis of kinetics data was examined using the classical Michaelis-Menten equation.

The initial concentration of propargyl acetate (**2a**) was $[\mathbf{S}]_0$ = 10 M >> $[\mathbf{NP1}]_0$ ($[\mathbf{NP1}]_0$ from 0.02 M to 0.05 M). Under such conditions the classical Michaelis-Menten equation becomes:

$$V = \frac{d[P]}{dt} = k_{cat}\,[\mathbf{NP1}]_0\,\frac{[S]_0}{K_M + [S]_0} \qquad (4.1)$$

By assuming K_M << $[\mathbf{S}]_0$

$$V = \frac{d[P]}{dt} \approx k_{cat}\,[\mathbf{NP1}]_0 \qquad (4.2)$$

Where V = d[P]/dt is the rate of reaction determined, as usual, from the initial slope of a plot of [P] *versus* time, at constant concentration of **NP1** , and K_M is the substrate concentration at which the reaction rate is half of the maximum reaction rate.

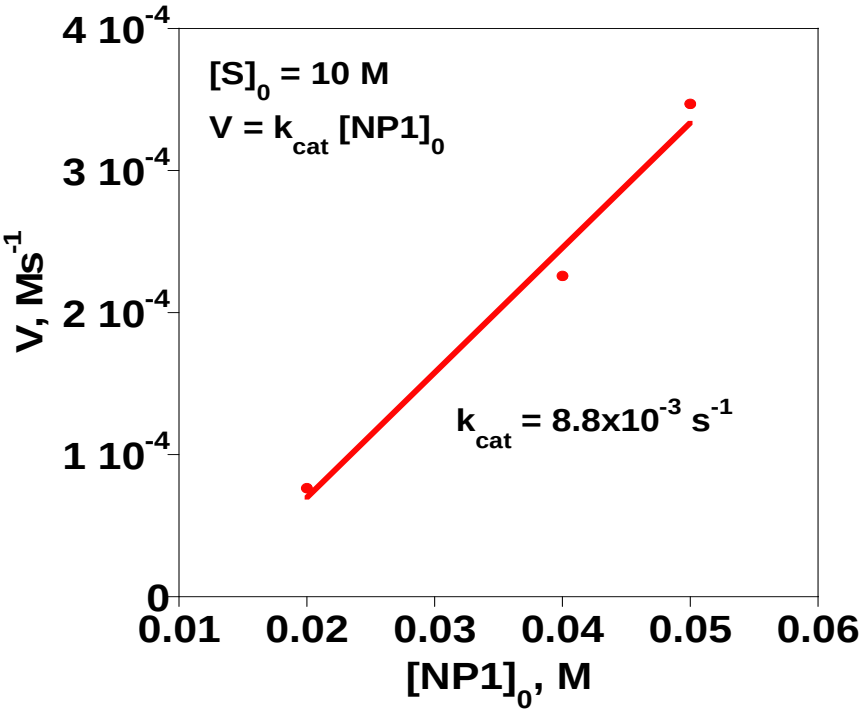

Figure 4.10. Analysis of kinetics data to determine the apparent catalytic constant (k_{cat}) for propargyl acetate (**2a**) dimerization catalyzed by **NP1.**

In order to investigate the potential formation of Cu(I) species during alkyne dimerization, the electronic absorption spectra of **NP1** was recorded at the beginning and at the end of the alkyne dimerization reaction (Figure 4.11).

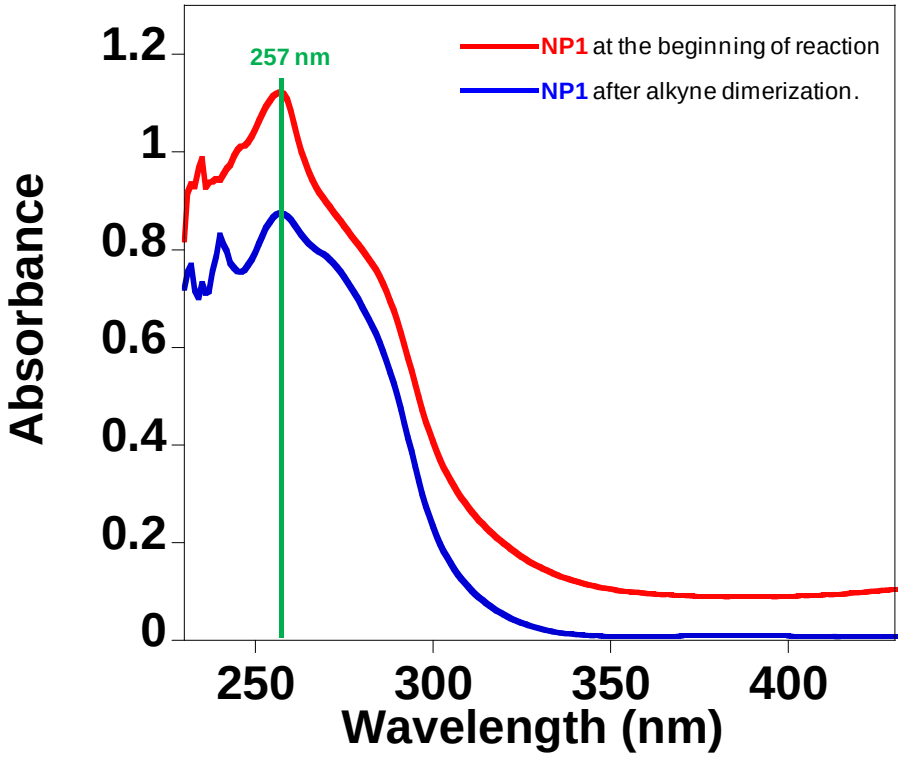

Figure 4.11. UV-Vis spectra of **NP1** in chloroform at the beginning and at the end of the reaction of alkyne dimerization.

Even though both spectra show a maximum absorbance at about 257 nm, some changes in the shape of the spectrum are observed that could potentially be attributed to the generation of Cu(I) species. To further investigate this issue, the synthesis of (1-benzyl-1*H*-1,2,3-triazol-4-yl) methyl acetate was attempted with SCNPs **NP1** that were used before in the synthesis of **2b**. As a control experiment the same reaction was carried out in presence of CuBr (Scheme 4.6).

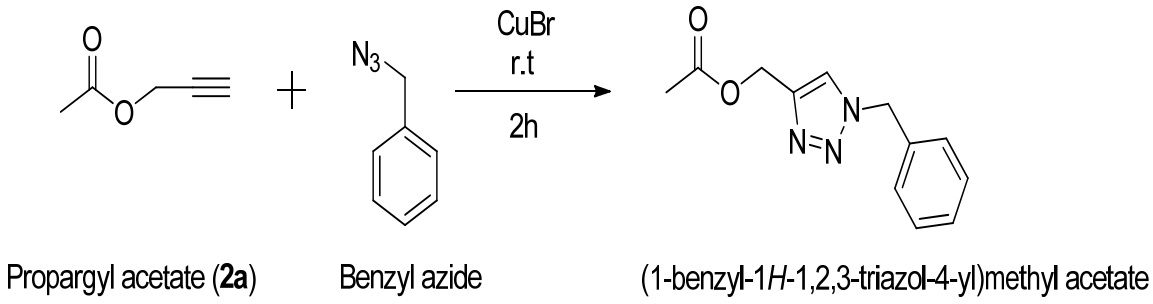

Scheme 4.6. Synthesis of (1-benzyl-1*H*-1,2,3-triazol-4-yl) methyl acetate using benzyl azide and propargyl acetate in presence of CuBr.

As illustrated in Figure 4.12, the formation of (1-benzyl-1*H*-1,2,3-triazol-4-yl) methyl acetate at a very low yield (6 %) in the presence of **NP1** suggests the potential presence of only a minor amount of Cu(I) in SCNPs **NP1** after alkyne dimerization.

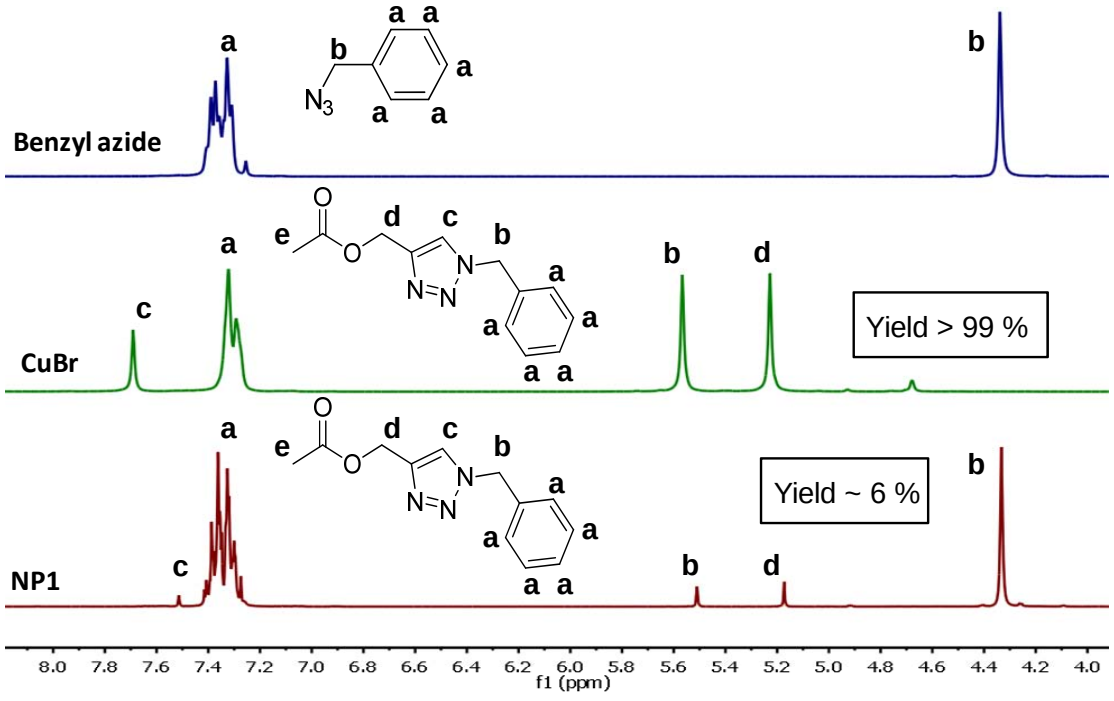

Figure 4.12. ^{1}H NMR spectra in $CDCl_3$ showing the formation of (1-benzyl-1*H*-1,2,3-triazol-4-yl) methyl acetate. Blue trace is the ^{1}H NMR spectrum of benzyl azide. Green trace is the ^{1}H NMR spectrum corresponding to the formation of (1-benzyl-1*H*-1,2,3-triazol-4-yl) methyl acetate using CuBr as "click" chemistry catalyst. Red trace is the ^{1}H NMR spectrum corresponding to the formation of (1-benzyl-1*H*-1,2,3-triazol-4-yl) methyl acetate (yield 6 %) using SCNP **NP1** that was used before in the synthesis of **2b**.

Interestingly, we have also observed that metallo-folded SCNPs are able to reversibly undergo a nanoparticle to coil transition by addition of hydrochloric acid (HCl, 1 M). To demonstrate the disassembly of these SCNPs, a few drops of hydrochloric acid (HCl, 1M) were added to the reaction medium where the SCNPs are, to cause acid-triggered disruption of the SCNPs. To our delight, the position at the peak maximum in the SEC trace of a solution containing metallo-folded SCNPs after treatment for 24 h with an excess of HCl (with respect to the **AEMA** content in **P2**), denoted as **P2´**, was found to be nearly identical to that of the initial precursor (**P2**), suggesting an efficient nanoparticle disassembly process (see Figure 4.13).

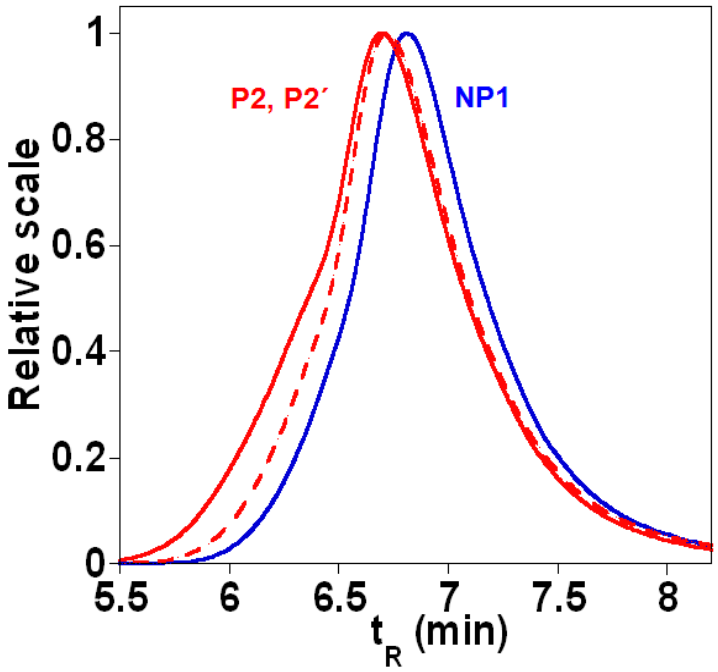

Figure 4.13. Illustration of metallo-folded SCNPs disassembly. SEC traces in THF for **P2** (red line), **NP2** (blue line) and **P2´** (broken red line).

4.5 Conclusion

In summary, we have synthesized catalytically active single-chain nanoparticles (SCNPs) based on metallo-folded polymer chains containing complexed Cu(II) ions by means of a mild and versatile concurrent binding/folding strategy. These synthetic soft nano-entities approaching the size of natural enzymes display catalytic specificity at low concentration of Cu(II) ions during the oxidative coupling of mixtures of chemically related terminal acetylene substrates, which cannot be attained with classical catalysts such as $CuCl_2$, $Cu(OAc)_2$ or $Cu(acac)_2$.

Such substrate specificity has been tentatively attributed to the presence in the metallo-folded nanoparticles of multiple, compartmentalized local catalytic sites composed of $Cu(AEMA)_2$ complexes surrounded by an environment of methyl methacrylate repeat units allowing an optimum transition state stabilization for the preferred substrates. The specificity displayed by the metallo-folded SCNPs is very promising, and the preparation of other metallo-folded soft nano-objects (based on Pd, Ni, Co, Fe, Mn and Mo instead of Cu), as well as the study of their enzyme-mimic characteristics is anticipated.

4.6 References

[1] a) Marinescu, L.; Bols, M. *Curr. Org. Chem.,* **2010**, *14*, 1380. b) Bellia, F.; La Mendola, D.; Pedone, C.; Rizzarelli, E.; Saviano, M.; Vecchio, G. *Chem. Soc. Rev.*, **2009**, *38*, 2756. c) D'Souza, V. T. *Supramol. Chem.,* **2003**, *15*, 221. d) Breslow, R.; Dong, S. D. *Chem. Rev.,* **1998**, *98*, 1997.

[2] a) Rodionov, V.; Gao, H.; Scroggins, S.; Unruh, D. A.; Avestro, A.-J.; Frechet, J. M. J. *J. Am. Chem. Soc.,* **2010**, *132*, 2570. b) Terashima, T.; Ouchi, M.; Ando, T.; Sawamoto, M. *J. Polym. Sci. Part A: Polym. Chem.,* **2010**, *48*, 373. c) Dichtel, W. R.; Baek, K.-Y.; Frechet, J. M. J.; Rietveld, I. B.; Vinogradov, S. A. J. *Polym. Sci., Part A: Polym. Chem.,***2006**, *44*, 4939. d) Helms, B.; Guillaudeu, S. J.; Xie, Y.; McMurdo, M.; Hawker, C. J.; Frechet, J. M. J. *Angew. Chem. Int. Ed.,* **2005**, *44*, 6384.

[3] Kirkorian, K.; Ellis, A.; Twyman, L. J. *Chem. Soc. Rev.,* **2012**, *41*, 6138.

[4] Van de Vyver, S.; Thomas, J.; Geboers, J.; Keyzer, S.; Smet, M.; Dehaen, W.; Jacobs, P. A. ; Sels, B. F. *Energy Environ. Sci.,* **2011**, *4*, 3601.

[5] Pastor-Perez, L.; Kemmer-Jonas, U.; Wurm, F.; Stiriba, S.-E.; Perez-Prieto, J.; Frey, H. *Macromolecules.,* **2010**, *43*, 9583.

[6] a) Zhang, D.; Ren, C.; Yang, W.; Deng, J. *Macromol. Rapid Commun.,* **2012**, *33*, 652. b) Yamamoto, T.; Yamada, T.; Nagata, Y.; Suginome, M. *J. Am. Chem. Soc.,* **2010**, *132*, 7899. c) Terada, K.; Masuda, T.; Sanda, F. *J. Polym. Sci. Part A: Polym. Chem.,***2009**, *47*, 4971. d) Maeda, K.; Tanaka, K.; Morino, K.; Yashima, E. *Macromolecules.,* **2007**, *40*, 6783.

[7] Caminade, A. M.; Ouali, A.; Keller, M.; Majoral, J. P. *Chem. Soc. Rev.,* **2012**, *41*, 4113.

[8] Helms, B.; Frechet, J. M. J. *Adv. Synth. Catal.,* **2006**, *348*, 1125.

[9] Bosman, A. W.; Janssen, H. M.; Meijer, E. W. *Chem. Rev.,* **1999**, *99*, 1665.

[10] Lerner, R. A.; Benkovic, S. J.; Schultz, P. G. *Science.,* **1991**, *252*, 659.

[11] Schultz, P. G.; Lerner, R. A. *Science.,* **1995**, *269*, 1835.

[12] Wulff, G.; Chong, B.-O.; Kolb, U. *Angew. Chem. Int. Ed.,* **2006**, *45*, 2955.

[13] Wulff, G.; Chong, B.-O. *Acc. Chem. Res.*, **2012**, *45*, 239.

[14] Wei, H.; Wang, E. *Chem. Soc. Rev.,* **2013**, *42*, 6060.

[15] Wang, G.-J.; Fife, W. K. *Macromolecules.,* **1999**, *32*, 559-564. b) Wang, G.-J.; Fife, W. K. *J. Am. Chem. Soc.,* **1998**, *120*, 883.

[16] Altintas, O.; Barner-Kowollik, C. *Macromol. Rapid Commun.,* **2012**, *33*, 958.

[17] Sanchez-Sanchez, A.; Perez-Baena, I.; Pomposo, J. A. *Molecules.,* **2013**, *18*, 3339.

[18] Sanchez-Sanchez, A.; Pomposo, J. A. *Part. Part. Syst. Charact*., **2014**, *31*, 11.

[19] Sanchez-Sanchez, A.; Akbari, S.; Etxeberria, A.; Arbe, A.; Gasser, U.; Moreno, A. J.; Colmenero, J.; Pomposo, J. A. *ACS Macro Lett.,* **2013**, *2*, 491.

[20] Sanchez-Sanchez, A.; Akbari, S.; Moreno, A. J.; Lo Verso, F.;Arbe, A.; Colmenero, J.; Pomposo, J. A. *Macromol. Rapid Commun*., **2013**, *34*, 1681.

[21] Huerta, E.; Stals, P. J. M.; Meijer, E. W.; Palmans, A. R. A. *Angew. Chem. Int. Ed.,* **2013**, *52*, 2906.

[22] Terashima, T.; Mes, T.; De Greef, T. F. A.; Gillissen, M. A. J.; Besenius, P.; Palmans, A. R. A.; Meijer, E. W. *J. Am. Chem. Soc.,* **2011**, *133*, 4742.

[23] Perez-Baena, I.; Barroso-Bujans, F.; Gasser, U.; Arbe, A.; Moreno, A. J.; Colmenero, J.; Pomposo, J. A. *ACS Macro Lett.,* **2013**, *2*, 775.

[24] a) Sanchez-Sanchez, A.; Fulton, D. A.; Pomposo, J. A. *Chem. Comm.,* **2014**, *50*, 1871. b) Whitaker, D. E.; Mahon, C. S.; Fulton, D. A. *Angew. Chem. Int. Ed.,* **2013**, *52*, 956. c) Tuten, B. T.; Chao, D.; Lyon, C. K.; Berda, E. B. *Polym. Chem.,* **2012**, *3*, 3068. d) Pomposo, J. A.; Perez-Baena, I.; Buruaga, L.; Alegria, A.; Moreno, A. J.; Colmenero, J. *Macromolecules.,* **2011**, *44*, 8644. e) Harth, E.; Horn, B. V.; Lee, V. Y.; Germack, D. S.; Gonzales, C. P.; Miller, R. D.; Hawker, C. J. *J. Am. Chem. Soc.,* **2002**, *124*, 8653.

[25] T. Nasuno, T. Takano, H. Kamitakahara, F. Nakatsubo, *Holzforschung*., **2006**, *60*, 2.

[26] Arranz, F.; Sánchez-Chaves M.; Jarrín, C. M. *Angew. Makromol. Chem*., **1986**, *143*, 101.

[27] Arranz, F.; Sánchez-Chaves, M.; Riofrio, A. *Makromol. Chem*., **1986** , *187*, 259.

[28] J. He, L. Tremblay, S. Lacelle and Y. Zhao, *Soft Matter*., **2011**, *7*, 2380.

[29] Sanchez-Sanchez, A.; Asenjo-Sanz, I.; Buruaga, L.; Pomposo, J.A. *Macromol. Rapid Commun*. **2012**, *33*, 1262.

[30] P. Bernado; D. I. Svergun, *Mol. BioSyst.,* **2012**, *8*, 2955.

[31] Rubinstein, M.; Colby, R. H. *Polymer Physics*; Oxford University Press: New York, **2003**.

[32] Mavila, S.; Diesendruck, C. E.; Linde, S.; Amir, L.; Shikler, R.; Lemcoff, N. G. *Angew. Chem. Int. Ed.,* **2013**, *52*, 5767.

[33] Xiao W.; Xie K.; Guo Q.; Wang E.G.; *J. Phys.: Condens. Matter.* **2003**, *15*, 1155.

[34] Kumar R.S; Kumar S. S; Kulandainathan M. A.; *Micropor. Mesopor. Mat.,* **2013**, *168*, 57.

[35] Cioffi, N.; Torsi, L.; Ditaranto, N.; Tantillo, G.; Ghibelli, L.; Sabbatini, L.; Bleve-Zacheo, T.; D'Alessio, M.; Zambonin, P.G.; Traversa, E.. *Chem. Mater.*, **2005**, *17*, 5255.

[36] a) Wang, D.; Li, J.; Li, N.; Gao, T.; Hou, S.; Chen, B. *Green Chem.,* **2010**, *12*, 45. b) Although 6 h of reaction time was reported as optimum reaction time, we found increased yields by extending the reaction time to 8 h.

[37] a) Mukai, M.; Kogiso, M.; Aoyagi, M.; Asakawa, M.; Shimizu, T.; Minamikawa, H. *Polym. J.,* **2012**, *44*, 646. b) Jahnke, E.; Millerioux, A.-S.; Severin, N.; Rabe, J. P.; Frauenrath, H. *Macromol. Biosci.,* **2007**, *7*, 136. c) Lindsell, W. E.; Preston, P. N.; Seddon, J. M.; Rosair, G. M.; Woodman, T. A. J. *Chem. Mater.,* **2000**, *12*, 1572.

[38] a) Jahnke, E.; Lieberwirth, I.; Severin, N.; Rabe, J. P. Frauenrath, H. *Angew. Chem. Int. Ed.,* **2006**, *45*, 5383. b) Martin, R. E.; Diederich, F. *Angew. Chem. Int. Ed.,* **1999**, *38,* 1350.

[39] a) Shun, A. L. K. S.; Tykwinski, R. R. *Angew. Chem. Int. Ed.,* **2006**, *45,* 1034. b) Shun, A. L. K. S.; Tykwinski, R. R. *J. Org. Chem.,* **2003**, *68*, 6810. c) DeCicco, R. C.; Black, A.; Li, L.; Goroff, N. S. *Eur. J. Org. Chem.,* **2012**, *25*, 4699. d) Eastmond, R.; Johnson, T. R.; Walton, D. R. M. *Tetrahedron.,* **1972**, *28*, 4601.

[40] a) Jin, H. R.; Zhao, J.; Zhang, Z.; Liao, Y.; Wang, C. Z.; Huang, W. H.; Li, S. P.; He, T. C.; Yuan, C. S.; Du, W. *Cell Death Dis.,* **2012**, *3*, e376. b) Dembitsky, V.

M. *Lipids.,* **2006**, *41*, 883. c) Setzer, W. N.; Gu, X.; Wells, E. B.; Setzer, M. C.; Moriarity, D. M. *Chem. Pharm. Bull.,* **2000**, *48*, 1776.

[41] Lever, A. B. P. *Inorganic Electronic Spectroscopy.,* 2nd Ed.; Elsevier: Amsterdam, **1984**; pp 553-572 and 636-638.

APPENDIX

A) Spectral data of the 1,3-diynes synthesized in this work.

Hexa-2,4-diyne-1,6-diyl diacetate (2b) [Zhang S. *et al. Adv. Synth. Catal*. **2011**, *353*, 1463]

^{1}H NMR (400 MHz, $CDCl_3$): δ (ppm) = 4.74 (s, 4H), 2.11 (s, 6H).

IR (KBr): 2139, 1723, 1438,1370, 890 cm^{-1}.

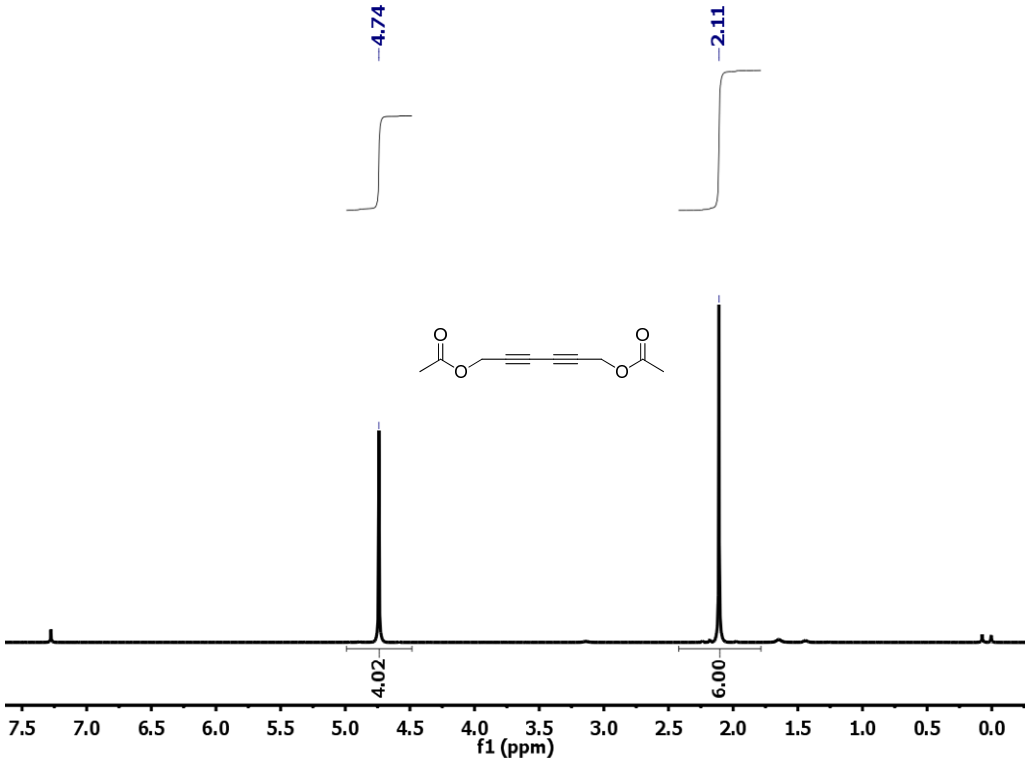

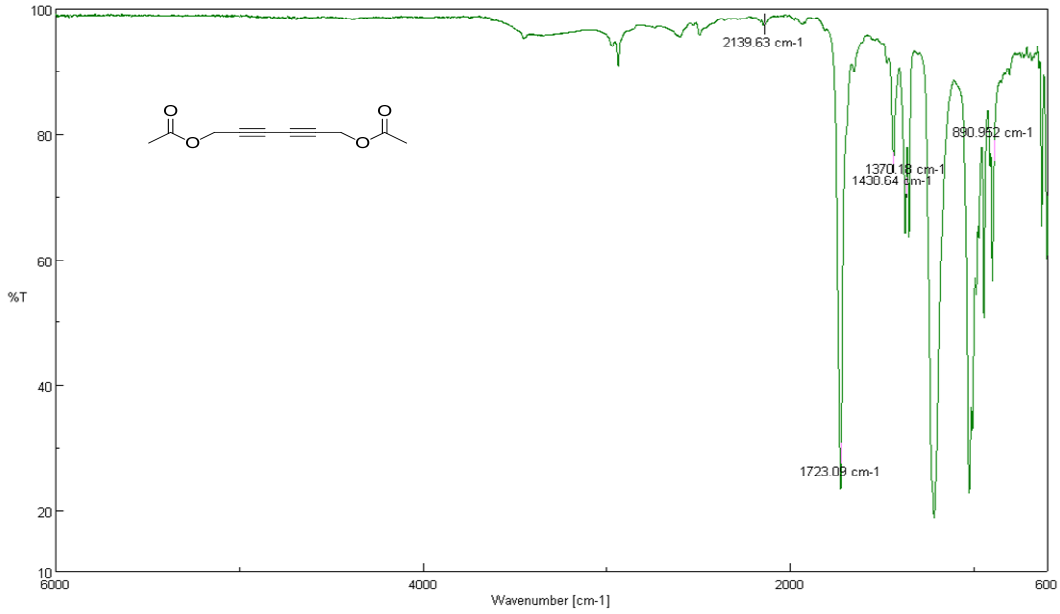

Hexadeca-7,9-diyne-6,11-diol (3b) [Setzer W. N. *et al. Chem. Pharm. Bull*. **2000**, *48*, 1776]

^{1}H NMR (400 MHz, $CDCl_3$) : δ (ppm) = 4.37 (m, 2H), 1.87 (s, 2H of hydroxyl), 1.67 (m, 4H), 1.38 (m, 4H),1.25 (m, 8H), 0.84 (t, 6H).

IR (KBr): 3368 (O-H Str), 2934, 2155, 1461, 1386, 1026, 657 cm^{-1}.

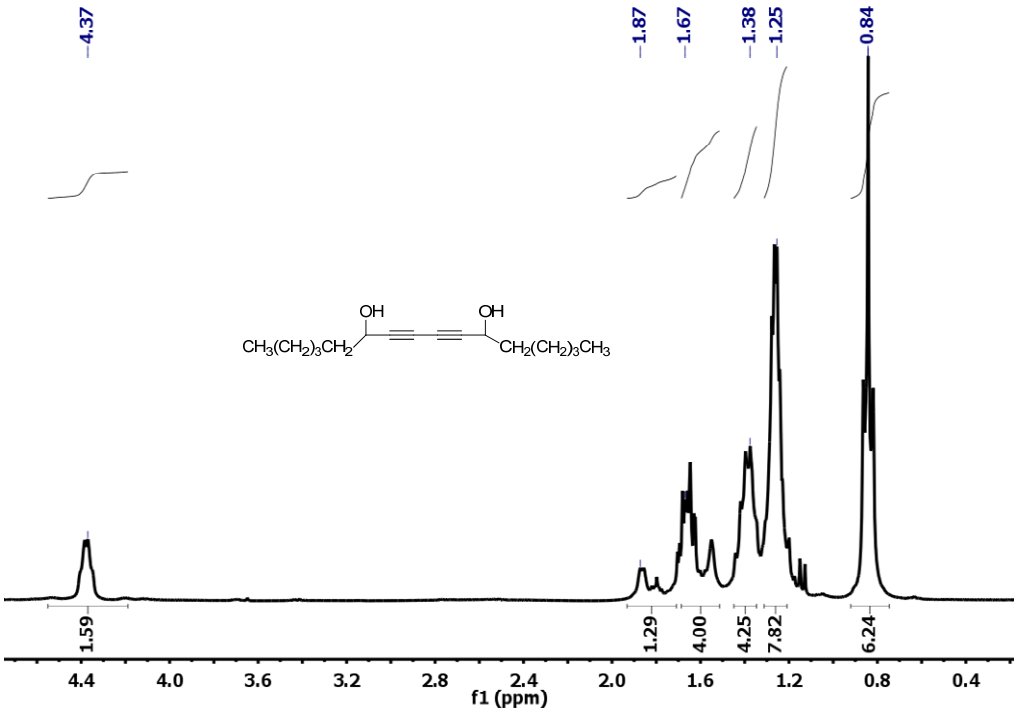

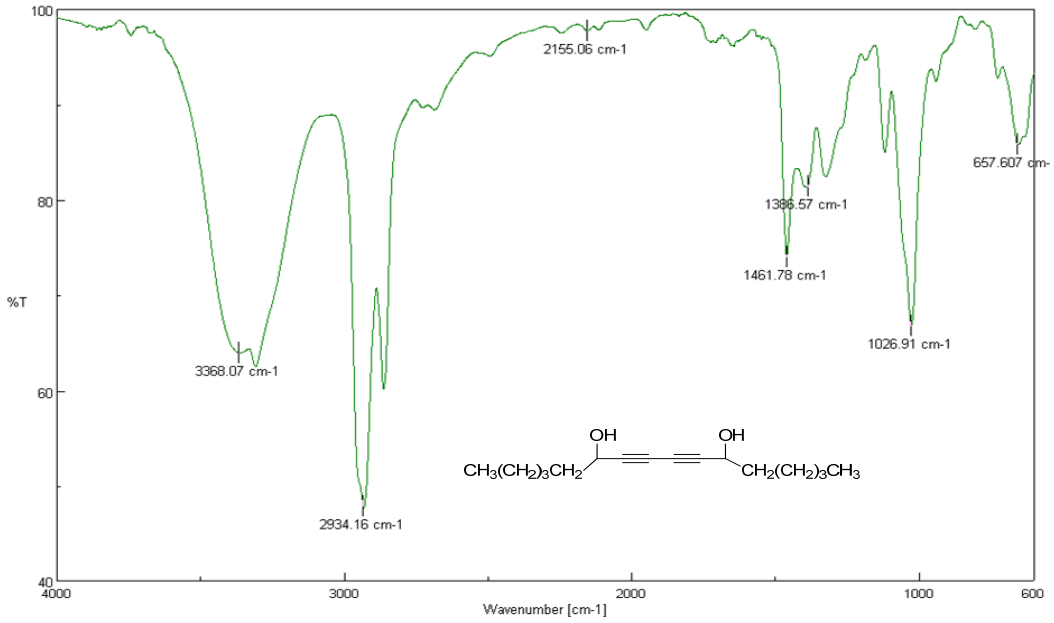

2,6-Hexadiyne-1,6-diol,1,6-dibenzoate (4b) [Xu R. *et al. J. Am. Chem. Soc.* **2006**, *128*, 5541]

^{1}H NMR (400 MHz, $CDCl_3$) : δ (ppm) = 8.08 (m, 4H), 7.58 (m, 2H), 7.45 (m, 4H), 4.93 (s, 4H).

IR (KBr): 2938, 2139, 1718, 1446, 1425, 1063, 702 cm^{-1}.

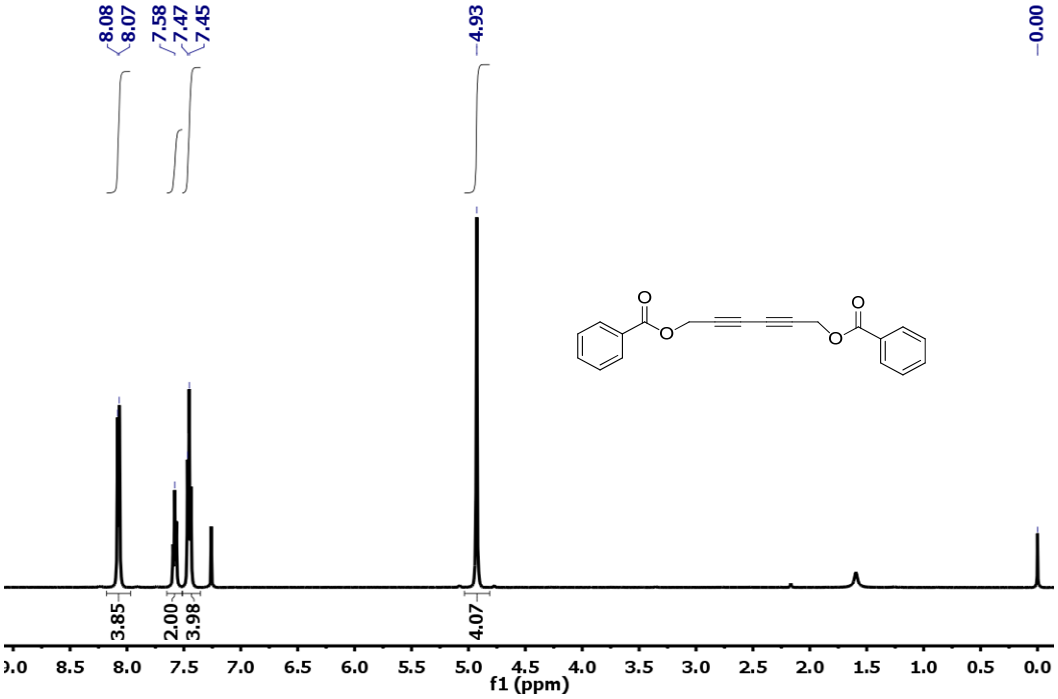

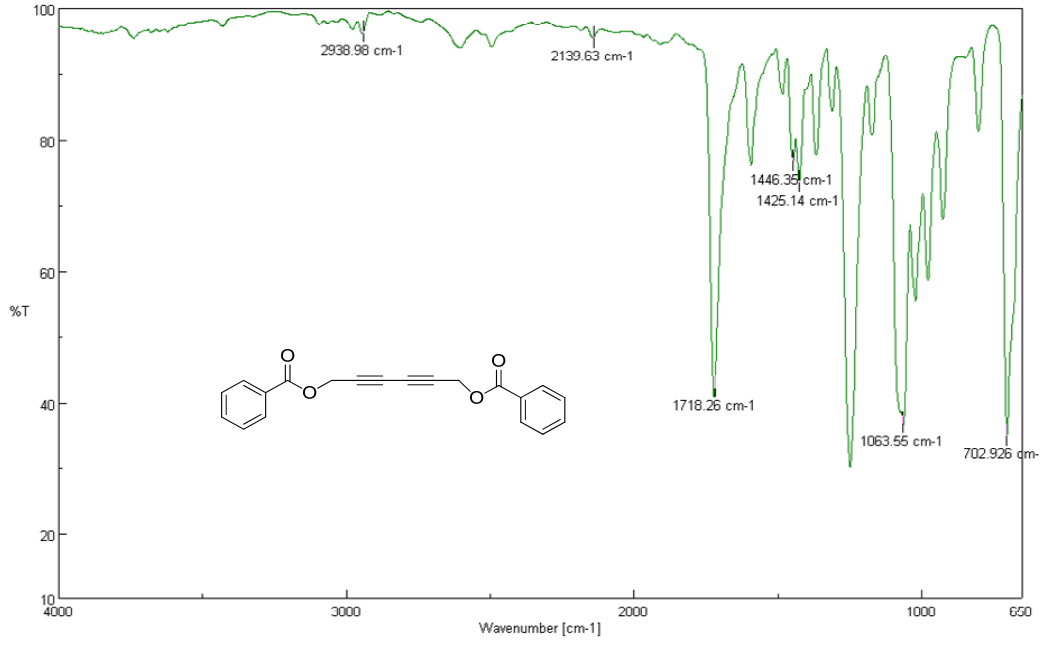

1,6-dicyclohexylhexa-2,4-diyne (5b) [Chen *Z. et al. J. Org. Chem*. **2010**, *75*, 6700]

^{1}H NMR (400 MHz, $CDCl_3$) : δ (ppm) = 2.11 (m, 4H), 1.75 (m, 4H), 1.67 (m, 4H),1.63 (m, 2H), 1.45 (m, 2H), 1.20 (m, 6H), 0.97 (m, 4H).

IR (KBr): 2919, 2853, 2156, 1453, 1369, 1309 cm^{-1}.

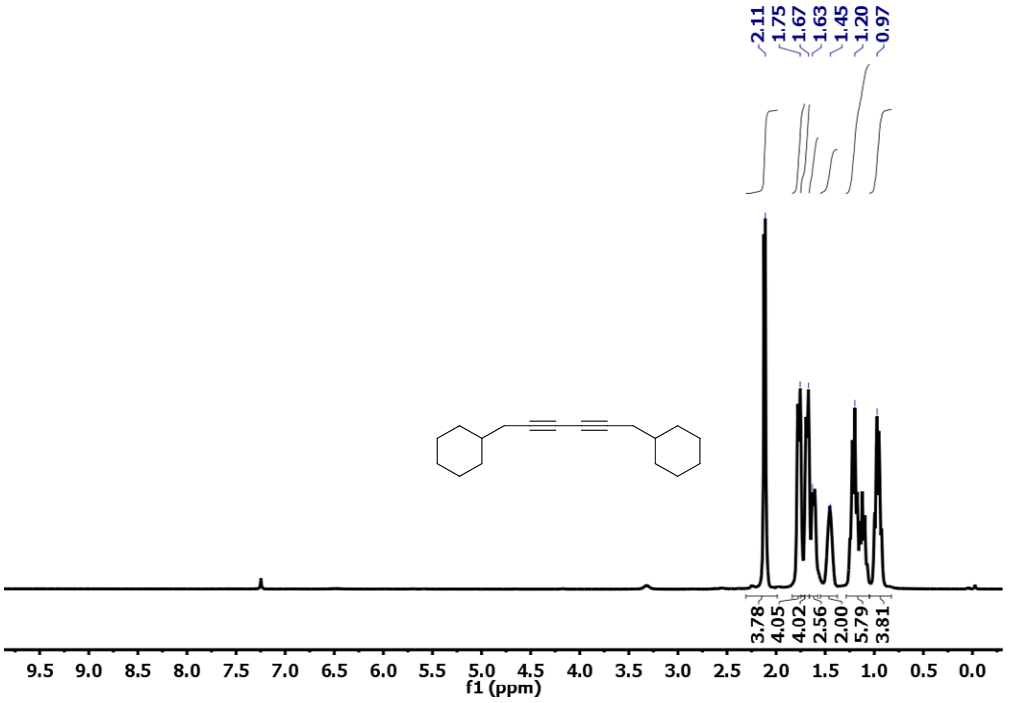

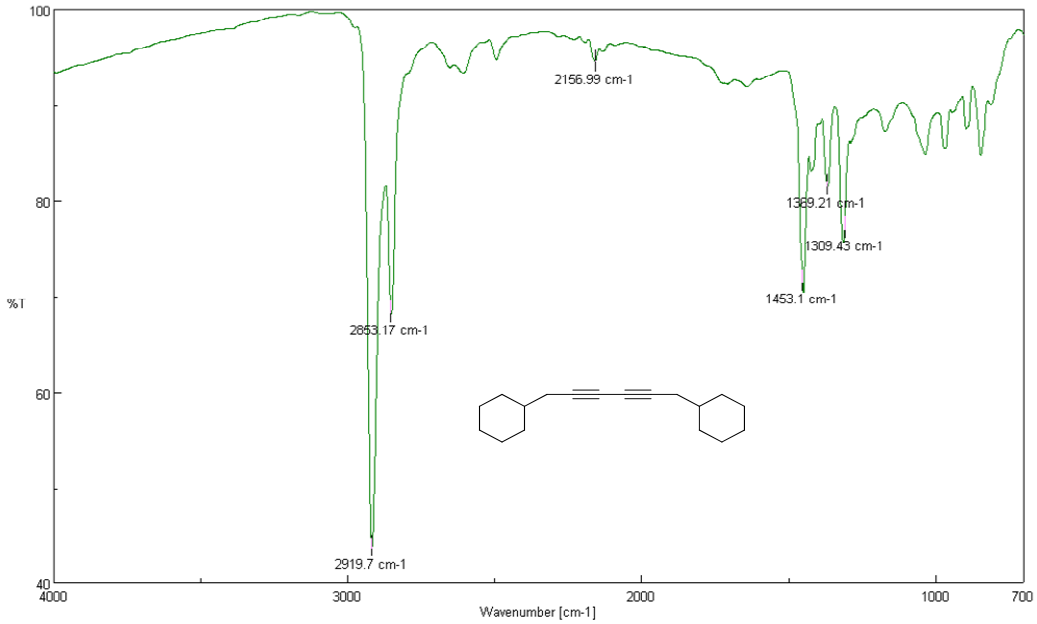

Hexa-2,4-diyne-1,6-diyl dipropionate (6b)[Makhsumov A. G. *et al. Uzbekskii K. Zhurnal.* **1985**, *1*, 36]

^{1}H NMR (400 MHz, $CDCl_3$) : δ (ppm) = 4.76 (s, 4H), 2.41 (m, 4H), 1.18 (m, 6H).

IR (KBr): 2980, 2155, 1749, 1457, 1428,1163 cm^{-1}.

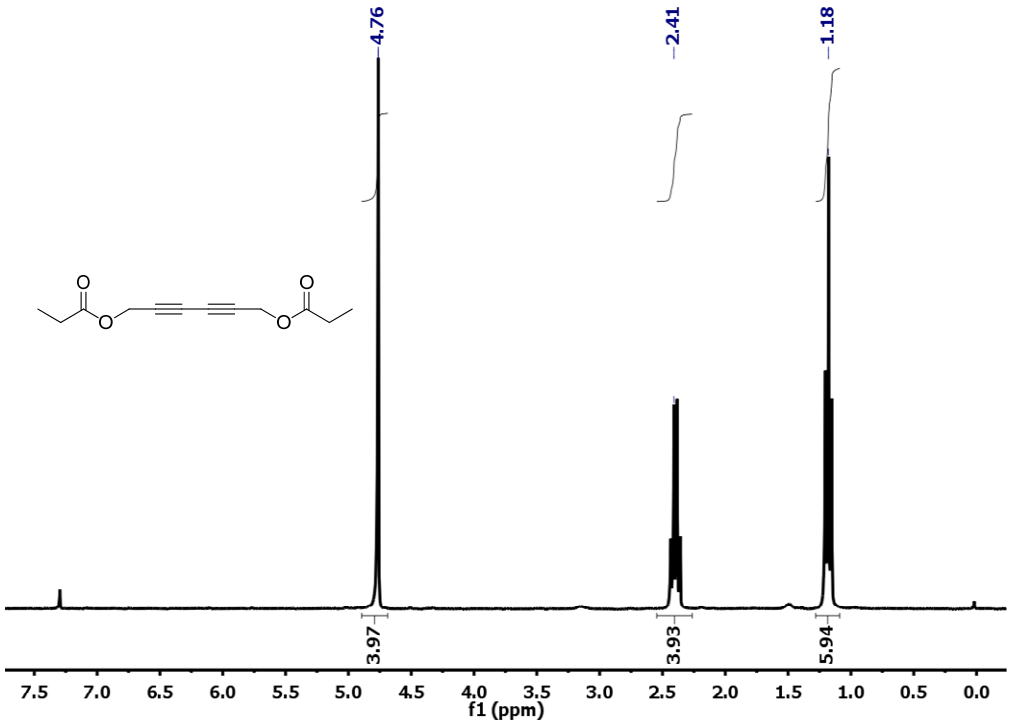

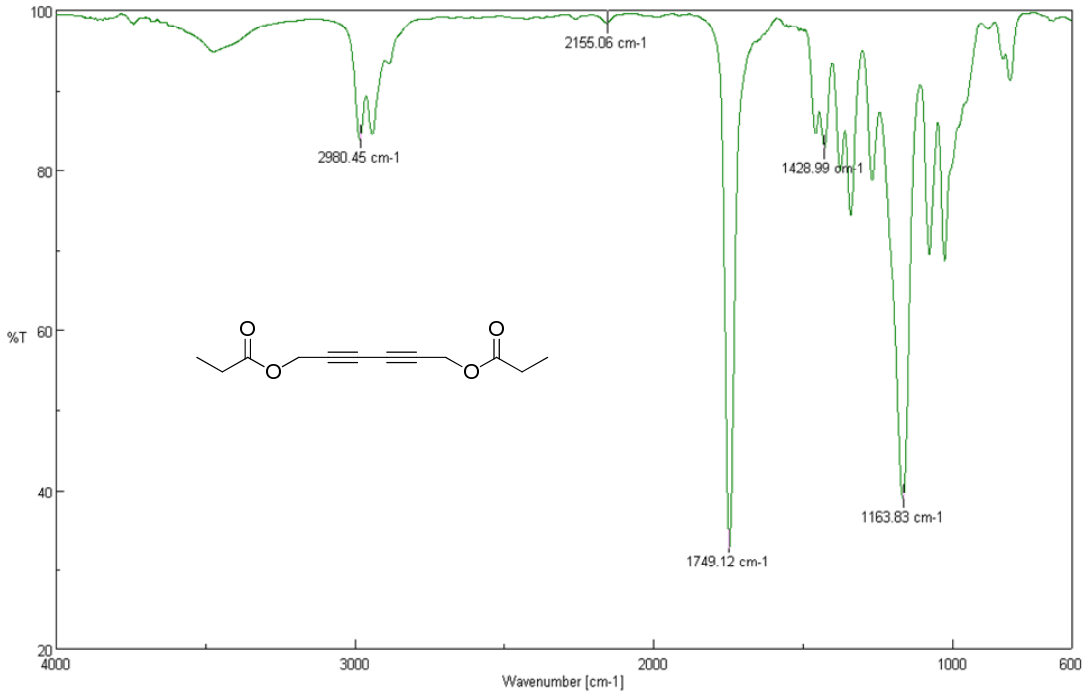

Hexa-2,4-diyne-1,6-diyl diacrylate (7b)

^{1}H NMR (400 MHz, $CDCl_3$): δ (ppm) = 6.47 (d, 2H), 6.19 (m, 2H), 5.94 (d, 2H), 4.79 (s,4H).

IR (KBr): 2272, 1749, 1378, 1217, 1163, 1030 cm^{-1}.

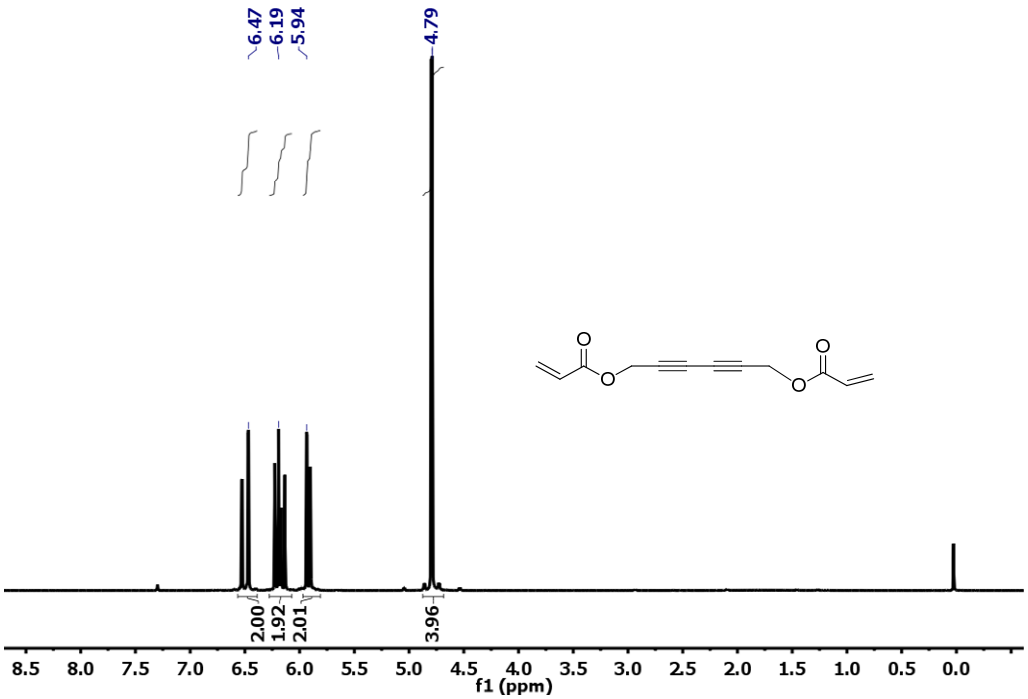

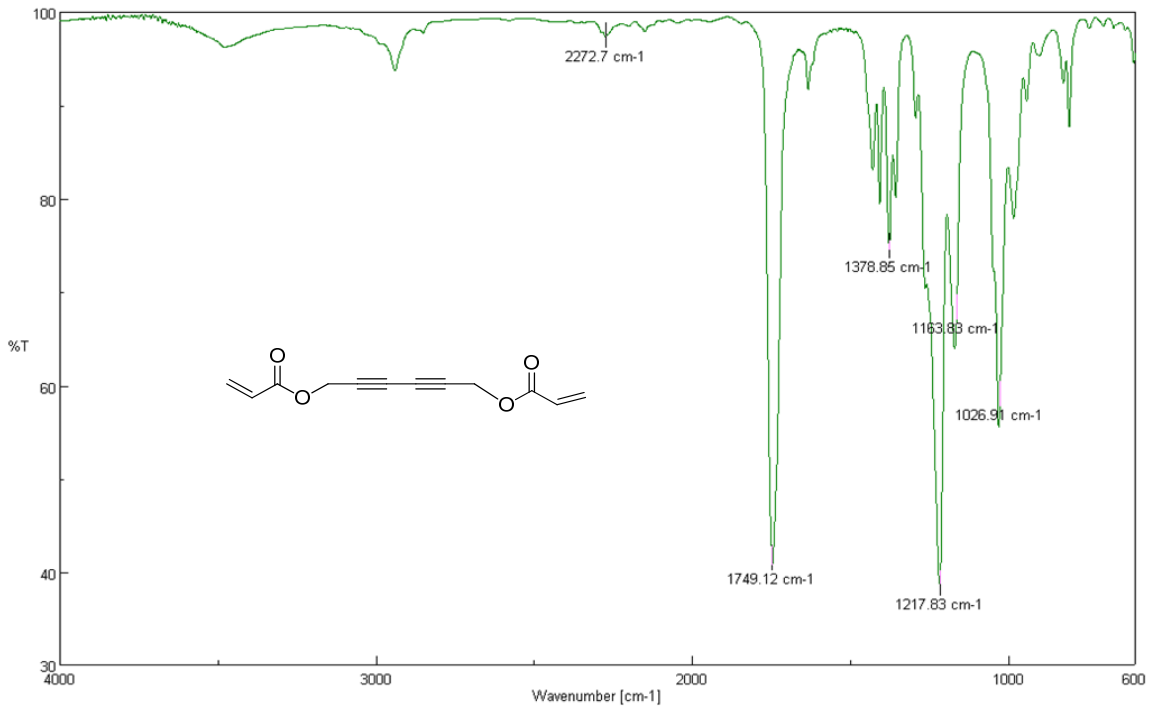

1,6-Diphenoxyhexa-2,4-diyne (9b)[Feng X. *et al. J. Organomet. Chem.* **2011**, *696*,1479]

^{1}H NMR (400 MHz, $CDCl_3$) : δ (ppm) = 7.3 and 6.99 (m, 10H), 4.65 (s, 4H).

IR (KBr): 1745, 1601, 1213, 1034, 754 cm^{-1}.

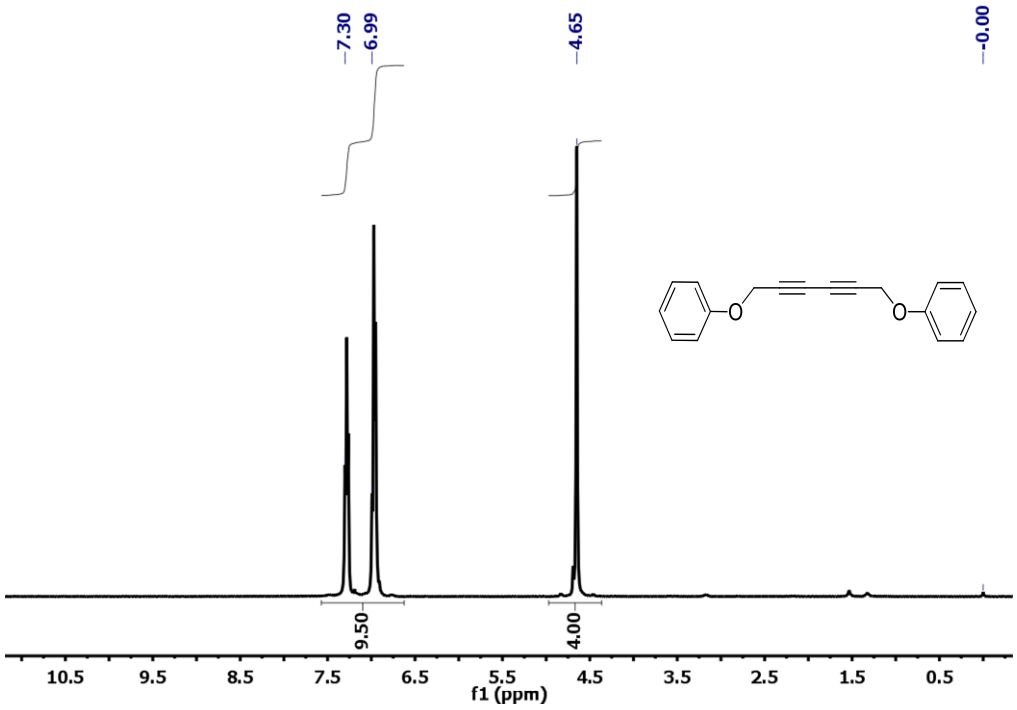

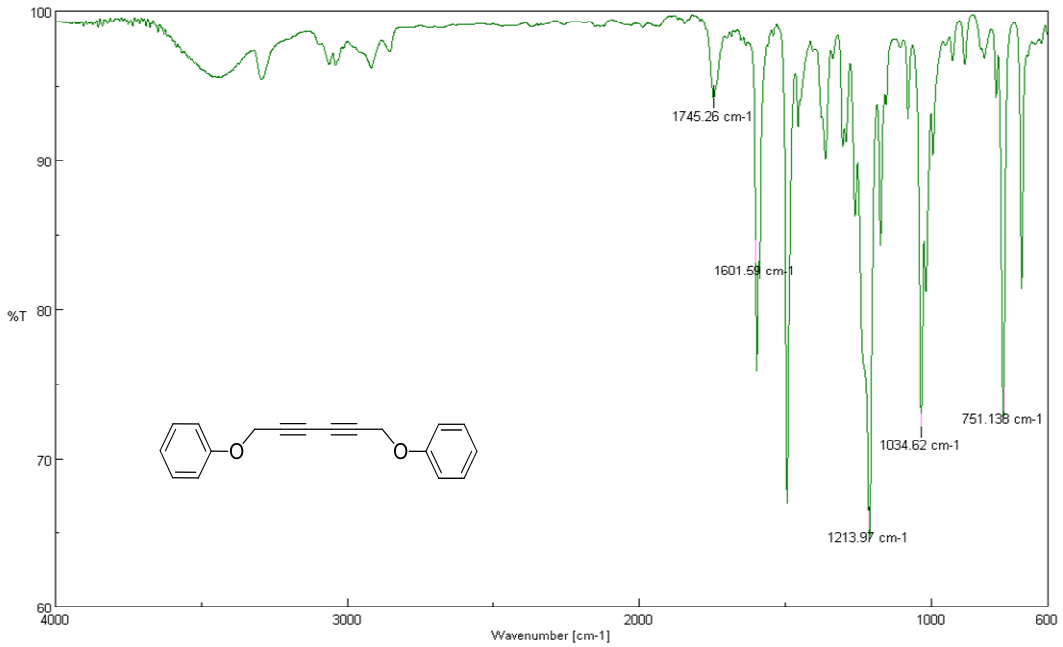

CHAPTER 5:

pH-responsive single-chain polymer nanoparticles utilising dynamic covalent enamine bonds

5.1 Introduction

Interest in dynamic covalent bonds (DCB)[1-3] that can be reversibly cleaved and reformed upon exposure to an external stimulus has grown significantly in recent years. In fact, emerging applications in materials, biomedicine, and nanosciences demand new polymeric materials which possess the capacity to adapt or undergo a macroscopic response to changes in their environments.[4] The incorporation of DCBs into polymeric systems (*e.g.*, micelles, films, fibers) allows access to dynamic structures which can respond macroscopically to a range of external stimuli (*e.g.*, temperature, pH, redox processes)[5-8]. The added value of DCBs is their capacity to undergo component exchange processes, which can present polymeric species with opportunities to adapt their constitutions by reorganizing components, and thus change their properties.[5]

The first example of dynamic covalent chemistry applied to single-chain polymer nanoparticle (SCNP) synthesis, was published by Fulton and Murray in 2011[9] exploiting the dynamic nature of hydrazone bonds (see Scheme 5.1). Linear poly(vinylbenzaldehyde) chains were decorated by reaction of their aldehyde units with monoacyl hydrazides and were then collapsed progressively to SCNPs simply through exchange reactions with bis-hydrazide crosslinkers, demonstrating for the first time the ability to adapt the architecture of a single polymer chain through dynamic covalent chemistry. In 2012, Berda and co-workers[10] demonstrated the utility of disulfide bridges in the fabrication of dynamic covalent bonded single-chain polymer nanoparticles that can reversibly undergo a coil to particle transition (see Scheme 5.2). The redox-responsiveness of the disulfide bond was used by these authors to fabricate a reversible diasassembly/asassembly system where the structure of the polymer could be reorganized from single-chain nanoparticles to individual polymer coils by changing the environment (from reductive/to oxidative) of the polymer.

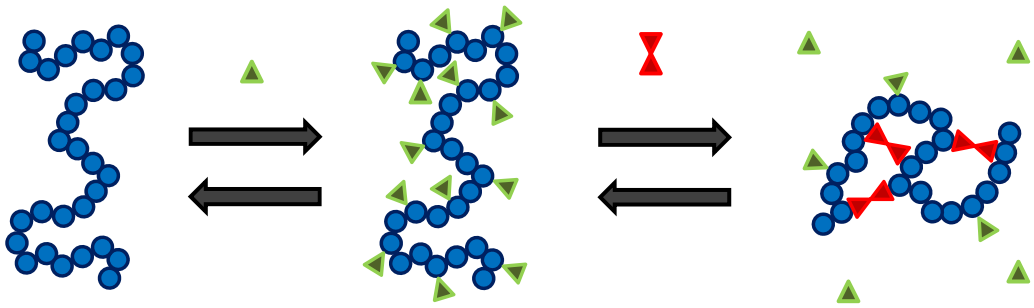

Scheme 5.1. By exploiting the dynamic nature of hydrazone bonds, linear poly(vinylbenzaldehyde) chains were decorated by reaction of their aldehyde units with monoacyl hydrazides (green symbols) and then intramolecularly cross-linked to single-chain nanoparticles through exchange reactions with a bis-hydrazide cross-linker (red symbols) at high dilution.[9]

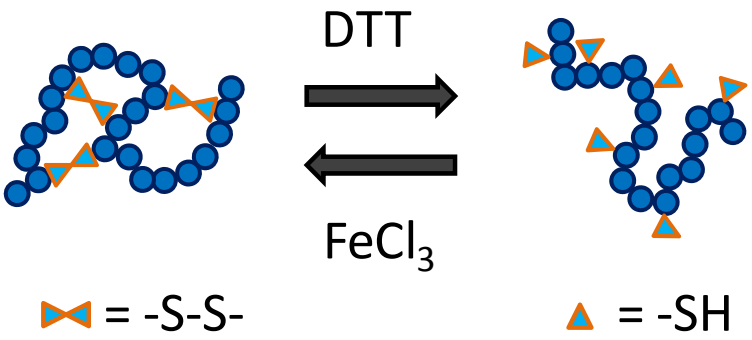

Scheme 5.2. Reversible SCNPs cross-linked with disulfide bonds can be disassembled to linear chains by reductive cleavage with dithiothreitol (DTT) and re-assembled to unimolecular nanoparticles by oxidation with iron (III) chloride ($FeCl_3$) under high dilution conditions.[10]

However, only a relatively small number of dynamic covalent bonds (*e.g.* imine, alkoxylamine, disulfide and hydrazone) have been utilized in the construction of dynamic polymeric materials[11-16], and to expand further their utilisation there exists a need for a greater selection of dynamic bonds. One potential dynamic covalent bond is the enamine bond. The enamine bond[17-19] belongs to the family of imine and hydrazone DCBs[18-20], however, to the best of our knowledge, it has not yet been employed for the development of structurally dynamic polymeric systems. The enamine bond can be formed through the crosslinking reaction between an acetoacetoxy group and an amine group.[21-25] Two routes of reaction can be identified because of the keto/enol tautomerization of the acetoacetoxy group.[21] Nevertheless, both routes result in the same product: an enamine (see Scheme 5.3). Moreover, the enamine bond

can potentially undergo different dynamic processes, hence displaying i) the possibility to reversibly cleave and reform under appropriate conditions, and ii) the ability to undergo component exchange. Both of these processes operate under thermodynamic control. A particular advantage of enamine DCBs is that a carbonyl reaction partner can be readily incorporated into polymer chains as the monomer 2-(acetoacetoxy) ethyl methacrylate—which displays a suitably reactive carbonyl function—is commercially available. This availability circumvents the need to synthesize designer monomers possessing reactive carbonyl groups, consequently making the incorporation of DCBs within dynamic polymer systems less time- and labour-consuming.

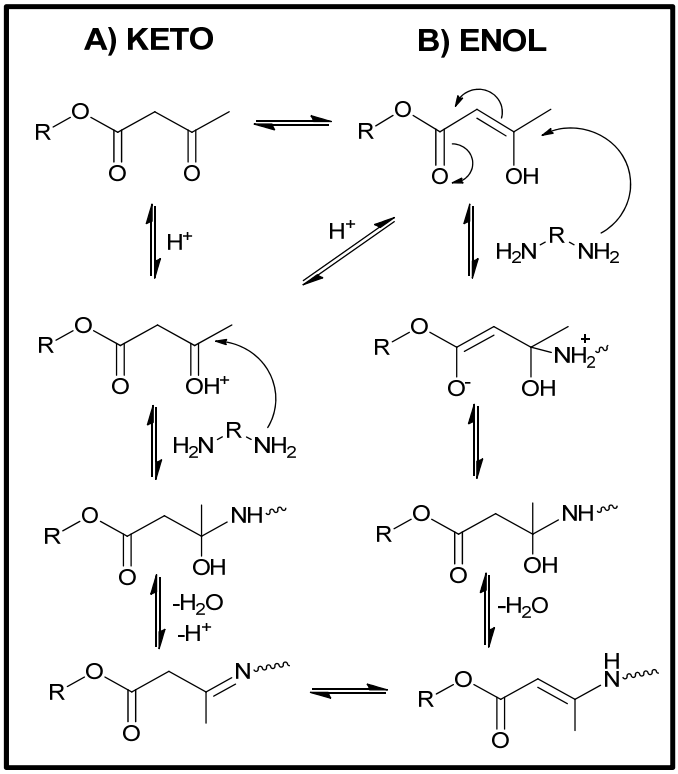

Scheme 5. 3. Crosslinking reaction of acecoacetoxy group with a generic diamine at r.t. Two reaction routes are identified. **A)** Starting from keto form. **B)** Starting from enol form.

5.2 Objectives

To demonstrate the utility of dynamic covalent enamine bonds in the preparation of responsive polymer materials, we report in this Chapter their utilisation to prepare pH-responsive single-chain polymer nanoparticles (SCNPs). As stated previously, SCNPs constitute a class of polymeric materials of intense current interest in which single linear polymer chains are intramolecularly cross-linked into ultra-small soft nano-objects[26-27] which show intriguing nanoscale properties and are of great interest for numerous potential applications[28-35] including their use as elastomeric polymers, nanocomposites and paints. The introduction of responsiveness into SCNPs through the use of DCBs[9-10] provides soft nano-objects with structurally dynamic properties which increase their potential utilisation as so-called 'smart' materials which may find application in nanomedicine, catalysis and the development of dynamic combinatorial libraries.[36, 37]

As explained above, pH-responsive SCNPs will be synthesized using dynamic covalent enamine bonds. The SCNPs precursors used in this work are P(MMA-*co*-AEMA) copolymers, previously described in Chapter 3. These, P(MMA-*co*-AEMA) copolymers were functionalized with an alkyl amine moiety and as will be demonstrated, these functionalized copolymers do undergo a component exchange process (in this case between *mono*-enamine and *bis*-enamine) leading to SCNPs. Afterwards, these SCNPs will be able to reversibly undergo a coil to particle transition *via* formation and cleavage of intramolecular dynamic enamine cross-links (Scheme 5.4).

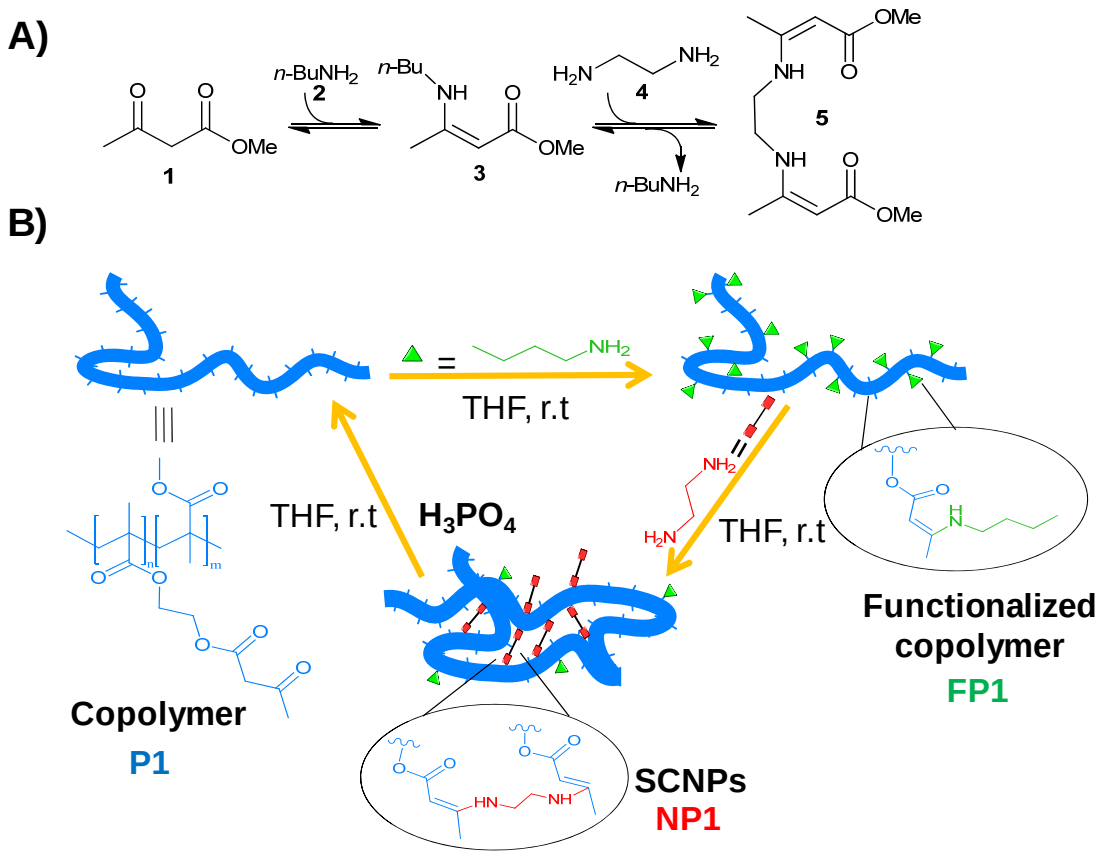

Scheme 5.4. A) The formation of an enamine **3** from the condensation of methyl acetoacetate (**1**) and *n*-butylamine (**2**), and its component exchange reaction with ethylenediamine (**4**) to form a *bis*-enamine (**5**). **B)** Schematic illustration of assembly / disassembly of SCNPs by means of dynamic covalent enamine bonds.

5.3 Experimental Section

In order to better understand the dynamic nature of the enamine bond some reactions with low molecular weight model compounds were first carried out.

a) Model reactions with low molecular weight model compounds.

In a typical procedure, methyl acetoacetate **(1)** (15 mg, 0.13 mmol) and butylamine **(2)** (9.5 mg, 0.13 mmol) were dissolved in deuterated chloroform (1 ml). The solution was left to stir for 24 h at r.t. After 24 h the ^{1}H NMR spectroscopy revealed signals associated to the enamine bond of (*E,Z*)-methyl 3-(butylamino)but-2-enoate **(3)** (see Scheme 5.5 A). Component exchange was induced by the addition of ethylenediamine (**4**) (3.9 mg, 0.065 mmol) to the

reaction mixture. The ^{1}H NMR spectrum revealed the formation of mono- (**5b**) and bis-enamines (**5a**) (see Scheme 5.5 B).

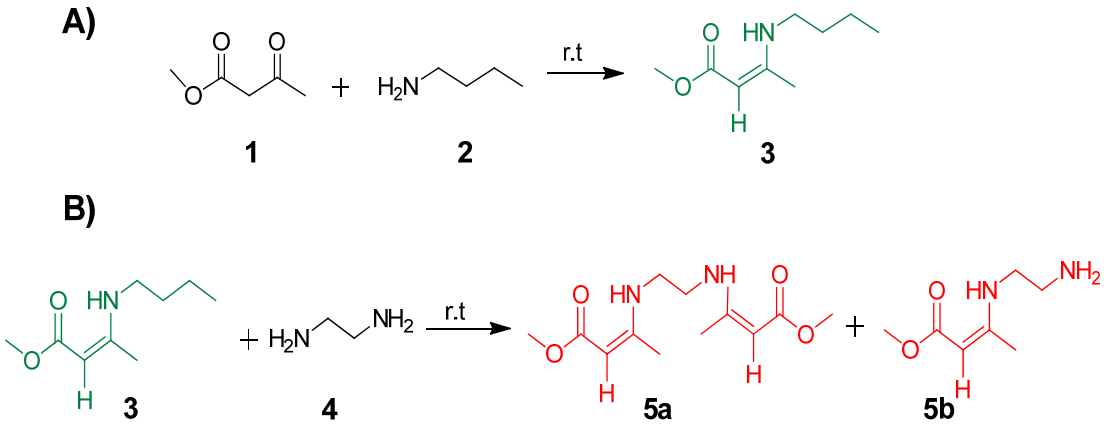

Scheme 5.5. A) The formation of an enamine with methyl acetoacetate (**1**) and butylamine (**2**) and **B)** its component exchange reaction with ethylenediamine (**4**) driving the formation of *mono*- and *bis*- enamine (**5a, 5b**).

b) Synthesis of P(MMA-*co*-AEMA) copolymers P1-P4.

Before copolymerization methyl methacrylate (**MMA**) was purified by distillation and 2-(acetoacetoxy) ethyl methacrylate (**AEMA**) was purified by passing through basic alumina**.** Normally**, MMA** (1 ml, 9.4 mmol), **AEMA** (0.6 ml, 3.1 mmol), 2-cyanoprop-2-yl-dithiobenzoate, (CPDB, 7.2 mg, 3.25×10^{-2} mmol) and 2, 2-azobis(2-methylpropionitrile), (AIBN, 0.8 mg, 4.9×10^{-3} mmol) were dissolved in ethyl acetate (3.2 ml). The reaction mixture was degassed by passing argon for 15 min. The copolymerization reaction was carried out at 65 ^{o}C for 18 h. The resulting P(MMA-*co*-AEMA) copolymer, **P1,** was isolated by precipitation in methanol and further drying (68% yield). The **AEMA** content in copolymer **P1,** was 31 mol% determined by ^{1}H NMR. The weight average molecular weight for **P1**, M_w: 30.9 kDa, polydispersity index, M_w / M_n: 1.05. The main characteristics of copolymers **P1-P4** are summarized in Table 5.2.

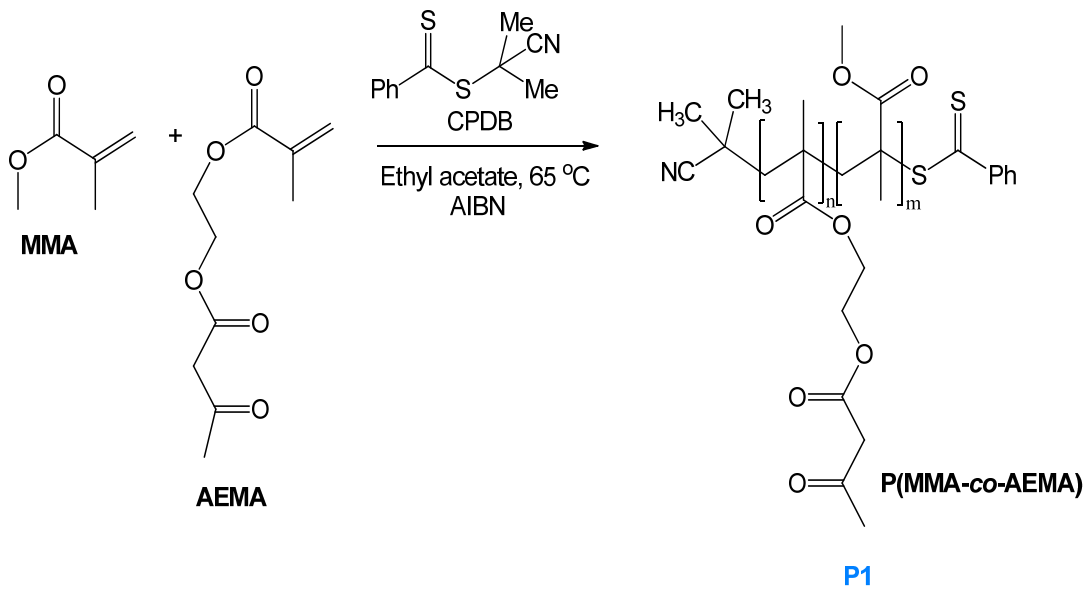

Scheme 5.6. RAFT copolymerization of **MMA** and **AEMA**.

c) Synthesis of alkyl amine-funcionalized P(MMA-*co*-AEMA) copolymers FP1-FP4.

Typically, P(MMA-*co*-AEMA) copolymer **P1** (100 mg, 0.3 mmol) and alkyl amine (butylamine, **2**: 0.04 ml, 0.6 mmol or hexylamine, **6**: 0.06 ml, 0.6 mmol) were dissolved in THF (30 ml) (see Scheme 5.7). The solution was left to stir for 24 h at r.t, concentrated under reduced pressure and precipitated by its drop-wise addition to hexane and then isolated by filtration. The main characteristics of functionalized copolymers **FP1-FP4** are summarized in Table 5.3.

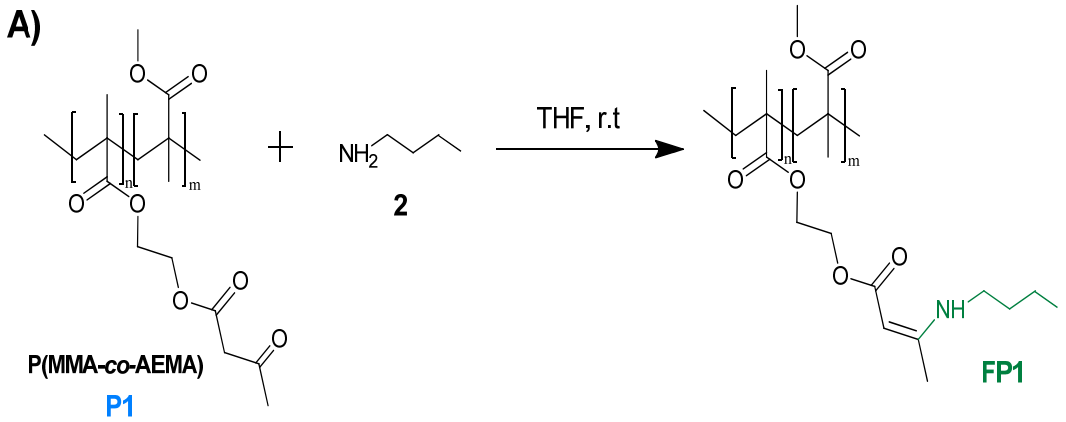

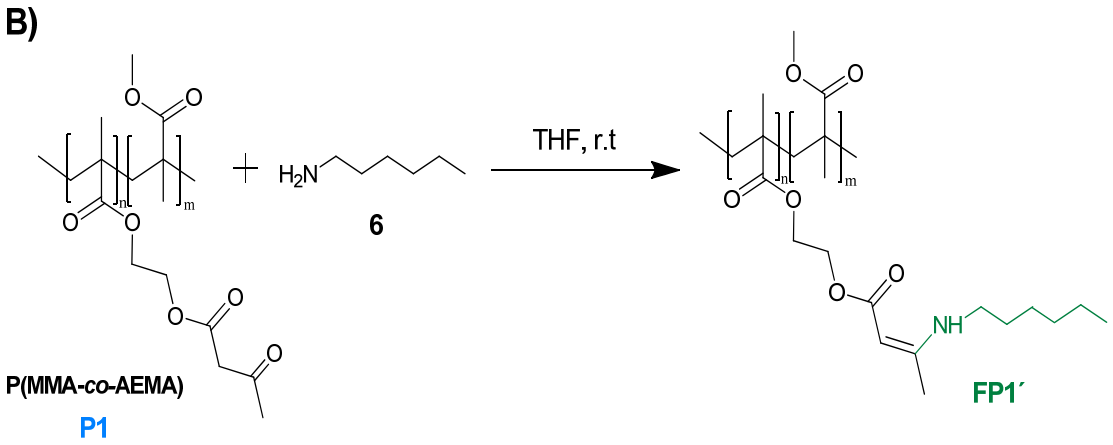

Scheme 5.7. P(MMA-*co*-AEMA) copolymer **P1,** functionalized *via* enamine formation with alkyl amine (**A:** with butylamine (**2**), **B:** with hexylamine(**6**)).

d) Synthesis of single-chain polymer nanoparticles (SCNPs) NP1-NP4.

In a round-bottom flask, alkyl amine-functionalized copolymer **FP1** (50 mg, 0.11 mmol) and cross-linker (ethylenediamine, **4**: 3.4 mg, 0.055 mmol) were dissolved in THF (50 ml) at room temperature (see Scheme 5.8). The progressive folding/collapse process was followed through simultaneous SEC/MALLS measurements. After reaction completion (24 h), the mixture was concentrated and SCNPs were isolated by precipitation in diethyl ether and further drying. The yield of the reaction for **NP1** was 79% determined by gravimetric measurements. The main characteristics of SCNPs **NP1-NP4** are summarized in Table 5.2.

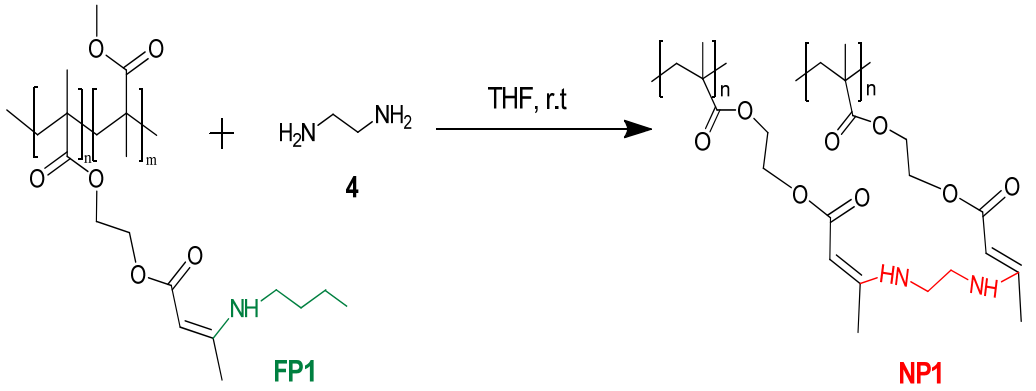

Scheme 5.8. Single-chain nanoparticle formation (**NP1**) from functionalized P(MMA-*co*-AEMA) copolymer **FP1,** *via* enamine formation.

e) Acid-triggered disassembly of SCNPs NP1-NP4.

NP1 (50 mg, 0.11 mmol) and phosphoric acid (H_3PO_4, an excess with respect to the **AEMA** content in **P1**) were dissolved in THF (50 ml) at room temperature. The unfolding process was followed as a function of pH and reaction time (see Table 5.1) through simultaneous SEC/MALLS measurements. After reaction completion, the mixture was concentrated and copolymer **P1´** was isolated by precipitation in distillated water and further drying (85% yield).

Table 5.1. Disassembly degree as a function of pH and reaction time.

pH	Reaction time (h)	Disassembly degree[a]
2-4	10	100 %
5	16	100 %
6	24	40 %

[a]Disassembly degree as determined from SEC retention times according to:

$$\textbf{Dissasembly degree (\%)} = (t_f - t_R) \,/\, (t_f - t_0) \times 100$$

t_0 = Retention time of the precursor.

t_f = Retention time of the SCNP.

t_R = Retention time of the SCNP after acidic treatment.

f) Re-assembly of SCNP NP1´.

In a regular procedure, **P1´** (50 mg, 0.11 mmol) and cross-linker (ethylenediamine, **4**: 3.4 mg, 0.055 mmol) were dissolved in THF (50 ml) at room temperature. The re-formation process to SCNPs was followed through simultaneous SEC/MALLS measurements. After reaction completion (24 h), the solution was concentrated and the re-formed SCNPs **NP1´** were isolated by precipitation in diethyl ether and further drying (78% yield).

5.4 Results and Discussion

In order to enlarge the selection of DCBs that can be used for the construction of responsive SCNPs we have firstly investigated the dynamic nature of enamine bonds with low molecular weight model compounds. Equimolar amounts of methyl acetoacetate (**1**) and butylamine (**2**) were reacted to form the *mono*-enamine **3**. After 24 h ^{1}H NMR spectroscopy revealed signals associated with the enamine bond of **3** that were clearly visible at 3.2 and 4.5 ppm (Figure 5.1 A). The conversion of **1** and **2** into **3** was estimated to be 83%, indicating that the equilibrium lies on the side of the enamine. Component exchange of the enamine bond was induced by the addition of ethylenediamine (**4**) (0.5 equivalents with respect to **1**) to the reaction mixture, driving the formation of the *mono*- and *bis*-enamines (**5a, 5b**). Examination of the ^{1}H NMR spectrum revealed the appearance of new enamine signals at 2.8, 3.30 and 4.55 ppm arising from compounds **5a** and **5b** (Figure 5.1B). The conversion for the exchange process was estimated to be 77%.

Additionally, we performed ^{1}H NMR experiments to investigate acid-triggered enamine bond rupture. Upon addition of phosphoric acid, as ^{1}H NMR spectroscopy indicated, a quantitative hydrolysis of enamine bonds occurred (Figure 5.1 C). Consequently, enamine bond can be broken back to starting materials by an acid treatment, in this case using phosphoric acid. Taken together, these preliminary experiments with model compounds demonstrate that enamines can form spontaneously, undergo component exchange processes, and quantitatively hydrolyse back to the starting materials upon the addition of an acid.

A

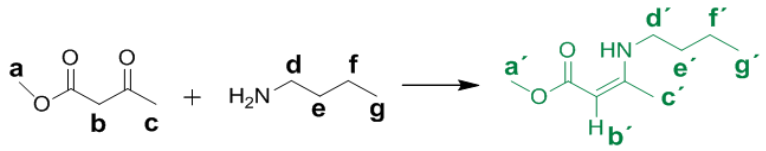

1 2 3

$$Yield = \frac{A_d}{(A_{d'} + A_d)} = 0.83$$

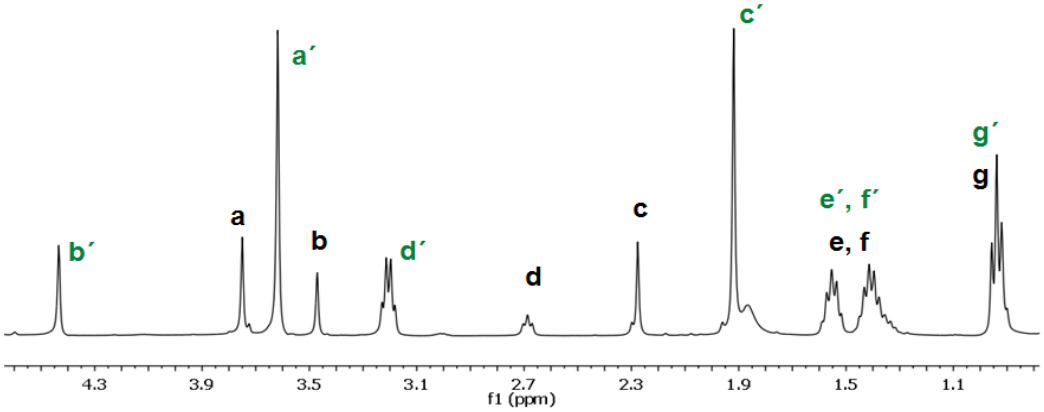

B

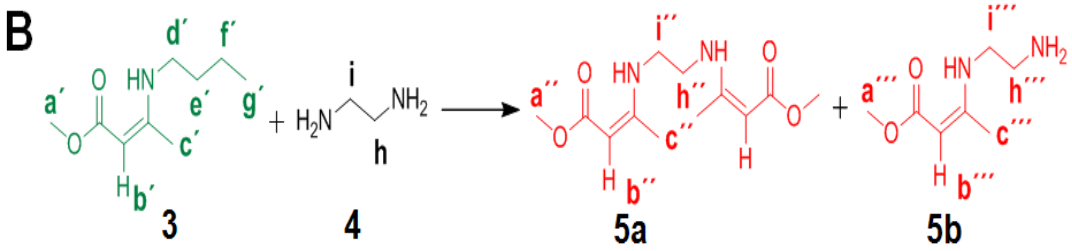

3 4 5a 5b

$$Yield\ (5a) = \frac{\frac{A_{i''+h''}}{4}}{\left(\frac{A_{i''+h''}}{4} + \frac{A_{d'}}{2}\right)} = 0.32$$

$$Yield(5b) = \frac{A_{i'''}}{A_{i'''} + A_{d'}} = 0.45$$

Exchange ≈ 0.77

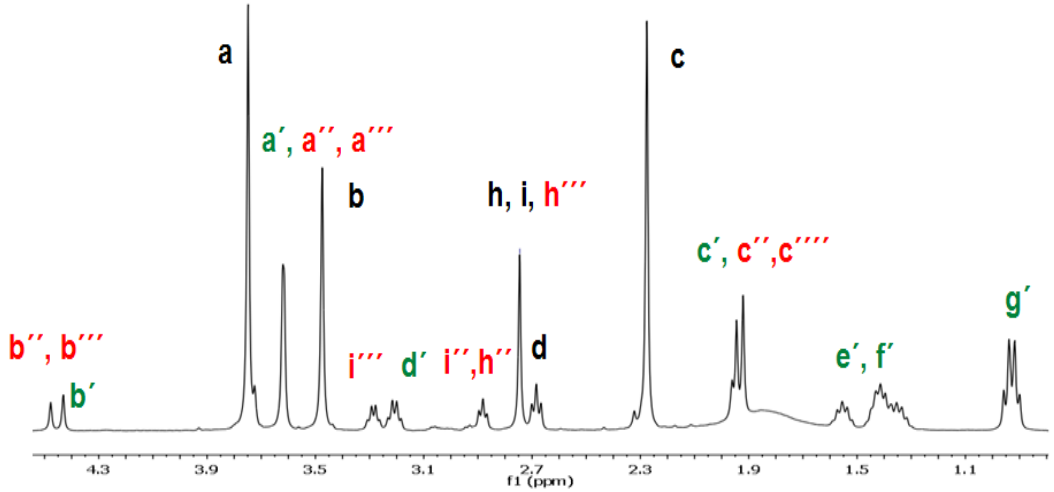

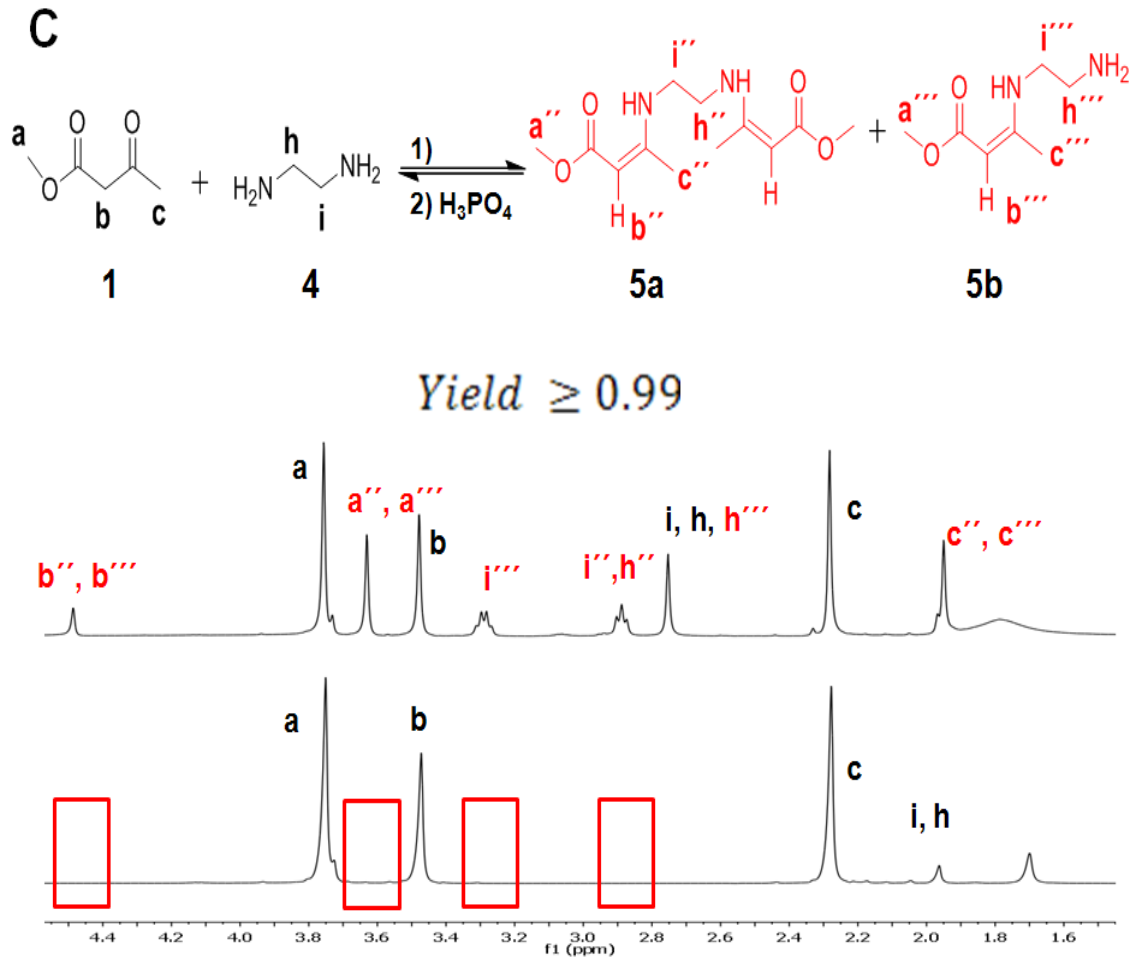

Figure 5.1. Low molecular weight compounds were selected for the investigation of enamine dynamic covalent bonds: **A)** Upon mixing methyl acetoacetate (**1**) and butylamine (**2**) for 24 h, the ^{1}H NMR spectrum shows the characteristics bands of enamine formation at 3.2 ppm and 4.5 ppm (see green letters) for the new compound (E,Z)-methyl 3-(butylamino)but-2-enoate (**3**). **B)** After addition of ethylenediamine (**4**) to the reaction medium, new bands (see red letters) associated to protons from compounds **5a** and **5b** appeared in the ^{1}H NMR spectrum upon enamine exchange reactions. **C)** Illustration of acid-triggered enamine disruption upon addition of deuterated phosphoric acid (bottom spectrum) to compounds **5a** and **5b** (upper spectrum).

We next explored the use of enamine DCBs for the construction of responsive SCNPs (Scheme 5.4 B). Four poly(methyl methacrylate-*co*-(2-acetoacetoxy)ethyl methacrylate) (P(MMA-*co*-AEMA)) random copolymers (**P1-P4**) featuring reactive *β*-ketoester functional groups of different molecular weights (Table 5.2) were synthesized through reversible addition-fragmentation chain-transfer (RAFT) polymerization.[38-40]

Table 5.2. Characteristics of copolymers **P1-P4** and SCNPs **NP1-NP4**.

Sample	M_w (g/mol) [a]	M_w/M_n	AEMA (mol%)	D_h (nm) [b]
P1	30900	1.05	31	7.8
P2	38000	1.06	30	8.5
P3	53500	1.05	26	10.6
P4	309400	1.3	30	27.7
NP1	29800	1.04	31	5.3
NP2	39100	1.04	30	5.7
NP3	52700	1.05	26	6.8
NP4	289900	1.2	30	14.1

[a]Actual weight average molecular weight as determined by combined SEC/MALLS measurements. [b]Hydrodynamic diameter, D_h, as determined by DLS in THF.

Then, copolymers **P1-P4** were functionalized *via* enamine formation with the monofunctional amine butylamine (**2**) in THF solution to afford the functionalized linear polymers **FP1-FP4** (Table 5.3). Fourier Transform Infrared (FTIR) Spectroscopy (Figure 5.2 B) confirmed successful enamine bond formation, as evidenced by the significant narrowing of the C=O stretch associated with the **AEMA** units and the appearance of new infrared vibration bands at 1650 cm^{-1} and 1605 cm^{-1} which we assign to stretching vibrations of enamine bonds (red arrows in Figure 5.2 B). The degree of functionalization was determined by ^1H NMR spectroscopy where the characteristic bands of enamine formation at 3.2 ppm and 4.5 ppm can be observed (Figure 5.2 A).

Table 5.3. Characteristics of alkyl amine-functionalized copolymers **FP1-FP4.**

Sample	M_w [a] (g/mol)	M_w/M_n	Functionalization[b]	Yield (%) [c]
FP1	32400	1.05	90	70
FP2	41800	1.05	92	69
FP3	53300	1.06	91	75
FP4	-	-	-	-

[a]Actual weight average molecular weight as determined by combined SEC/MALLS measurements (dn/dc= 0.083).[b]Content of alkyl amine-functionalizated AEMA units (mol%) in the copolymer as determined by ^1H NMR spectroscopy. [c]Calculated as grams of functionalized copolymer /initial grams of copolymer × 100.

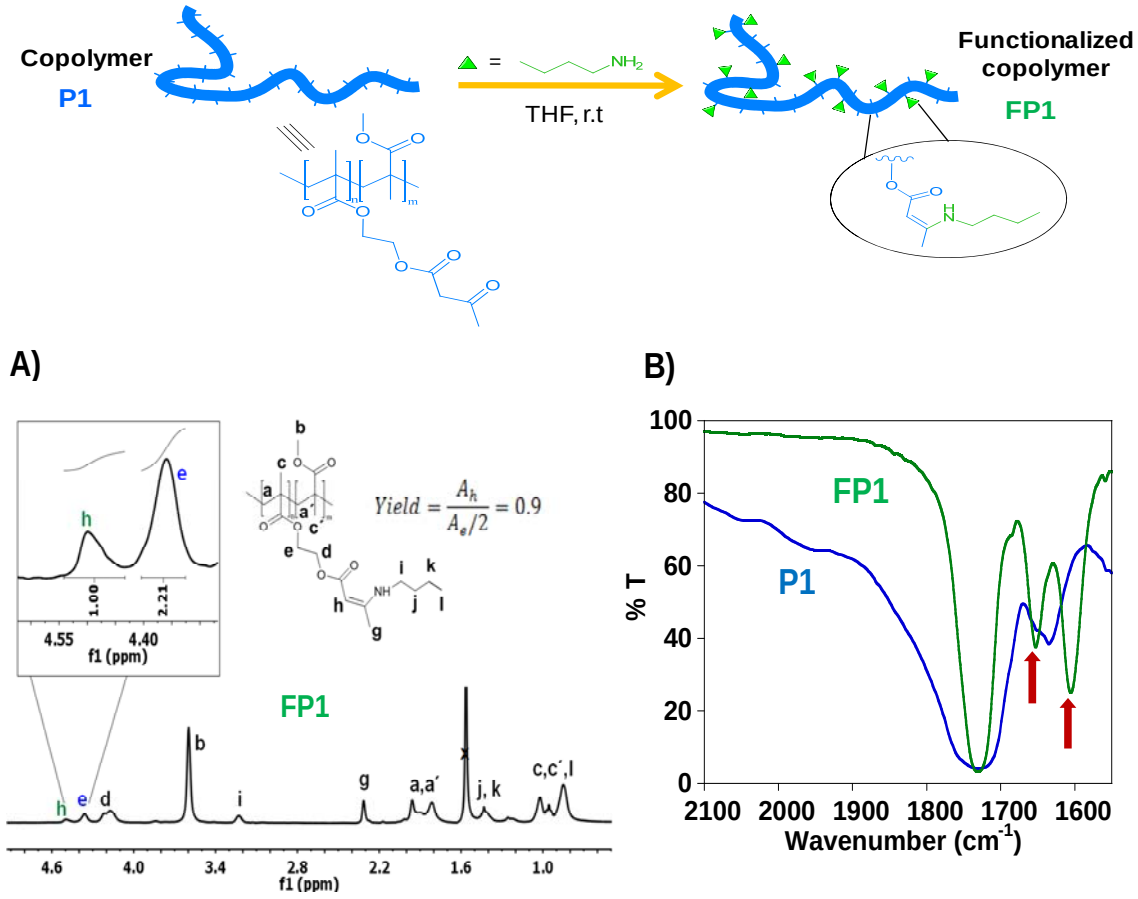

Figure 5.2. Copolymer functionalization *via* enamine formation. **A)** Content of alkyl amine in the functionalizated copolymer as determined by ^{1}HNMR spectroscopy. Upon mixing copolymer and butylamine the ^{1}HNMR spectrum shows the characteristic bands of enamine formation at 3.2 ppm (**i**) and 4.5 ppm (**h**). **B)** FTIR spectra corresponding to: 1) P(MMA-*co*-AEMA) copolymer **P1** (blue line), 2) butylamine-functionalized copolymer **FP1** (green line).

The functionalized linear polymers **FP1-FP4** were then collapsed progressively to SCNPs through exchange reactions with ethylenediamine (**4**), which takes the role of an intrachain cross-linker (Figure 5.3). SCNP synthesis was performed in THF at a concentration of 1 mg/ml of copolymer using equimolar concentrations of β-ketoester and amine functional groups. The chain collapse process was followed by size exclusion chromatography (SEC) (Figure 5.3 A), which revealed a significant increase in retention times (t_R) relative to **FP1-FP4**. These observations are consistent with a reduction in hydrodynamic sizes[41-42] which strongly suggests that intramolecular collapse induced by cross-linking has occurred *via* exchange reactions of the pendant enamines in **FP1-FP4** with the bifunctional ethylenediamine units.

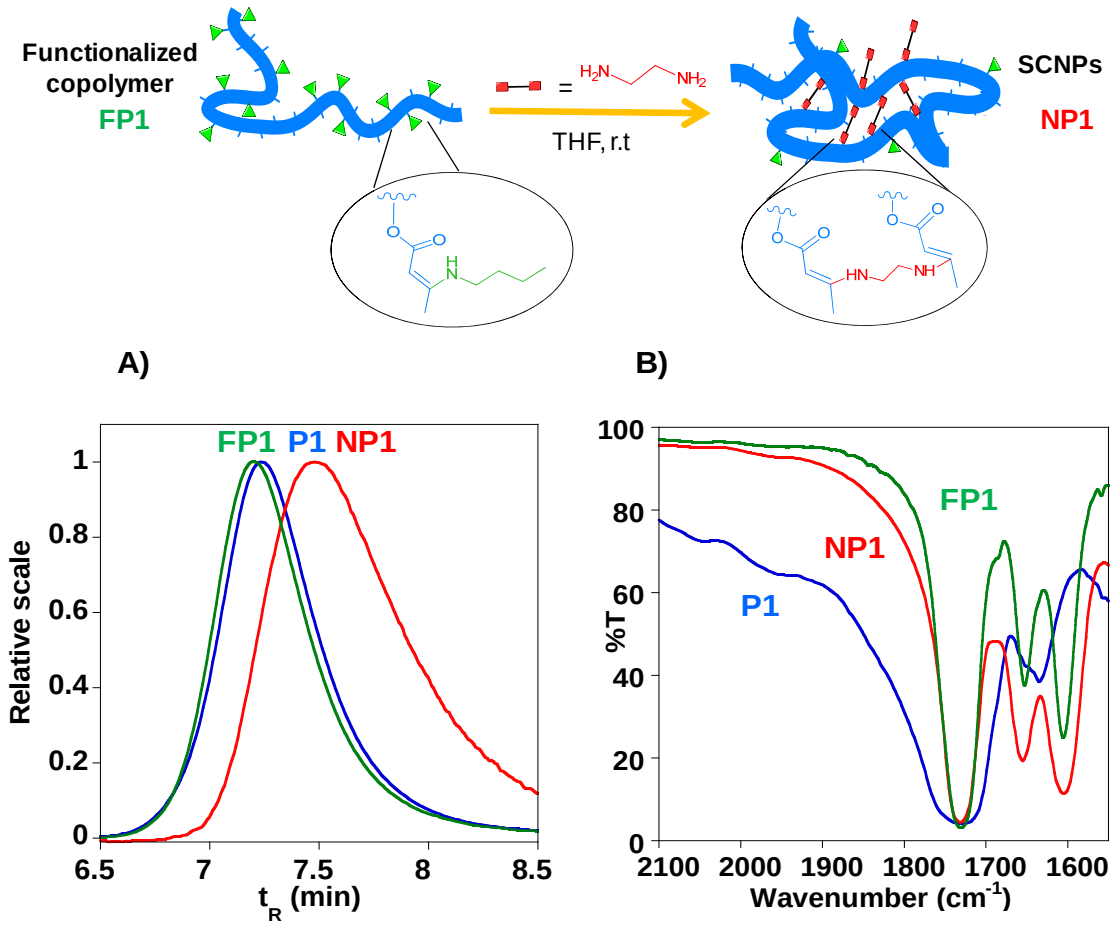

Figure 5.3. Single-chain polymer nanoparticle (SCNP) construction *via* enamine dynamic covalent bonds (DCBs): **A)** Illustration of SEC traces for **P1** (blue line), **FP1** (green line), and **NP1** (red line). **B)** FTIR spectra corresponding to: 1) P(MMA-*co*-AEMA) copolymer **P1** (blue line), 2) butylamine-functionalized copolymer **FP1** (green line), and 3) SCNPs **NP1** synthesized through dynamic butylamine / ethylenediamine exchange (red line).

In order to quantify the changes in hydrodynamic sizes between **P1-P4** and their corresponding SCNPs **NP1-NP4**, dynamic light scattering (DLS) measurements were performed in THF. As a representative example, the size of copolymer **P1** reduced from D_h = 7.8 nm to D_h = 5.3 nm upon SCNP formation (Table 5.2 and Figure 5.4 A). Further evidence supporting SCNP formation was obtained by ^{1}H NMR spectroscopy. Comparison of the ^{1}H NMR spectrum of the P(MMA-*co*-AEMA) random copolymer **P1** with that of its corresponding SCNP **NP1** (Figure 5.4 B) reveals significant peak broadening upon intramolecular cross-linking. Insets in Figure 5.4 B show clear band broadening in signals arising from –CH= protons of enamine groups (4.3 ppm, broad signal) and -CH_3 protons of the main-chain methyl groups (0.7–1.2 ppm, broad signal) of

NP1. For SCNPs, signal broadening in the ^{1}H NMR spectrum can be attributed to the restricted mobility of some of the SCNP protons as a consequence of the progressive cross-linking and is a well-documented signature of SCNPs formation.[43-45] Taken together, these experiments demonstrate that enamine exchange processes can successfully facilitate the formation of SCNPs.

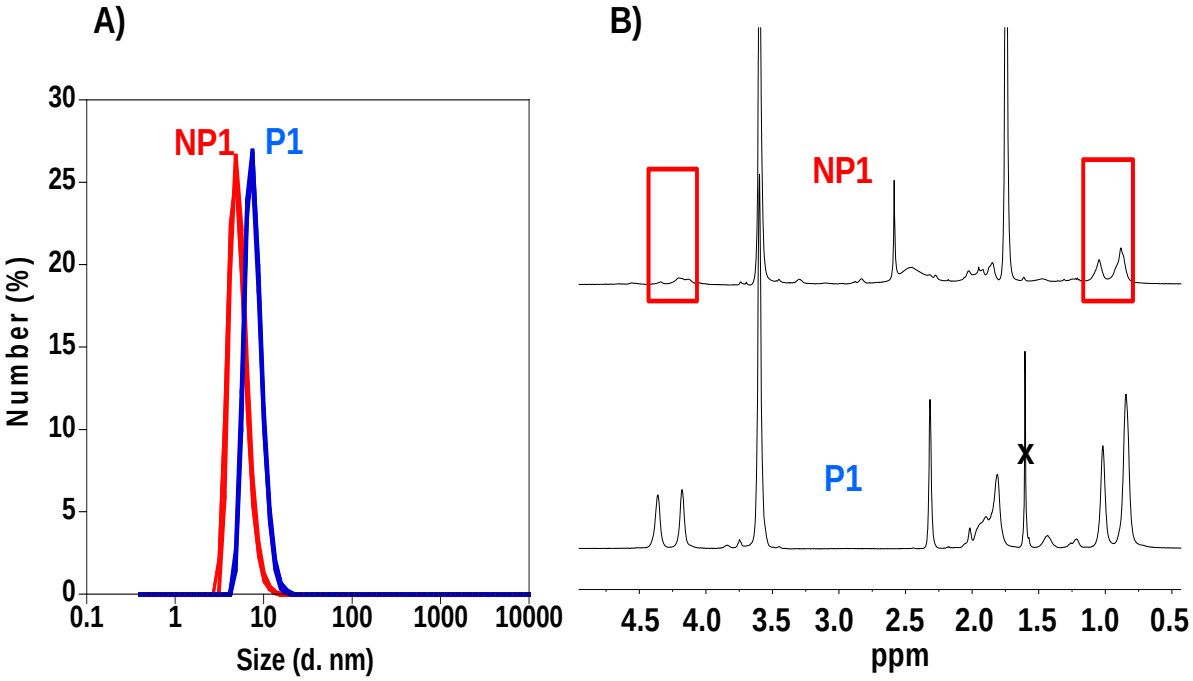

Figure 5.4. A) Hydrodynamic diameter (D_h) distribution for **P1** (blue line) and **NP1** (red line), as determined by DLS in THF. The average D_h changes from 7.8 nm to 5.3 nm upon SCNP formation. **B)** Comparison of the ^{1}H NMR in d-THF spectrum of the P(MMA-*co*-AEMA) random copolymer **(P1)** with that of its corresponding SCNP **(NP1)**.

To demonstrate the pH-responsiveness of these SCNPs, phosphoric acid (H_3PO_4) was added to the reaction medium to cause acid-triggered disassembly of the SCNPs. Preliminary experiments showed a disassembly degree of 100 % at pH = 5 in 16 h of reaction time, whereas at pH = 6, the disassembly degree amounted to 40 % after 24 h (see Table 5.1). Upon acid treatment of **NP1** a decrease in retention time in the SEC trace was observed (Figure 5.5 A) suggesting an increase in the hydrodynamic size. After treatment with an excess of H_3PO_4 for 24 h the collapsed copolymer chains re-expand to their original hydrodynamic size (based on SEC retention time of the original copolymer **P1**) regardless of the amount of cross-linker originally added,

confirming a highly efficient acid-triggered SCNP disassembly process. In fact, SEC traces of the original P(MMA-*co*-AEMA) copolymer **P1** and the disassembled SCNPs, denoted as **P1´**, were found to be nearly identical (Figure 5.5 A). Upon SCNP disassembly the specific enamine infrared vibration bands that appear in unimolecular nanoparticles (**NP1**) at 1605 and 1650 cm^{-1} totally disappeared (Figure 5. 6 B) and the ^1H NMR spectrum of **P1´** (Figure 5.5 B) was found to be very similar to that of the initial copolymer **P1.** The resulting copolymer **P1´** was successfully isolated by precipitation in water, drying under vacuum and redissolved in THF.

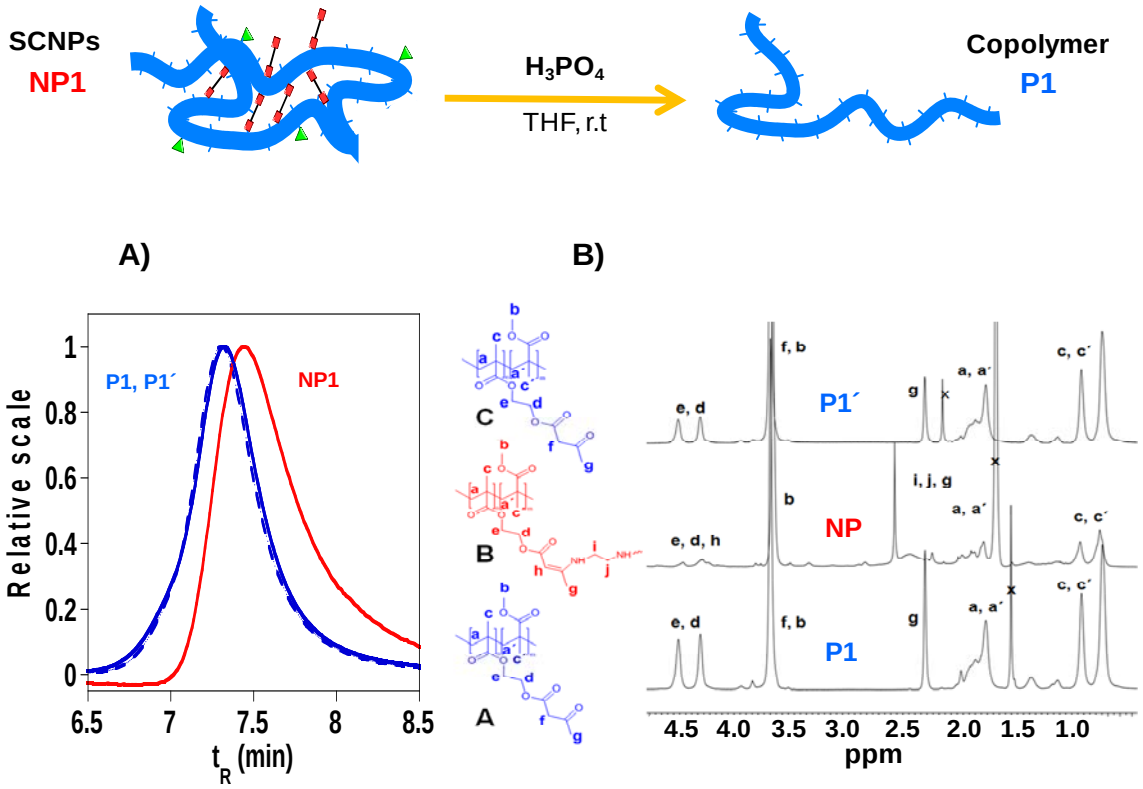

Figure 5.5. Illustration of SCNP disassembly**. A)** SEC traces in THF for **P1** (blue line), **NP1** (red line) and **P1´** (broken blue line). **B)** ^1H NMR spectra in d-THF corresponding to: A) P(MMA-*co*-AEMA) copolymer **P1**. B) SCNPs **NP1** synthesized through dynamic alkyl amine / alkyl diamine exchange. C) Disassembled SCNPs, denoted as **P1´**, after addition of an excess of H_3PO_4 with respect to the amount of enamine DCBs in **NP1.**

To further demonstrate the possibilities of enamine DCBs, the reorganization of **P1´** into a SCNP, denoted as **NP1´**, was triggered *directly* by addition of cross-linker ethylenediamine (**4**) (0.5 equivalents with respect to **AEMA** groups) to **P1´**. As expected (Figure 5.6 A), a significant shift in the SEC trace towards

longer retention time was clearly observed, again indicating a reduction in hydrodynamic size upon the reformation of the enamine bonds and the concomitant intrachain cross-linking. Figure 5.6 A shows overlays of the chromatograms for the original SCNPs **NP1** and the reformed SCNPs **NP1´**, showing very similar SEC traces. Furthermore, as it is depicted in Figure 5.6 B upon reorganization of **P1´** to **NP1´** the specific enamine infrared vibration bands appeared again.

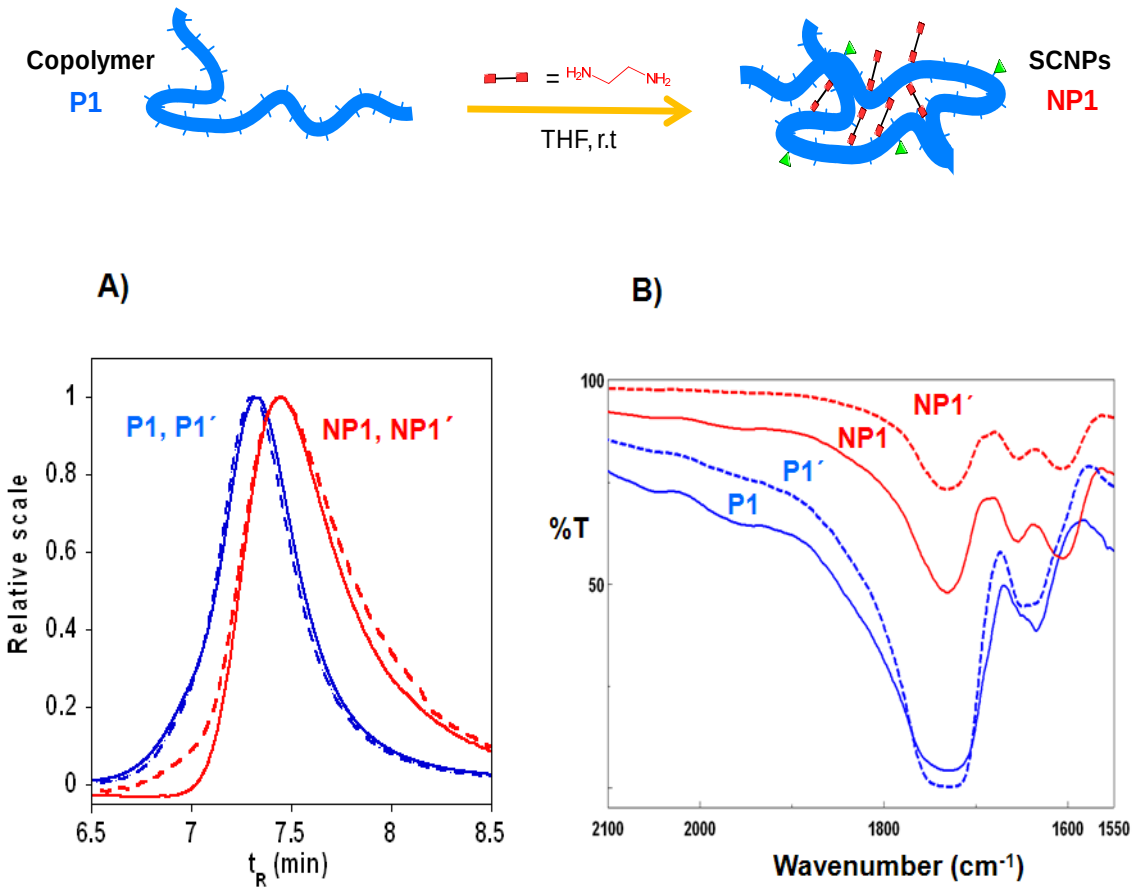

Figure 5.6. Illustration of SCNP disassembly and reassembly: **A)** SEC trace of **NP1** (continuous red line), SEC trace of **NP1** after H_3PO_4 addition (**P1´**) (broken blue line) and SEC trace of the re-formed SCNP **NP1´** synthesized directly from **P1´** (broken red line). SEC trace of **P1** (continuous blue line) is also included for comparison. **B)** FTIR spectra corresponding to: **P1** (blue line), **NP1** (red line), **P1´** (broken blue line), and **NP1´** (broken red line).

Moreover, both exchange reactions between alkyl monoamine/alkyl diamine and acid-triggered disassembly of the SCNPs can be easily performed in a one-pot fashion as illustrated in Figure 5.7.

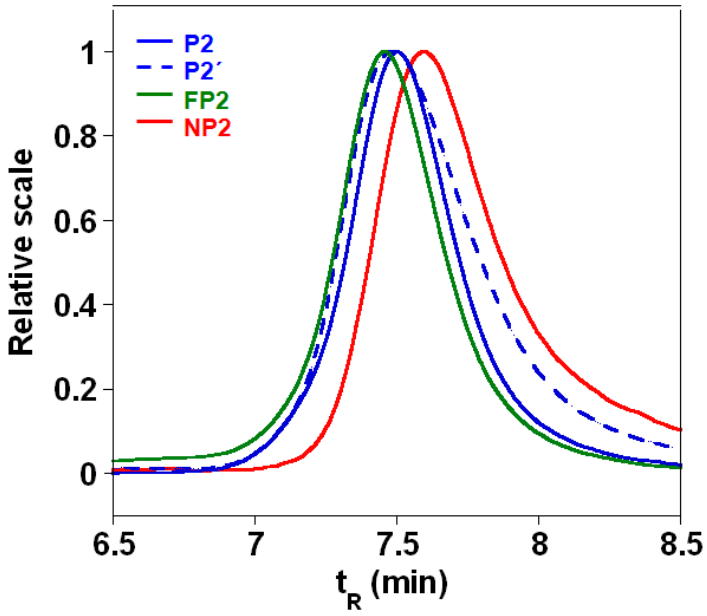

Figure 5.7. Facile one pot SCNP assembly/disassembly demonstrated by SEC measurements: SEC trace of **P2** (continuous blue line), SEC trace of **FP2** synthesized directly from **P2** and **6** (hexylamine) (green line), SEC trace of SCNPs **NP2** synthesized through dynamic alkyl amine **6** / alkyl diamine **4** exchange (red line), and SEC trace of **NP2** after H_3PO_4 addition (**P2**´) (broken blue line).

5.5 Conclusion

In conclusion, we have demonstrated the facile one-pot reversible conversion of linear polymer chains into pH-responsive SCNPs by means of enamine DCBs. These pH-responsive SCNPs can undergo component exchange processes between alkyl monoamine/alkyl diamine and quantitatively hydrolyse back to linear polymer chains upon the addition of a strong acid. This proof of concept paves the way to the use of enamine DCBs for the construction of other responsive, structurally dynamic polymeric systems beyond SCNPs. Due to the availability and important antitumor role of some naturally occurring diamines (*e.g.*, norspermidine), the use of enamine DCBs for the development of responsive therapeutic nanocarriers and/or innovative sensor nanodevices is envisioned. This work will also renew interest in enamines as DCBs, which have been surprisingly overlooked as a dynamic covalent bond. Our preliminary results suggest that this "*forgotten*" DCB will become a valuable addition to the growing 'toolbox' of dynamic covalent chemistry.

5.6 References

[1] S. J. Rowan, S. J. Cantrill, G. R. L. Cousins, J. K. M. Sanders and J. F. Stoddart, *Angew. Chem. Int. Ed.*, **2002**, *41*, 898.

[2] J. M. Lehn, *Chem. Soc. Rev.*, **2007**, *36*, 151.

[3] P. T. Corbett, J. Leclaire, L. Vial, K. R. West, J.-L. Wietor, J. K. M. Sanders and S. Otto, *Chem. Rev.*, **2006,** *106*, 3652.

[4] M. A. C. Stuart,W. T. S. Huck, J. Genzer,M. Muller, C. Ober,M. Stamm, G. B. Sukhorukov, I. Szleifer, V. V. Tsukruk, M. Urban, F.Winnik, S. Zauscher, I. Luzinov, S. Minko, *Nat. Mater*., **2010**, *9*, 101.

[5] a) T. Maeda, H. Otsuka and A. Takahara, *Prog. Polym. Sci*., **2009**, *34*, 581. b) J. M. Lehn, *Aust. J. Chem*., **2010**, *63*, 611.

[6] R. J. Wojtecki, M. A. Meador and S. J. Rowan, *Nature Mater*., **2011**, *10*, 14.

[7] J. M. Lehn, *Prog. Polym. Sci*., **2005**, *30*, 814.

[8] C.J. Kloxin, T. F. Scott, B.J. Adzima and C.N. Bowman, *Macromolecules.*, **2010**, *43,* 2673.

[9] B. S. Murray and D. A. Fulton, *Macromolecules*., **2011**, *44,* 7242.

[10] T. Tuten, D. Chao, C. K. Lyonb and E. B. Berda. *Polym. Chem*., **2012,** *3*, 3068.

[11] Alexander W. Jackson and David A. Fulton, *Polym. Chem*., **2013**, *4*, 31.

[12] H.Otsuka, K. Aotani, Y. Higaki, Y. Amamoto, A. Takahara, *Macromolecules.,* **2007**, *40*, 1429.

[13] X. Chen, M. A. Dam, K. Ono, A. Mal, H. Shen, S. R. Nutt, K. Sheran, F. Wudl, *Science.,* **2002**, *295*, 1698.

[14] G. Deng, C. Tang, F. Li, H. Jiang, Y. Chen, *Macromolecules.,* **2010**, *43*, 1191.

[15] Y. Xin and J. Yuan, *Poly. Chem.,* **2012**, *3*, 3045.

[16] M. E. Belowich and J. F. Stoddart, *Chem. Soc. Rev*., **2012**, *41*, 2003.

[17] L. Buruaga, J. A. Pomposo, *Polymers.,* **2011**, *3*, 1673.

[18] J. A. West, *J. Chem. Educ*., **1963**, *40*, 194.

[19] D. Sánchez, D. Bastida, J. Burés, C. Isart, O. Pineda and J. Vilarrasa, *Org. Lett.,* **2012**, *14*, 536.

[20] Sanchez-Sanchez, A.; Pomposo, J. A. *Part. Part. Syst. Charact*., **2014,** *31*, 11.

[21] R. J. Esser, J. E. Devona, D. E. Setzke, L.Wagemans, *Prog.Org. Coat*., **1999**, *36*, 45.

[22] W. Schubert, *Prog. Org. Coat*., **1993**, 22, 357.

[23] J. Feng, H. Pham, P. McDonald, M. A.Winnik, J. M. Geurts, H. Zirkzee, S. van Es, A. L. German, *J. Coat. Technol*., **1998**, *70*, 57.

[24] J. M. Geurts, *PhD Thesis*, University of Eindhoven., **1997**.

[25] Y. J. Park, M. J. Monteiro, S. van Es, A. L. German, *Eur. Polym. J*., **2001**, *37*, 965.

[26] O. Altintas and C. Barner-Kowollik, *Macromol. Rapid Commun.,* **2012**, *33*, 958.

[27] A. Sanchez-Sanchez, I. Perez-Baena and J. A. Pomposo, *Molecules*., **2013**, *18*, 3339.

[28] A. Sanchez-Sanchez, S. Akbari, A. Etxeberria, A. Arbe, U. Gasser, A. J. Moreno, J. Colmenero and J. A. Pomposo, *ACS Macro Letters*., **2013**, *2*, 491.

[29] Willenbacher J, Altintas O, Roesky PW, Barner-Kowollik C. *Macromol Rapid Commun.,* **2013,** *35*, 45**.**

[30] He J, Tremblay L, Lacelle S, Zhao Y, *Soft Matter*., **2011**, *7*, 2380.

[31] Gillissen M. A. J, Voets I.K, Meijer E.W, Palmans A. R. A, *Polym Chem*., **2012**, *3*, 3166.

[32] Perez-Baena I, Barroso-Bujans F, Gasser U, Arbe A, Moreno A. J, Colmenero J, Pomposo J. A. *ACS Macro Letters*., **2013**, *2*, 775.

[33] Hosono N, Gillissen M.A. J, Li Y, Sheiko S.S, Palmans A.R. A, Meijer E. W. *J Am Chem Soc*., **2013**, *135*, 501.

[34] Terashima T, Mes T, De Greef T.F.A, Gillissen M.A. J, Besenius P, Palmans A. R. A, Meijer E. W. *J Am Chem Soc*., **2011**, *133*, 4742.

[35] Wang Y, Dong L, Xiong R, Hu A. J. *Mater Chem C*., **2013**, *1*, 7731.

[36] D.E. Whitaker, C.S. Mahon and D. A. Fulton, *Angew. Chem. Int. Ed.,* **2013**, *52*, 956.

[37] C. S. Mahon, A. W. Jackson, B. S. Murray and D. A. Fulton, *Chem. Commun.,* **2011**, *47*, 7209.

[38] G. Moad, E. Rizzardo and S. H. Thang, *Polymer*., **2008**, *49*, 1079.

[39] G. Moad, E. Rizzardo, S.H. Thang. *Aust J. Chem*., **2005**, *58*, 379.

[40] T. Krasia, R. Soula, H. G. Borner and H. Schlaad, *Chem. Commun*., **2003**, *4*, 538.

[41] J. A. Pomposo, I. Perez-Baena, L. Buruaga, A. Alegría, A. J. Moreno and J. Colmenero, *Macromolecules*., **2011**, 44, 8644.

[42] P. Frank, A. Prasher, B. Tuten, D. Chao, E. Berda. *Applied Petrochemical Research*:, **2014**, doi: 10.1007/s13203-014-0046-1.

[43] J. He, L. Tremblay, S. Lacelle and Y. Zhao, *Soft Matter*., **2011**, *7*, 2380.

[44] Sanchez-Sanchez, A.; Asenjo-Sanz, I.; Buruaga, L.; Pomposo, J.A. *Macromol. Rapid Commun*., **2012**, *33*, 1262.

[45] Jackson A.J, Fulton D.A. *Macromolecules*., **2012**, *45*, 2699.

CHAPTER 6:

Experimental Techniques and Molecular Dynamics Simulations

6.1 Experimental Techniques

In this section the experimental techniques used for the characterization of the samples are briefly described. In addition, a brief description is given of the physical quantities measured using these techniques, and the basic equations involved therein, are also explained.

6.1.1 Nuclear magnetic resonance (NMR)

Nuclear magnetic resonance (NMR) is a phenomenon that gives deep insight on the structure of matter by measuring the interaction of the nuclear spin with its environment (electric and magnetic field). A nuclear spin is like a small bar magnet spinning about its own axis. The spins of interest are the spins with a non-integer value, the proton (nucleus of hydrogen) being the most popular.

In this work, proton nuclear magnetic resonance (^{1}H-NMR) spectra were recorded at room temperature on a Bruker spectrometer operating at 300 MHz, 400 MHz or 500MHz in different deuterated solvents. Signals were referenced to the characteristic signals arising from traces of protonated solvent. (e.g. $CHCl_3$ or TMS)

Figure 6.1. Bruker 300 MHz spectrometer employed in this work.

The equation that is used to calculate the monomer to polymer conversion (c) through NMR spectroscopy is:

$$c = \frac{{}^{A_p}/_{n°H}}{\left({}^{A_p}/_{n°H} + {}^{A_m}/_{n°H}\right)} \quad (6.1)$$

where A_p is the integral area of a polymer band and A_m is the integral area of a monomer band and nº H are the number of protons corresponding to each band. Furthermore, ^{1}H-NMR spectroscopy was used to determine the composition of the polymers and the kinetics of reaction processes.

6.1.2 Size-Exclusion Chromatography / Multi-Angle Laser Light Scattering (SEC / MALLS)

Size exclusion chromatography (SEC), is an entropically controlled separation technique that depends on the relative size or hydrodynamic volume of a macromolecule with respect to the average pore size of the packing. With a properly calibrated SEC column, all the statistical average molecular weights of a polymer can be determined, as well as the molecular weight distribution. Absolute molecular weight measurements are possible with the use of either an on-line light-scattering detector (without column calibration) or an on-line viscometer (with universal calibration) in combination with a refractive index (RI) detector.[1]

In a multi-angle laser light scattering (MALLS)[2] experiment, we are able to obtain both the *actual* weight average molecular mass (M_w) and the average radius of gyration (R_g) of polymer chains in an extremely dilute solution simply from the angular dependence of the excess absolute scattering intensity, known as the Rayleigh ratio, R(θ), by:

$$\frac{KC}{R(\theta)} \cong \frac{1}{M_W}\left(1 + \frac{1}{3}R_g^2 q^2\right) \quad (6.2)$$

where K is an optical constant and $q=(4\pi n/\lambda_0)\sin(\theta/2)$ with n, λ_0, and θ being the solvent refractive index, the incident radiation wavelength at vacuum, and the scattering angle, respectively.

In this work, SEC/ MALLS measurements were performed at 30 ^{o}C on an Agilent 1200 system equipped with PLgel 5µm Guard and PLgel 5µm MIXED-C columns, a differential refractive index (RI) detector (Optilab Rex, Wyatt) and a multi angle laser light scattering (MALLS) detector (MiniDawn Treos, Wyatt). Data analysis was performed with ASTRA Software from Wyatt. THF was used as eluent at a flow rate of 1 ml / min. dn/dc values in THF were taken from the literature or were determined using the Optilab Rex detector on line when required.

Figure 6.2. SEC/MALLS/RI equipment employed in this work.

6.1.3 Thermal Gravimetric Analysis (TGA)

Thermogravimetric Analysis or Thermal Gravimetric Analysis (TGA) is a thermo-analytical technique based on continuously recording the changes in the mass of a sample, as a function of temperature with time. Typically, TGA measurements are performed on samples of about 5-10 mg. The temperature is controlled in a preprogrammed temperature/time profile and the experiments are carried out in a nitrogen environment.

The thermal gravimetric measurements were performed in a Q500 set-up with TA Instruments which can be seen in figure 6.3. The samples were heated from room temperature to 1000 ºC at a rate of 10 ºC/min.

Figure 6.3. TGA Q500 from TA Instruments employed for the thermal gravimetric analysis.

6.1.4 Transmission Electron Microscopy (TEM)

Transmission electron microscopy (TEM) is a widely used technique for direct visualization of local structure at the atomic scale.[3] TEM is a technique where an electron beam is transmitted through an ultra-thin specimen. The electron beam interacts with the sample as it passes through and forms an image in an analogous way to a light microscope. The image is magnified and focused onto an imaging device, on a layer of photographic film, or to be detected by a sensor such as a CCD (Charge-Coupled Device) camera. In our case, the obtained images provide information about the size, size distribution and morphology of the synthesized SCNPs. Successful imaging of nanoparticles using TEM depends on the contrast of the sample relative to the background.

TEM measurements were carried out using a high-resolution transmission electron microscope TECNAI G220 TWIN operating at an accelerating voltage of 200 kV, under low dose conditions and at room temperature. These measurements were performed at the SGIker polymer characterization unit of

the University of the Basque Country (UPV/EHU). The procedure to prepare the sample was the deposition of a drop of nanoparticle solution (1mg/ml in chloroform) in a copper grid (300 mesh) which was coated with carbon. After that, it was kept at room temperature to allow the evaporation of the solvent (chloroform). In the case of SCNPs synthesized by Michael addition (Chapter 3), the nanoparticles were stained using Tangstophosphoric acid (TPA) in order to obtain more contrast.

Figure 6.4. TECNAI G220 TWIN employed in this work.

6.1.5. Fourier Transform Infrared Spectroscopy (FTIR)

Fourier Transform Infrared Spectroscopy (FTIR) is a technique that deals with the infrared region of the electromagnetic spectrum (750 nm – 1 mm). The term FTIR reflects the fact that a Fourier Transform is required to turn the raw data into the final spectrum. This technique is based on the absorption of the electromagnetic radiation by the molecules at specific frequencies (resonant frequencies) that are characteristic of their structure. Thus, the frequency of the vibrations can be associated with a particular bond type. In this work, the polymer precursors were studied by FTIR in order to compare the obtained results with those of the SCNPs.

FTIR spectra were recorded at room temperature on a JASCO 3600 FTIR spectrometer. Spectra were obtained by using 50 scans with 4 cm^{-1} resolution. All the samples were prepared by blending the polymer sample with KBr powder and after that pressing the blend to obtain a KBr pellet.

Figure 6.5. FTIR spectrometer employed for the analysis.

6.1.6. Ultraviolet / visible (UV / VIS) spectroscopy

In an ultraviolet-visible (UV/Vis) spectroscopic measurement, light absorption as a function of wavelength provides information about electronic transitions occurring in the material. The fraction of light transmitted is described by the Beer-Lambert law, which states that the fraction of the light measured after interaction with the sample (I, usually measured as transmittance or reflectance) versus the incident intensity (I_0) is dependent on the path length of light through the sample (l), the absorption cross section (σ) of the transition, and the difference in the population of the initial state (N_1) and final state (N_2) of the initial (E_1) and final (E_2) electronic energy levels.[4]

$$\frac{I}{I_0} = e^{-\sigma(N_1 - N_2)l} \quad (6.3)$$

This is often written in a form referred to simply as Beer´s Law valid for ($A \leq 1.0$):

$$A = \varepsilon c l = -\log_{10}\left(\frac{I}{I_0}\right) \quad (6.4)$$

where *A* is the absorbance, ε is the molar absorptivity coefficient of the material, c is the concentration of the absorbing species, and *l* is the path length of light through the sample.

UV/Vis spectroscopy measurements were carried out at 25 ºC in an Agilent 8453A apparatus with a Peltier thermostatic cell holder, T-controller 89090A.

Figure. 6.6. UV/Vis equipment employed in this work: Agilent 8453A spectrometer (right), and T-controller 89090A Peltier thermostatic cell holder (left).

6.1.7. Small Angle X-Ray Scattering (SAXS)

Small angle X-ray scattering (SAXS) reveals solution structures of macromolecules and synthetic nanoparticles at 1-2 nm resolution.

SAXS is a universal technique applicable to a broad range of particle sizes, from small peptides to huge macromolecular NPs. The main principles of SAXS were developed in the late 1930s by A. Guinier with his studies of metallic alloys. In the very first monograph on a SAXS instrument, Guinier and Fournet (1955) demonstrated that the method yields not just information on the sizes and shapes of particles but also on the internal structure of disordered and partially ordered systems.[5]

In a SAXS instrument a monochromatic beam of X-Rays is brought to a sample from which some of the X-Rays scatter, while most simply go through the sample without interacting with it. The scattered X-Rays form a scattering pattern which is then recorded in a detector. Scattering of X-Rays is caused by differences in electron density.

In this study, SAXS experiments were conducted on Rigaku 3-pinhole PSAXS-L equipment operating at 45 kV and 0.88 mA. The MicroMax-002+ X-Ray Generator System is composed of a microfocus sealed tube source module and an integrated X-Ray generator unit which produces CuKα transition photons of wavelength λ=1.54 Å. The flight path and the sample chamber in this equipment are under vacuum. The scattered X-Rays are detected on a two-dimensional multiwire X-Ray Detector (Gabriel design, 2D-200X) and converted to one-dimensional scattering curves by radial averaging. This gas-filled proportional type detector offers a 200 mm diameter active area with c.a. 200 μm resolution. After radial integration, the scattered intensities were obtained as a function of momentum transfer Q, $Q = 4\pi\lambda^{-1} \sin\theta$, where θ is half the scattering angle.

Reciprocal space calibration was carried out using silver behenate as standard. The sample to detector distance was 2 m, covering a Q-range between 0.008 $Å^{-1}$ and 0.15 $Å^{-1}$. The measurements were performed at room temperature on solutions of single-chain NPs or precursors in tetrahydrofuran at a concentration of 8 mg/ml in capillaries of 2 mm thickness. The data were background corrected by subtracting the result of a measurement on the capillary filled with THF and applying the proper transmission corrections.

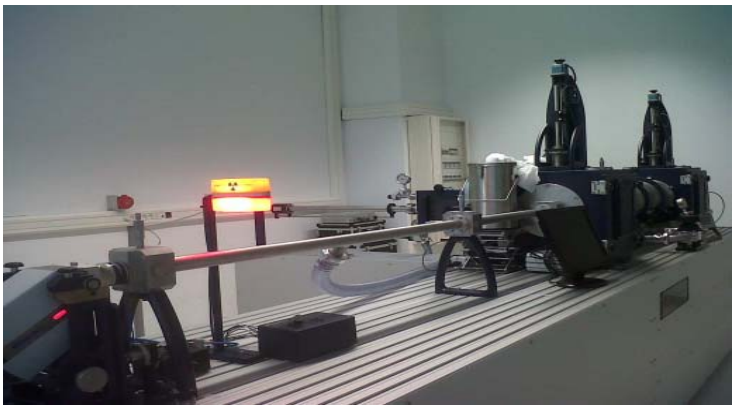

Figure. 6.7. Equipment employed for SAXS experiments.

6.1.8 Small Angle Neutron Scattering (SANS)

Small Angle Neutron Scattering (SANS) is a neutron scattering technique that enables the study of materials at nanometre to micrometre length scales. The experiment consists of a well collimated beam of neutrons being passed through a sample and detectors to count the number of neutrons scattered as a function of angle and neutron wavelength. This data can then be used to extract information about the shape, size, arrangement, and interactions of the components of the sample.

SANS measurements were performed at the SANS-II instrument at the Swiss spallation neutron source SINQ, Paul Scherrer Institute, Villigen, Switzerland. By using two incoming wavelengths (l=10.5 and 5.27 Å) and three different sample-detector distances (6, 4 and 1.2 m) a momentum transfer range from Q= 0.0035 $Å^{-1}$ to Q= 0.25 $Å^{-1}$ was covered. Solutions of the nanoparticles at 25 ^{o}C in deuterated N,N-dimethyl formamide at a concentration of 8 mg/ml were investigated in quarz cells of 2 mm thickness. The data were corrected for background scattering due to sample cuvettes and detector dark counts; the detector efficiency was calibrated with a H_2O measurement.

In this work, scattering patterns I(q) are shown using a so-called Kratky plot ($q^2I(q)$ vs q). This graphical representation emphasizes the differences at large

angles between the profiles of a compact object, for instance a globular, structured sample, that exhibits a pronounced maximum (bell-shaped curve) and that of a random chain, for instance an unfolded polymer chain, which displays a plateau instead.[6]

Figure. 6.8. SANS-II: Small Angle Neutron Scattering Instrument.

6.1.9 X-ray Photoelectron Spectroscopy (XPS)

X-ray Photoelectron Spectroscopy (XPS), also referred to as Electron Spectroscopy for Chemical Analysis (ESCA), irradiates the sample surface with a soft (low energy) X-ray. This X-ray excites the electrons of the sample atoms and if their binding energy is lower than the X-ray energy, they will be emitted from the parent atom as a photoelectron. Only the photoelectrons at the extreme outer surface (10-100 Angstroms) can escape the sample surface, making this a surface analysis technique.

XPS is a surface-sensitive technique that can be used to measure the elemental composition at the parts per thousand range, empirical formula, chemical state and electronic state of the elements that exist within the surface of a material.

XPS spectra were recorded at room temperature on a SPECS-XPS apparatus. Al K_α X-ray line at 1486 eV was used. A SCNP solution in chloroform (3

mg/ml) was added dropcast onto a Au/SiO_2 substrate, allowed to dry to form a thin film. The spectra were referenced to the SiO_2 signal of the substrate.

Figure. 6.9. SPECS-XPS apparatus employed in this work.

6.1.10 Gas chromatography (GC)

Gas chromatography (GC) is an analytical separation technique that is used to analyze volatile substances in the gas phase. In gas chromatography, the components of a sample are dissolved in a solvent and vaporized in order to separate the analytes by distributing the sample between two phases: a stationary phase and a mobile phase. The mobile phase is a chemically inert gas that serves to carry the molecules of the analyte through the heated column. The stationary phase is a microscopic layer of liquid or polymer on an inert solid support, inside a piece of glass or metal tubing called a column.

GC was performed in a Shimadzu GC 14A gas chromatograph. The GC instrument was operated in split mode with a ratio of 40:5 and the column head pressure was 100 kPa. The GC injector was maintained at 200°C and the detector at 200°C.

Figure. 6.10. Shimadzu GC 14A gas chromatograph.

6.1.11 Dynamic Light Scattering (DLS)

Dynamic light scattering (DLS) is a non-invasive technique for measuring the size of nanoparticles in a solution. Macromolecules or colloidal particles dissolved in a solvent undergo Brownian motion. DLS measures the light scattered from a laser that passes through a colloidal solution and by analyzing the modulation of the scattered light intensity as a function of time, the hydrodynamic size of particles can be determined. Larger particles will diffuse slower than smaller particles and the DLS instrument measures the time dependence of the scattered light to generate a correlation function that can be mathematically linked to a particle size.

By measuring the diffusion coefficient and assuming the spherical shape of the molecules, one can calculate the hydrodynamic radius using Stokes-Einsten relation:

$$R_h = \frac{k_B T}{6\pi\eta D} \quad (6.5)$$

where R_h is the hydrodynamic radius, D is the measured diffusion coefficient, k_B is Boltzmann's constant, T is temperature, η is the solvent viscosity. The hydrodynamic radius R_h that is measured, is the radius of the so-called hydrodynamically equivalent sphere that would have the same diffusion coefficient as the nanoparticles under investigation.

DLS measurements were performed in a Malvern Zetasizer Nano ZS apparatus to determine the hydrodynamic radius of the copolymers and the corresponding SCNPs at room temperature in THF solvent. The "size distribution by number" plot was employed in this work.

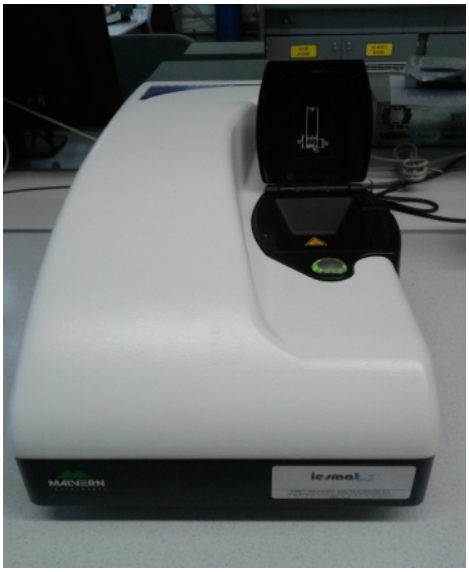

Figure. 6.11. The Malvern Zetasizer employed for DLS measurements.

6.2 Molecular Dynamics (MD) Simulations

In order to obtain valuable information about the structure in solution of SCNPs synthesized through Michael addition (Chapter 3) MD simulations were carried out.

MD simulations of isolated polymers were performed by using the well-known bead-spring model of Grest and Kremer.[7] The precursor was modeled as a linear backbone of N beads, with an attached side group per backbone bead. Unactive and active side groups contained one and three beads respectively. In the following we denote the fraction of active side groups as f. The cross-linkers were the end beads of the active groups. See figure 6.12 for a schematic representation of the molecular architecture. The excluded-volume interactions between any two given beads (of "size" σ and mass m) were modeled by a Lennard-Jones (LJ) potential:

$$V_{LJ}(r) = 4\varepsilon\,[(\sigma/r)^{12} - (\sigma/r)^{6} + 1/4] \qquad (6.6)$$

for $r \le r_c$ and $V_{LJ}(r)=0$ for $r > r_c$. We used a cutoff $r_c = 2^{1/6}\sigma$, so that the potential is purely repulsive and has no local minima, with the aim of mimicking the excluded volume in good solvent conditions. Moreover, the standard FENE potential[6] was used to model bonding between connected beads,

$$V_{FENE}(r) = -15\varepsilon\, R_0^2 \ln[1 - (r/R_0\sigma)^2] \qquad (6.7)$$

with $R_0 = 1.5$. The sum of the LJ and the FENE potential yields a total potential between connected beads with a sharp minimum at $r \approx 0.98\sigma$, which guarantees uncrossability of the bonds.[7]

In a bead-spring polymer a bead represents qualitatively a group of 4-5 "big" atoms (C, O, N...) and their bonded hydrogens. Thus, mapping to real units can

be made by using the approximate conversion factors σ~1 nm and m ~100 Da.[7] The polymers were propagated at temperature $T = \varepsilon$ by means of Langevin dynamics[8], without explicit solvent and neglecting hydrodynamic effects (polymer-solvent interactions were simulated by drag and random forces obeying fluctuation-dissipation.[8]) A time step of $0.01\sigma(m/\varepsilon)^{1/2}$ was used. Conformations of the precursor chains were considered equilibrated by inspection of the average radius of gyration. This quickly reached a plateau (see figure 6.13), though the equilibration run was further extended over several millions of MD steps to accumulate configurations for statistical averages.

After equilibration of the conformations of the unlinked precursor chains, intrachain cross-linking was activated. Two linker beads formed a bond if their mutual distance was smaller than the 'capture radius'. As usual in simulations of network formation[9], this was 30% larger than the bead size. In the case of multiple options for bonding (several linkers within the same capture radius), the pairs to form bonds were randomly selected. Once a bond was formed between two given linkers, it remained permanent during the rest of the simulation, and bonding to other linkers was not permitted. The case of tri-functionality was simulated by allowing the linker to form permanent bonds with two other different beads. Integration of the equations of motion was performed in the velocity-Verlet scheme, following the impulse approach.[10] MD runs were performed until cross-linking was totally completed, i.e., until all linkers formed mutual bonds. Then they were further extended over several millions of MD steps to accumulate configurations for statistical averages. Even for fixed values of N and f, the time needed for completing cross-linking showed a broad distribution for the different precursors, with a dispersion of about three time decades. This is a direct consequence of the highly stochastic character of the cross-linking process. According to the number of beads per polymer, $2(N+f)$, the longest times extended from a few million steps (for N ~ 100) to several hundred million steps (for N ~ 400). For each fixed N and f, statistical averages were performed over 200 different polymers and using

typically 100-1000 configurations per polymer. The average monomer displacement, *relative to the polymer center-of-mass*, between two consecutive configurations used for averages was of about twice the average radius of gyration, i.e, the expected limit for uncorrelated configurations. The investigated molecular weights qualitatively corresponded to the experimental range of 10 kDa – 100 kDa. Likewise, relevant cross-linker fractions (in the range of 8 % - 40 %) were investigated. For the largest investigated systems, full cross-linking led to a reduction in the polymer size by 25-35 %, as deduced by analyzing radii of gyration R_g. Results for the radius of gyration of the investigated systems in the bifunctional case are shown in figure 6.14. The change in the nature of the cross-linked conformations, with respect to the unlinked precursors is evident, not only from the size reduction, but also from the change in the scaling exponent for the power-law $\langle R_g^2 \rangle \sim N^v$. Whereas v ≈1.3 for the precursors, resembling the Flory exponent for self-avoiding chains, we find v ≈1.1 for the cross-linked polymers, closer to the behavior of Gaussian chains.

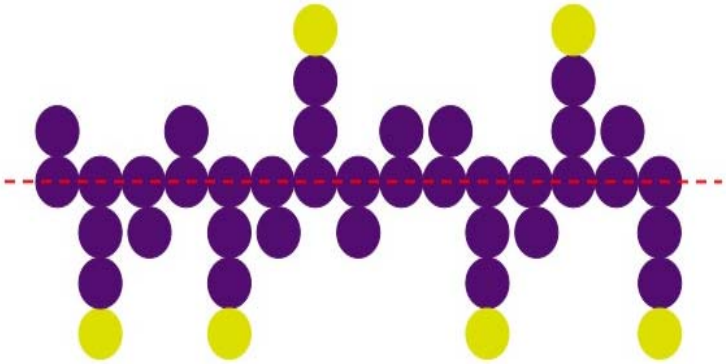

Figure 6.12. Scheme of the simulated bead-spring model in the precursor state. Linkers are yellow colored. The dashed line indicates the main backbone.

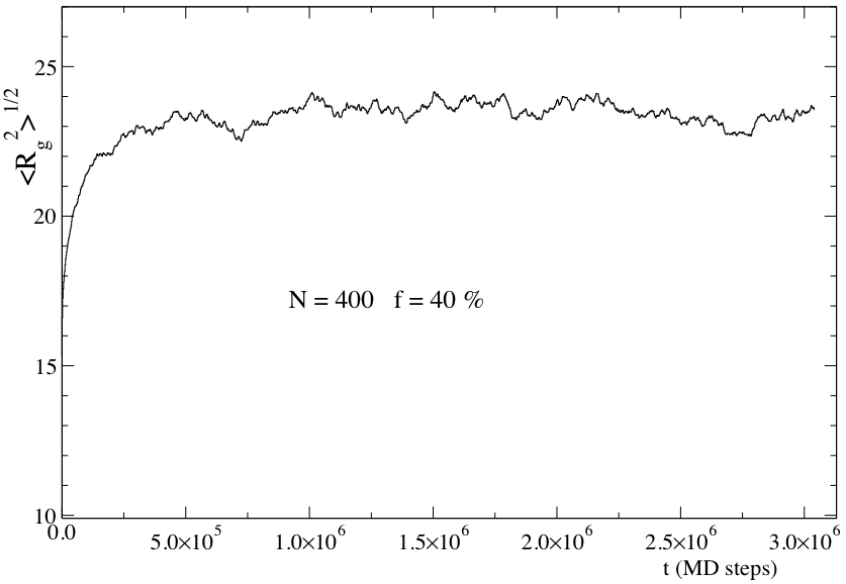

Figure 6.13. Typical evolution of the average radius of gyration during equilibration of the precursor. At each time step, the latter is averaged over 200 different polymers.

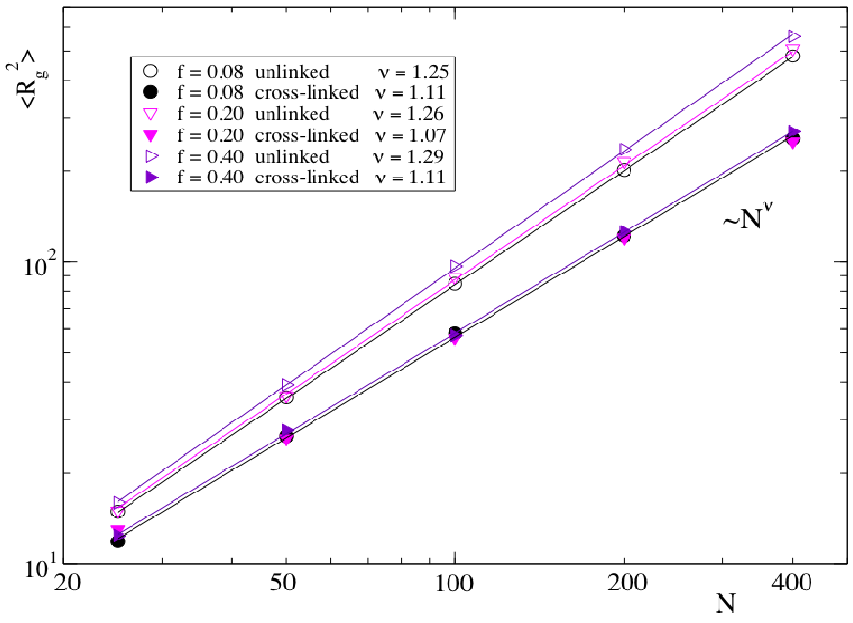

Figure 6.14. Scaling laws for the average squared radius of gyration vs. the backbone length N, and for several fractions of cross-linkers f (bifunctional case). Symbols are simulation data. Error bars are of the order of the symbol size. Lines represent power-law behavior $\langle R_g^2 \rangle \sim N^{\nu}$. Exponents are given in the legend.

6.3 References

[1] Howard G. Barth, Barry E. Boyes and Christian Jackson. *Anal. Chem*., **1996**, *68*, 445R.

[2] Xiaohui W., Xinping Q., Chi W. *Macromolecules*., **1998**, *31*, 2972.

[3] Sarah J. Haigh, Hidetaka Sawada and Angus I. Kirkland. *PRL*., **2009,** 103, 126101.

[4] Chen, Z., T. G. Deutsch, et al. UV-Vis Spectroscopy. *Photoelectrochemical Water Splitting*., **2013**, Springer**:** 49.

[5] Koch, M.H.J., Vachette, P., Svergun, D.I. *Q. Rev. Biophys*., **2003**, 36, 147.

[6] Dominique Durand et al. *Journal of Structural Biology.,* **2010,** 169, 45.

[7] Kremer, K., Grest, G. S. *J. Chem. Phys.,* **1990**, *92*, 5057.

[8] Allen, M. P., Tildesley, D. J. *Computer simulation of liquids*, Oxford University Press, Oxford (UK), **1989**.

[9] Rottach, D. R., Curro, J. G., Budzien, J., Grest, G. S., Svaneborg, C., Everaers, R. *Macromolecules.,* **2006**, 39, 5521.

[10] Izaguirre, J.A., Catarello, D. P., Wozniak, J. M., Skeel, R. D. *J. Chem. Phys.,* **2001**, 114, 2090.

CHAPTER 7:

Final conclusions

Final Conclusions

Mimicking the behavior of naturally occurring macromolecules – such as proteins – is one of the key aims of advanced polymer chemistry. The folding of single polymer chains has steadily been growing in popularity, especially for the preparation of covalently bonded polymeric nanoparticles. In the present thesis, initial attempts towards mimicking the structure of natural biomacromolecules *via* single-chain folding of well-defined linear synthetic polymer precursors have been presented through four new synthetic routes: alkyne homocoupling, Michael addition, copper complexation and enamine formation.

First, a significant breakthrough in the field has been made by the construction of single-chain nanoparticles at r.t under normal atmospheric conditions *via* intrachain Glaser-Hay coupling. In this case, P(MMA-*co*-PgA) copolymers were synthesized *via* redox initiated RAFT polymerization at room temperature. Accurate control over the molecular weight, polydispersity and composition of the linear P(MMA-*co*-PgA) precursor was demonstrated by working up to a maximum polymerization time of 20 h and a maximum PgA monomer content in the feed of 35 mol%. The versatility of such "self-clickable" P(MMA-*co*-PgA) precursors has allowed, for the first time, the rapid and highly-efficient preparation of uniform single-chain polymer nanoparticles at r.t. through copper-catalyzed alkyne homocoupling (C-C "click" chemistry).

Next, by taking inspiration from the function of intrinsically disordered proteins (IDPs), transient binding disordered SCNPs have been synthesized from which the controlled delivery of both dermal protective (vitamin B_9) and anticancer cargos (hinokitiol) has been carried out. Random copolymers P(MMA-*co*-AEMA) of high molecular weight and relatively narrow size dispersity were first synthesized by RAFT copolymerization. Unimolecular nanoparticles were then formed *via* the multidirectional self-assembly of

polymeric chains driven by multiple intrachain Michael addition reactions. By using single-chain Michael nanoparticles as vitamin B_9 and hinokitiol nanocarriers, the simultaneous delivery of vitamin B_9 and hinokitiol to water solutions at a relevant pH has been demonstrated.

Moreover, we have synthesized catalytically active single-chain nanoparticles (SCNPs) based on P(MMA-*co*-AEMA) copolymers that feature β-ketoester functional groups which can be folded/collapsed *via* intrachain Cu (II) complexation of **AEMA** units. These synthetic soft nano-entities approaching the size of natural enzymes display catalytic *specificity* a low concentration of Cu(II) ions during the oxidative coupling of mixtures of chemically related terminal acetylene substrates. Such specificity is not afforded by classical catalysts (*i.e.,* $CuCl_2$, $Cu(OAc)_2$, $Cu(acac)_2$) under exactly the same reaction conditions.

Finally, taking into account the great potential of dynamic covalent bonds (DCBs) for the development of new stimuli-responsive polymer nanoparticles, pH-responsive SCNPs have been obtained by enamine dynamic covalent bonds. These pH-responsive SCNPs can undergo component exchange processes between alkyl monoamine/alkyl diamine and quantitatively hydrolyse back to linear polymer chains upon the addition of a strong acid. This proof of concept paves the way to the use of enamine DCBs for the construction of other responsive, structurally dynamic polymeric systems beyond SCNPs.

This thesis has contributed to the following publications:

- **Ana Sanchez-Sanchez**, Arantxa Arbe, Juan Colmenero and J. A. Pomposo. *Polymer Synthesis from Water-Borne Metallo-Folded Single-Chain Nanoparticles*. (In preparation).

- **Ana Sanchez-Sanchez**, Arantxa Arbe, Juan Colmenero and J. A. Pomposo (2014). *Metallo-Folded Single-Chain Nanoparticles with Catalytic Selectivity*. ACS Macro Letters. **2014**, 3, 439-443.

- **Ana Sanchez-Sanchez,** D. A. Fulton, and J. A. Pomposo (2014). *pH-responsive single-chain polymer nanoparticles utilising dynamic covalent enamine bonds.* Chemical Communications. **2014**, 50, 1871-1874.

- **Ana Sanchez-Sanchez** and J. A. Pomposo (2014). *Single-Chain Polymer Nanoparticles via Non-Covalent and Dynamic Covalent Bonds (Review).* Particle & Particle Systems Characterization. **2014**, 31, 11-23. (**BACK COVER**).

- Angel J. Moreno, Federica Lo Verso**, Ana Sanchez-Sanchez**, Arantxa Arbe, Juan Colmenero and J. A. Pomposo (2013). *Advantages of Orthogonal Folding of Single Polymer Chains to Soft Nanoparticles*. Macromolecules. **2013**, 46, 9748-9759.

- **Ana Sanchez-Sanchez**, Somayeh Akbari, Angel J. Moreno, Federica Lo Verso,Arantxa Arbe, Juan Colmenero and J. A. Pomposo. *Design and Preparation of Single-Chain Nanocarriers Mimicking Disordered Proteins for Combined Delivery of Dermal Bioactive Cargos*. Macromolecular Rapid Communications. **2013**, 34, 1681-1686. (**FRONT COVER**)

- **Ana Sanchez-Sanchez**, Somayeh Akbari, Agustin Etxeberria, Arantxa Arbe, Urs Gasser, Angel J. Moreno, Juan Colmenero and J. A. Pomposo. *"Michael" Nanocarriers Mimicking Transient-Binding Disordered Proteins.* ACS Macro Letters. **2013**, 2, 491-495.

- **Ana Sanchez-Sanchez**, Irma Perez-Baena, Jose A. Pomposo. *Advances in Click Chemistry for Single-Chain Nanoparticle Construction (Review)*.Molecules. **2013**, 18, 3339-3355.

- **Ana Sanchez-Sanchez**, Isabel Asenjo-Sanz, Lorea Boruga and J. A. Pomposo. *Naked and Self-Clickable Propargylic-Decorated Single-Chain Nanoparticle Precursors via Redox-Initiated RAFT Polymerization*. Macromolecular Rapid Communications. **2012**, 33, 1262-1267.